'Complex tracer mobilities in polymer networks revealed by Fluorescence Correlation Spectroscopy'

Dissertation
zur Erlangung des Grades
‘Doktor der Naturwissenschaften’
(Dr. rer. nat.)
im Promotionsfach Chemie

am Fachbereich Chemie, Pharmazie und Geowissenschaften

der Johannes Gutenberg–Universität Mainz

vorgelegt von

M.Sc.Chem. Eng. Apostolos N. Vagias

geboren in Athen,Hellas

Mainz, 2013

Die vorliegende Arbeit wurde im Zeitraum von September 2010 bis Juni 2013 am Max-Planck-Institut für Polymerforschung in Mainz unter der Anleitung von Herrn Prof. Dr. XXXX, Herrn Prof. Dr. XXXX und Dr. XXXX angefertigt.

Tag der mündlichen Prüfung: xx.xx.xxxx

Dekan: Prof. Dr.

Erster Berichterstatter: Herr Prof. Dr.

Zweiter Berichterstatter: Herr Prof. Dr.

ΑΡΧΙΜΗΔΗΣ (287-212 π.Χ.): ‘ΔΟΣ ΜΟΙ ΠΑ ΣΤΩ ΚΑΙ ΤΑΝ ΓΑΝ ΚΙΝΑΣΩ‘

Archimedes (Doric Hellenic dialect), 287-212 B.C:

‘Give me a spot to stand still and I can move the earth‘

Archimedes (Dorische Hellenische Dialekt), 287-212 B.C:

‘Gib mir ein Punkt zu stehen und ich kann die Erde bewegen.‘

Contents

Abstract

Gels are elastic porous polymer networks that are accompanied by pronounced mechanical properties. Due to their biocompatibility, 'responsive hydrogels' (HG) have many biomedical applications ranging from biosensors and drug delivery to tissue engineering. They respond to external stimuli such as temperature and salt by changing their dimensions. Of paramount importance is the ability to engineer penetrability and diffusion of interacting molecules in the crowded HG environment, as this would enable one to optimize a specific functionality. Even though the conditions under which biomedical devices operate are rather complex, a bottom-up approach could reduce the complexity of mutually coupled parameters influencing tracer mobility. The present thesis focuses on the interaction-induced tracer diffusion in polymer solutions and their homologous gels, probed by means of Fluorescence Correlation Spectroscopy (FCS). This is a single-molecule-sensitive technique having the advantage of optimal performance under ultralow tracer concentrations, typically employed in biosensors. Two different types of hydrogels have been investigated, a conventional one with broad polydispersity in the distance between crosslink points and a so-called 'ideal', with uniform mesh size distribution. The former is based on a thermoresponsive polymer, exhibiting phase separation in water at temperatures close to the human body temperature. The latter represents an optimal platform to study tracer diffusion. Mobilities of different tracers have been investigated in each network, varying in size, geometry and in terms of tracer-polymer attractive strength, as perturbed by different stimuli. The thesis constitutes a systematic effort towards elucidating the role of the strength and nature of different tracer-polymer interactions, on tracer mobilities; it outlines that interactions can still be very important even in the simplified case of dilute polymer solutions; it also demonstrates that the presence of permanent crosslinks exerts distinct tracer slowdown, depending on the tracer type and the nature of the tracer-polymer interactions, expressed differently by each tracer with regard to the selected stimulus. In aqueous polymer solutions, the tracer slowdown is found to be system-dependent and no universal trend seems to hold, in contrast to predictions from scaling theory for non-interacting nanoparticle mobility and empirical relations concerning the mesh size in polymer solutions. Complex tracer dynamics in polymer networks may be distinctly expressed by FCS, depending on the specific synergy among-at least some of - the following parameters: nature of interactions, external stimuli employed, tracer size and type, crosslink density and swelling ratio.

Zusammenfassung

Gele sind elastische, poröse Polymernetzwerke, die besondere mechanische Eigenschaften haben. Aufgrund ihrer Biokompatibilität, haben "Hydrogele" (HG) viele biomedizinische Anwendungen im Bereich von Biosensoren und Wirkstoffabgabe bis hin zur Gewebezüchtung. Darüber hinaus reagieren sie auf externe Stimuli, wie Temperatur und Salz, durch Veränderung ihrer Abmessungen. Von größter Wichtigkeit ist die Möglichkeit, Durchlässigkeit und Diffusion von wechselwirkenden Molekülen in der überfüllten HG Umgebung zu erzeugen, da dies ermöglicht, die Design-Parameter biosensorbezogener Anwendungen zu optimieren. Die Bedingungen, unter denen biomedizinische Geräte arbeiten, sind zwar sehr komplex, aber ein Bottom-up-Ansatz könnte den Zusammenhang der miteinander gekoppelten Parameter, die die Tracer Mobilität beeinflussen, sowie die Grundlagen der Tracer-Polymer-Wechselwirkungen erklären. Die vorliegende Arbeit behandelt die Wechselwirkungsinduzierte Diffusion von Tracern in Polymerlösungen und derer homologen Gele, sondiert mittels Fluoreszenz-Korrelations-Spektroskopie (FCS). Dies ist eine Einzel-Molekül-sensitive Methode, die den Vorteil hat, bei ultraminimalen Tracerkonzentrationen, die typischerweise bei Biosensoren vorliegen, optimale Ergebnisse zu erzielen.Zwei verschiedene Typen von Hydrogelen wurden untersucht, eine herkömmliche mit breiter Polydispersität der Abstände zwischen den Vernetzungsstellen und ein sogenanntes "ideales" Gel, mit gleichmäßiger Verteilung der Maschenweiten. Die erstgenannte Art von Gel ist auf einem thermoresponsiven Polymer basiert, das eine Phasentrennung in Wasser bei Temperaturen nahe der Temperatur des menschlichen Körpers aufweist, die ihre häufige Verwendung als Baustoff für Biosensorplattformen rechtfertigt. Die zweite Art ist ein ideal vernetztes Polymernetzwerk, das man als Modelsystem für Untersuchung von Tracer Diffusion verwenden könnte. Die Beweglichkeit von verschiedenen Tracern wurden in beiden Netzwerktypen untersucht, die sich in Größe, Geometrie und in der anziehenden Kraft der Tracer-Polymere voneinander unterscheiden und die auch durch äußere Einflüsse variiert werden. Die Arbeit zeigt die Bedeutung der FCS im Studium komplexer Mobilität in Polymernetzwerken. Sie untersucht systematisch die Stärke und Beschaffenheit der verschiedenen Tracer-Polymer-Wechselwirkungen; sie beschreibt auch, dass die oben genannten Wechselwirkungen auch in dem vereinfachten Fall von verdünnten Polymerlösungen sehr wichtig sein können. In der Arbeit wird auch gezeigt, dass permanente Vernetzungspunkte unterschiedliche Verlangsamungen der Tracer Diffusion verursachen. Die Verlangsamungen hängen vom Tracer-Typ und der Art der Tracer-Polymer-Wechselwirkungen ab, die von jeder Größe in Abhängigkeit vom Stimulus anders beeinflusst wird. Die Verlangsamung von der Tracer Mobilität in wässrigen Polymerlösungen war systemabhängig. Kein einziger universeller Trend scheint zu existieren, was den Vorhersagen, die man mittels der Skalentheorie von der Mobilität von nicht-wechselwirkenden Nanopartikeln und zur empirischen Beziehungen bezüglich der Maschengröße von Polymerlösungen machen würde, widerspricht. Komplexe Tracer Dynamiken in Polymernetzwerken können sehr gut mittels der FCS beobachtet werden. Dies hängt von der spezifischen Synergien zwischen zumindest einigen der folgenden Parameter ab: Art der Wechselwirkungen, äußere eingesetzte Reize, Art und Größe der Tracer, Vernetzungsdichte und Schwellungsverhältnis.

Motivation and outline of the thesis

The motivation for performing this thesis has been five-fold:

(1) To identify and elucidate the nature of tracer-polymer interactions, even for the simplified case of molecular tracers.
(2) To assess the additional influence of permanent crosslink and crosslink density.
(3) To quantify changes in network's swollen thickness and tracer mobilities, as a result of external stimuli perturbation (salt or temperature)
(4) To extend the afore-mentioned motivating points towards a more biosensor application-oriented problem. Namely, to address the corresponding influences on antibody mobilities in grafted hydrogel layers.
(5) To investigate mobilities of different tracers (solid particles vs. flexible macromolecules) in a so-called 'ideal hydrogel', a gel network type namely employed for the first time for solute transport studies. Moreover, to compare these findings with mobility in homologous homopolymers and to examine if scalability of the diffusion slowdown holds taking into account system-dependent parameters.

The 1st Chapter begins with a brief outline of different types of interactions of potential interest to the experimental results of the following Chapters. Next, fundamentals concerning conformations and scaling relations of uncharged macromolecules, under different solvency conditions, are presented. An analogous description then follows for the case of charged macromolecules, following a brief introduction to the Poisson-Boltzmann equation, a relevant topic for this thesis.

In the 2nd Chapter, the experimental setup of FCS is presented, followed by fundamentals concerning the theory of FCS and associated fitting equations used to describe the tracer dynamics in the experiments of this thesis. In the same Chapter, the materials and the associated structures, as well as the sample preparation for the experiments of this thesis, are presented. The Chapter ends with a short review of additional characterization methods, supporting directly or indirectly the different projects outlined in Chapters 3, 4 and 5.

Results concerning tracer mobilities in Poly-(N-isopropylacrylamide) (PNiPAAm) networks are presented in Chapters 3 and 4, and analogous mobility findings in Tetra-PEG hydrogels in Chapter 5. The description of molecular tracer mobilities in thermoresponsive polymer (PNiPAAm) networks proceeds on a bottom-top approach, starting from PNiPAAm solutions in Chapter 3 and going on to crosslinked PNiPAAm gels in Chapter 4. In Chapter 3, a combination of FCS experimental findings and

results from MD simulations concerning complex tracer mobilities in dilute PNiPAAm solutions at good solvency is presented. Chapter 4 addresses the influence of permanent crosslinks and crosslink density on molecular tracer mobility. The findings are presented in good solvency conditions (section I), while in poor solvency conditions (section II) the influence of external stimuli (salt, temperature) on the corresponding tracer mobility has been additionally investigated. Chapter 4 ends with section III, where results concerning mobility of an antibody in grafted hydrogel layers are demonstrated and discussed, towards a biosensor application.

The experiment of the 5th Chapter has been performed with the aim to potentially represent a model study based on which future tracer mobility studies in hydrogels may be compared with. The diffusion of different types of particles, exhibiting differences in size and/or geometry (branched or linear) has been studied in 'ideal' Tetra-PEG hydrogels. Such ideality stems from a narrow pore size distribution and was absent from the PNiPAAm matrix investigated in Chapters 3 and 4. Selective mobility data in Tetra-PEG hydrogels have been compared with corresponding data in PEO aqueous solutions, to address the influence of crosslinks at the same monomer concentration. Different scaling attempts for the diffusion slowdown in the homopolymer networks are presented and discussed, with the goal being to reach a reliable prediction of transport features based on few characteristic physical parameters for the tracer and the host matrix.

Chapter 1: Theoretical background

1.1. Short summary of interactions between colloidal particles

In this thesis, experimental findings involving tracer-polymer interactions are described. It is hence necessary to briefly present associated interparticle interactions related with the topics of this thesis. There are different ways to classify interparticle interactions in polymer systems:

(i) based on their length-scale: short-range and long-range,

(ii) in view of the specificity - or not- of the interactions.

(iii) A last -less conceptually sharp- conventional classification is a separation between DLVO and non-DLVO forces.

Two of the most classical long-range interparticle interactions are the hydrodynamic and Coulombic interactions. The long range nature of both is that the potential decays with the inverse of the interparticle distance (r):

$$V'(r) \sim \frac{1}{r} \qquad (1.1.1)$$

An 'in-depth' presentation on hydrodynamic interactions can be found by the book of J. K.G. Dhont [1]. In the case of solvent-solute interactions, a given solute particle A that undergoes Brownian motion with a certain velocity, $V_A(t)$, induces flow to its neighboring solvent molecules. Then, momentum, $\boldsymbol{J_{AB}(t_0)}$, will propagate at t_0 through the solvent continuum from particle A until it encounters another Brownian particle B, initially inert at t_0, with a momentum transfer from A to B, as illustrated in Fig.1.1.1.

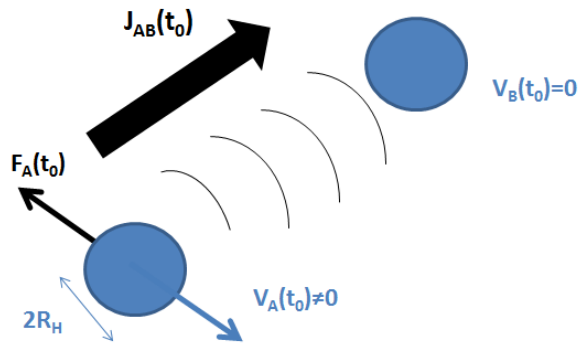

Fig.1.1.1. Qualitative depiction of hydrodynamic interactions (according to [1]) for a 'two-body' problem at a given instant, t_0. Momentum, $J_{AB}(t_0)$, is transferred from particle A with non-zero velocity $(V_A(t_0) \neq 0)$, through the solvent continuum to another immobilized particle $(V_B(t_0) = 0)$. The 'echo' of the propagating momentum are denoted by the black curves, moving away from particle A. Due to backflow of momentum, a hydrodynamic force, $F_A(t_0)$; is exerted by the solvent to particle A.

The hydrodynamic interaction problem may be envisaged either at the single particle level (i.e. interaction of one solute particle with another solute particle), or it is a many-body problem (one solute particle in a solvent continuum in presence of many other particles[1]. In the simplest case of two-body interactions (very dilute solution), the hydrodynamic force exerted at a given particle i, at a given instant t_0, is described by [1]:

$$\boldsymbol{F_i} = -\gamma \cdot V_{\mathrm{i}} \tag{1.1.2}$$

Here $\gamma(= 6 \cdot \pi \cdot R_{\mathrm{h,np}} \cdot \eta_{\mathrm{s}})$ is the particle's friction coefficient, V_{i} is the i[th] particle's velocity, $R_{\mathrm{h,np}}$ is the particle's hydrodynamic radius and η_{s} is the solvent's viscosity [2]. A second type of long-range interactions encountered in charged colloidal particles are Coulombic interactions[3]. These can be repulsive or attractive and the Coulombic potential, $V'_{\mathrm{coulombic}}(\mathrm{r})$, between two charges $\boldsymbol{q}_1$ and $\boldsymbol{q}_2$ separated by a distance, r, in vacuum with dielectric pemitivity, ε_0, is described by the following equation, according to Carrillo and coworkers [4]:

$$V'_{\mathrm{coulombic}}(\mathrm{r}) = \frac{\boldsymbol{q}_1 \cdot \boldsymbol{q}_2}{4 \cdot \pi \cdot \varepsilon_0 \cdot \mathrm{r}} \tag{1.1.3}$$

A modified form of the Coulombic potential when an electrostatic double layer exists and/or when the particles may no longer be considered as point-like, is the so-called Yukawa potential [5]. This form is frequently applied when interparticle distances are quite large and the Coulombic potential is not too strong. By taking into account the Debye layer thickness, K^{-1}, along the line of the Debye-Hückel theory[3] (discussed in the section for the Poisson-Boltzmann equation in this chapter), the electrostatic potential obtains the following screened Coulombic form:

$$V'_{\mathrm{Yukawa}}(\mathrm{r}) = V'_{\mathrm{coulombic}}(\mathrm{r}) \cdot \mathrm{e}^{-\mathrm{K}\cdot\mathrm{r}} \tag{1.1.4}$$

Short range interactions can be hydrophobic interactions, excluded volume interactions, hydrogen bonds and Van der Waals interactions. In the case of dipole-dipole interactions (permanent, induced or combination), the short range interparticle interactions are usually described by a Lennard-Jones potential [6]:

$$V'_{\mathrm{sr}}(\mathrm{r}) = 4 \cdot \varepsilon \cdot \left(\left(\frac{\sigma}{\mathrm{r}}\right)^6 - \left(\frac{\sigma}{\mathrm{r}}\right)^{12}\right) = \begin{cases} 0, & \mathrm{r} \geq \mathrm{r_{cut}} \\ 4 \cdot \varepsilon \cdot \left(\left(\frac{\sigma}{\mathrm{r}}\right)^6 - \left(\frac{\sigma}{\mathrm{r}}\right)^{12}\right) - 4 \cdot \varepsilon \cdot \left(\left(\frac{\sigma}{\mathrm{r_c}}\right)^6 - \left(\frac{\sigma}{\mathrm{r_c}}\right)^{12}\right), & \mathrm{r} < \mathrm{r_{cut}} \end{cases} \tag{1.1.5}$$

where $V'_{\mathrm{sr}}(\mathrm{r})$ represents the short-range potential, ε the potential's attractive well depth, σ the hard sphere diameter (for hard core particles) and $\mathrm{r_{cut}}$ represents a critical distance, beyond which the potential decays to zero. The term $\left(\frac{\sigma}{\mathrm{r}}\right)^6$ corresponds to Van der Waals attractions, while $\left(\frac{\sigma}{\mathrm{r}}\right)^{12}$ corresponds to excluded volume interactions between two given hard spheres, with the exclusion distance being equal to $2 \cdot \sigma$, twice their diameter.

1.2. Solvency and structural conformations for uncharged polymers

The present section is devoted to static properties of polymer chains. The common backbone of the experiments described in this thesis has been tracer diffusion in aqueous polymer solutions and dense polymer networks (gels), examined under different solvency conditions. The description proceeds with the presentation of scaling relations at the level of single polymer chain in a solvent, up to the more complex case of swollen polymer networks. For a more thorough description of polymer physics, the following works [7-9] are recommended.

Depending on the interplay of the associated solvent-monomer interactions, a polymer chain in solution can be viewed as an ideal or a real. In an ideal chain, interactions between monomers along the same chain are neglected and the distribution of monomers (end-to-end distance of the chain) follows a Gaussian distribution [7]. Such interchain or intrachain monomer-monomer interactions are explicitly considered in a case of a real chain [7].

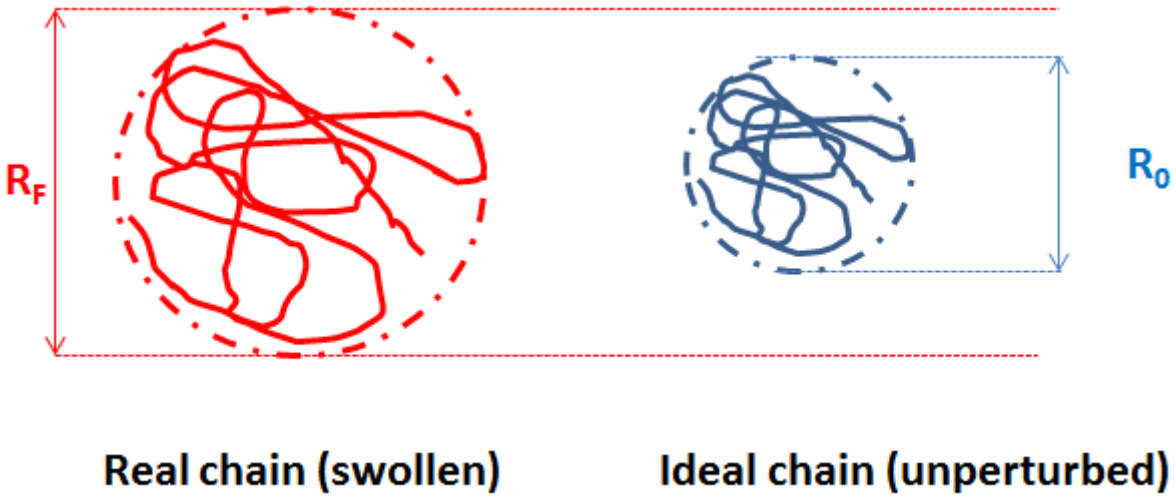

Fig.1.2.1. Qualitative representation of a real chain with excluded volume interactions with a coil dimension, R_F, (left) and an ideal chain with coil dimension, R_0 (right).

Concerning polymer solvency, [10] Flory has described in a mean field approach, a thermodynamic relation between solvency of a real chain and solvent-polymer interactions. Although the theory neglects chain connectivity, is still employed as it provides plausible qualitative information. As has been stated by M. Rubinstein and R. Colby, the equilibrium size of the real (fully swollen) chain in a given solvent, $\mathrm{R_F}$, degree of polymerization, N, and monomer excluded volume, $\mathbf{v}$, stems from the minimization of the chain's Helmholtz Free Energy (A) with respect to the size $(\frac{\partial \mathrm{A(R)}}{\partial \mathrm{R}} = 0)$. The overall chain's free energy is the sum between favorable excluded volume interactions per chain

(A_{int}) that promote chain swelling [11] and the entropic cost per chain (A_{ent}) related with the increasing order imposed upon swelling (eq. 1.2.1) [12], described as[7]:

$$A = A_{int} + A_{ent} \cong k_B \cdot T \cdot (\mathbf{v} \cdot \frac{N^2}{R_F^3} + \frac{R_F^2}{N \cdot b^2}) \quad (1.2.1)$$

The excluded volume, $\mathbf{v}(T)$, is a temperature-dependent parameter related with the segmental volume, b^3:

$$\mathbf{v}(T) = b^3 \cdot (\frac{T-\boldsymbol{\theta}}{T}) \quad (1.2.2)$$

The relative temperature deviation from the so-called $\boldsymbol{\theta}$ temperature, $(\frac{T-\boldsymbol{\theta}}{T})$ (1.2.2), is what determines the sign of the excluded volume. Based on the value of $\mathbf{v}(T)$, different polymer solvency conditions (solvent quality parameter, ν) emerge that dictate distinct chain conformations at equilibrium:

(i) A good solvent is the one where the excluded volume has positive value (monomer-monomer attractions are weaker than monomer-solvent attractions), with chain size, R_F [7]:

$$R_F = b \cdot ((\frac{\mathbf{v}}{b^3})^{2\cdot\nu-1}) \cdot N^{\nu}, (\nu = 0.588) \quad (1.2.3)$$

(ii) In a theta solvent ($\nu = 0.5$), the excluded volume is exactly zero ($\mathbf{v}(\boldsymbol{\theta}) = 0$) [7]:

$$R_0 = b \cdot N^{1/2} \quad (1.2.4)$$

(iii) Finally, in a non-solvent[7], the monomer-monomer attractions are significantly stronger than monomer-solvent attractions, leading to a characteristic size:

$$R_{non-solvent} (= b \cdot N^{\cdot 1/3}) \quad (1.2.5)$$

The parameter $\mathbf{v}(T)$ cannot be experimentally accessible; it is, however, related with the experimentally measurable Flory's interaction parameter, ($\chi(T)$) [7], as: $\mathbf{v}(T) = (1-2\cdot\chi(T))\cdot b^3$. For a monomer A dissolved in solution, the parameter ($\chi(T)$) describes a relation between the monomer-monomer (ε_{AA}), solvent-solvent (ε_{BB}) and the monomer-solvent (ε_{AB}) interactions and the coordination number, z',of monomer A in the solution and expresses the solubility of monomer A in the mixture of A and B[9],[13]:

$$\chi(T) = \frac{z'}{2} \cdot \frac{(2 \cdot \varepsilon_{AB} - \varepsilon_{AA} - \varepsilon_{BB})}{k_B \cdot T} \quad (1.2.6)$$

Using regular solution theory for the distribution of polymers on a lattice, Flory and Huggins [10] have proposed a relation between the Free energy of polymer-solvent mixing (ΔA_{mix}), the monomer volume fraction (ϕ), the degree of polymerization (N) and the interaction parameter (χ):

$$\Delta A_{mix} = k_B \cdot T \cdot (\left(\frac{\phi}{N}\right) \cdot \ln\phi + (1-\phi) \cdot \ln(1-\phi) + \chi \cdot \phi \cdot (1-\phi)) \quad (1.2.7)$$

The underlying assumptions have been that: (1) the distribution of monomer units on a given lattice is random; (2) the size of solvent and monomer units is similar; (3) the volume of the mixture does not change upon polymer solvation ($V_{mixture} = V_{polymer} + V_{solvent}$). By means of Flory-Huggins equation (eq. 1.2.7), the phase behavior of a polymer chain or polymer network in a given solvent (for known interaction parameter,χ) can be predicted, as a function of the monomer volume fraction, ϕ. In an alternative approach, one may use eq.1.2.7 to calculate the ϕ values required to achieve either single component system, or to have phase separation.

1.2.1. Polymer topology and solvent-polymer interactions at the many-chain level

The polymer overlap concentration, c^*, is a topology determining parameter, discriminating dilute ($c < c^*$) from semidilute ($c > c^*$) polymer solutions. For uncharged polymer solutions, c^* is internally related with the weight-average polymer molecular weight,M_w, and the polymer's hydrodynamic radius, R_H:

$$c^* = \frac{M_w}{(\frac{4}{3} \cdot \pi \cdot R_H^3 \cdot N_A)} \quad (1.2.8)$$

The concept of Gaussian coils, applicable in dilute polymer solutions (Fig.2.1), is not further used at $c > c^*$, as coils start to overlap. Instead, the characteristic length scales that are employed are, with increasing size, the thermal blob ξ_T and the correlation blob ξ [7]. The parameter ξ_T represents the thermal blob size, the smallest representative fractal size for the chain, which is smaller than the ideal chain size (eq. 1.2.5). The thermal blob size, ξ_T, determines the length scale below which intrachain excluded volume interactions are screened. When $c > c^*$ and for distances $r < \xi_T$, monomer-solvent hydrodynamic interactions are not screened, but the chain dimensions are unperturbed from ideal chain conformation. When $c > c^*$ and $r > \xi_T$, excluded volume interactions exist and the chain statistics can no longer be considered ideal. The correlation length, $\xi = R_g \cdot (\frac{c}{c^*})^{-\frac{\nu}{3\cdot\nu-1}}$, is the distance between the overlapping points of two neighboring identical chains with R_g the gyration radius of each chain and ν, the solvency parameter. Alternatively, ξ can also be expressed as a function of the monomer's excluded volume, $\mathbf{v}$, and the solvency conditions, ν and ϕ as follows:

$$\xi = b \cdot ((\frac{b^3}{\mathbf{v}})^{(\frac{2\cdot\nu-1}{3\cdot\nu-1})} \cdot \phi^{-(\frac{\nu}{3\cdot\nu-1})}) \quad (1.2.9)$$

The correlation size, ξ, is related to the osmotic pressure of semidilute polymer solutions, Π_{osm}. Hence, the value of ξ can be determined from osmometry via the measured osmotic pressure, Π_{osm}, as follows[7]:

$$\Pi_{osm} = \frac{k_B \cdot T}{\xi^3} \qquad (1.2.10)$$

Alternatively, ξ can be calculated from scattering measurements[14]. The whole polymer chain is quite often envisioned as a sequence of correlation blobs, each of size ξ.

1.3. Basics of gelation theory and rubber elasticity

Linked by a brief introduction on the topology of polymer solutions, the concept of gelation is presented first in this section, subsequently followed by a brief classification of gels by the crosslink type. Topics on rubber elasticity are selectively outlined, with emphasis on the swelling of rubbery networks and associated theories therein. Gels are materials exhibiting hybrid features from solids and liquids. Submicrometrically, gel networks are polymer structures where many polymer chains overlap with crosslink joints. These crosslinks are knots where applied load (energy) can be stored. The network's mechanical strength increases with increasing crosslink density. Depending on the type and strength of the bonds, gels can be either physical [15]or chemical [16]. In physical gels, crosslinks are only temporary and the gels adopt their stable form under the presence of electrostatic forces or pH alterations [17], or some form of specific interactions, such as hydrogen bonds or short-range interactions. Depending on the ratio between lifetime of crosslink's stability and the experimental time scale, physical gels may be further categorized as strong or weak (for instance, pH-dependent gels [17]). On the other hand, the crosslinks in chemical gels are covalent and hence, permanent. Such covalent linkage can be accomplished either during or after (post) polymerization. In the case of permanent crosslinking, the functionality of the participating macromolecules must be greater or equal to two, in order for covalent bonds between different chains to be formed and hence, the network formation to propagate. Another group of polymer structures that are crosslinked networks are vulcanized natural rubbers, where covalent bonding occurs by crosslinking with sulphur bridges (Goodyear, 1839).

1.3.1. Gelation and percolation transition

The first scientific reports concerning gelation stem back to the independent pioneering works of Stockmayer [18] and Flory [19], who described gelation as a progressive increase of the polymer network to a growing branched cluster whose molecular weight asymptotically approaches an

infinite value. At the gelation point, the polymer network undergoes a continuous transition from a viscous system to an amorphous solid [7], with corresponding changes reflected by i.e an onset of elastic shear modulus. Being related with the polymer molecular weight, also the polymer's viscosity beyond gelation approaches an infinite value and the structure becomes a bicontinuous network of a solvent and a polymer phase. Gelation can also be explained by the critical percolation theory [20, 21]. In brief, percolation theory describes that the viscosity of a polymer solution, $\eta = \eta(\mathbf{p})$), when plotted as a function of the extend of the branching reaction, $\mathbf{p}$, diverges as the gelation point, $\mathbf{p}^*$, is approached from below (Fig. 1.3.1). At $\mathbf{p}$>$\mathbf{p}^*$, shear storage modulus, $\boldsymbol{G}'(\mathbf{p})$, sets in, thus reflecting the onset of elastic properties.

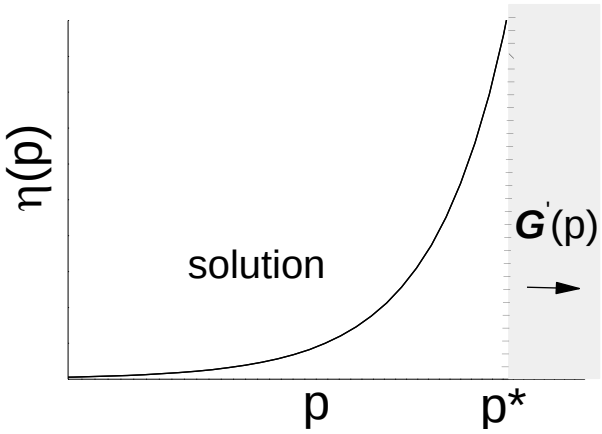

Fig.1.3.1. Qualitative schematic of viscosity ($\eta = \eta(\mathbf{p})$) divergence in a polymer network as the critical extend of percolation transition (gelation point), $\mathbf{p}^*$, is approached from below (redrawn scheme, according to [7]).

When the percolation reaction progresses towards completion, the initially increasing elastic modulus, $\boldsymbol{G}'(\mathbf{p})$, eventually approaches a plateau, being a sign that the reaction has indeed completed. The viscoelastic properties of a polymer network, such as $\eta(\mathbf{p})$, $\boldsymbol{G}'(\mathbf{p})$, are typically described as normalized power-law expressions of the relative difference in extend of reaction, $\mathbf{p} - \mathbf{p}^*$, from the critical extend of reaction at the gelation point, $\mathbf{p}^*$[20, 21].

1.3.2. Mechanical properties of rubbers

Because of the pronounced shear modulus, their elasticity and the frequently accompanied biocompatibility[16, 22], gels have been intensively employed as scaffolds for various bio-related applications[23, 24]: drug delivery, tissue engineering or protein separations and biosensors[25, 26], to name a few. Gels, as they belong to rubbery polymers, are polymer networks that exhibit large strain deformation upon application of an external force and also recover their initially unperturbed dimensions, after removal of the externally applied stress [27]. The restoring force acting on an ideal

rubber is elasticity, which has solely entropic nature: after stress removal, the number of available configurations of the strands between crosslinks, Ω , and hence entropy, S, is again maximized:

$$S = k_B \cdot \ln\Omega \tag{1.3.1}$$

The differential equation of state for rubber elasticity [7], is expressed in terms of total differentials for the free energy, dA, as the sum of internal energy, dU, and of the work of deformation considering an elongation dL induced by an applied force $\boldsymbol{F}$:

$$dA = dU - d(T \cdot S) = -S \cdot dT - p \cdot dV + \boldsymbol{F} \cdot dL \tag{1.3.2}$$

Without showing some intermediate equations concerning partial derivatives of the Helmholtz free energy with respect to its independent variables ($A = A(T, V)$), as well as Maxwell relations, the resulting elastic force, $\boldsymbol{F}$:

$$\boldsymbol{F} = \boldsymbol{F}_{\text{energetic}} + \boldsymbol{F}_{\text{elastic}} = \left(\frac{\partial U}{\partial L}\right)_{T,V} + T \cdot \left(\frac{\partial \boldsymbol{F}}{\partial T}\right)_{V,L} \tag{1.3.3}$$

is the sum of an energetic and an entropic (elastic) component for a rubbery material.

1.3.3. Swelling of unentangled polymer networks

The equilibrium dimensions (i.e. fully swollen volume) of the fully swollen gel network stem from the interplay between excluded volume interactions and the enthalpy of mixing, or, by the balance between the elastic modulus (retraction-favoring entropic force) and the enthalpy-driven (expansion-favoring) osmotic pressure of an equivalent polymer solution of the same monomer volume fraction, ϕ [28]. As previously mentioned, the solvency conditions are determined by the interaction parameter, χ (eq. 1.2.7). Moreover, the swelling properties of the network clearly depend on whether the network is suspended in a solution (isotropic three-dimensional swelling without restrictions in swelling), or grafted (one-dimensional swelling). It is noted that the initial description holds for unanchored networks (free three-dimensional swelling). The Flory-Rehner equation (1.3.4) is an expression describing chemical potential equilibrium for the fully swollen gel. It designates that the chemical potential difference between mixing and elasticity terms for the fully swollen network is zero:

$$\frac{\Delta\mu_{gel}}{R \cdot T} = \left(\frac{\partial A_{mix}}{\partial V}\right)_{T,n} + \left(\frac{\partial A_{el}}{\partial V}\right)_{T,n} = \Pi_{osm,mix} + \Pi_{osm,el} = 0 \tag{1.3.4}$$

Using the ϕ-dependent expressions for the 'mixing energy-related' osmotic pressure ($\Pi_{osm,mix}$) contribution:

$$\Pi_{osm,mix} = -\ln(1-\phi) + \phi + \chi \cdot \phi^2 \tag{1.3.5}$$

and the 'elasticity related' osmotic pressure contribution ($\Pi_{osm,el}$):

$$\Pi_{osm,el} = n^{\#} \cdot V_{solvent} \cdot (\phi - \phi^{\frac{1}{3}}) \quad (1.3.6)$$

one obtains the well-known Frenkel-Flory-Rehner formula:

$$-(\ln(1-\phi) + \phi + \chi \cdot \phi^2 = n^{\#} \cdot V_{solvent} \cdot (\phi^{\frac{1}{3}} - \phi) \quad (1.3.7)$$

The term $V_{solvent}$ in eq.1.3.7 denotes the molar volume of the solvent and the parameter $n^{\#}$ denotes the number of strands between crosslinks. The swelling of rubbery networks has been described so far by one of the following theories, depending on the assumptions concerning the mobility of permanent crosslinks and also on the monomer concentration [7]: the affine deformation theory, the phantom theory or a constrained junction model. Both affine and phantom models visualize the rubbery network as a set of chains being virtually attached to an elastic background (blue rectangular surface, Fig.1.3.2.a) via their crosslinks.

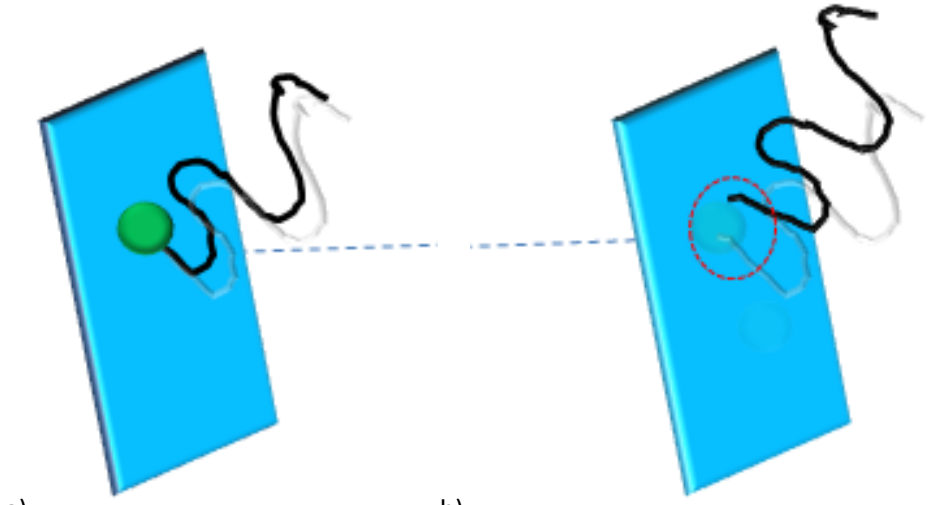

a) b)

Fig.1.3.2. Affine (a) and phantom (b) models for rubber deformation. The permanent crosslinks are represented by the intersection of the chains before (grey) and after (black) swelling with a virtual elastic background (blue rectangular surface) upon which chains are attached. Horizontal dashed line is drawn to guide the eye to the permanent crosslink position in either model (according to [7]).

According to the affine deformation model, the permanent crosslinks (green dots in Fig.1.3.2a) are completely immobile before (grey curve in Fig.1.3.2a) and after (black curve in Fig.1.3.2a) swelling[7]. A fully swollen rubbery network can be envisaged as an elastic structure that undergoes self-similar deformation, relative to its initial dimensions, upon interaction with the solvent. 'Self-similarity' means that the relative deformation is the same, irrespective of the examined polymer length scale- either on a submicrometric or on a macroscopic level. It should be also noted that the Flory-Rehner relation, in particular, is based on the affine deformation model.

An alternative description of network deformation is provided by the phantom model[7]. In contrast to the affine theory, the phantom model takes into account thermal fluctuations of the permanent crosslinks around equilibrium positions, which (fluctuations) are allowed within a certain area (denoted by the dashed red circle, Fig.1.3.2b). Since fluctuations of the crosslinks are allowed, these lead to a decreased shear elastic modulus associated with the phantom model, as compared to the one calculated by the affine model. The corresponding shear elastic moduli, $\boldsymbol{G}'$, between the two models differ, as follows[7]:

$$\boldsymbol{G}'_{\mathbf{phantom}} = \boldsymbol{G}'_{\mathbf{affine}} \cdot \left(\frac{\mathrm{x}' - 2}{\mathrm{x}'}\right) = n^{\#} \cdot \mathrm{k_B} \cdot \mathrm{T} \cdot \left(\frac{\mathrm{x}' - 2}{\mathrm{x}'}\right) \tag{1.3.8}$$

As shown in eq.1.3.8, the afore-mentioned models do not differ concerning the number of strands, $\mathrm{n}^{\#}$, for a network of a given functionality, x'.

1.4. Theory of polyelectrolytes

The previous section has addressed structural properties of uncharged polymer solutions-networks. More often than not, macromolecules possess charges. The presence of charges along the backbone of macromolecules has significant influence on their swellability, their phase behavior, as well on associated thermodynamic variables, such as the osmotic pressure of the polymer network. In this thesis, thermoresponsive copolymers containing methacrylic acid comonomers (monovalent weakly charged polyelectrolytes) have been employed in Chapters 3 and 4. Hence, scaling relations concerning conformations and dynamic properties of polyelectrolytes in solutions are briefly addressed in the present section. In the same framework, the Poisson-Boltzmann equation and its linearized form, namely the Debye-Hückel approximation, equations frequently encountered in charged soft matter systems, are shortly presented. Finally, qualitative and quantitative differences in structural features between solutions of uncharged polymers and of polyelectrolytes are stressed. For a more substantial reading, the following sources [3, 12, 29, 30], among others, can be suggested.

A polyelectrolyte is a macromolecule that contains a sequence of charged monomers along its backbone, surrounded by a distribution of corresponding counterions in the solution[30]. Depending on the distribution in the number and positions of charged monomers, polyelectrolytes can be classified as quenched or annealed [29, 31]. The former case includes polyelectrolytes where charged and uncharged comonomers are assembled with a fixed charge distribution along the macromolecular backbone during polymerization [29]. In annealed polyelectrolytes, the charge depends on the pH of the solution (case of polybases and polyacids [29]). It is then straightforward

that in polyelectrolyte solutions or networks, electrostatic interactions between macromolecules, or between macromolecules and solvent molecules or other co-ions should also be taken into account. In addition to the factors that already influence swellability in uncharged (neutral) polymers, the swelling properties in the fully swollen state sensitively depend on the interplay between -at least some of- the following parameters: pH, ionic strength, counterion valency [32], dielectric constant mismatch between the polyelectrolyte and the solvent, degree of charge dissociation from the polyelectrolyte and electrostatic interactions [29].

On a bottom-up approach of the polyelectrolyte chain features, the total persistence length of a polyelectrolyte, $l_{p,tot}$, is the fundamental length that differentiates static and dynamic properties between a polyelectrolyte chain and an uncharged polymer, exactly because of the presence of electrostatic interactions [29, 30, 33, 34]. An additional fundamental parameter for polyelectrolytes, apart from $l_{p,tot}$, is the Bjerrum length, l_B [12]. The latter (l_B) corresponds to the distance between two elementary unit charges along the backbone of a charged polyelectrolyte embedded in a solvent with certain dielectric constant, ε_r, at which (distance) the electrostatic energy is of the same order as the thermal energy, $k_B \cdot T$. The Bjerrum length is a fundamental parameter involved directly (or not) in several scaling relations for both static and dynamic properties of polyelectrolytes. For flexible polyelectrolytes, l_B represents the smallest unit length based on which electrostatic interactions can be described.

1.4.1. Poisson-Boltzmann equation and the Debye-Hückel approximation

In a seminal work about 100 years ago, Gouy and Chapman [35, 36] have derived a relation connecting the surface potential between two charged planar surfaces to the total charge density and the dielectric constants of the solvent/other cosolutes. The main assumptions of their derivation have been [30]: (i) The various charges are point-like[12]; (ii) the particle density and the electrostatic potential are related by Poisson equation;(iii) the solvent is treated as a continuum with a certain value of dielectric constant (mean field approximation) and (iv) ion-ion correlations, i.e. correlations between charged particles in the solution, are neglected. In view of (ii) and of the fact that the charge density was described by a Boltzmann distribution, the relation was termed as Poisson-Boltzmann (PB) equation. PB equation describes the relation between the surface potential of a charged surface, the charge density, the dielectric constants of the medium and vacuum and the density of the solution.

The Poisson-Boltzmann (PB) equation has been originally derived by minimizing the 1st derivative to the Poisson-Boltzmann functional of the Helmholtz free energy for particular charged particles with respect to the particle density, using the canonical ensemble from statistical mechanics [30]. The

derivation is lengthy and only the resulting functional is referred to in this thesis. The PB functional of the Helmholtz free energy, $F_B[n(r)]$, for charge density, $n(r)$, is the following:

$$F_B[n(r)] = \int \left\{ \mathbf{z} \cdot e \cdot n(r) \cdot \left[\frac{1}{2} \cdot \psi_{free}(r) + \psi_f(r) \right] + k_B \cdot T \cdot n(r) \cdot \left[\ln\left(n(r) \cdot \lambda_T^3\right) - 1 \right] \right\} d^3r \quad (1.4.1)$$

The terms $\psi(r)$ and $\psi_f(r)$ in eq.1.4.1 correspond to free ion and fixed ion density (macromolecular charge) potentials, respectively. The parameter $\mathbf{z}$ corresponds to the valency of the ions, $\lambda_T = \sqrt{2 \cdot \pi \cdot \mathbf{m}' \cdot k_B \cdot T}$ is the thermal de Broglie wavelength for a particle with mass $\mathbf{m}'$, e is the unit charge and $n(r)$ is the charge density in solution. In addition, the total surface potential, $\psi(r)$, is described as the sum of contributions from charges fixed on the surface $\psi_f(r)$ and charges not bound on the surface ($\frac{1}{2} \cdot \psi_{free}(r)$):

$$\psi(r) = \frac{1}{2} \cdot \psi_{free}(r) + \psi_f(r) \quad (1.4.2)$$

Using the assumption (ii) and the following expression for the charge density, $n(r)$, with $\beta = \frac{1}{k_B \cdot T}$:

$$n(r) = \lambda_T^{-3} \cdot e^{-\beta \cdot (\mathbf{z} \cdot e \cdot \psi(r) + \mu_0)} \quad (1.4.3)$$

The final form of PB equation is at last retrieved:

$$\nabla^2 \psi = -\frac{\rho}{\varepsilon_0 \cdot \varepsilon_r} = -\frac{e}{\varepsilon_0 \cdot \varepsilon_r} \cdot \left[z \cdot n_0 \cdot e^{-\beta \cdot \mathbf{z} \cdot e \cdot \psi(r)} + n_f(r) \right] \quad (1.4.4)$$

In eq.1.4.4, ρ represents the total charge density and $n_f(r)$ represents the charge density only from free ions. PB equation can be solved analytically only for the case of planar and cylindrical geometries[30]. In the case of spherical geometries, the equation can only be solved numerically. PB equation is more suitable for potential distributions in the case of monovalent ions and systems with low charge densities. In the case that the electrostatic work is much smaller than the thermal energy ($e \cdot \psi \ll k_B \cdot T$), Debye and Hückel [37] have shown that the Poisson-Boltzmann equation (eq.1.4.4) can be linearized. Under such conditions, they reported that the electrostatic energy term in the charge density relation (eq.1.4.4) can be expanded as follows :

$$e^{-\beta \cdot \mathbf{z} \cdot e \cdot \psi(r)} \cong 1 - \beta \cdot \mathbf{z} \cdot e \cdot \psi(r) + \left(\frac{1}{2!}\right) \cdot \left(\beta \cdot \mathbf{z} \cdot e \cdot \psi^2(r)\right) \quad (1.4.5)$$

Neglecting the 2nd term on the right hand side (eq.1.4.5), the total charge density for n ionic species in the solution can be written, using n_i^{∞} as the total charge density of the ith species in the bulk (away from the charged surface), as:

$$\rho = \sum_{i=1}^{n} \mathbf{z}_i \cdot n_i^{\infty} \cdot e \cdot (1 - \beta \cdot e \cdot \psi(r)) \quad (1.4.6)$$

And by taking into account the electroneutrality principle:

$$\sum_{i=1}^{n} \mathbf{z}_i \cdot n_i^{\infty} \cdot e = 0 \tag{1.4.7}$$

The total charge density for n ionic species in the solution can be simplified as:

$$\rho = -\beta \cdot \sum_{i=1}^{n} \mathbf{z}_i^2 \cdot n_i^{\infty} \cdot e \cdot \psi(r) \tag{1.4.8}$$

Hence, using (1.4.7-1.4.8), the DH approximation obtains the following form:

$$\nabla^2 \psi(r) = -\frac{\rho}{\varepsilon_0 \cdot \varepsilon_r} = \frac{\beta \cdot \sum_{i=1}^{n} \mathbf{z}_i^2 \cdot n_i^{\infty} \cdot e^2 \cdot \psi(r)}{\varepsilon_0 \cdot \varepsilon_r} \tag{1.4.9}$$

The ψ-independent term corresponds to the Debye parameter, K^2:

$$K^2 = \frac{\beta \cdot \sum_{i=1}^{n} \mathbf{z}_i^2 \cdot n_i^{\infty} \cdot e^2}{\varepsilon_0 \cdot \varepsilon_r} \tag{1.4.10}$$

For charged particles in a solution, the following regimes are associated with the corresponding surface potential, $\psi(r)$, as a function of distance, r, from the particle's surface. Following H.J. Butt et al.[38], at very short distances from the surface, a very thin layer, termed as 'Stern layer', is encountered first. This is the distance where counterions are quasi-immobilized on the surface. The Stern layer consists of sub-sections with increasing distance from the particle's surface termed as inner Helmholtz plane and outer Helmholtz plane, with corresponding potentials ψ_0 and ψ_ζ, ($\psi_0 > \psi_\zeta$) respectively. The latter value (ψ_ζ) is the zeta potential that represents the measurable charge on the surface of a colloidal particle and can be measured by one of the following methods: electrophoresis, sedimentation potential and/or electroosmosis[38]. Using the following boundary conditions:

$$\begin{cases} \psi(r = 0) = \psi_0 \\ \psi(r \to \infty) = 0 \end{cases}$$

the DH equation for the simplest one dimensional case ($\nabla^2 \psi = -K^2 \cdot \psi, \psi = \psi(r)$) can be solved analytically:

$$\psi(r) = \psi_0 \cdot e^{-K \cdot r} \tag{1.4.11}$$

Eq.1.4.11. describes that for distances larger than the outer Helmholtz plane, an intermediate regime between the surface of the charged particle and the bulk solution is retrieved, in which the surface potential exhibits an exponential decay with respect to distance r from the particle's surface. The Debye length, K^{-1}, is defined as the distance, beyond which the electrostatic potential, $\psi(r)$, has practically decayed to zero: $\psi(K^{-1}) \to 0$.The Debye length, K^{-1}, is frequently used in scaling relations for polyelectrolyte properties and is hence discussed in the next sections of this chapter.

1.4.3. Structural conformations and scaling relations in polyelectrolyte solutions (absence of salt)

In analogy to a similar description for the uncharged polymers (section 1.2), scaling properties and chain-solvent interactions of polyelectrolytes are summarized in this section. When energy fluctuations become comparable to the thermal energy, $k_B \cdot T$, the intrachain electrostatic interactions favor chain swelling. The equilibrium size of a polyelectrolyte chain with a degree of polymerization N and degree of charge, $\mathbf{f}'$, (total number of charged monomers on a chain: $\mathbf{f}' \cdot N$) in a solvent with dielectric constant, ε_r, is simply a coil conformation (in good solvency conditions) with an end-to-end size, $R_{e,el}$, retrieved from the minimization of the chain's total Flory energy with respect to the polymer size: $\frac{\partial A(R)}{\partial R} = 0$. The equilibrium size of the polyelectrolyte chain, $R_{e,el}$, is a function of the unit charge, e, the uncharged monomer's segment length, b, the interaction parameter, $u(=\frac{l_B}{b})$ [12], of $\mathbf{f}'$and of the degree of polymerization, N [12]:

$$R_{e,el} = b \cdot N \cdot u^{\frac{1}{3}} \cdot \mathbf{f}'^{\frac{2}{3}} \cdot \ln\left(e \cdot N \cdot (u \cdot \mathbf{f}'^{2})^{2/3}\right)^{\frac{1}{3}} \qquad (1.4.12)$$

The characteristic lengths for a polyelectrolyte chain[39], are featured in Fig.1.4.1:

(i) the electrostatic blob with characteristic diameter D_e, an analog to the thermal blob (ξ_T) in uncharged polymer chains (i.e. a length scale below which unperturbed/ideal chain statistics apply) and

(ii) the correlation blob [12] with diameter ξ ($\xi < D_e$).

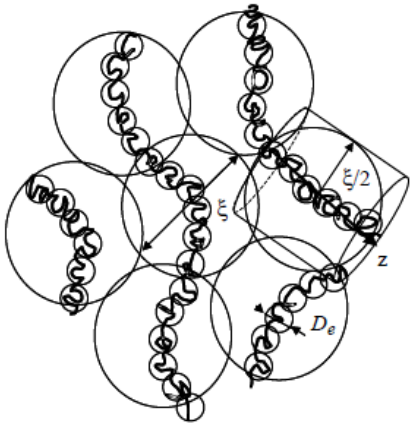

Fig.1.4.1. Representation of the different scaling lengths of a polyelectrolyte chain in solution, in absence of salt: electrostatic blob, D_e, correlation blob, ξ, and diameter of a virtual tube, z, into which a given polyelectrolyte chain is enclosed. Reprinted from 'Theory of polyelectrolytes in solutions and at surfaces', 30 (11), Andrey V. Dobrynin, M. Rubinstein, p.1066 , Elsevier Ltd. (2005), with permission (Elsevier License, Figs.S7-S9) granted from the Copyright Clearance Center.

According to Dobrynin and Rubinstein, the counterion concentration in dilute polyelectrolyte solutions is very low. As such, an unscreened Coulomb potential ($K^{-1} \gg 1$) describes the intrachain Coulombic interactions [12]. This leads to accumulation of charges at the chain ends, which in turn, promoting more significant swelling in the latter chain sections. The overlap concentration, c^*, in polyelectrolyte solutions, is a function of the monomer's segment length, b, the interaction parameter, $u(=\frac{l_B}{b})$ [11], the fraction of charged monomers along the polyelectrolyte backbone, of $\mathbf{f}'$, the degree of polymerization, N and the number of monomers per electrostatic blob, g_e [11]:

$$c^* \cong b^{-3} \cdot u^{-1} \cdot \mathbf{f}'^{-2} \cdot N^{-2} \cdot \ln(\frac{N}{g_e})^{-1} \quad (1.4.13)$$

In semidilute unentangled solutions ($c > c^*$), the following classification holds, depending on the examined length scale. When $r < D_e$, chain statistics are ideal - the dimensions are unperturbed from electrostatics. At $\xi > r > D_e$, existing electrostatic interactions induce chain swelling. The correlation length, ξ, represents the next largest characteristic (screening) length scale of the semidilute polyelectrolyte solutions, after D_e. When $c > c^*$ and also $r < \xi$, the chain conformation becomes Gaussian as excluded volume interactions are screened, while electrostatic interactions are also screened by both counterions and overlapping chains. In contrast to uncharged semidilute polymer solutions, entanglements between polyelectrolyte chains appear, only when $c \geq 1000c^*$ [12]. In analogy to the shear modulus for uncharged polymer chain networks (eq. 1.3.8), the entanglement shear modulus of the polyelectrolyte chain, $\boldsymbol{G'_{ent,charged}}$, with number of strands between entanglements, ν_e:

$$\boldsymbol{G'_{ent,charged}} = \nu_e \cdot k_B \cdot T \quad (1.4.14)$$

represents the energy stored by the network for intermediate times of a chain's motion (times less or equal to the tube's renewal time) and exhibits a characteristic plateau when plotted vs. frequency, ω.

Finally, the description of polyelectrolyte chain conformation under poor solvency conditions [40, 41] remains rather not elaborated, as the topic is quite distant from the major scope of this thesis. Under poor solvency conditions, the polyelectrolyte chain forms pearl-necklace conformations (instead of globular conformation for uncharged polymers). A pearl-necklace asymmetric conformation consists of larger correlation blobs (diameter: D_{blob}) that themselves are assemblies of even smaller thermal blobs, D_T. Different thermal blobs are connected by strings of certain length, l_{string}, the latter being elongated sequences of charged monomers. For a more elaborate discussion on the topic, the reader is prompted to [12],[29, 30].

1.4.4. Structural conformations and scaling relations in polyelectrolyte solutions in presence of salt

The addition of external salt inflicts a charge redistribution in a polyelectrolyte solution. Specifically, the added salt reduces Coulombic repulsions between like-charged intrachain and interchain monomer units. As such, l_B gets reduced (monomers get less charged) and the polyelectrolyte chain becomes more flexible[29]. In presence of salt, the significant lengths in a semidilute polyelectrolyte solution become the electrostatic blob size, D_e^0, the correlation blob size, ξ (Fig.1.4.1), as well as the electrostatic persistence length, l_{scr}. In presence of salt, l_{scr} depends also on the salt concentration (c_s) and on the modified –due to the presence of salt- fraction of charged units on the macromer, $\mathbf{f}^*$, as follows:

$$l_{scr} = (\frac{\mathbf{f}^*}{u})^{\frac{1}{6}} \cdot b^{-\frac{1}{2}} \cdot (c \cdot \mathbf{f}^* + 2 \cdot c_s)^{-\frac{1}{2}} = \xi(c) \cdot (1 + 2 \cdot \frac{c_s}{\mathbf{f}^* \cdot c})^{-1/2} \quad (1.4.15)$$

Following Dobrynin and Rubinstein[12], when $l_{scr} > \xi$, there is no screening of electrostatic interactions. When $l_{scr} < \xi$, electrostatic interactions are screened at length scales larger than the electrostatic screening length ($r > l_{scr}$), while when $r < l_{scr}$, the chain sections appear rod-like. When $\xi > r > l_{scr}$, chain conformation is described by self-avoiding walk of electrostatic blobs with size, l_{scr}, stretched by intrachain electrostatic repulsions. Finally, when $r > \xi$, the chain statistics become 'ideal'-like. In presence of salt, the correlation length of a polyelectrolyte solution, ξ, displays the following monomer concentration dependence, depending on c_s:

$$\begin{cases} \xi \sim c^{-1/2}, & c_s \to 0 \\ \xi \sim c^{-3/4}, & c_s \gg 0 \end{cases}$$

The persistence length, $l_{p,tot}$, also exhibits salt dependence [12]. Finally, any static property of a polyelectrolyte, X, in a solution with salt concentration, c_s, degree of charging in the macromer, $\mathbf{f}^*$and polyelectrolyte's monomer concentration, c, is related with its corresponding property in absence of salt, X_0 , as [12]:

$$X = X_0 \cdot (1 + \frac{2 \cdot c_s}{\mathbf{f}^* \cdot c})^{m} \quad (1.4.16)$$

The parameter m represents some scaling-related parameter. Thus, having presented selective scaling relations for polyelectrolyte chains in absence or presence of salt, the counterion condensation, a central phenomenon related with weak and strong polyelectrolyte chains, is shortly introduced next. It is necessary to devote some text for this phenomenon, as it is related with the weak polyelectrolytes used in the experiments of Chapters 3 and 4.

1.4.5. Counterion condensation

For the description of counterion distribution around strongly charged polyelectrolytes of infinite length in solution, Oosawa [42] and Manning [43] proposed the counterion condensation model (Fig.1.4.2). According to the counterion condensation model, chain end effects are neglected since the charged macromolecules are visualized as infinitely long chains, while the charge is assumed to have a uniform distribution along the backbone[12]. The charged macromolecules are enclosed in virtual cylinders of diameter $2 \cdot \boldsymbol{r}$ (Fig.1.4.2), in absence of externally added salt.

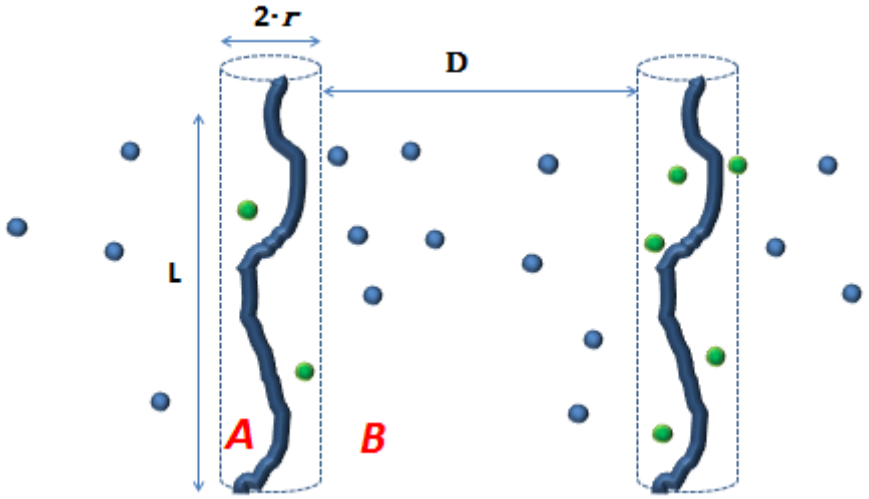

Fig.1.4.2. Qualitative sketch of the counterion condensation model. An infinitely long ($\mathbf{L} > 2 \cdot \boldsymbol{r}$) polyelectrolyte chain is enclosed in a virtual cylinder with condensed counterions (green dots) shown by region A and is separated by a distance D from a nearest-neighboring chain. The total number of counterions present in the solution is the sum of counterions in the adjacent solution (region B) and within the tube (region A). Reprinted from 'Theory of polyelectrolytes in solutions and at surfaces', 30 (11), Andrey V. Dobrynin, M. Rubinstein, p. 1064, Elsevier Ltd. (2005), with permission (Elsevier License, Figs.S7-S9) granted from the Copyright Clearance Center.

Given a total sum of $\mathrm{n_{c,1}} + \mathrm{n_{c,2}}$ counterions present in the solution, $\mathrm{n_{c,1}}$ of them are distributed in the interior of the cylinder (region A) with a corresponding degree of condensation:

$$1 - \mathbf{f}' = \frac{\mathrm{n_1}}{\mathrm{n_1} + \mathrm{n_2}} \tag{1.4.17}$$

while the remaining $\mathrm{n_{c,2}}$ remain in the cylinder's exterior/bulk solution (region B). The electrochemical equilibrium between regions A and B considering a condensation degree on the chain, $1 - \mathbf{f}'$, a total monomer volume fraction, ϕ and $\Delta\psi$ being the electrostatic potential difference between the two phases, reads[12]:

$$\ln\left(\frac{1 - \mathbf{f}'}{\mathbf{f}'}\right) = \ln\left(\frac{\phi}{1 - \phi}\right) - \Delta\psi \tag{1.4.18}$$

The resulting counterion distribution is dictated by the balance between counterion entropy and electrostatic binding attraction. An additional dimensionless parameter associated with the Bjerrum length, l_B (1.4), of a polyelectrolyte rod with length, L, having a total fraction of charged species along the backbone, $\mathbf{f}' \cdot N$, is the Oosawa-Manning (counterion condensation) parameter, γ_0 [12]:

$$\gamma_0 = \frac{l_B \cdot \mathbf{f}' \cdot N}{L} \tag{1.4.19}$$

The emerging counterion condensation depends on the following parameters: macromolecular concentration and solvent's dielectric constant [12]. Concerning the influence of macromolecular concentration, the entropy cost is high in dilute solutions of strong polyelectrolyte chains for the counterions to bind- hence: $\gamma_0 \ll 1$ and all counterions remain in the bulk. Nevertheless, at the other extreme limit of Manning's condensation ($\gamma_0 \gg 1$), condensation of counterions is observed [12]. The solvent's dielectric constant on the other hand can also influence counterion condensation, as a decrease in a solvent's dielectric constant can augment counterion condensation. With increasing counterion condensation, the chain's size tends to decrease, as intrachain repulsion is more effectively screened. The counterions exert significant influence on the osmotic pressure of polyelectrolyte solutions, as described in the next section.

1.4.6. Osmotic pressure in polyelectrolyte solutions

In salt-free polyelectrolyte solutions, the osmotic pressure, $\Pi_{osm,e}$, has contributions from both the macromolecules ($\Pi_{osm,mac}$) and the counterions ($\Pi_{osm,cn}$):

$$\Pi_{osm,e} = \Pi_{osm,cn} + \Pi_{osm,mac} = k_B \cdot T \cdot (\mathbf{f}' \cdot c + \xi^{-3}) \tag{1.4.20}$$

In most cases, the dominant contribution to the overall osmotic pressure is the contribution from the counterions ($\Pi_{osm,cn}$) [12]. After salt has been added, the Donnan equilibrium can express the charge neutrality in polyelectrolyte solutions. The Donnan equilibrium can be illustrated by considering a virtual vessel with two domains separated by a semipermeable membrane. In the one side of the semipermeable membrane is the salt reservoir, while on the other side is the polyelectrolyte solution and the membrane is permeable to salt ions (concentration of salt ions is denoted by c_S). According to the principle of charge neutrality, the total number of negative ions (including charges on an i.e. negatively charged macromolecule, $\mathbf{f}^* \cdot c$) should equal the total positive ions everywhere in the solution [12]:

$$c_s^+ = c_s^- + \mathbf{f}^* \cdot c \tag{1.4.21}$$

After external salt is added, a pressure difference across the membrane is generated. By skipping several intermediate equations [12], osmotic pressure emerges as the net effect from the pressure difference due to ion concentration difference between the two sides of the membrane considering the effect of mobile ions (ionic contribution) and from the macromolecule (polymeric contribution, $\Pi_{\mathrm{pol,salt}} \propto \xi^{-3}$ in eq.1.2.10):

$$\Pi_{\mathrm{osm,salt}} = \mathrm{k_B} \cdot \mathrm{T} \cdot (\Pi_{\mathrm{ion,salt}} + \Pi_{\mathrm{pol,salt}}) = \mathrm{k_B} \cdot \mathrm{T} \cdot [((\mathrm{f}^* \cdot \mathrm{c})^2 + 4 \cdot \mathrm{c_s^2})^{0.5} - 2 \cdot \mathrm{c_s} + \xi^{-3}] \quad (1.4.22)$$

Following Dobrynin and Rubinstein, the ionic contribution dominates (free counterions) at low salt concentrations. At higher salt concentrations, the osmotic pressure eventually reaches a plateau in its value[12]. The presentation so far has involved scaling properties in uncrosslinked networks. In the next section, thermodynamics for swelling of polyelectrolyte gel networks are briefly reported.

1.4.7. Swelling of polyelectrolyte gel networks in presence of salt

The equilibrium conformation of a polyelectrolyte network, with an end-to-end distance at equilibrium $\mathrm{R_e}$ and Debye length, $\mathrm{K^{-1}}$ (eq.1.4.11), is determined, according to Dobrynin [44], by the balance between an osmotic pressure-related term due to small ions (free counterions and coexisting salt ions), dominated from the entropy of the counterions [29]:

$$\mathrm{A_{ion}} = \frac{\mathrm{c} \cdot \mathrm{k_B} \cdot \mathrm{T}}{\mathrm{N}} \cdot \frac{\mathbf{f}^{*2} \cdot \mathrm{N}^2 \cdot \mathrm{l_B}}{\mathrm{R_e}} \cdot \frac{1}{1 + \mathrm{K}^2 \cdot \mathrm{R_e^2}} \quad (1.4.23)$$

and the stored elastic energy, $\mathrm{A_{elastic}}$, when a deformation, $\boldsymbol{\gamma}$, is applied to the gel's crosslinks (i.e. due to solvency and under the influence/or not of added salt):

$$\mathrm{A_{elastic}} = \frac{\mathrm{c} \cdot \mathrm{k_B} \cdot \mathrm{T}}{\mathrm{N}} \cdot \frac{\boldsymbol{\gamma}^2 \cdot \mathrm{R_e^2}}{\mathrm{N} \cdot \mathrm{b}^2} \quad (1.4.24)$$

At fully swollen equilibrium in a charged network, the afore-mentioned energetic contributions equal each other: $\mathrm{A_{ion}} = \mathrm{A_{elastic}}$. Depending on the absence (or not) of salt [29], the network's characteristic size, $\mathrm{R_e}$, is given by:

$$\begin{cases} \mathrm{R_e} = \mathrm{N} \cdot \mathrm{b} \cdot \mathbf{f}'^{\frac{1}{2}} \ (\text{no salt}) \\ \mathrm{R_e} = \mathrm{N}^{3/5} \cdot \mathrm{b} \cdot (\dfrac{\mathbf{f}^{*2}}{2 \cdot \pi})^{\frac{1}{5}} \ (\text{presence of salt}) \end{cases} \quad (1.4.25)$$

Having presented scaling relations for charged and uncharged macromolecules in separate sections, it would be helpful to summarize main scaling relations in the same section. This would assist on systematically identifying and rationalizing the possible differences between charged and uncharged polymer solutions.

1.4.8. Differences between uncharged polymer and polyelectrolyte solutions

Selective physical properties for polyelectrolyte solutions (in absence of external salt) and uncharged polymer solutions [12], are summarized in Table 1.1 with their associated scaling relations and are shorty discussed thereafter.

Table 1.1. Comparison between scaling relations (dependence on monomer concentration,c) for the size of the correlation blob (ξ), the intrinsic polymer viscosity (η-η_s) and the tube's diameter (α') in semidilute solutions for uncharged polymers and polyelectrolytes in salt-free polyelectrolyte solutions[39],[45]

Static polymer property	Uncharged polymer chain	Polyelectrolyte chain
Size of the correlation blob, $\boldsymbol{\xi(c)}$	$\xi(c) \sim N^0 \cdot c^{-3/4}$	$\xi(c) \sim N^0 \cdot c^{-1/2}$
Solution's viscosity, $\boldsymbol{\eta}$	$\eta \sim c$	$\eta \sim c^{0.5}$
Intrinsic viscosity (Polymer's contribution to solution viscosity), $\boldsymbol{\eta - \eta_s}$	$(\eta - \eta_s) \sim N^3 \cdot c^{3.9}$	$(\eta - \eta_s) \sim N^3 \cdot c^{3/2}$
Tube's diameter ($\boldsymbol{\alpha'(c)}$)	$\alpha'(c) \sim N^0 \cdot c^{-3/4}$	$\alpha'(c) \sim N^0 \cdot c^{-1/2}$

Selected differences between polyelectrolyte solutions (in absence of external salt) [39] and uncharged polymer solutions are that:

1) The polyelectrolyte solutions exhibit a broader concentration range of the semidilute unentangled regime. The upper concentration boundary of semidilute unentangled solutions (i.e.transition to entangled network) occurs when the correlation blob size becomes comparable to the entanglement tube diameter, $\alpha'(c)$. Hence, one possible reason for the observed difference in concentration width of semidilute unentangled regime may be explained by the weaker c-dependence of the correlation blob size in polyelectrolyte solutions ($\xi(c)$,Table 1.1) than in uncharged polymer solutions: at the same c, $\xi(c)$ decays much faster in semidilute unentagled uncharged solutions than in salt-free polyelectrolyte solutions. An additional reason may be the weaker c-dependence of the intrinsic viscosity (η-η_s) in polyelectrolyte solutions than in uncharged polymer solutions (Table 1.1).

2) The overlap concentration (c^*) in the polyelectrolyte solutions is, in general, much smaller than the analogous for uncharged polymer solutions. As scaling relations of static parameters (Table 1.1) do not differ with respect to their dependence on polymer size (N), this difference may relate with the different scaling relation for the solution viscosity with respect to their c-dependence: The

viscosity of the semidilute polyelectrolyte solution scales as $\eta \sim c^{0.5}$ (empirical Fuoss' law [45]), while for uncharged polymer solutions, it scales linearly with concentration ($\eta \sim c$).

3) At the same c, the osmotic pressure in the polyelectrolyte solutions is higher compared to the one of the uncharged polymer solutions, due to the additional and predominant contribution from counterions in the former case. The osmotic pressure in the polyelectrolyte solutions is linearly dependent on c, exhibits dependence on c_s and is independent of polymer M_w.

4) Semidilute polyelectrolyte solutions exhibit a peak in the respective neutron scattering pattern at $q = \frac{2 \cdot \pi}{\xi}$, while semidilute uncharged polymer solutions do not.

5) In poor solvents, polyelectrolytes form pearl-necklace structures, while uncharged polymers form globules.

1.5. Transport properties in polymer and polyelectrolyte networks

1.5.1. General overview of diffusive transport

In this section, fundamental concepts regarding diffusive transport are first presented. A brief review of the nature of diffusion and its relation with system's properties is outlined, following Pecora and Berne [46]. In polymer solutions and in absence of external fields (i.e. no Coulombic interactions), random thermal fluctuations in the solvent medium induce concentration fluctuations (δc) and fluctuations in the dielectric constant of the medium ($\delta \varepsilon_r$). The collision between solute and solvent molecules is what generates motion for the solute molecules with statistical nature, namely solute diffusion.

For a given colloidal particle with mass, $\mathbf{m}'$, the velocity, $V(t)$, at a given instant, t, is the solution of the stochastic Langevin equation of motion[46]:

$$\mathbf{m}' \cdot \ddot{x} = -\gamma \cdot \dot{x} + \boldsymbol{\xi}(t) \qquad (1.5.1)$$

$\ddot{x}$ is the 2nd derivative of position, $x = \dot{V}(t)$ is the velocity and γ is the friction coefficient, while $\boldsymbol{\xi}(t)$ represents a stochastic term, knows as thermal noise. In the classical Langevin equation of motion, the solute is considered a much larger particle than the solvent molecules. Therefore, the friction coefficient, γ, is a constant parameter, independent of time [47]. Two prepositions need to hold both, in order to have normal Fickian diffusion (non-anomalous Brownian motion) for a tracer:

(1) the term $\boldsymbol{\xi}(t)$ in eq.1.5.1, also called the Gaussian white noise, should exhibit the following properties: (i) $<\boldsymbol{\xi}(t)>=0$;(ii) $<\boldsymbol{\xi}(t) \cdot \boldsymbol{\xi}(t-\tau)>=2 \cdot k_B \cdot T \cdot \boldsymbol{\delta}(t-\tau)$.

(ii) The probability distribution of jump lengths, $\mathrm{R} = \Delta\mathrm{r}(\mathrm{t})$, from the tracer's initial, unperturbed position (r_0') to its final position (r_f') over a corresponding time t, should obey the central limit theorem of statistics (hence, should be Gaussian). Since normal diffusion is a statistical (random) transport process, the central limit theorem from statistics suggests that the probability distribution function $\mathrm{p}(\mathrm{R},\mathrm{t})$ for a Brownian tracer to get displaced from its initial (t=0), unperturbed position (r_0') to final position (r_f') being a short distance R apart after a corresponding time t, with a corresponding mean square displacement ($\langle\Delta\mathrm{r}^2(\mathrm{t})\rangle$, obeys Gaussian statistics [46]:

$$\mathrm{p}(\mathrm{R},\mathrm{t}) = \left[\left(\frac{2\cdot\pi}{3}\right)\cdot\langle\Delta\mathrm{r}^2(\mathrm{t})\rangle\right]^{-3/2}\cdot \mathrm{e}^{-3\cdot\frac{\mathrm{R}^2}{2}\cdot\langle\Delta\mathrm{r}^2(\mathrm{t})\rangle} \qquad (1.5.2)$$

When both prepositions (i) and (ii) hold, then the colloidal tracer experiences normal (non-anomalous) Brownian motion, due to concentration fluctuations. Under such conditions, the fluctuation-dissipation theorem connects the diffusion coefficient D (being the inverse of the particle's friction coefficient) with its velocity fluctuations[46]:

$$\mathrm{D} = \frac{1}{3}\cdot\int_0^{\infty}\langle V(\mathrm{t})\cdot V(0)\rangle\,\mathrm{dt} \qquad (1.5.3)$$

In the case of Newtonian fluids, the solute's diffusion coefficient, D, describes the time it takes for a particular Brownian particle to get displaced over a distance equal to its hydrodynamic size. By skipping some intermediate steps starting from eq. 1.5.1 and eq. 1.5.3, the well-known Stokes-Einstein (SE) relation is obtained, which relates the diffusion coefficient, D, for a Brownian particle of mass, $\mathbf{m}'$, and hydrodynamic radius, $\mathrm{R}_{\mathrm{h,np}}$, in a Newtonian fluid with solvent viscosity, η_s:

$$\mathrm{D} = \frac{\mathrm{k_B}\cdot\mathrm{T}}{6\cdot\pi\cdot\eta_\mathrm{s}\cdot\mathrm{R_{h,np}}}\ \text{(while, in three-dimensions: } \mathrm{D} = \frac{\langle\Delta\mathrm{r}^2(\mathrm{t})\rangle}{6\cdot\mathrm{t}}\text{)} \qquad (1.5.4)$$

Due to its statistical nature, the diffusion coefficient, D, for a Brownian tracer can also be expressed with probabilistic expressions. Although the expressions are more complicated, it is worth to briefly mention them here. The conditional probability $\Psi(\mathrm{r}_f',\mathrm{r}_0';\mathrm{t})$ describes the probability that a particle reaches its final position (r_f') at time t, under the condition that it was initially located at position (r_0) at t=0. In absence of any external fields (for instance, neither hydrodynamic nor electrostatic interactions being present), the diffusion coefficient, D, of a particle is provided by the solution of the Smoluchowski equation, being a subclass of the vectorial Fokker-Planck equations. The Smoluchowski equation is an expression that relates the temporal evolution of $\Psi(\mathrm{r}_f',\mathrm{r}_0';\mathrm{t})$,($\frac{\partial\Psi(\mathrm{r}_f',\mathrm{r}_0';\mathrm{t})}{\partial\mathrm{t}}$), with the product of the particle's diffusion coefficient, D,multiplied by the divergence of the gradient of the conditional probability $\nabla\cdot[\mathrm{D}\cdot\nabla\Psi(\mathrm{r}_f',\mathrm{r}_0';\mathrm{t})]$ [1]:

$$\begin{cases} \frac{\partial \Psi\left(r'_f, r'_0; t\right)}{\partial t} = \nabla \cdot [D \cdot \nabla \Psi\left(r'_f, r'_0; t\right)] \\ \lim_{t \to 0} \Psi\left(r'_f, r'_0; t\right) = \delta(r'_f - r'_0) \end{cases} \quad (1.5.5)$$

Distinct transport processes spanning over certain timescales may be observed for a diffusing particle when $\langle \Delta r^2(t) \rangle$ is plotted vs. t. Such processes depend on the time scale under observation, as well as on a particular combination of crowding factors (i.e. complexity of the matrix, possibly co-existing tracer-matrix interactions, size of the particle). In absence of crowding effects, the motion of a particle at very short times after its perturbation by the solvent molecules and before diffusion appears is termed as 'ballistic motion'[48], or activated transport. During the ballistic regime, the solute molecule has not even encountered other particles and the (mean square displacement) MSD scales stronger than linearly with time ($\langle \Delta r^2(t) \rangle \sim t^2$), when plotted vs. t on a double-log plot. At relatively longer time scales, the particle under observation encounters other particles and a crossover from ballistic to diffusive regime appears [48]. For free Fickian diffusion, the MSD is linearly related with time, also when displayed on a double logarithmic plot.

When at least one of the (or both) prepositions related with eq.1.5.1 and 1.5.2 mentioned earlier in this section are violated (and/or, when: $\lim_{t \to 0} \Psi\left(r'_f, r'_0; t\right) \neq \delta(r'_f - r'_0)$ in the probabilistic expression of eq.1.5.5), deviations from normal Fickian diffusion are observed over certain timescale. This can be the case, when either the concentration of matrix increases and/or tracer-matrix interactions become more significant. As mentioned in the previous paragraph, such conditions of the surrounding environment of the diffusing tracer are called 'crowded', the complexity of the corresponding solute dynamics increases and their respective quantitative description becomes ambiguous[49-51]. Among different reported examples concerning such complex dynamics, few are mentioned below: (i) when the probability distribution of the particle's displacements, $p(\Delta r(t), t)$, deviates from Gaussian distribution but the MSD grows linearly with t (case of anomalous, yet Brownian diffusion) [52], or (ii) when the MSD grows nonlinearly with time over certain time scale (not necessarily over the whole time scale of the particle's motion)-the latter is frequently called subdiffusive motion [53]:

$$\langle \Delta r^2(t) \rangle \sim t^{\alpha}, \ (0 < \alpha < 1) \quad (1.5.6)$$

A particular type of subdiffusive process is the single file diffusion typically encountered in biology, i.e. RNA complex diffusion amid DNA chains, where the RNA spends certain time bound with the DNA and propagating along its contour, exhibiting diffusion in one dimension ($\langle \Delta r^2(t) \rangle \sim t^{0.5}$) [54]. In some of these cases, the probability distribution for the jump lengths of the diffusant may be described by a power-law expression[55], suggesting e.g. that the coordinates from a previous position of the tracer may influence the direction of the next jump (memory effects), thus violating the randomness,

being a central preposition of Brownian motion[56]. Another type of motion that is frequently categorized by anomalous mobility is the so-called 'activated transport', where $\langle \Delta r^2(t) \rangle \sim t^{\alpha}$, (α>1)[57].The state-of-the-art concerning the afore-mentioned types of complex diffusion in crowded environments in general, continues in the 3rd, 4th and 5th chapter of this thesis, as well.

1.5.2. Diffusion in polymer systems

A short theoretical overview of self-diffusion of uncharged polymers in solutions and their associated conformations, is presented in this section [7], [58]. Consecutively, models that describe diffusion in polymer networks are briefly described, in view of some representative works for polymer solutions [59] and gels [60, 61].

1.5.2.1. Conformation & self-diffusion of an uncharged chain in uncharged polymer solutions

In a recent work, Dünweg et al. [58] presented a bifurcation plot depicting the various conformations of uncharged polymer chains and the corresponding polymer dynamics, as a function of monomer concentration and of excluded volume interactions (Fig.1.5.1). The classification of structural conformations for a polymer chain (solvency) in presence of interactions (real) or not (ideal), was already discussed in section 1.2. In this section, however, chain dynamic properties in a solution are shortly summarized together with the corresponding length-scale dependent chain conformations.

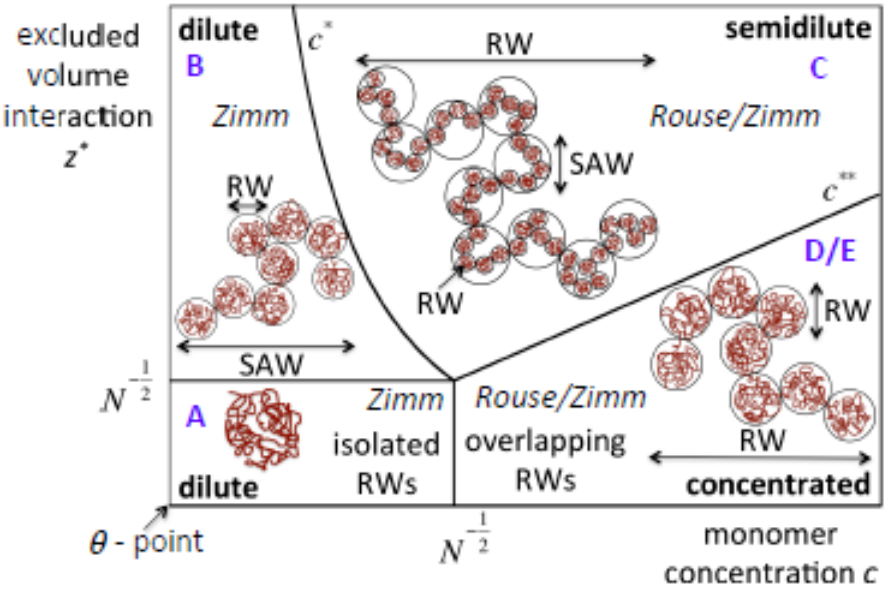

Fig. 1.5.1. Phase diagram of polymer chain solvency and dynamics (excluded volume interactions), as a function of monomer concentration, c. Representation of the different scaling lengths of an uncharged polymer chain in solution, in absence of salt, with increasing size in regime C (corresponding dynamics and fractal size): (RW) thermal blob, ξ_T; (SAW) correlation blob, ξ; and (RW) chain size with end-to-end distance, R_e. The figure has been adapted with permission from the coauthors of the original paper[58].

In brief, an ideal chain is characterized by no net interactions, since excluded volume interactions exactly cancel out solvent-monomer interactions. Therefore, the corresponding conformation of an ideal chain (regime A, Fig.1.5.1) in its solution is described by a random walk (RW). The same is true at high monomer concentrations (regime D/E), where RW statistics apply at different length scales. When excluded volume interactions are present (regime B, Fig.1.5.1), however, the real chain model is used. The arrangement of the (whole) real chain is characterized by a self-avoiding walk [58], according to which the chain cannot cross the same point more than once. The latter feature is not a prerequisite for the pure random walk model in the case of ideal chains. In presence of excluded volume interactions (regime B, Fig.1.5.1), bifurcations in conformations between self-avoiding walk (SAW) and random walk (RW) may occur, depending on the characteristic polymer's length scale: (i) when $r < \xi$, RW statistics are predicted; (ii) the conformation of the whole chain is described by the SAW. In presence of excluded volume interactions, but at higher monomer concentrations (regime C, Fig.1.5.1): (i) RW describes the conformation of chain segments up to the thermal blob size ($r < \xi_T$); (ii) at intermediate length scales ($\xi_T < r \leq \xi$) SAW is predicted and (iii) the conformation of the whole chain is again described by RW, since at that whole chain length scale excluded volume interactions are screened by other chains.

I. Self-diffusion in dilute polymer solutions: the Zimm model

In dilute polymer solutions ($c < c^*$), hydrodynamic interactions between monomers along the same chain, as well as between monomer and solvent molecules are present. The polymer chain dynamics in this concentration regime are described by the Zimm model [7]. Along the line of the Zimm model, the diffusion of the whole polymer chain, D_{zimm}, can be represented by a diffusing (solid) spherical blob with diameter R_e that encapsulates both the whole chain with end-to-end distance, R_e, as well as solvent molecules dragged by the chain during its motion[7]:

$$D_{zimm} = \frac{k_B \cdot T}{\eta_s \cdot R_e} = \frac{k_B \cdot T}{\eta_s \cdot b \cdot N^{\nu}} \quad (1.5.7)$$

$$\tau_{zimm} = \frac{R_e^2}{D_{zimm}} \quad (1.5.8)$$

Nevertheless, the relaxation of even smaller sub-sections ($r < R_e$)–mobility at different length scales-can be described by the Zimm modes[7]:

$$\tau_p = \tau_0 \cdot \left(\frac{N}{p^{\#}}\right)^{3 \cdot \nu} \quad (1.5.9)$$

Here, the $p^{\#th}$ mode corresponds to relaxation of a chain section containing $\frac{N}{p^{\#}}$ monomers. The relaxation of a monomer and the whole chain is described by the N^{th} Zimm mode ($\frac{N}{p^{\#}} = 1$) and 1^{st} Zimm mode ($\frac{N}{p^{\#}} = N$), respectively.

II. Semidilute unentangled polymer solutions: Rouse model

In semidilute unentangled polymer solutions, hydrodynamic interactions are screened at sections of the chain with size larger than the thermal blob size ($r > \xi_T$). Under such conditions, the Rouse model is employed to describe chain dynamics. Historically the first among other reported models for polymer dynamics, the Rouse model [62] has been a coarse-grained representation of a polymer chain in a semidilute solution or a melt. According to this model, a chain is visualized as a sequence of beads connected with massless springs, while the beads fluctuate around a mean position. With the exception of interactions for a given bead with its nearest neighbouring beads, the motion of each bead is independent from the motions of other beads, even within the same chain. For a chain of N beads, the total friction coefficient is the product of the number of beads N times the respective monomer friction coefficients, γ_b, per bead:

$$\gamma_R = N \cdot \gamma_b \tag{1.5.10}$$

And the associated Rouse diffusion coefficient and Rouse diffusion time read as follows:

$$D_{Rouse} = \frac{k_B \cdot T}{\gamma_R} = \frac{k_B \cdot T}{\gamma \cdot N} \tag{1.5.11}$$

$$\tau_{Rouse} = \frac{R_e^2}{D_{Rouse}} \tag{1.5.12}$$

Similar to the Zimm modes, relaxation times of sub-sections of the whole a chain are described by the so-called 'Rouse modes'. For a chain with N monomers, the longest relaxation time corresponds to the 1^{st} Rouse mode, while the monomer's motion is associated with the shortest relaxation time (N^{th} Rouse mode).

1.5.2.2. Cooperative diffusion coefficient

In either semidilute entangled networks or in crosslinked hydrogels where the concentration in the as-prepared state is in the semidilute entangled regime, a synergistic motion of the polymer matrix has been experimentally observed [63-65], known as the cooperative diffusion coefficient, $D_{coop}(c)$. As stated by de Gennes [9], $D_{coop}(c) = D_{zimm} \cdot (\frac{c}{c^*})^{\frac{\nu}{3 \cdot \nu - 1}}$, describes the colligative motion of several monomers constituting the matrix of the semidilute polymer solution, when the network is visualized

as an array of several correlation blobs. $D_{coop}(c)(=\frac{k_B \cdot T}{6 \cdot \pi \cdot \eta_s \cdot \xi(c)})$ is a function of the blob size $\xi(c)$ and is a relatively faster process with respect to the polymer self-diffusion in semidilute polymer solutions or with solute diffusion in polymer networks. It is related to the osmotic pressure of the polymer solution and scales with increasing concentration of the network, as [66]: $D_{coop}(c) \sim c^{3/4}$.

1.5.2.3. Tracer diffusion in polymer solutions

In this present section, selective findings from a recent theoretical work concerning non-interacting nanoparticle diffusion in polymer solutions, is presented. M. Rubinstein and coworkers have published a scaling theory for non-sticky nanoparticle diffusion slowdown in polymer liquids [7], namely for solutions and melts. Their theory [59] based on an initial work by Brochard and de Gennes [67] predicts distinct trends for the diffusion coefficient of the non-interacting nanoparticle, as a function of at least two of the three following parameters being floating (the other one may remain constant): (i) monomer concentration, (ii) ratio between tracer size and characteristic size of the polymer network (i.e. correlation length, ξ, or tube's diameter, α') and (iii) the degree of polymerization, N. To calculate any scaling relations for a given diffusing particle, first the regime of the particle size and the concentration regime need to be calculated, as defined by the theory. Scaling predictions vs. ϕ for a given non-interacting nanoparticle diffusant, in view of the theory [59], are possible only after having identified the tracer's position in the two regimes reported by the authors: tracer size regime and concentration regime.

Tracer size regime. The actual particle's diameter, d, is compared with the following characteristic lengths: (i) segment length, b; (ii) tube's diameter in the melt, $\alpha'(\phi=1)$ and (iii) size of the unperturbed chain in the melt, $R_e(\phi=1)$ [59]. The theory predicts three different tracer size regimes: small particle size ($b < d < \xi(\phi)$), intermediate sized particles ($\xi(\phi) < d < \alpha'(\phi)$) and large particles ($d > \alpha'(\phi)$).

Concentration regime. According to the theory [59], two monomer concentration thresholds are declared, based on which scaling predictions for $D(\phi)$ vs. ϕ can be presented: ϕ_d^{ξ} and ϕ_d^{a} denote the lower and upper boundary of the semidilute unentangled regime (in view of the theory) and represent the ϕ values where the tracer size, d, equals $\xi(\phi)$ and $a(\phi)$, respectively. At $\phi < \phi_d^{\xi}$, the tracer is in the dilute regime, while at $\phi > \phi_d^{a}$ the tracer is found in the semidilute entangled solution. In Tables 1.2 and 1.3, basic scaling relations for small and intermediate sized particles are summarized, since only such particles have been examined in the experiments of this thesis. Table 1.2 presents in brief scaling relations for the MSD and the diffusion coefficient of the nanoparticle,

depending on the tracer size regime and the relation between time scales (the corresponding time, t vs. the characteristic relaxation time of the polymer matrix). The theory predicts a crossover from diffusive to subdiffusive MSD at intermediate size range for intermediate times (due to relaxation of the correlation blobs controlling the system's viscosity-and hence, the nanoparticle mobility), which eventually crosses over to diffusive regime at long times [59].

Table 1.2. Tracer-size dependent expressions for the (i) relaxation times of the polymer matrix (for the monomer (τ_0), the correlation blob (τ_ξ) and for a chain section equal to the tracer size (τ_d)) the (ii) tracer's diffusion coefficient (D_s and D_t represent D values for the tracer based on solvent viscosity (η_s) or an effective viscosity, $\eta_{eff}(\tau_d)$) and (iii) the tracer's MSD

Tracer size regime	Relaxation time	D ($m^2 \cdot s^{-1}$)	MSD ($\langle \Delta r^2(t) \rangle$)
$b < d < \xi(\phi)$	τ_0(monomer segment)	$D_s = k_B \cdot T / (\eta_s \cdot d)$	$\langle \Delta r^2(t) \rangle \sim t$
$\xi(\phi) < d < \alpha'(\phi)$	τ_0	$D_s = k_B \cdot T / (\eta_s \cdot d)$, $\tau_0 < t < \tau_\xi$	$\langle \Delta r^2(t) \rangle \sim t$, $\tau_0 < t < \tau_\xi$
$\xi(\phi) < d < \alpha'(\phi)$	$\tau_\xi = \tau_0 \cdot (\frac{\xi}{b})^3$	$D_t = D_s \cdot (t/\tau_\xi)^{-1/2}$, $\tau_\xi < t < \tau_d$	$\langle \Delta r^2(t) \rangle \sim t^{-1/2}$, $\tau_\xi < t < \tau_d$
$d > \alpha'(\phi)$	$\tau_d = \tau_0 \cdot (\frac{d}{\xi})^4$	$D_t = k_B \cdot T / (\eta_{eff}(\tau_d) \cdot d)$, $t > \tau_d$	$\langle \Delta r^2(t) \rangle \sim t$, $t > \tau_d$

Similar to Table 1.2, the scaling predictions for the diffusion coefficient, $D(\phi)$ vs. ϕ, as a function of concentration regime and the tracer size regimes are shown in Table 1.3.

Table 1.3. Tracer's diffusion coefficients ($D(\phi)$) as a function of tracer-size and concentration regimes. The D_s and D_t represent D values for the tracer based on solvent viscosity or an effective viscosity, $\eta_{eff}(\tau_d)$, respectively

Tracer size regime	Concentration regime	$D(\phi)$ ($m^2 \cdot s^{-1}$)
$b < d < \xi(\phi)$	$\phi < \phi_d^\xi$	$D_s \sim \phi^0$
$\xi(\phi) < d < \alpha'(\phi)$	$\phi < \phi_d^\xi$	$D_t \sim D_s \sim \phi^0$
$\xi(\phi) < d < \alpha'(\phi)$	$\phi_d^\xi < \phi < \phi_d^a$	$D_t(\phi) \sim D_s \cdot \phi^{-1.52}$
$d > \alpha'(\phi)$	$\phi > \phi_d^a$	$D_t(\phi) \sim D_s \cdot \phi^{-3.93}$

Among other findings, the theory from Rubinstein et al. predicts no slowdown in dilute polymer solutions for non-interacting nanoparticles of intermediate particle size (Table 1.3, 2nd line).This is necessary information, when comparing with diffusivity data of the 3rd and 5th Chapter in this thesis. Finally, the theory predicts scaling relations of the form ($D_t = D_t(N)$), at the same ϕ. Due to the limited number of different polymer sizes into which nanoparticle diffusion in semidilute polymer solutions was investigated (e.g. totally 3 different polymer sizes in Chapter 5), the presentation of such scaling relations is beyond the scope of this thesis.

Other models describing nanoparticle diffusion in polymer solutions, already classified by Massaro and Zhu[60], are shortly summarized in the following lines: (i) obstruction models; (ii) hydrodynamic models and (iii)models based on free volume theory. The common feature in all these models is that they describe exponential dependence of the diffusion slowdown,D/D_0, on monomer concentration, c. The obstruction models are rather suitable for small solute and solvent diffusants, as compared to the hydrodynamic models and to a greater extend, to the free volume models. The main underlying assumption of these models is that the chain is relatively immobile compared to the tracer's mobility (solvent or solute molecule).They are suitable for dilute and semidilute polymer solutions and most of them can more optimally describe diffusion of small tracers.

Next, the hydrodynamic models presuppose the existence of hydrodynamic interactions. The latter interactions get screened, beyond a given distance, called the hydrodynamic screening length, δ. According to Masaro and Zhu [60]: '...The Cukier model, assumes that the polymer solution is relatively immobilized compared to the mobile solute, when the latter diffuses in a Navier-Stokes (incompressible) fluid.' For a hydrodynamic screening length, δ, the equation that describes the solute diffusivity, D, with diffusion coefficient in absence of polymer matrix, D_0, is:

$$D = D_0 \cdot e^{-\delta \cdot R_{H,np}} \quad (1.5.13)$$

The latter equation can be simplified for dilute solutions as:

$$D = D_0 \cdot \left(1 - \delta \cdot R_{H,np}\right) \quad (1.5.14)$$

The Cukier model is optimal for small-sized diffusants[60]. Finally, the Phillies model is a phenomenological approach that describes the diffusion slowdown in presence of hydrodynamics [68]. According to the Phillies' model, the chains of the polymer network are considered immobile sets of spheres connected by rods. Any constraints to mobility are attributed, according to Phillies' model, to hydrodynamic interactions. This feature differentiates the aforementioned model from the de Gennes' tube model, where topological constraints (e.g. entanglements) appear in concentrated semidilute solutions[9].The solute's diffusivity in the solution bears a stretched exponential dependence on monomer concentration, as follows:

$$D = D_0 \cdot e^{-y \cdot c^{\beta}} \quad (1.5.15)$$

where y is a parameter related with the polymer molecular weight and β is a related with the size of the diffusant. Last, models based on free volume theory describe that the solute (or solvent) diffusivity through the free region between the polymer chains is proportional to the probability of encountering free volume between the chains. These models are applicable for semidilute solutions, except the Peppas-Reinhart model [60] that is suitable for solute diffusion through crosslinked gels only.

1.5.2.4. Macromolecular translocation through polymer hydrogels and related polymer conformations

In the 5th Chapter of this thesis, diffusion of various soft macromolecules (linear and branched polymers) has been examined through ideal hydrogels. The 5th Chapter, in particular, presents cases of tracer diffusion where the tracer size is comparable with (and or larger than) the pore size of the hydrogel. In view of these experiments, a scaling theory for translocation of branched macromolecules through nanopores from de Gennes and coworkers [61] is considered as a closest analogue and is thus mentioned hereafter. According to the aforementioned theory, when the diameter of a pore (d_{pore}) in the polymer matrix (i.e. in a gel) becomes comparable to (or smaller than) the size of the branched macromolecule (R_F) in the bulk solution (no confinement), the macromolecule may be 'sucked' towards the interior of the pore having by means of flow, $J_{suction}$, when the thermal energy of the branched macromolecule overcomes a critical energy barrier ($J_{suction} > J_c = \frac{k_B \cdot T}{\eta_s}$), η_s being the solvent's viscosity. This occurs when the critical sucked length of the macromolecule (y^*) becomes comparable to the pore diameter ($d_{pore} \approx y^*$) and the energetic cost is equal to $k_B \cdot T$ [61]. The theory is briefly described in the following lines. Scaling predictions apply also in the case of translocated macromolecules, as the chain can be always visualized as a self-similar arrangement of blobs. Fig. 1.5.2. shows (i) the fully swollen size, R_F, for a polymer chain in the bulk solution (no translocation) and (ii) a pore geometry with certain length, L_{pore}, and diameter, d_{pore}, including the polymer chain under translocation, with the critical translocated length, y^*.

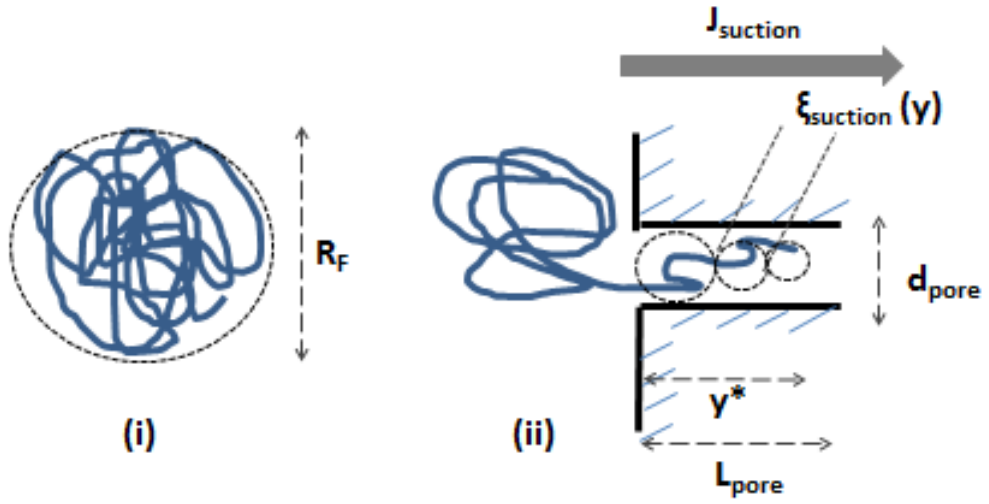

Fig.1.5.2. (i) Fully swollen size, R_F, for a polymer chain in the bulk solution (no translocation); (ii) pore geometry with length L_{pore}, and a diameter d_{pore}, showing the polymer chain under translocation, with a total translocated length, y^*, dictated by the minimization of the Flory energy for the translocated polymer, A_{conf}. Totally P out of N monomers of the chain are translocated through the pore, while the translocated section of the chain can be described as an array of suction blobs with size $\xi_{suction}(y)$. The sizes of the chain (R_F) and the pore diameter (d_{pore}) are not drawn in real scale. The thick grey arrow (ii, upper part) denotes the direction of propagating suction flow, $J_{suction}$, due to hydrodynamics.

The total Flory's energy, A_{conf}, for the confined section of chain (P confined monomers, out of totally N monomers for the whole chain) with segment length, b, through a pore with diameter, d_{pore}, can be written as:

$$A_{conf} = k_B \cdot T \cdot \left(\frac{P^2 \cdot b^3}{y \cdot d_{pore}^2} + \frac{y^2}{b \cdot P^{1/4}}\right) \qquad (1.5.16)$$

The denominator in the right hand side of eq. 1.5.16 ($b \cdot P^{1/4}$) denotes the ideal size of the partially translocated section of the chain. The sizes of the chain (R_F) and the pore diameter (d_{pore}) are not drawn in real scale (Fig.1.5.2). Translocation through the pore will occur when the net energy balance from hydrodynamic forces and confinement forces exceeds the critical energy barrier, $A_{conf}^* = k_B \cdot T \cdot \left(\frac{y^*}{d_{pore}}\right)^{8/5}$. This is the case when $\frac{y^*}{d_{pore}} \approx 1$. The translocated section of the chain can be described as an array of suction blobs with size $\xi_{suction}(y)$, being a decreasing function of y. The rate-limiting step in the translocation process is the insertion of the very first suction blob $\xi_{suction}(y)$ into the pore. Inside each suction blob, the confinement effect is negligible. The total translocated length, y, for a total of P sucked monomers (the chain consists of N monomers, $N > P$) will be given by minimization of the Flory's free energy for the confined chain(eq.1.5.16) ($\frac{\partial A_{conf}(y)}{\partial y} = 0$), with respect to the distance, y, along the pore length, L_{pore}:

$$\frac{y}{d_{pore}} = \left(\frac{b}{d_{pore}}\right)^{5/3} \cdot P^{5/6} \qquad (1.5.17)$$

The thick grey arrow (Fig.1.5.2, upper part) denotes the direction of propagating suction flow, $J_{suction}$, due to hydrodynamics. With progressively increasing translocation length ($y > y^*$), the hydrodynamic force dominates over the confinement force and the translocation of the whole chain is further enhanced and finally accomplished. Following the authors [61], this suction mechanism does not dependent on either the polymer molecular weight, or on the geometry of the macromolecule (being branched or not). Last, it is mentioned that in the case of translocation through a pore, the correlation size is a decreasing function of the translocation distance along the pore, $\xi_{suction}(y)$, (Fig.1.5.2), in contrast to the decreasing c-dependence of the analogous correlation blob in semidilute polymer solutions in absence of confinement ($\xi(c)$) [9].

Chapter 2: An overview of FCS, materials and supporting characterization techniques

Following the description about concepts from polymer physics closely related with the topics of this thesis, the present section provides an overview to FCS. The experimental FCS setup used in the experiments of this thesis is briefly presented, followed by a brief introduction to the theory of Fluorescence Correlation Spectroscopy (FCS). Next, a brief overview of fundamental concepts concerning energetic transitions of emitters is outlined, as well as a description of the appropriate fitting functions to the experimental autocorrelation functions used everywhere in this thesis. The used materials and the associated sample preparation for the experiments described in the following chapters of this thesis are shortly presented. Last, this Chapter concludes with a description of the supporting characterization methods that have been used by collaborators, in relation with the present FCS findings of this thesis.

Initially developed from Elson, Webb and Magde [69], FCS has been proposed as an analog to Dynamic Light Scattering (DLS), with the specific aim to detect the kinetics of DNA binding with ethydium bromide, via change in the emitted fluorescence upon binding to DNA. In these early experiments a well-defined small probing volume was illuminated by a laser beam and the fluorescent light originating from this volume was collected and directed to a fast photodetector. The photodetector was used to record the temporal fluctuations of the fluorescence light intensity that were related to either concentration fluctuations caused by the diffusion of the fluorescent species through the illumination spot, or to fluctuations in the emission efficiency due to binding. An auto-correlation analysis on the measured fluorescent intensity fluctuations yielded information on the chemical rate constants and diffusion coefficients and demonstrated the coupling among these parameters [69]. Later on, the initially encountered problems in FCS experiments, related to strong background scattering and low signal to noise ratio have been minimized by employing the so-called confocal excitation/detection configuration[70] and the use of avalanche photodiodes with single photon counting sensitivity as detectors. Over the years, FCS has been drastically developed [71], [72] and its current application range spans from molecular and cell biology to colloids and polymer systems [73].

2.1. The experimental setup of FCS

A standard modern FCS setup is based on an inverted confocal microscope as schematically shown in Fig. 2.1. A laser beam is reflected on a dichroic mirror and consecutively tightly focused by a high

numerical aperture microscope objective to a diffraction-limited illumination spot in the sample. The emitted fluorescence is collected by the same objective, transmitted through the same dichroic mirror and through a confocal pinhole to finally reach an avalanche photodiode detector (APD), capable of single-photon counting. These arrangements result in the formation of an extremely small FCS observation volume (V_{FCS}) around the laser focus (Fig.2.1). Fluorescent light originating only from this volume can reach the APD.

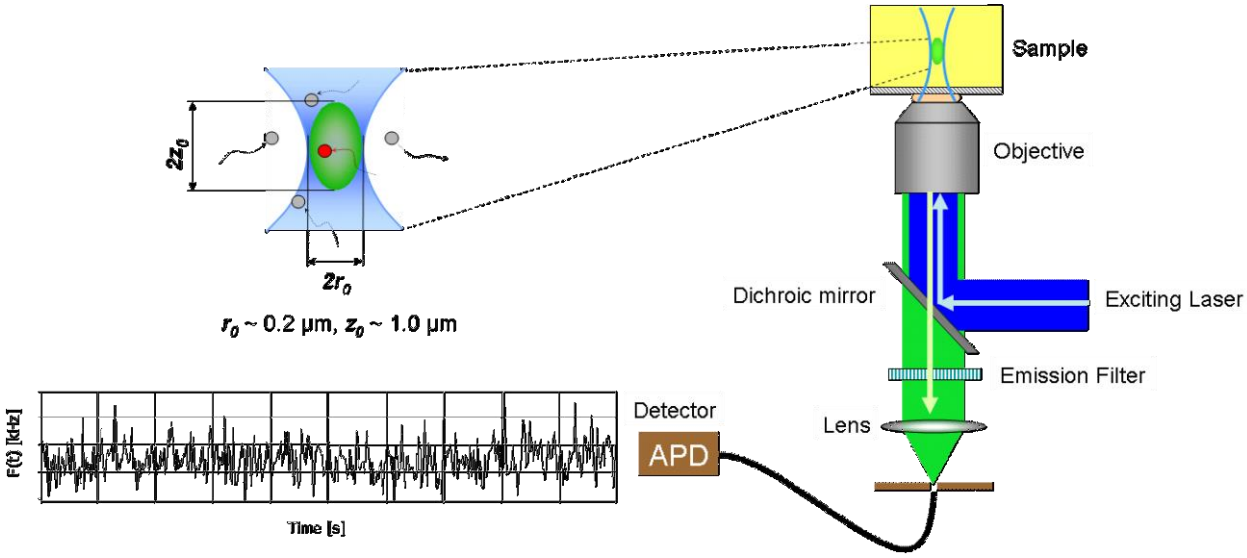

Fig.2.1. FCS setup (right part), a magnification of the FCS illumination spot (blue) and detection spot (green) spot (upper left) and the time trace i.e. the fluorescent intensity fluctuations vs. time (lower, left). The latter fluctuations are recorded from the photodetector (avalanche photodiode, APD), capable of single photon counting.

The temporal fluctuations of the detected fluorescence intensity, $\delta I_F(t)$, are recorded and evaluated in terms of an autocorrelation function[74]:

$$G(t) = \frac{< \delta I_F(t) \cdot \delta I_F(t+\tau) >}{< I_F(t) >^2} = G'(t) - 1 = \frac{< I_F(t) \cdot I_F(t+\tau) >}{< I_F(t) >^2} - 1 \qquad (2.1.1)$$

The term $\delta I_F(t) = I_F(t) - < I_F(t) >$ denotes the instantaneous fluctuation of the fluorescence intensity from the average value of the fluorescent intensity, $< I_F(t) >$, while the angular brackets denote it is an ensemble average. All measurements in this thesis were performed on a commercial FCS setup (Carl Zeiss, Jena, Germany) consisting of the module ConfoCor2, and an inverted microscope, Axiovert 200. A 40× (magnification) Plan Neofluar objective was used, bearing the following operating features: high numerical aperture-NA (NA=1.2), working distance 0.28 mm and water as immersion liquid.

2.2. Theory of Fluorescence Correlation Spectroscopy (FCS)

The concept of correlation function is closely related to the fluctuation-dissipation theorem from statistical thermodynamics [46], as was described in the 1st Chapter. For a measurement time, $\Delta\boldsymbol{t}$, the fluorescent intensity autocorrelation function describes the temporal self-similarity from time $\tau' = \mathrm{t}$ until a later time, $\tau' = \mathrm{t} + \tau$, for the detected fluorescence intensity, $\mathrm{I_F(t)}$ [46]:

$$\langle \mathrm{I_F(t)} \cdot \mathrm{I_F(t+\tau)} \rangle = \lim_{\Delta\boldsymbol{t}\to\infty} \frac{1}{\Delta\boldsymbol{t}} \int_0^{\Delta\boldsymbol{t}} \mathrm{I_F(t)} \cdot \mathrm{I_F(t+\tau)} \mathrm{dt} \tag{2.2.1}$$

In a typical FCS experiment, the average number of particles, $\mathrm{N'}$, in the FCS observation volume is relatively low, hence Poisson distribution describes the statistics of events stemming from such molecules crossing the FCS observation volume[74]. Hence, the signal-to-noise ratio of FCS is described as:

$$\frac{\sqrt{\langle (\delta \mathrm{N'}^2) \rangle}}{\langle \mathrm{N'} \rangle} = \frac{\sqrt{(\mathrm{N'} - \langle \mathrm{N'} \rangle)^2}}{\langle \mathrm{N'} \rangle} = \frac{1}{\sqrt{\langle \mathrm{N'} \rangle}} \tag{2.2.2}$$

The signal-to-noise ratio (eq.2.2.2) gets maximized when the number of tracers decreases. However, the ultralow concentration requirements should be compromised by avoiding to drastically reduce the number of photon events from the emitter. In fact, there should be a balance between low concentration for a given tracer and the collected intensity [74]. Fluctuations in fluorescent intensity, $\delta \mathrm{I_F(t)}$, can be in general caused due to a fluorescent tracer (i) either crossing the FCS observation volume (upper left, Fig.2.1), or (ii) undergoing some change in its emission properties while in the observation volume, e.g. because of binding to another molecule, chemical reaction or a photophysical process. The description below is focused on the most common case that is also appropriate for the experiments of this thesis, namely when the fluctuations in fluorescent intensity, $\delta \mathrm{I_F(t)}$, stem only from concentration fluctuations, $\delta \mathrm{c}(\boldsymbol{r}, \mathrm{t})$, due to diffusion of the fluorescent tracers through the observation volume[74]. The afore-mentioned fluctuations are interrelated, via the spatial distribution of the excitation intensity with $\mathrm{I_{exc,0}}$ its maximum value, $\mathrm{I_{exc}}(\boldsymbol{r})$, the spatial collection efficiency, $\mathrm{S_c}(\boldsymbol{r})$, the quantum yield, $\mathrm{Q'}$, the molecular absorption cross-section, $\boldsymbol{\sigma}'$, and the overall detection efficiency, κ, as[74]:

$$\delta \mathrm{I_F(t)} = \boldsymbol{\kappa} \cdot \int_0^{\mathrm{V_{FCS}}} \mathrm{I_{exc}}(\boldsymbol{r}) \cdot \mathrm{S_c}(\boldsymbol{r}) \cdot \delta(\mathrm{c}(\boldsymbol{r}, \mathrm{t})) \mathrm{dV_{FCS}} \tag{2.2.3}$$

The parameter $\boldsymbol{\kappa} = \mathrm{I_{exc,0}} \cdot \kappa \cdot \boldsymbol{\sigma}' \cdot \mathrm{Q'}$ denotes an overall detection efficiency, where its constituents do neither depend on distance, $\boldsymbol{r}$, nor on time, t. The quantum yield, $\mathrm{Q'}$, stands for a ratio of radiative decay over all different (both radiative and non-radiative) decays to the ground energy state, after excitation of the molecule to a higher excited state. The integration in eq.2.2.3 is

performed over the whole FCS observation volume, V_{FCS}.The parameter $S_c(\boldsymbol{r})$ describes the collection efficiency by the high NA objective and the pinhole set. A convolution, denoted by '⊗', between $I_{exc}(\boldsymbol{r})$ and $S_c(\boldsymbol{r})$ provides the molecular detection function, $W(\boldsymbol{r})$ (=$I_{exc}(\boldsymbol{r})\otimes S_c(\boldsymbol{r})$) [74]. The latter parameter describes the field of the detected fluorescent intensity distribution and may be well approximated, under certain circumstances, by a Gaussian profile (blue profile, upper left part of Fig.2.1), as[74]:

$$W(\boldsymbol{r}) = e^{-\frac{2\cdot(x^2+y^2)}{r_0^2}}\cdot e^{-\frac{2\cdot z^2}{z_0^2}} \tag{2.2.4}$$

The variables r_o and z_o denote the lateral and axial size of the detection volume (green ellipsoid, upper part in Fig.2.1). Using eq. 2.2.4, into eq.2.2.3, one may obtain the following form for $\delta I_F(t)$:

$$\delta I_F(t) = \boldsymbol{\kappa}\cdot\int_0^{V_{FCS}} W(\boldsymbol{r})\cdot\delta(c(\boldsymbol{r},t))dV_{FCS} \tag{2.2.5}$$

By rewriting eq.2.1.1 using eq. 2.2.5, one obtains:

$$G(t) = \frac{\int_0^{V_{FCS}} W(\mathbf{r})\cdot\delta(c(\mathbf{r},t))\cdot\int_0^{V_{FCS}} W(\mathbf{r}')\cdot\delta(c(\mathbf{r}',t+\tau))dV_{FCS}dV'_{FCS}}{(\int W(\mathbf{r})\cdot\langle\boldsymbol{c}'\rangle\, dV_{FCS})^2} \tag{2.2.6}$$

The term $\langle\boldsymbol{c}'\rangle$ stands for the average concentration of fluorescent tracers in the illumination volume, per measurement time. Using: $\langle\delta(c(\mathbf{r},t)\cdot\delta(c(\mathbf{r}',t+\tau))\rangle=\frac{\langle\boldsymbol{c}'\rangle}{(4\cdot\pi\cdot D\cdot t)^{-\frac{3}{2}}}\cdot e^{-\frac{|\mathbf{r}'-\mathbf{r}|^2}{4\cdot D\cdot t}}$, eq.2.2.6 becomes:

$$G(t) = \frac{\int_0^{V_{FCS}} W(\mathbf{r})\cdot\int_0^{V_{FCS}} W(\mathbf{r}')\cdot\langle\boldsymbol{c}'\rangle\cdot e^{-\frac{|\mathbf{r}'-\mathbf{r}|^2}{4\cdot D\cdot t}}dV_{FCS}dV'_{FCS}}{(4\cdot\pi\cdot D\cdot t)^{\frac{3}{2}}\cdot(\int W(\mathbf{r})\cdot\langle\boldsymbol{c}'\rangle\, dV_{FCS})^2} \tag{2.2.7}$$

By employing the relation between the translational diffusion time, τ, a tracer needs to laterally cross (two-dimensions) the FCS observation volume ($\tau = \frac{r_o^2}{4\cdot D}$), and taking into account that the FCS detection volume is given by[1]:

$$V_{FCS} = \frac{(\int W(\mathbf{r})\, dV_{FCS})^2}{\int W(\mathbf{r})\cdot W(\mathbf{r})dV_{FCS}} = \pi^{\frac{3}{2}}\cdot z_o\cdot r_o^2 \tag{2.2.8}$$

[1] In the next sections and everywhere else in the thesis, the symbol w has been employed instead of r_o.

one may retrieve, after skipping some lengthy derivations, the following analytical form for the $G(t)$ of a freely diffusing fluorescent tracer:

$$G(t) = \frac{1}{\langle c' \rangle \cdot V_{FCS} \cdot (1 + \frac{t}{\tau}) \cdot (1 + \frac{t}{S^2 \cdot \tau})^{\frac{1}{2}}} \tag{2.2.9}$$

The product $\langle c' \rangle \cdot V_{FCS}$ equals the average number, N', of fluorescent tracers in the observation volume. Eq.2.2.9 describes the autocorrelation function resulting purely from the diffusion of one type of identical fluorescent species, through the FCS observation volume. No additional photophysical processes have been included in eq.2.2.9.

Even though both FCS and DLS methods provide information about tracer dynamics via fluctuations in solute's concentration, DLS differs from FCS in the following aspects:

(i) Concentrations of solute are much larger in the former case (10^{-6} M) as compared to the nM concentrations) employed in FCS[74].

(ii) FCS is sensitive only to fluorescent molecules, thus eliminating the influence from backscattering that could potentially influence the DLS measurements[71].

(iii) FCS is suitable for resolution of relatively smaller tracers (molecular size), compared to DLS.

Several photophysical and transport processes for a fluorescent emitter that can be resolved by a representative $G(t)$, are displayed in Fig.2.2 and subsequently outlined.

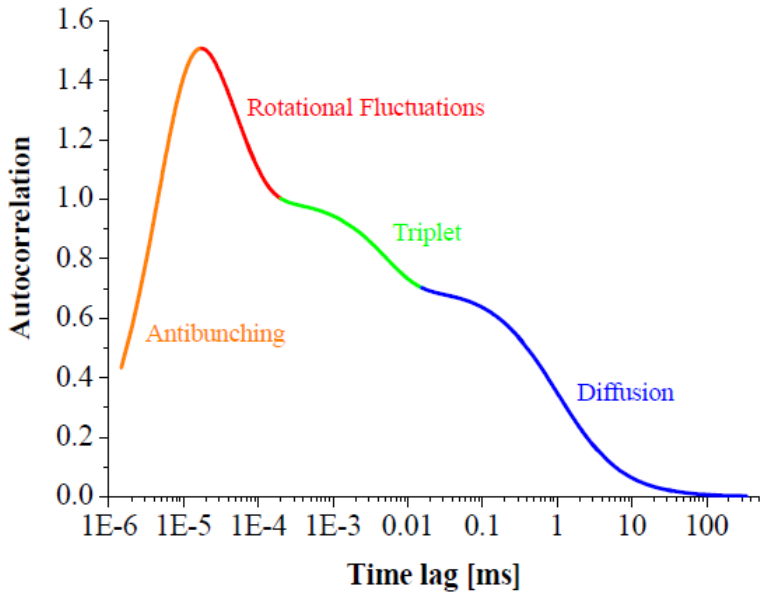

Fig.2.2. Fluorescent intensity autocorrelation functions, $G(t)$, vs, time, t, for a fluorescent emitter. Various independent processes are depicted. Reprinted from 'Fluorescence Correlation Spectroscopy: 'An introduction to its concepts and applications', Petra Schwille, Elke Haustein, (2005), with permission granted from the authors.

For most fluorophores, the tracer's translational diffusion through the diffraction limited illumination spot occurs at relatively large time scales ($10^{-5} - 10^{-1}$ s). The characteristic diffusion time is approximately given by the inflection point of $G'(t)$.

Transition to triplet state ($3 \cdot 10^{-7} - 2 \cdot 10^{-5}$ s) may occur due to vibronic coupling between an excited state and the triplet state, or by spin-orbit coupling. During the triplet relaxation time, the molecule may reside within the illumination spot, but appears dark. According to Pauli's principle [75], two electrons in an atom are allowed to occupy different orbitals, as long as they possess opposite spin angular momenta. In the case of triplet state, however, two electrons located in two orbitals of the same atom have the same –and not the opposite-spin angular momentum. In all reported experiments of the present dissertation, the triplet relaxation time has been at least 10 times smaller than the free diffusion time of the examined fluorophores.

Rotational dynamics ($4 \cdot 10^{-8} - 3 \cdot 10^{-7}$ s) may also be probed provided a polarized excitation and detection by an analyte are both ensured. Again, the relevant time scale is very short comparable to the lower threshold in the temporal resolution for the $G(t)$ related with the FCS setup used in this thesis ($\sim 2 \cdot 10^{-7}$s).Therefore, resolution of tracer's rotational dynamics has not been possible for the setup employed in this thesis.

Antibunching is a very fast process ($10^{-9} - 10^{-8}$ s) and the relevant time scale is very short comparable to the lower threshold in detection time for the FCS setup used in this thesis ($\sim 2 \cdot 10^{-7}$s). The process of antibunching describes [70] that the probability for two photons to arrive at the same time at the detector is minimal, after an emitter has been excited to a higher energy state from a lower energy state with energy absorption. Specifically, after a first photon has been excited from a fluorescent emitter, the emitter returns to the ground state and certain time needs to elapse before a molecule gets reexcited (after when it can emit a second photon) [70].

The last paragraphs of this section are devoted to possible energetic transitions of an emitter. Fluorescent molecules are typically conjugated aromatic structures. The conjugation stems from the presence of delocalized electrons from π- wavefunctions, originating from corresponding π- orbitals of carbon atoms in the aromatic groups of fluorescent molecules. The intermolecular and intramolecular energy redistributions that can follow the absorption of some photon by a fluorescent molecule is typically visualized by the Jablonski diagram[70] in Fig.2.3. This diagram represents the different energy levels, each with the corresponding vibration bands per energy level, as a function of the reaction coordinate (i.e. wavelength). The ground state corresponds to the lowest energy state. Upon absorption of energy (i.e. by excitation laser light) equal to the energy difference between different energy levels, a conjugated molecule can get excited from its ground state of

lowest energy (S_0) to higher excited singlet states (S_1, S_2 etc.), the latter representing higher energy levels. The process of excitation for a molecule can be followed by one of the following (radiative and non-radiative) quite often competing decay mechanisms, back to lower energy states and eventually to the ground state [76]. The relaxation mechanism of major interest for this thesis is fluorescence (dotted green arrow, Fig.2.3), which corresponds to a direct relaxation to the ground state (S_0) from the first excited singlet state (S_1).

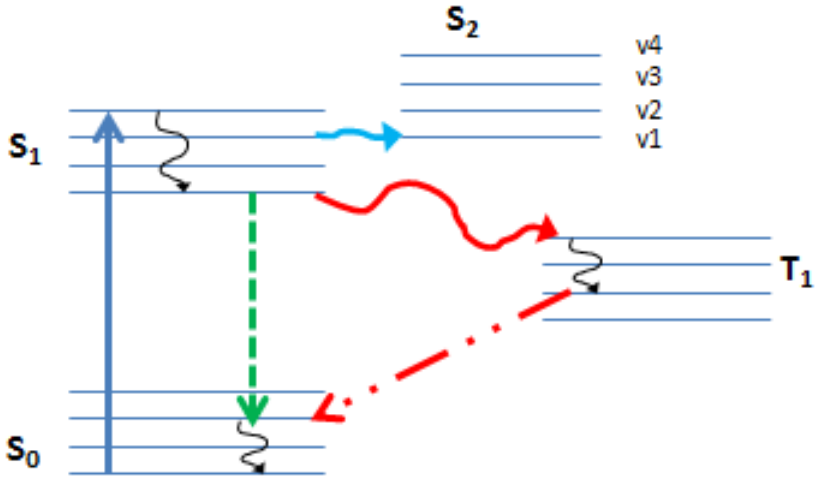

Fig.2.3. A schematic of the Jablonski diagram showing the different energy levels ($S_0 - S_2$) for a fluorescent emitter. The following energetic transitions are shown: absorption of energy (blue arrow), vibrational relaxation (curved black arrow), internal conversion (curved cyan arrow), intersystem crossing (curved, solid red arrow), phosphorescence (dashed-dotted red arrow), fluorescence (dotted green arrow). Each energy level comprises several different vibrational levels (v1-v4).Redrawn from [74].

Another relaxation pathway is the intersystem crossing (known as singlet to triplet transition) shown by the solid red arrow in Fig.2.2. This is a non-radiative energy transfer between the first excited singlet state (S_1) and the triplet state (T_1) that can occur, when the vibrational energy levels between the afore-mentioned states match. In the triplet state, at least one electron is unpaired. The transition from the singlet to the triplet state depends on several features, such as [75]: solubility of oxygen, pH, temperature, chemical structure of the emitter (presence of aromatic groups, halogenated atoms etc.). After intersystem crossing has occurred (S_1 to T_1 transition), relaxation to the ground energy state (S_0) may follow photon emission via phosphorescence (dashed red arrow, Fig.2.3), which is a relatively slow radiative process with lifetimes up to seconds ($10^{-2} - 100$ s). It is noted that the lifetime of fluorescence ($\sim 10^{-8}$s) is much shorter than that of phosphorescence ($10^{-5} - 10^{-8}$s).

An additional relaxation mechanism to the ground state involves internal conversion. Vibrational relaxation (curved black arrow, Fig.2.3) is one of the internal relaxation methods that can occur after

excitation. This is a very fast process within an energy level, according to which an electron relaxes from higher vibration bands to lower ones. Last, when the vibronic levels of different excited states overlap, an additional non-radiative transition can occur from a higher excited singlet state (S_{x}) to lower excited singlet states ($S_{\mathrm{x-n}}, \mathrm{n} \geq 1$), known as internal conversion. Of course, external relaxation may also occur. The latter is a non-radiative process, according to which energy is transferred from the fluorescent molecule to another solvent or solute molecule (as such, it is an 'external' process).

2.3. FCS data analysis

In the presence of a photophysical process (e.g. triplet relaxation) that also contributes to the fluorescent intensity fluctuations, the total $\mathrm{G(t)}$ can be written as the product of the two independent contributions [74], one related with diffusion, $\mathrm{G'_{dif}(t)}$, and another one with photophysics, $\mathrm{Q(t)}$:

$$\mathrm{G'(t) = G'_{dif}(t) \cdot\ Q(t)} \qquad (2.3.1)$$

Furthermore, if n types of different fluorescent species are simultaneously present in the system (e.g. dye-labeled polymers, and non-attached dyes remaining from the labeling process) the diffusion part of the autocorrelation function (eq. 2.2.9) should be a sum of totally n terms (eq. 2.3.2 below). Except for quantum dots, the experimentally measured autocorrelation curves for all other tracers employed in this thesis were represented by some simplification of the multicomponent diffusion correlation function including contribution from triplet relaxation, in the following form[71],[77]:

$$\mathrm{G'(t) = 1 + \frac{1}{N'} \cdot \sum_{i=1}^{n} \frac{F_i}{\left(1 + \frac{t}{\tau_i}\right) \cdot \sqrt{\left(1 + \frac{t}{\mathbf{S}^2 \cdot \tau_i}\right)}} \cdot \left(1 + \frac{T'}{1 - T'} \cdot e^{-\frac{t}{\tau_T}}\right)} \qquad (2.3.2)$$

Here $\mathrm{F_i}$ and τ_i, are the amplitude and the lateral diffusion time of the $\mathrm{i^{th}}$ species, $\mathrm{N'}$ represents the average number of diffusing fluorescent species in the FCS observation volume, $\mathrm{T'}$and τ_T are the fraction and the decay time of the triplet state, and $\mathbf{S} = \frac{z_o}{w}$ is the so called structural parameter ($\mathbf{S}$ values between 5 and 8 have been used everywhere in the experiments of this thesis), with $2 \cdot z_o$ and $2 \cdot$ w the axial and lateral size of the observation volume, respectively. The axial (z_o) and the lateral (w) dimensions of the Gaussian confocal observation volume for each excitation wavelength have been obtained by calibration measurements with dilute (10 nM) aqueous solutions of the molecular tracers Alexa488 (A488), Rhodamine 6G (Rh6G) and Alexa647 (A647), using published values of their diffusion coefficients in pure water [78]. Furthermore, in all fits the triplet time and fraction were used as free fit parameters. The obtained triplet times have been in the range 1-3 μs, as expected for the studied dyes.

The Quantum Dots (QDs) that were also used as fluorescent tracers in this work are core-shell nanoparticles, with semiconductor properties and do not exhibit triplet as photophysical relaxation mechanism: instead, QDs may exhibit prolonged interruptions in their emitted fluorescence (blinking), which has a stochastic nature (Fig.2.4a). This fluorescence intermittency is a photophysical process with very broad time scale ($10^{-7} - 10^{1}$ s) [79, 80].

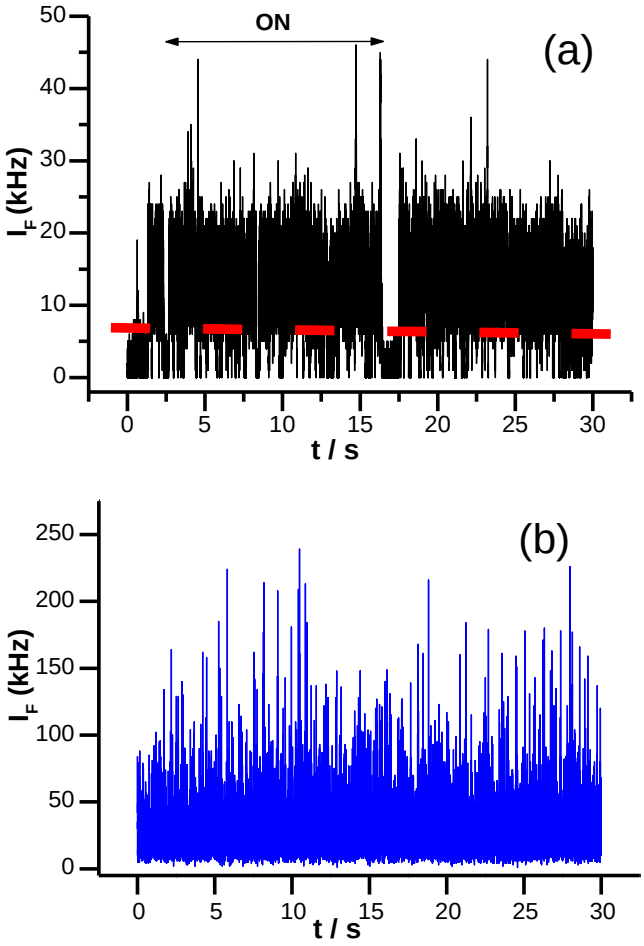

Fig.2.4. Fluorescent intensity fluctuations, $I_F(t)$, vs. t, for (a) fluorescence intermittency (blinking of CdSe/ZnS Carboxyl Quantum Dots 585 in Tetra-PEG 20k hydrogels –Chapter 4 of this thesis) and (b) for constant fluorescent emission (CdSe/ZnS Carboxyl Quantum Dots 525 in water).The dashed horizontal red line in (a) corresponds to the background intensity level.

Different models have been employed to describe the autocorrelation curves when such blinking is present[70, 79]. For QDs everywhere in this thesis, the respective fit to the autocorrelation functions has been the following [81]:

$$G'(t) = 1 + \frac{1}{N'} \cdot (1 - B \cdot t^{2-m}) \sum_{i=1}^{n} \frac{F_i}{\left(1 + \frac{t}{\tau_i}\right) \cdot \sqrt{\left(1 + \frac{t}{S^2 \cdot \tau_i}\right)}} \qquad (2.3.3)$$

Here, B and m represent blinking-related parameters that depend on the structure of the QD, the excitation intensity, its environment and the observation time [81]. Both B and m have been treated as free parameters of the model with the constraint that they undertake exclusively positive values ($\mathrm{B} > 0, m > 0$). For the simplest case of QD diffusion in mili-Q water, the inflection point of the autocorrelation function, $\mathrm{G(t)}$, corresponds to the QD translational diffusion time (dashed vertical line, Fig.2.5).

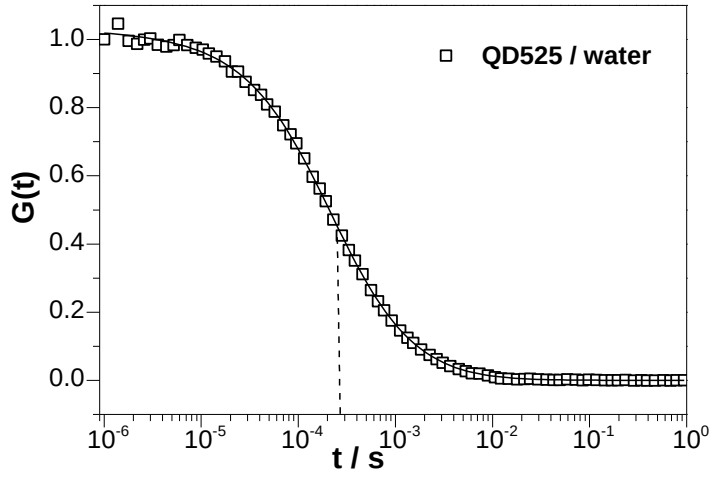

Fig.2.5. Normalized fluorescent intensity autocorrelation functions, $\mathbf{G(t)}$, vs. t, for quantum dots in water (no additional polymer). Solid curve through the data (black squares) denotes the single Fickian diffusion fit. The vertical dashed line denotes the extracted diffusion time by the single Fickian diffusion fit.

In absence of blinking, other candidate equations (instead of eq.2.3.2) that could be employed to fit the FCS autocorrelation curves for tracer diffusion in complex polymer networks (i.e. presence of interactions) , in view of the following Chapters of the thesis, have been the following: the diffusion & rare strong adsorption [82] or a diffusion & reaction model [83, 84]. However, the former models did not successfully fit the experimental data, as is discussed in the respective Chapters 3 and 4. In addition, the so-called subdiffusive model ($< \Delta \mathrm{r}^2(\mathrm{t}) > \sim \mathrm{t}^{\alpha}, 0 < \alpha < 1$) has been often used in FCS studies to account for deviations from single Fickian diffusion of biomolecules in crowded matrix environments [50, 85-87]. Even though such a model can adequately fit some of the experimental $\mathrm{G(t)}$ reported in the present study, the direct assignment of certain physical significance to the stretched exponential parameter 'α' is rather not straightforward and should be carefully justified[88, 89]. Accordingly, no attempts have been made to interpret the present data using subdiffusion models for the FCS autocorrelation curves, although the fit works apparently well when deviations from single Fickian diffusion have been recorded.

2.4. Molecular dynamics (MD) simulations

MD simulations have been kindly performed by Peter Košovan (ICP Stuttgart/ Charles University, Prague and Christian Holm, ICP Stuttgart), in order to investigate the effect of polymer-tracer interactions and to support the analysis of the corresponding experimental $G'(t)$ of Chapter 3. Specifically, MD simulations of generic tracer and polymer models have been accomplished and the respective $G'(t)$ have been also calculated (3rd Chapter), for analogous tracers as the ones used in the experiments (Chapter 3). The standard Kremer-Grest polymer model [90] with the purely repulsive (athermal) [9] WCA potential [91] has been used to account for the excluded volume of all particles, with a diameter of $\sigma = 1.0\ \mathrm{nm}$. This is approximately the size of four PNiPAAm monomers or of one molecular tracer. Attractive polymer-tracer interactions were modeled by the Lennard-Jones (LJ) potential with an adjustable attraction parameter, ε. Simulations were performed with 20 polymers consisting of 50 segments ($R_H = 25\ \mathrm{nm}$), 20 athermal and 5 attractive tracers per simulation box, in an implicit solvent employing a Langevin thermostat [90], using the ESPReSSo software [92]. The polymer was simulated by a generic bead-spring model. Excluded volume interactions are accounted for by the Lennard-Jones (LJ) potential:

$$V'_{sr}(r) = 4 \cdot \varepsilon \cdot \left(\left(\frac{\sigma}{r}\right)^{12} - \left(\frac{\sigma}{r}\right)^{6}\right) + C(r_{cut}), \text{for } r < r_{cut} \qquad (2.4.1)$$

where $C(r_{cut})$ has been chosen such as to obtain $V'_{sr}(r_{cut}) = 0$, while it has been defined that $V'_{sr}(r > r_{cut}) = 0$. The parameter σ roughly defines the hard sphere's diameter and was deliberately chosen as $\sigma = 1.0\ \mathrm{nm}$. Connectivity of the monomers in a polymer chain configuration has been accounted for by using a FENE potential of the form:

$$U_{FENE} = -\frac{1}{2} \cdot K_{FENE} \cdot R_{FENE}^2 \cdot \ln\left(1 - \left(\frac{r}{R_{FENE}}\right)^2\right) \qquad (2.4.2)$$

where the values for the stiffness constant $K_{FENE} = \frac{7\ k_B \cdot T}{nm^2}$ and for the cutoff radius $R_{FENE} = 2.0\ \mathrm{nm}$. By choosing $r_{cut} = \sigma^{1/6}$, the LJ potential becomes purely repulsive and in combination with the FENE potential in eq.2.4.2, the behavior of an athermal polymer is reproduced. To simulate the various polymer-tracer interactions, a value of $r_{cut} = 2.5\ \mathrm{nm}$ has been selected, so that the potential becomes attractive with the minimum at $\sigma = 1.0\ \mathrm{nm}$. The tracer-polymer attractive strength has been varied by changing ε which is the depth of the potential well. In the preparation round, a single polymer chain of the desired length was simulated for about 10^7 time steps which produced about 100 uncorrelated chain conformations. These conformations were then used to set up the polymer solution, consisting of 20 chains. When setting up the solution, the pre-computed conformations were inserted randomly into the simulation box. To speed up equilibration, before inserting tracers, the chains were moved using Monte Carlo with about 100 attempted moves per chain, average

attempted displacement of 1/4 interchain separation and the Metropolis acceptance criterion. In between the moves, 100 MD integration steps were performed to further relax the conformation. After that, tracer particles were inserted at random, followed by a short MD integration period where their interactions were switched on gradually.

Finally, a production run of about 10^8 time steps was performed which is about 100 times longer than the free diffusion time of the polymer, to ensure good statistics. Data for time-correlation functions ($G'(t)$) and $MSD\ (t)$ were collected every 10 time steps and correlated using the multiple tau correlator algorithm [92]. The correlation functions were computed for each tracer separately. Assuming that the diffusing tracers were independent, the statistical error of the obtained correlation functions was computed for each value of t as the standard deviation of the correlation functions obtained for individual tracers. For a given tracer, the final reported $G(t)$ is the average over –at least- 3 individual measurements per monomer concentration (either in solutions or hydrogels). The curves were fitted using the Levenberg-Marquardt algorithm provided by the Gnuplot plotting software. The fitting routine gave relatively stable results when amplitudes of the slow and the fast process were both $0.1 < F_i < 0.9$. Outside this range two components could not be safely resolved and one-component fits were sufficient.

2.5. Materials and sample preparation

The examined PNiPAAm terpolymer (Fig.2.6) consisted of 94% mol poly(N-isopropylacrylamide) as well as of hydrophilic (5% mol of methacrylic acid) and hydrophobic (1% mol of benzophenone methacrylate) groups. It was synthesized by free radical polymerization as described elsewhere [64],[93]. Its polydispersity index (PI) was PI=2.7, as obtained from gel permeation chromatography, while the overlap concentration, $c^* = \frac{M_w}{(\frac{4}{3})\cdot\pi\cdot R_H^3\cdot N_A} = 2.6\cdot 10^{-3}$ g·ml^{-1}, N_A being the Avogadro number, R_H ($= 15$ nm) the hydrodynamic radius of the polymer and weight-averaged molecular weight, $M_w = 280$ kg·mol^{-1} (hereafter referred to as 280k). Unless otherwise noted, 280k PNiPAAm has been used everywhere in the experiments described in this thesis. The benzophenone groups served as the cross-linking agent between the polymer chains, upon illumination with UV light at wavelength λ =365nm.

Preparation of poly-(N-isopropyl-acrylamide) (PNiPAAm) solutions: Several PNiPAAm solutions (results described in Chapters 3 and 4) were prepared below and above the overlap concentration, c^*. Namely, certain quantity of solid PNiPAAm was added in an empty glass and subsequently certain volume of aqueous fluorescent dye solution (10nM concentration for each dye: A647 and either Rh6G, or A488) was added in the sample to reach the desired PNiPAAm concentration. The samples

were stored overnight in the fridge ($T = 4$ ℃), in order to facilitate polymer solubilization (mili-Q water for all tracers has been employed, except for IgG where 10mM acetate buffer has been used).

Preparation of grafted PNiPAAm layers: Round microscope cover glass slides (2.5 cm diameter, 160 mm thickness) were treated with a 1 mM ethanol solution of 4-(3-triethoxysilyl) propoxy-benzophenone ethanolic solution overnight, in order to functionalize the glass slide with benzophenone groups. The benzophenone groups would then serve as anchoring agents, thus enabling the following spin-coated PNiPAAm terpolymer to covalently anchor at a later step. A 10 wt% PNiPAAm solution in ethanol was spin coated at room temperature onto the pre-functionalized round microscope cover glass slides (diameter 25 mm, thickness: 0.16 mm) at certain spinning speed (250 rpm) and spinning time (60 sec). After spin coating, the slides were annealed for 1 hour at $T = 170$ ℃ (a temperature higher than the glass transition temperature of PNIPAAm) in vacuum, in order to relieve the polymer system from possible stresses. The slides were then dried at $T = 50$ ℃ (overnight in vacuum), to remove any traces of the solvent and then subsequently crosslinked by UV irradiation (Stratalinker 2400, Stratagene) at $\lambda = 365\ \mathrm{nm}$ (1 hour of crosslinking corresponds to an irradiation energy dose of about $6.28\ \frac{\mathrm{J}}{\mathrm{cm}^2}$). Consecutively, the slides were rinsed 15 times in situ with absolute ethanol, to remove any uncrosslinked chains; between all steps before crosslinking, the slides were kept in argon atmosphere. The dry thickness was measured by a profilometer (KLA-Tencor Stylus P-16+) in 5-6 different locations of the dried sample, after the crosslinked polymer had been rinsed in ethanol. The measurements in the grafted hydrogels were performed 30' after addition of the fluorescent tracer aqueous solution, to ensure that the gel has fully reached swelling equilibrium. For the molecular tracers of this thesis (in solutions and grafted hydrogels, 3rd Chapter), only ultrapure deionized water was used (filtered through a MilliQ purification system, resistivity 18.2 MΩ·cm) without any buffers. However, only for the study of antibody diffusion (4th Chapter, section III) acetate buffer was used to swell the gels. The temperature-dependent swelling ratio, $R_s(T)$, was determined as the ratio between the fully swollen thickness and the dry thickness. The dry thickness has been measured by a step profiler (KLA-Tencor Stylus P-16+ profilometer) as mentioned previously, while the thickness of the fully swollen hydrogels was determined using the FCS setup. By shifting the microscope objective, the position of the FCS observation volume was scanned in z-direction (normal to the film plane) with a step of 1 μm and the average fluorescence intensity signal that is proportional to the local density of the tracers was recorded as a function of the focus position (z-scan). A typical z-scan (Fig.3.1) depicts 2 transition regions, representing the hydrogel/water and glass/hydrogel interfaces. The distance between these regions represents the thickness of the fully swollen gel. The monomer concentrations (monomer volume fractions, $\phi(T) = R_s^{-1}(T)$) for the studied hydrogels (HG) are shown in Tables 4.1 and 4.2(4th Chapter).

Fluorescent tracers: Fluorescently labeled polystyrene nanoparticle spheres (PS-NP) have been synthesized by Umaporn Paiphanshiri (MPIP), as reported elsewhere[94]. They have been kindly provided by Karmena Jaskiewicz (MPIP). The following fluorescent tracers, A488 (Alexa Fluor 488 5-TFP, A-30005), A647 (Alexa Fluor 647 cadaverine, disodium salt, A30679), QD (Qdot® 525 ITK™ carboxyl quantum dots, Q21341MP) and Rh6G (Rhodamine 6G Chloride, R634) were all purchased from Life Technologies GmbH/Invitrogen Inc. Fluorescein Isothiocyanate) FITC- labeled dextran in 5 different M_w(Dex4k, Dex20k, Dex70k) and single stranded Alexa488-labelled DNA were purchased from Sigma Aldrich. In addition, A488 5- sulfodichlorophenol ester from Invitrogen (Life Technologies, GmbH) was used to label PEO, to be used as a fluorescent tracer. Moreover, a goat-antimouse IgG covalently labeled with A647 (A-21235, Invitrogen) was kindly provided by Khulan Sergelen (Austrian Institute of Technology, Vienna). The repeat unit of the PNiPAAm terpolymer and available structures of fluorescent tracers employed in Chapters 3 and 4 are shown in Fig.2.6. The chemical structures of A647 and of QD are not publicly available.

Regarding the tracer charges, Rh6G is a positively charged tracer[95], while zeta potential measurements in mili-Q water (Karmena Jaskiewicz, MPIP) revealed that A488 and PNiPAAm are strongly negatively charged and slightly negatively charged, respectively. As A647 lacked any attractive interactions with the examined PNiPAAm [77], it was simultaneously present in the studied samples with the other dyes as a 'control' tracer. An argon ion (Ar^+) laser at λ=488 nm was used to excite Alexa488 (A488), quantum dots (QDs), fluorescein isothiocyanate (FITC)-dextran, polystyrene latex nanoparticles (PS-NP), single stranded A488-labeled DNA and labeled linear polyethylene oxide (PEO). Alexa647 (A647) and A647-labeled IgG tracers were excited by a HeNe laser at λ=633 nm, while a HeNe laser at λ =543 nm was used to excite Rhodamine 6G (Rh6G). The base sequence for the A488-labeled single stranded DNA (PAGE purified) is shown in Fig.2.7a. The exact A488 used for labeling is patented and hence, not publicly available. Fig.2.7b shows the structure of A488 used for covalently labeling PEO as a fluorescent tracer in the 5th Chapter. The repeat unit of FITC-dextran is shown in Fig.2.8.

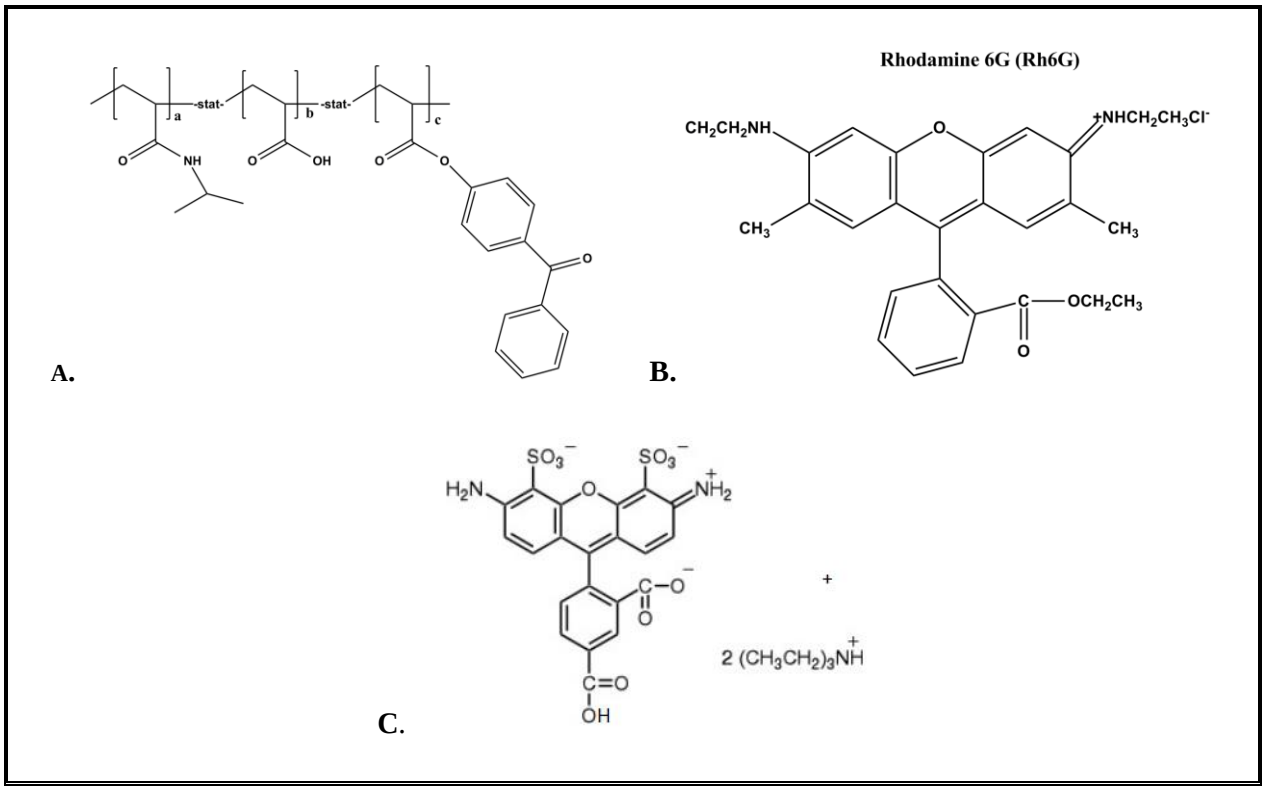

Fig.2.6. Chemical structure (A)–repeat unit- for the poly(N-isopropylacrylamide) based terpolymer; chemical structures of the strongly (Rh6G) (B) and the weakly (A488 acid derivative) (C) interacting tracers. Structures of the the repulsive A647 and of the labeled antibody (IgG) are not publicly available.

(a) [A488]TAACAGGATTAGCAGAGCGAGGTAACAGGATTAGCAGAGCGAGGTAACAGGATTAGCAGA GCGAGGTAACAGGATTAGCAGAGCGAGG

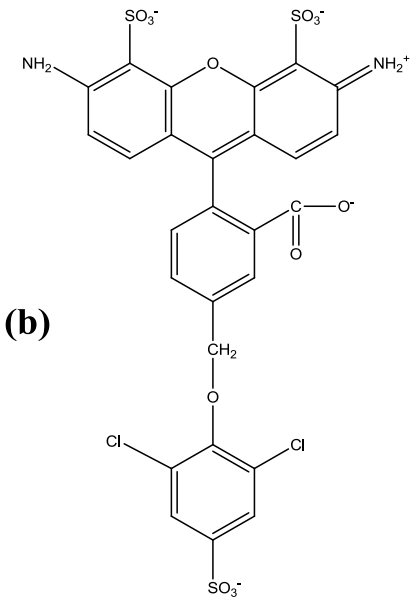

Fig.2.7. Schematic of the (a) A488-labelled single stranded DNA with 88 bases, and (b) of the A488 5- sulfodichlorophenol ester (for labeling of PEO tracer) used in the experiments of the 5th chapter.

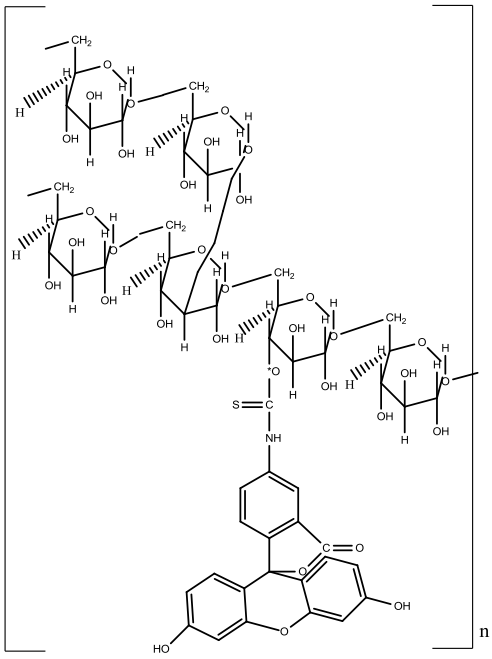

Fig.2.8. Schematic of FITC-labelled dextran (repeat unit) employed in the experiments of the 5th chapter.

Tetra-PEG hydrogels: Tetra-PEG hydrogels of three different pore sizes were synthesized by the group of Prof. Mitsuhiro Shibayama (Tokyo University) using 'click' chemistry between star Tetra-PEG polymers (Fig.2.9), bearing tetra-amine and N-hydroxysuccinimide ester terminal groups [96].

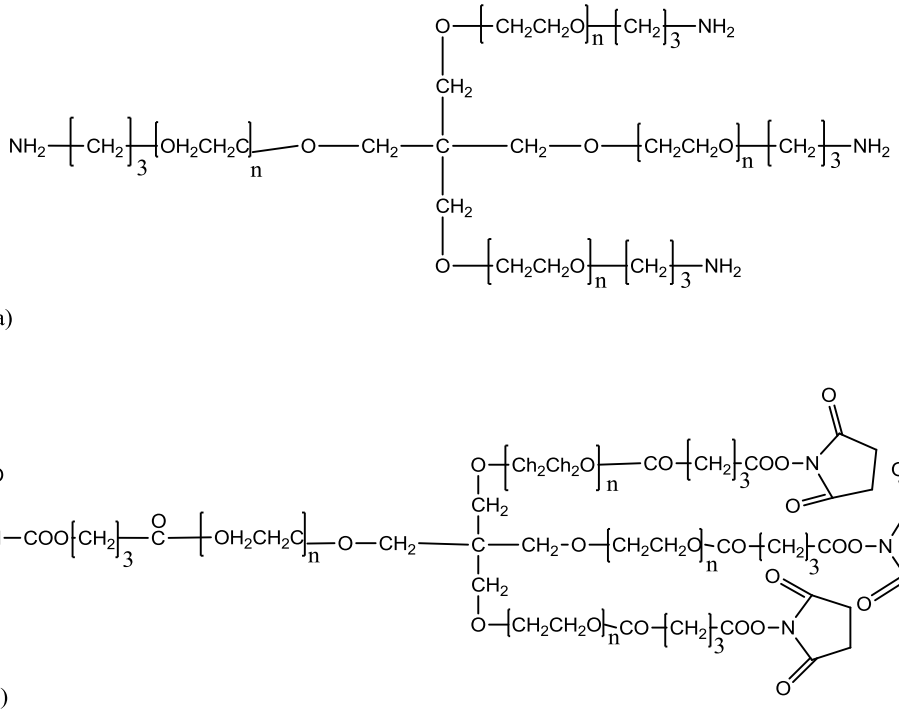

Fig.2.9. Repeat unit of Tetra-PEG star macromers bearing (a) amine and (b) N-hydroxysuccinimide ester terminal groups. Using click chemistry, structures (a) and (b) covalently bind within 10 minutes in situ, to form the Tetra-PEG hydrogel. Redrawn based on [96].

Tetra-PEG hydrogels at 3 different M_w were sent (Prof. Mitsuhiro Shibayama's group, University of Tokyo) at concentration 0.1 g·ml^{-1} (concentration in the as-prepared state) in thin rectangular films of the following (xyz) dimensions: 3 mm vertical thickness (z), 70 mm lateral dimension (x), 40 mm axial (y dimension). A certain volume from a mili-Q water fluorescent tracer solution was added in an 8-well NUNC chamber (Thermo Scientific) of borosilicate substrate and polystyrene cover. Using a clean metal scarpel and PTFE tweezers (Carl Roth), a $3\,\mathrm{mm} \times 3\,\mathrm{mm}$ piece from the Tetra-PEG hydrogel in the 'as-prepared' state was cut and consecutively added in a given well of the 8-well NUNC chamber (where the chamber consisted of polystyrene and the cover glass of borosilicate, provided by Thermo Scientific Inc.), only after the fluorescent tracer's solution had been added. This approach facilitated swelling of the hydrogel from either side. By means of an Eppendorf tip, the solution was homogenized vigorously, in order to accelerate and facilitate the approach of chemical potential equilibrium of fluorescent tracer between the supernatant and 'in-hydrogel' phases. Depending on the interplay between size/fractal dimension of the tracer and hydrogel's mesh size, the approach of chemical equilibrium lasted from several minutes (molecular tracers or dextrans) to several weeks (weeks, in the case of: Quantum Dots in Tetra-PEG 20k and/or Tetra-PEG 10k).

Swelling ratio of Tetra-PEG hydrogels: The position of the FCS observation volume was scanned in z-direction by shifting the microscope objective (normal to the film plane) with a step of 1 μm. The average fluorescence intensity signal that is proportional to the local concentration of the fluorescent tracer was recorded as a function of the focus position (z-scan). A typical z-scan (Fig.3.1) depicts two transition regions, representing the hydrogel/water and glass/hydrogel interfaces. The distance between these regions represents the thickness of the fully swollen gel .The monomer volume fraction, ϕ, has been determined as the ratio between the fully swollen thickness and the thickness in the as-prepared state times the gel's concentration in the as-prepared state.

PEO polymers: The PEO polymers employed in the experiments of this chapter (5th Chapter-sections II and III) have been synthesized by living anionic polymerization (Polymer Source Inc.).The repeat unit is shown in Fig.2.10.

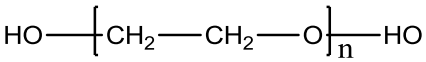

Fig.2.10. Repeat unit of the linear PEO polymers (Invitrogen Inc.) used in this thesis.

Totally, 3 different M_w of linear PEO, namely 20k (#P4208-EG2OH), 100k (#P5377-EG2OH) and 481k (#P5617-EG2OH) exhibiting a very narrow polydispersity index (PI=1.05-1.1), as reported from the manufacturer (size exclusion chromatography, product sheet by Polymer Source Inc.), have been

employed as the polymer matrix. Several aqueous PEO solutions of the fluorescent tracer of choice (mentioned next) were prepared below and above the overlap concentration, c^* (Chapter 5), using mili-Q water only. The samples were stirred overnight at 400 rpm at room temperature.

Sample holders. 8-well NUNC chambers (where the chamber consisted of polystyrene and the cover glass of borosilicate, provided by Thermo Scientific Inc.) were used for loading the following samples: aqueous solutions of either (i) PEO or (ii) PNiPAAm and (ii) for loading the Tetra-PEG gels with the aqueous solution of fluorescent tracers. In order to prevent solvent evaporation during the experiments, the NUNC chamber was sealed with parafilm and stored in the fridge ($\mathrm{T} = 4\,℃$) for several days, when experiments had to be repeated.

Concerning the experiments for the grafted PNiPAAm hydrogel layers, two different reusable Attofluor steel chambers were used as sample holders: one for the grafted PNiPAAm hydrogel layers and another one for both pinhole and focal volume calibration (aqueous solution of standard fluorescent tracer). In order to prevent solvent evaporation during the experiments, the Attofluor sample chamber was covered with a round microscope glass slide.

2.6. Supporting characterization techniques

In this section, additional experimental techniques are presented that have contributed, either directly or indirectly, to the results of this thesis.

Static Light Scattering (SLS). LS experiments have been performed in FORTH, Heraklion (Hellas) by Antje Larsen for the determination of hydrodynamic parameters (gyration radius,$\mathrm{R_g}$) of the polyethylene oxide (PEO) and poly-N-isoprolylacrylamide (PNiPAAm) polymers employed in the present thesis (3rd and 4th chapter). Static Light Scattering is an absolute method for the determination of the weight-average molecular weight, $\mathrm{M_w}$, the 2nd virial coefficient for a polymer in a given solvent, $\mathrm{A_2}$, and the gyration radius, $\mathrm{R_g}$ [66], [7]. In SLS, light is scattered from a light source onto a colloidal particle and the polymer's weight average molecular weight ($\mathrm{M_w}$) is determined on account of the differences in scattered intensity between the polymer and the solvent. Depending on the size of the scatterer with respect to the wavelength of incident light, the scattered intensity may exhibit (or not) angular dependency. The following equation relates the polymer size ($\mathrm{M_w}$) with $\mathrm{A_2}$ and the scattering parameters $\mathrm{R_\theta}, K$ and $\mathrm{P(\theta)}$ [66]:

$$\frac{\mathrm{K^{\#}} \cdot \mathrm{c}}{\mathrm{R_\theta}} = \left(\frac{1}{\mathrm{M_w}} + 2 \cdot \mathrm{A_2} \cdot \mathrm{c}\right) \cdot \frac{1}{P(\theta)} \qquad (2.6.1)$$

$\mathrm{R_\theta}$ is the Rayleigh ratio that denotes the ratio of scattered light over the incident light:

$$R_\theta = \frac{I_{SC,A} \cdot \boldsymbol{n}'^2}{I_T \cdot \boldsymbol{n}_T^2} \cdot \boldsymbol{R}_T \quad (2.6.2)$$

Where $\boldsymbol{n}_T, \boldsymbol{n}'$ and $\boldsymbol{R}_T$ correspond to toluene's scattering intensity, refractive index and an optical constant, respectively, as reference values. The terms $I_{sc,A}$ and I_T correspond to the residual scattering intensity of the analyte (relative difference in scattering intensity between solution and pure solvent) and the incident intensity, respectively. The parameter $K^{\#}$ is the optical constant and incorporates the solvent's viscosity n_s and the refractive index increment, $\frac{d\boldsymbol{n}'}{dc}$:

$$K^{\#} = \frac{2 \cdot \pi^2}{\lambda_0^4 \cdot N_A} \cdot (n_s \cdot \frac{d\boldsymbol{n}'}{dc})^2 \quad (2.6.3)$$

And $P(\theta)$ is the angular dependence of the sample's scattering intensity, with incident wavelength, λ_0 and scattering angle θ, known as form factor:

$$P(\theta) = 1 + \frac{16 \cdot \pi^2 \cdot n_s^2 \cdot R_g^2}{3 \cdot \lambda_0^2} \cdot \sin^2(\theta) \quad (2.6.4)$$

For scatterers with size much smaller than the incident wavelength, λ_0: $P(\theta) = 1$. SLS differs from DLS, in the sense that the scattered intensity from a colloidal particle of interest in the former case is averaged over long time for different polymer concentrations. In DLS, on the contrary, the temporal intensity fluctuations are averaged over a large number of scatterers (ensemble average).

Photon Correlation Spectroscopy. Photon Correlation Spectroscopy (PCS), also known as Dynamic Light Scattering (DLS), represents an established absolute method (no calibration needed) to measure solute concentration and to determine diffusion coefficients of solutes, in respective polymer solutions. According to the general scattering principle in a DLS setup (Fig.2.11) [46], polarized incident light impinges on a scattering volume (a diffusing solute) having different dielectric constant than the surrounding environment. The light gets then scattered, due to infinitesimal differences (fluctuations) in the dielectric constant, before and after the light has encountered the given scattering volume.

After passing through an analyzer, the scattered light is then collected by a photomultiplier tube (D), where the recorded dielectric constant fluctuations are transformed to intensity fluctuations. Bragg's law [46] relates the refractive index, $\boldsymbol{n}'$, the incident wavevector, k_i, the scattering angle, θ, and the scattering wavevector, q:

$$q = 2 \cdot k_i \cdot \sin\frac{\theta}{2} = \frac{4 \cdot \pi \cdot \boldsymbol{n}'}{\lambda_i} \cdot \sin\frac{\theta}{2} \quad (2.6.5)$$

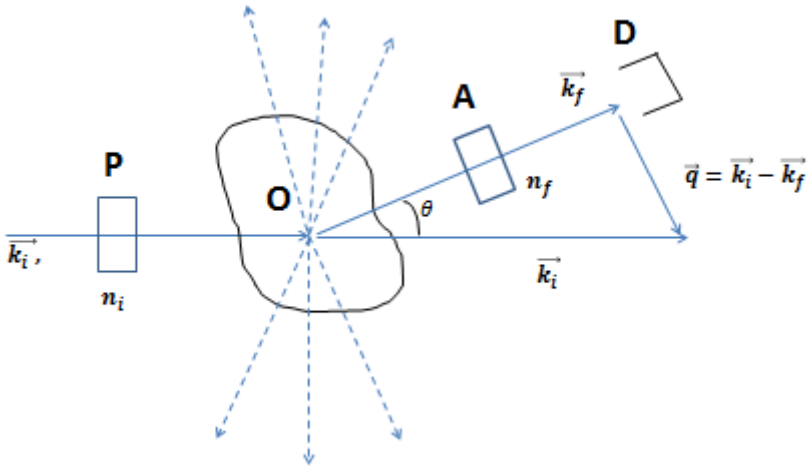

Fig.2.11. Qualitative sketch of light scattering concept in a DLS setup. Monochromated light passes through a polarizer (P) with an incident wavevector, $\vec{k_i}$ and polarization, n_i. Upon incidence on a scattering object (O), the detector (D) can collect only the light that gets scattered at a certain angle, θ, with respect to the incident direction accompanied by a corresponding scattered wavevector, $\vec{k_f}$ and polarization, n_f. Redrawn based on [46].

The autocorrelation function for the intensity of the scattered light describes the temporal self-similarity in the intensity of the scattered light:

$$\langle I_{SC}(0) \cdot I_{SC}(t) \rangle = \lim_{T \to \infty} \frac{1}{T} \int_0^T I_{SC}(t) \cdot I_{SC}(t+\tau) dt \qquad (2.6.6)$$

For an ensemble of N Brownian particles in DLS, the autocorrelation function can be written as:

$$g_2(\tau) = 1 + |g_1(\tau)|^2 = 1 + e^{-2 \cdot D \cdot q^2 \cdot \tau} = \frac{\langle I_{SC}(t) \cdot I_{SC}(t+\tau) \rangle}{\langle (I_{SC}(t))^2 \rangle} \qquad (2.6.7)$$

By fitting the intensity autocorrelation function, $g_2(\tau)$, by particular models[46], the diffusion coefficient of the given colloidal particle, D, can be obtained.

Size exclusion chromatography (SEC). In contrast to SLS, SEC, also called gel permeation chromatography (GPC), presents a relative method for the determination of the weight-average and number-average molecular weights, M_w and M_n, of polymeric materials and their polydispersity index (PI=$\frac{M_w}{M_n}$). GPC measurements for the experiments in this thesis have been performed by Sandra Seywald (Polymer Analytics' group) at the MPIP-Mainz, in order to analyze the size distribution of PNiPAAm polymers synthesized by Katja Nilles (4th Chapter) and the labeled PEO for the 5th Chapter, labeled by Dapeng Wang. The separation principle is based on the different retention times of polymer molecules by a stagnant phase on account of the differences in the polymer radii, compared to the pore size of the stagnant phase. A polymer solution flows through a sequence of chromatographic columns filled with a porous stagnant phase. Separation of different polymer

molecular weights occurs due to their size-dependent mobilities through a stagnant (gel) phase. Polymers with larger size than the pore size of the stagnant phase can be more easily get through the interstitial space within the column, while the opposite occurs with decreasing particle size (increased retention). The optimal range for polymer molecular weight to be resolved is between $10^3 - 10^7$ g·mol^{-1} [97-99]. The size –and thus, molecular weight- can be estimated by the eluted volume at certain times, being inversely related to the intrinsic polymer's viscosity. The size determination is accomplished by using one of the following types of detectors: UV-VIS or IR detectors, detectors based on differential refractive index and static light scattering detectors. The polymer size, $\mathrm{R}\,(\text{or}\,\mathrm{M})$, is related with the intrinsic viscosity, $[\eta]$, by means of the Mark-Houwink relation [7] with $\Phi^{\#}$ and K° constants that can be retrieved in various handbooks of polymer physics:

$$[\eta] = \Phi^{\#} \cdot \frac{\mathrm{R}^3}{\mathrm{M}} = \mathrm{K}^{\circ} \cdot \mathrm{M}^{3\cdot\nu-1} \qquad (2.6.8)$$

Profilometry. The estimation of dry film thicknesses of grafted PNiPAAm layers (Materials-2nd Chapter), has been accomplished by means of a stylus profilometer (KLA-Tencor Stylus P-16+), by Apostolos Vagias, at the MPIP-Mainz ('hands-on' training had been performed by Ms. Gabi Hermann). Before attempting any measurements of dry profile thickness, a scratch of about $1\mathrm{mm}$ length was first performed on the dry gel's surface using a metal needle and pressurized air was blown to remove the displaced material from the indentation. According to the operating principle, a scanning force is applied via a stylus with a diameter of 10 μm having a sharp conical tip that comes in contact with a given surface topology (roughness). Upon changes of surface roughness (i.e. deviation from an average roughness value), a piezoelectric capacitor changes the stylus-surface distance and the profile of a dry thickness is obtained. The prerequisite is that the surface is harder than –therefore, not deformable upon contact with - the stylus. Hence, soft and sticky surfaces have to be avoided, to prevent stylus contamination. The applied scanning force is in the range of $1\ \mathrm{mg} - 2\ \mathrm{mg}$. The vertical range of the stylus is $327\mu\mathrm{m}$ and surface features can be resolved within the range $7.8\ \mathrm{nm} - 13\mu\mathrm{m}$. The maximum scanned rectangular area has the following dimensions: $200\ \mathrm{mm} \times 200\ \mathrm{mm}$.

Chapter 3: Complex Tracer Diffusion Dynamics in Polymer Solutions

Abstract

Before addressing the more complex case of polymer hydrogels, this chapter describes how fluorescence correlation spectroscopy (FCS) experiments and coarse-grained molecular dynamics (MD) simulations have been employed to study the mobility of tracers in polymer solutions. It was found that excluded volume interactions result in crowding-induced slowdown, where the latter depends only on the monomer concentration. In the presence of specific tracer-polymer attractions, the tracer is slowed down at much lower concentrations, and a second diffusive component appears that is sensitive to the polymer chain length. The two components can be resolved by FCS, only if the distance traveled by the tracer in the polymer-bound state is greater than the FCS focal spot size. The tracer dynamics can be used as a sensitive probe of the nature and strength of interactions, which (despite their local character) emphasize the role of chain connectivity.

3.1. Introduction

Fluorescence correlation spectroscopy (FCS) is a technique typically employed to study the dynamics of small molecules in complex environments [50, 52, 72, 100]. It has become overwhelmingly popular in biological sciences due to its single molecule sensitivity and non-invasive nature [51, 101]. Fluctuations of the fluorescence intensity due to individual tracer molecules crossing the focal spot of the excited laser beam reveal distinct tracer dynamics [69, 72]. When fitting the fluorescence intensity autocorrelation function, $G'(t)$, by a single Fickian process, one can extract the diffusion constant [72]. If $G'(t)$ cannot be described by a one-component diffusion, the interpretation becomes unclear unless the applied model can be validated independently [50],[102, 103]. This ambiguity limits the application of FCS and the amount of useful information that could be obtained concerning diffusion in the presence of interactions with the host environment. However, investigations of such media are of paramount importance for biomedical applications[104].This chapter describes results concerning the diffusion of several tracers in dilute poly(N-isopropyl acrylamide) PNiPAAm solutions, where the tracers exhibit different interactions with PNiPAAm. PNiPAAm is a thermoresponsive polymer typically utilized in biosensor applications [25, 26].The particular simplified polymeric model system has been deliberately selected in order to mimic a crowded environment with possible attractive interactions frequently encountered in biological and soft matter systems [83, 105, 106]. In addition, molecular dynamics (MD) simulations have been performed on a system that entails an interacting spherical tracer in a solution of bead-spring

polymers. Simulated and experimentally measured $G'(t)$ are compared. It is demonstrated that in the case of attractive tracer-polymer interactions a two-component diffusion process can model the experimental $G'(t)$, whereas a subdiffusive model to $G'(t)$ can be safely ruled out. For the former model, the fast component corresponds to free diffusion, whereas the slow one stems from the polymer-bound tracer. This picture is supported by constructing a simple binding model that explains the MD data in terms of fractions of bound and free tracers. The ability to resolve the two diffusion processes depends crucially on the FCS focal volume which defines the available length and time scales necessary to resolve the underlying processes [88, 107].

3.2. Materials

The chemical structure of the PNiPAAm terpolymer unit used in this Chapter is shown in Fig.2.6 (2nd Chapter) and the synthesis is reported elsewhere [64, 93]. The NiPAAm provides the thermo-responsive characteristics to the terpolymer, the methacrylic acid allows for post-synthetic modification with proteins, while the benzophenone moiety enables the photo-crosslinking of the terpolymer. All experiments in this chapter were performed at 25°C in aqueous polymer solutions containing PNiPAAm terpolymers with M_w= 280 kg·mol^{-1} (hydrodynamic radius R_H= 15 nm) [18], unless otherwise noted. All fluorescent tracers, A488 (Alexa Fluor 488 5-TFP, A30005), A647 (Alexa Fluor 647 cadaverine, disodium salt, A30679), Quantum Dots (QD)-(QDot 525 ITK Carboxyl Quantum Dots-Q21341MP) and Rh6G (Rhodamine 6G Chloride, R634), were purchased from Invitrogen Inc. The publicly available chemical structures for the fluorescent tracers used in this Chapter, namely for A488 and Rh6G, are shown in Fig.2.6 (2nd Chapter). The sample preparation is also reported in the 2nd Chapter. As A647 lacked any attractive interactions with the polymer system [77], it was simultaneously present in the polymer samples together with the other dyes, acting as a 'control' tracer. In FCS experiments, tracers present at nanomolar concentrations in PNiPAAm aqueous solutions were excited pairwise simultaneously, for two excitation wavelengths: A647 by a HeNe laser (λ=633 nm), A488 and/or QD by an Ar^+ laser (λ =488 nm) and Rh6G by a He-Ne laser (λ =543 nm). To investigate the effect of polymer-tracer interactions, MD simulations of generic tracer and polymer models have been accomplished by Peter Košovan (Charles University, Prague) to calculate $G'(t)$. The standard Kremer-Grest model [108] with the purely repulsive (athermal) [9] WCA potential [91] has been used to account for the excluded volume of all particles, with a diameter of σ = 1.0 nm. This is approximately the size of four PNiPAAm monomers or the molecular tracers. Attractive polymer-tracer interactions were modeled by the Lennard-Jones (LJ) potential with an adjustable attraction parameter, ε. Simulations were performed with 20 polymers consisting of 50 segments (R_H=25 nm), 20 athermal and 5 attractive tracers per simulation box, in an implicit solvent employing

a Langevin thermostat [19], using the ESPResSo software [22]. Specific details on the methodology of the corresponding MD simulations have been reported in the 2nd Chapter.

3.3. Results

The four fluorescent tracers were selected, on account of their different interactions with PNiPAAm: Alexa 647 (A647, $R_{h,np} = 0.67$ nm), Alexa 488 (A488, $R_{h,np} = 0.54$ nm), Rhodamine 6G (Rh6G, $R_{h,np} = 0.60$ nm), and CdSe/ZnS quantum dots (QD, $R_{h,np} = 6.1$ nm), where $R_{H,np}$ is the particle's hydrodynamic radius. Differences in polymer-tracer interactions are illustrated in Fig.3.1 that shows tracer concentration profiles, i.e. fluorescence intensity as a function of the position of the microscope objective (z-scans) measured for PNiPAAm hydrogels (HG) swollen with aqueous solutions of the corresponding tracers. The tracer's fluorescent intensity is proportional to the corresponding tracer's concentration in the given phase, HG (white) or supernatant solution (grey).For each tracer, the displayed intensity values correspond to the ratios between intensity in the HG at a given distance from the glass substrate/HG interface, z, normalized by the intensity value of the same tracer at the supernatant solution. The following conclusions can be drawn: (i) A488 and A647 were depleted within the PNiPAAm HG compared to the aqueous phase above the gel, at 25°C, indicating tracer-PNiPAAm repulsive Coulombic interactions; (ii) QD had virtually constant concentration profile suggesting weak interactions and Rh6G accumulated in the gel, suggesting strongest attractive interactions with PNiPAAm, among all other tracers examined.

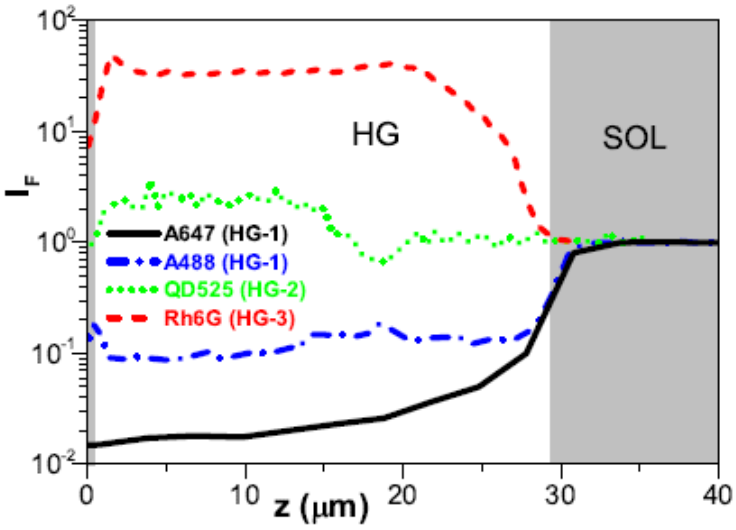

Fig.3.1. Tracer concentration profiles: normalized fluorescence Intensity (I_F) vs. distance, z, normal to the substrate for four tracers: A647 (black solid), A488 (blue dash-dot), QD (green dotted) and Rh6G (red dashed) in three different grafted hydrogels (HG) of the PNIPAAm terpolymer under good solvency conditions. Polymer volume fraction is ϕ=0.15 in all three gels (HG-1, 2, 3). Supernatant solution (SOL) and substrate regions are denoted with gray color, while the HG region is denoted with white.

The experimental $G(t)$ curves for the mobility of A647, A488 and Rh6G measured in dilute aqueous PNiPAAm (280k) solutions at $25℃$ are shown in Fig. 3.2a. As discussed in chapter 2, in order to obtain quantitate information for the tracer diffusion, these curves have to be fitted with a model function e.g. with eq.2.3.2, being rewritten here in a normalized form [72]:

$$G(t) = G'(t) - 1 = \frac{Q(t)}{N'} \cdot \sum_{i=1}^{n} F_i \cdot \left[\left(1 + \frac{4 \cdot D_i \cdot t}{w^2}\right)^{-1} \cdot \left(1 + \frac{4 \cdot D_i \cdot t}{\mathbf{S}^2 \cdot w^2}\right)^{-0.5} \right] \qquad (3.1)$$

Here, D_i, and F_i are the diffusion constants and the amplitudes of the i-th process, while N'denotes the number of diffusing fluorophores in the focal volume. The parameter w is the lateral dimension of the focal volume and $\mathbf{S}$ is the structure parameter (2nd Chapter). The initial decay function, $Q(t)$, accounts for photo-physical relaxation processes specific for a particular fluorophore, such as triplet decay or blinking (for QD).

In the absence of specific tracer-polymer interactions, $G(t)$ should be described by a single diffusion coefficient ($n = 1$ in eq. 3.1). This is indeed true for A647 (not shown) and for A488, but not for Rh6G, as seen from the fits in Fig. 3.2a. Instead, eq. 3.1 using $n = 2$ could adequately represent the experimental Rh6G data, yielding the values of a fast and a slow diffusion constants, $D_i, i \in \{\text{fast}, \text{slow}\}$ and their amplitudes,F_i, where $F_{\text{slow}} = 1 - F_{\text{fast}}$ (dashed black curve in Fig.3.2a).

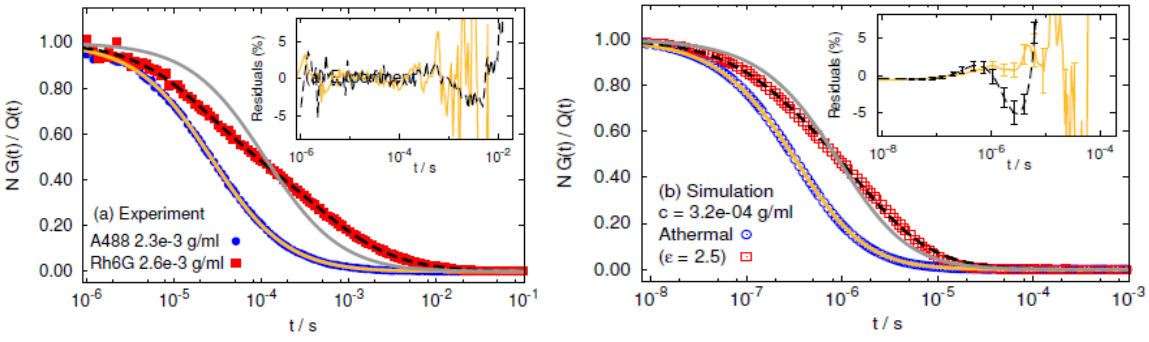

Fig.3.2. Normalized FCS autocorrelation functions, $G(t)$, from experiments and simulations: (a) Rh6G and A488 at c=c* in PNiPAAm aqueous solutions at 25 ℃; (b) the simulated athermal and the strongly attractive ($\varepsilon = 2.5\ k_B \cdot T$) tracer in dilute (c<c*) PNiPAAm aqueous solutions at 25 ℃. Solid and dashed lines denote the single ($n = 1$) and two-component ($n = 2$) representation of $G(t)$ by eq. 3.1. Insets: residuals of the accepted fits (colors match the corresponding fits of the main plot).

Fig.3.2b shows $G(t)$ computed from simulation trajectories. To calculate these $G(t)$ (Fig.3.2b), the following formula [109] was used: $G(t) = \langle \exp(-\frac{\Delta x^2(t)}{w^2} - \frac{\Delta y^2(t)}{w^2} - \frac{\Delta x^2(t)}{\mathbf{S}^2 \cdot w^2}) \rangle$, where $\Delta x^2(t) = |x(t_0) - x(t + t_0)|^2$; $\Delta y^2(t)$ and $\Delta z^2(t)$ have analogous meanings, while w and $\mathbf{S}$ denote the waist and structural parameter of the FCS focal volume, respectively. In simulations, w is not bound by the diffraction limit but by the ballistic motion on short time scales due to the Langevin thermostat [108].

For convenience, the values **S** = 1 and w = 30nm were used for the intensity profile. For the chosen w, $G(t)$ is not affected by the initial ballistic motion. It is about 10 times smaller than in the experiment, shifting the time scale of $G(t)$ by a factor of 100 to smaller times compared to the experimental $G(t)$. The observed single Fickian diffusion of A488 and A647 (not shown) is well captured by the MD simulations of the athermal tracer. In agreement with the experiment, the MD simulations of the strongly attractive tracer ($\varepsilon = 2.5 k_B \cdot T$), as the counterpart of Rh6G, yielded $G(t)$ that clearly deviates from single diffusion already at $c < c^* \sim M/R_H^3$[9], but can be satisfactorily represented with two Fickian diffusion components, using eq. 3.1 with $n = 2$. Before proceeding with further discussion, the possibility that the observed deviation from single Fickian diffusion does not stem from the simultaneous presence of two diffusion processes, but e.g. from subdiffusion [55, 85], has also been considered. Indeed, a subdiffusive model (eq.3.2) has been often invoked in literature to describe complex shapes of experimental $G(t)$, measured in crowded environment and yields a concentration dependent exponent $0.1 < \alpha(c) < 1.0$. Considering Γ as the fractional mobility and α the subdiffusion exponent in the relation: $MSD(t) \sim \Gamma \cdot t^{\alpha}$, this model lead to the following analytical form of the $G(t)$ [55] [85]:

$$G(t) = G'(t) - 1 = \frac{Q(t)}{N} \cdot \left(1 + \left(\frac{4 \cdot \Gamma \cdot t}{w^2}\right)^{\alpha}\right)^{-1} \cdot \left(1 + \left(\frac{4 \cdot \Gamma \cdot t}{s^2 \cdot w^2}\right)^{\alpha}\right)^{-0.5} \qquad (3.2)$$

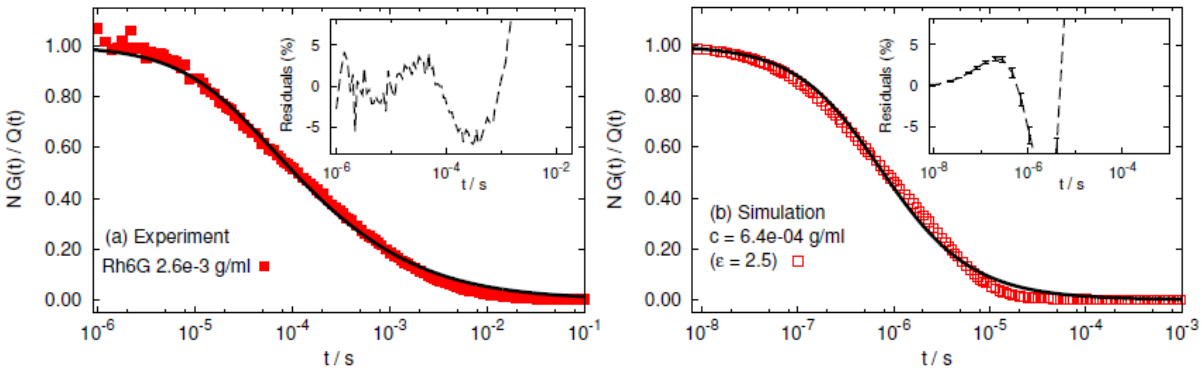

Fig. 3.3. Subdiffusive fits (eq. 3.2) to $G(t)$ in PNiPAAm aqueous solutions for (a) Rh6G at c=c* and for (b) the strongly interacting tracer from simulations at c<c* Both fits yielded a subdiffusive exponent, α =0.4. Insets: residuals of the accepted fits (colors match the corresponding fits of the main plots).

Although commonly used in literature, eq. 3.2 has been rigorously derived only for a specific form of the probability distribution of particle displacements [110]. Therefore, if conclusions are drawn from fits with eq.3.2, its use should be independently justified. Fits to both, the experimental $G'(t)$ of Rh6G and the simulated $G'(t)$ of the attractive tracer, are slightly worse than the two-component diffusion fits (Fig.3.3), but significantly better than the single-component normal diffusion. Based solely on the fit quality, subdiffusion would seem less appropriate than the two-component diffusion

but one would not be able to safely rule it out completely. To obtain further evidence as to whether the subdiffusive model can be safely excluded or not, the probability distribution of the lifetimes for the free and bound states of the tracer have been also calculated. To compute lifetimes of the bound and free states of the tracer, the following steps have been followed: the time-evolution of state of each individual particle has been tracked with resolution of 10 MD time steps; binding and unbinding events have been recorded, the time difference between these types of events has been calculated and a histogram of the differences has been plotted, throughout the whole simulation. The final histogram yields the probability that the bound (or free) state survives for a particular time interval. In Fig. 3.4, one can see that the distributions of both (a) bound and (b) free state lifetimes closely follow a single exponential decay.

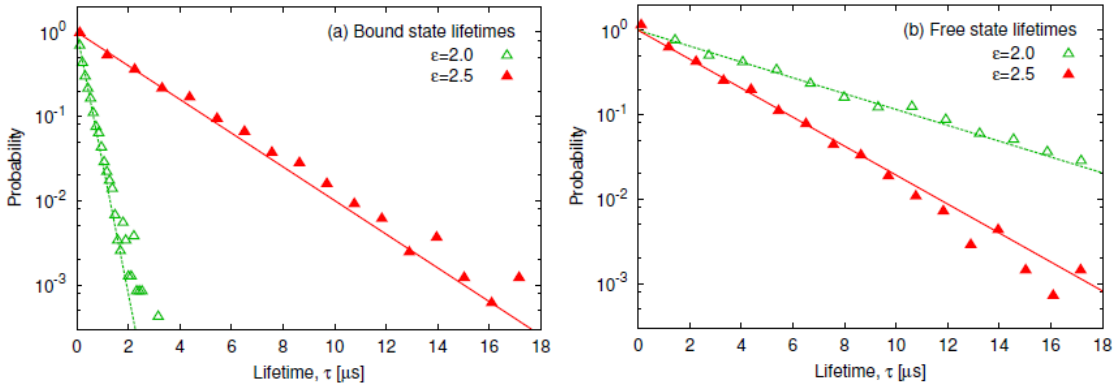

Fig.3.4. Probability distribution of lifetimes of the tracer in the bound state (a) and in the free state (b), shown for the weakly and strongly attractive tracer at $c = 4.5 \cdot 10^{-4}$ g ml^{-1}. Lines represent single-exponential fits.

Using $D_{free} = 3.7 \cdot 10^{-10}$ m^2·s^{-1} and $D_{bound} \approx D_{pol} = 6.7 \cdot 10^{-11}$ m^2·s^{-1} and the obtained lifetimes (Fig.3.4), the corresponding length scales of the free ($L^2_{free} \approx 6 \cdot D_{free} \cdot \tau_{free}$) and bound ($L^2_{bound} \approx 6 \cdot D_{bound} \cdot \tau_{bound}$) diffusion have been obtained, values of which are shown in Table 3.1.

Table 3.1. The lifetimes of bound and free states, as obtained from fits to Fig. 3.3 and the corresponding distances, L_{bound} and L_{free} over which the tracer diffuses in the given state

$\varepsilon\ (k_B \cdot T)$	$t_{bound}\ (s)$	$L_{bound}\ (m)$	$t_{free}\ (s)$	$L_{free}\ (m)$
2.0	$2.8 \cdot 10^{-7}$	$1.1 \cdot 10^{-8}$	$4.6 \cdot 10^{-6}$	$1.0 \cdot 10^{-7}$
2.5	$2.2 \cdot 10^{-6}$	$3.0 \cdot 10^{-8}$	$2.5 \cdot 10^{-6}$	$7.5 \cdot 10^{-8}$

Further evidence concerning the possibility that subdiffusion is present can be revealed by analyzing the mean square displacement (MSD), from the MD simulations of the PNIPAAm chains related with this study (Fig. 3.5). Even though the MSD as quantity provides a link between the length and time

scales, the quantity $\mathrm{MSD}/6 \cdot D_0 \cdot \mathrm{t}$ facilitates the identification of deviations from normal diffusion: the slope of the plot is $(\alpha - 1.0)$.

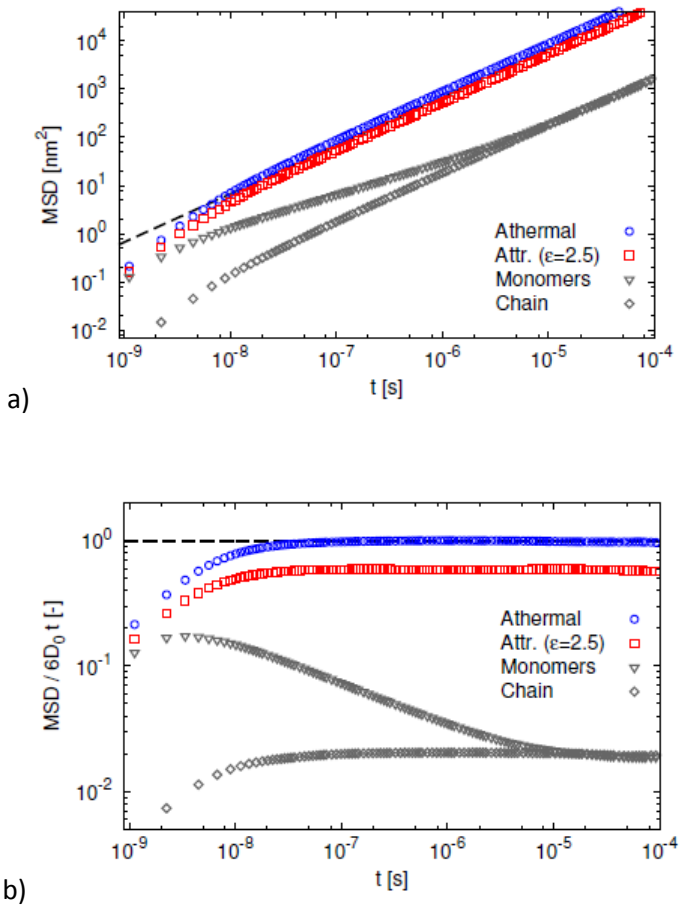

Fig. 3.5. Mean square displacements: (a) MSD and (b) $\mathrm{MSD}/6 \cdot D_0 \cdot \mathrm{t}$ of different species as indicated in the legend for the same system as Fig. 1.1.3. Normal diffusion with $\mathrm{MSD} = 6 \cdot D_0 \cdot \mathrm{t}$ is shown for reference (dashed line).

All curves in Fig. 3.5 display superdiffusive $(< \Delta \mathrm{r}^2(\mathrm{t}) > \sim \mathrm{t}^{\alpha}, \alpha > 1)$ characteristics on a very short time scale, whose duration is set by the friction constant of the Langevin thermostat [90]. From the lower panel it is clearly seen that the behavior becomes (normal) diffusive for both tracers on time scales $\mathrm{t} > 10^{-7}\mathrm{s}$ which corresponds to MSD $\approx 100\ \mathrm{nm}^2 \ll \mathrm{w}^2 \approx 10^3\ \mathrm{nm}^2$. Evidently, the MSD in Fig. 3.5 is incompatible with $\alpha \approx 0.4$ obtained from fits in Fig. 3.5. On account of both (i) the single exponential decay of escape lifetime probabilities ruling out infinite hierarchy of trapped states [55], as well as (ii) on the transition to normal diffusive MSD occurring for both tracers and polymer on length scales smaller than the focal spot size, true anomalous diffusion [50] is certainly not the appropriate model to describe the measured and simulated $\mathrm{G}'(\mathrm{t})$ curves of this Chapter. Therefore in all following discussion the double Fickian component model (eq. 3.1 with $n = 2$) was used to evaluate the tracer diffusion coefficients. The tracer diffusion from experiments and simulations,

relative to the tracer's free diffusivity, D/D_0, is presented in Fig.3.6a as a function of polymer concentration.

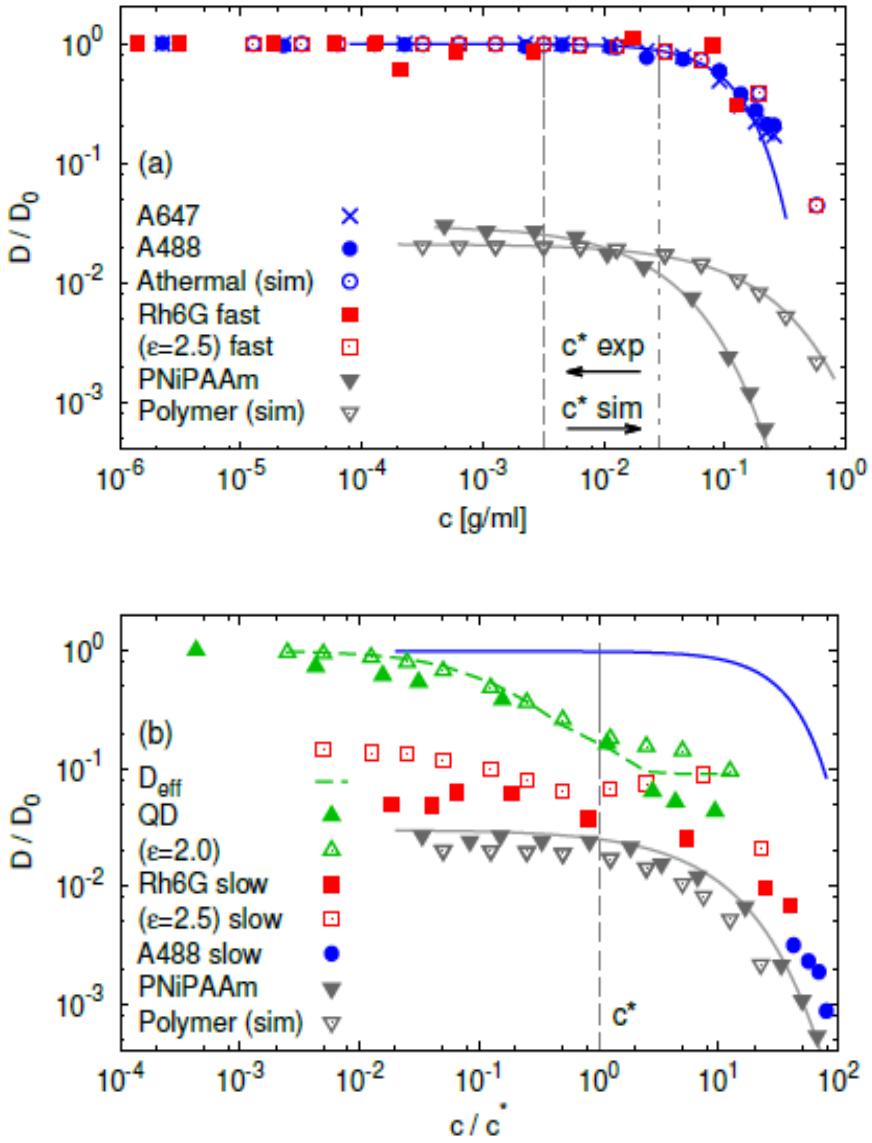

Fig.3.6. Diffusion slowdown, D/D_0, as a function of polymer concentration. (a) Crowding-induced tracer slowdown as a function of total monomer concentration, c: A647, A488 and the simulated athermal tracer (single diffusion) and the fast diffusion components of Rh6G and of the strongly attractive tracer ($\varepsilon = 2.5k_B \cdot T$); (b) Macromolecular tracer slowdown as a function of reduced concentration, c/c^*: polymer self-diffusion and slow diffusion components of Rh6G and of the strongly attractive tracer. The diffusion of the QD and of the weakly attractive tracer ($\varepsilon = 2.0k_B \cdot T$) in panel (b) with its effective diffusion, $D_{eff}(c)$, described in the text follow neither type of master curve. The master curves for crowding-induced slowdown (blue) and macromolecular tracer slowdown (grey) are shown as solid lines, together with data on polymer self-diffusion. Vertical lines indicate c^*.

For A647 and A488, it has been experimentally shown that a superposition on a single master curve is successful in the plot of $D(c)/D_0$ vs. c [111].The superposition vs. c holds also for the - analogous to A647- athermal tracer from MD simulations (Fig. 3.6a), as well as for the fast component of Rh6G diffusion and of the simulated strongly attractive tracer ($\varepsilon = 2.5k_B \cdot T$) which also follow the same

master curve. In contrast, superposition for $D_{slow}(c))/D_0$ is achieved vs. c/c^*, in Fig. 3.6b. Both, $D_{slow}(c)$ from simulation and experiment, and polymer self-diffusion, $D_{pol}(c)$, collapse on a master curve for macromolecular diffusants [111]. As c^* depends on polymer molecular weight, such a representation scales out the effect of chain length. Remarkably, the slow component of Rh6G diffusion as well as the slow component of the simulated strongly attractive tracer both mimic the master curve for polymer self-diffusion. This observation emphasizes the role of polymer chain length in the diffusion slowdown, when specific interactions are present and clearly indicates that the slow component originates from fluorescent molecules attached and diffusing together with a polymer chain. Moreover, a slow component shows up also in the diffusion of A488 at high c, mimicking $D_{pol}(c)$, similar to $D_{slow}(c)$ of both Rh6G and of the simulated strongly attractive tracer. The onset of additional, slower process for A488 suggests that concentration needs to be high enough, so that Van der Waals A488-PNiPAAm attractions overcome the strong A488-PNiPAAm Coulombic repulsions (Fig.3.1) and the A488 attaches to a PNiPAAm chain. For the weakly attractive QD, $G(t)$ is well represented by a single Fickian diffusion, but $D = D_0$ drops below unity even at $c \ll c^*$ (solid green triangles in Fig. 3.6b). Remarkably, the simulated weakly attractive tracer with $\varepsilon = 2.0 k_B \cdot T$ (open green triangles in Fig. 3.6b) also yields a single-component $G(t)$ with $D = D_0$ following practically the same gradual decrease like QD, at $c \ll c^*$. In view of this trend in both experiment and simulation, QD and the weakly attractive tracers exhibit intermediate behavior between the athermal (A647) and the strongly attractive (Rh6G) case. For Rh6G and the simulated attractive tracer, F_{slow} was found to increase with PNiPAAm concentration (Fig. 3.7).

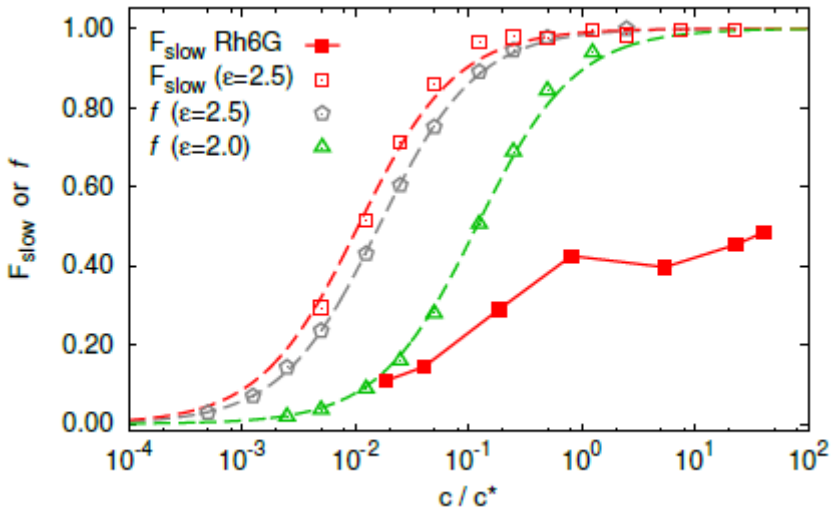

Fig. 3.7. The amplitude of the slow process, F_{slow}, as a function of c/c^*. Solid and empty symbols refer to F_{slow} from the experimental and simulated $G(t)$, respectively. The bound fraction, f, obtained from the simulations for weakly and strongly attractive tracers is shown for comparison. Dashed lines are fits of the simple binding model with K_{eq} = 94, 61 and 8.4 (from left to right).

The simulations also allow to calculate the fraction of bound tracers, f, by counting their number within the interaction range of the polymer. $F_{slow}(c)$ from the simulated $G(t)$ and f, agree remarkably, indicating that $D_{slow}(c)$ can indeed be attributed to the polymer-bound tracers. The c-dependence of f, and F_{slow} can be represented by a simple binding model (dashed lines in Fig. 3.7) with binding constant: K_{eq} = [T][P]/[TP] where [T], [P] and [TP] are the concentrations of free tracer, free polymer and tracer polymer complex. This also applies to f of the weakly attractive tracer; F_{slow} is not available, since $G(t)$ is described by a single diffusion process. The experimental F_{slow} of Rh6G in Fig. 3.7 increases with c qualitatively similar to the simulations. However, a variation of K_{eq}, which is the only adjustable parameter of the above model, can only shift the curve left or right but cannot account for the weaker slope of the experimental F_{slow}. Phenomenologically, this could be accounted for by using K_{eq} which decreases with c. This, however, cannot be captured by the present model with constant ε.

Nevertheless, there is agreement between the experimental and simulated D_{fast} and D_{slow}, conforming to universal master curves (Fig. 3.6). Note that $K_{eq} \sim e^{-\frac{V'_{sr}(r)}{k_B \cdot T}}$ [26] implies that the binding strength and hence both F_{slow} and f are sensitive to the short-range interaction potential, $V'_{sr}(r)$.In contrast, $D_{fast}(c)$ (free tracer diffusion) is independent of specific polymer-tracer interactions, while $D_{slow}(c)$ (the polymer-bound diffusion) only exists in the presence of specific interactions but its value is virtually independent of their strength. The assertion is that the underlying diffusion process is indeed two-component in both cases, showing that $D(c)$ obtained from $G(t)$ of the weakly attractive case can be reconstructed using the effective diffusion coefficient, $D_{eff}(c) = (1 - f(c)) \cdot D_{fast}(c) + f(c) \cdot D_{slow}(c)$. $D_{eff}(c)$, shown by the dashed green line in Fig. 3.6b, is reconstructed assuming the same $D_{slow}(c)$ and $D_{fast}(c)$ as for $\varepsilon = 2.5 k_B \cdot T$, but using $f(c)$ for $\varepsilon = 2.0\ k_B \cdot T$.

3.4. Discussions

It is intriguing that a small change of attraction changes $G(t)$ qualitatively, from single to two-component diffusion. This can be rationalized by comparing the lateral dimension of the FCS observation volume, w, to the system-relevant length scales. At $c < c^*$, there is dynamic exchange between the polymer-bound and free state of the tracer in the free volume between separated coils. The tracer undergoes free diffusion with D_0 for a time duration t_{free} and diffuses bound to the polymer with $D_{bound} \approx D_{pol}$ for a time t_{bound} with the corresponding displacements (Table 3.1): $L^2_{free} \approx D_0 \cdot t_{free}$ and $L^2_{bound} \approx D_{bound} \cdot t_{bound}$. As discussed elsewhere [107],[112], a particular process can be resolved by FCS only when its characteristic length scale is greater than w. Thus, $w < L_{bound}$ results in a bimodal $G(t)$, whereas $w > L_{bound}$ results in an effective single $G(t)$.

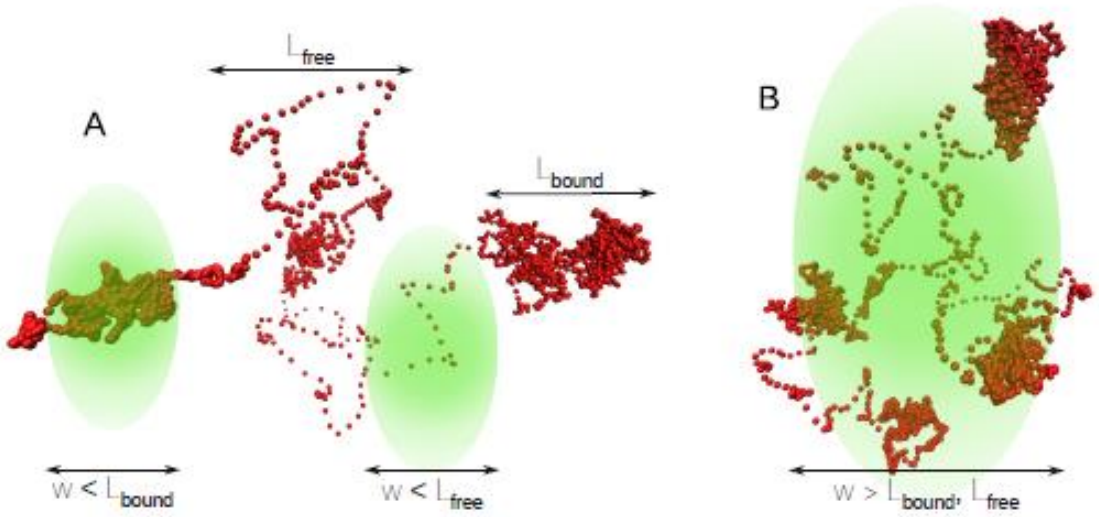

Fig.3.8. Simulated trajectories of the attractive tracer $\varepsilon = 2.5k_B \cdot T$ in dilute polymer solution mapped on different focal spot diameters, w: (A) $w \approx 30nm < L_{bound}$ and (B) $w \approx 60nm > L_{bound}$, where L_{bound} is the distance traveled by the tracer bound to the polymer. Different spheres are positions of the tracer separated by a constant time step. Regions with high density of spheres correspond to small displacements and slow (bound) diffusion, while regions with low sphere density correspond to large displacements and fast (free) diffusion.

From the MD data for $\varepsilon = 2.5k_B \cdot T$, a bimodal $G'(t)$ was found with $D_{bound} \approx 4 \cdot 10^{-11}\ m^2 \cdot s^{-1} \approx 0.09 \cdot D_0$ and $t_{bound} \approx 2.2\mu sec$, leading to: $L_{bound} \approx 54\ nm > w = 30\ nm$ (Fig.3.8). For $\varepsilon = 2.0k_B \cdot T$, $G'(t)$ conforms to a unimodal shape with $D_{eff}(c) < D_0$ and $t_{bound} \approx 0.45\mu sec$. Assuming the same D_{bound}, $L_{bound} \approx 11\ nm < w$. In the latter case, the two distinct mechanisms exist but are averaged out before the tracer leaves the focal spot, yielding the effective $D_{eff}(c)$. Since $t_{bound} \sim e^{-\frac{V_{sr}}{k_B \cdot T}}$, a minor increase in the attraction significantly increases t_{bound}. To illustrate the link between L_{bound} and w, Fig. 3.8 demonstrates a snapshot of the simulation trajectory for the strongly attractive tracer, compared to focal spots of different sizes. Regions with high density of spheres correspond to small displacements and hence slow (bound) diffusion, while regions with low sphere density correspond to large displacements and hence fast (free) diffusion. In Fig. 3.8, both L_{free} and L_{bound} exceed the focal spot size (A), while in (B) the focal spot is greater than both L_{free} and L_{bound}. Commensurability between w and the size of fixed confinement domains, r, has been shown earlier to result in an effective diffusion coefficient [88],[113]. Despite an apparent similarity, what is commensurate with w in this study is not the domain size $r \approx R_H \ll w$ but the length scale which arises from combination of binding strength and domain mobility through $L_{bound}^2 \approx D_{bound} \cdot t_{bound}$.

3.5. Conclusions

In conclusion, probing tracer dynamics by means of FCS has shown that even in dilute polymer solutions, where the separation between polymers is much greater than their size, complex tracer diffusion can be observed. In absence of analytical theory, MD simulations of a generic bead-spring polymer model and spherical tracers with no attraction (single diffusion), weak (single slow diffusion) and strong (double diffusion) attraction to the polymer were shown to semi-quantitatively capture the three experimentally observed behaviors as well as to reveal the exact underlying process. An increase of the attractive strength led to more significant deviations from single Fickian behavior. The corresponding experimentally measured $G'(t)$ could be fitted by several different model equations by which no unique diffusion constant could be extracted and the exact underlying process cannot be easily revealed (Fickian vs. anomalous diffusion[50]). A true anomalous diffusion was rejected in the case of Rh6G in PNiPAAm solutions, due to the absence of an infinite hierarchy of binding traps. The lifetime of the bound state sensitively depends on the interaction energy, while the distance traveled by the bound tracer may or may not exceed the probed length scale. A fast and a slow process can be resolved for the interacting tracers, only when their length scales are larger than the fixed dimensions of the FCS illumination volume. The two diffusion components could be attributed to bound and freely moving tracers. The lifetime of the bound state sensitively depends on the interaction energy, while the distance travelled by the bound tracer may or may not exceed the probed length scale. Consequently, FCS experiments yield quantitatively different decay functions, even though the microscopic diffusion mechanism does not change. Specific interactions of diffusants with the surrounding macromolecular environment are commonly encountered in soft matter and biology. The presented results imply that such specific interactions can be unambiguously identified from slowdown at high dilution. In this respect, this work lays the foundation for a systematic application of FCS to study single molecule transport in such environments.

Chapter 4: Tracer diffusion in aqueous thermoresponsive polymer networks: influence of swelling ratio, interactions, permanent crosslinks and external stimuli

Abstract

Using FCS, the translational mobility of a fluorescently labeled IgG antibody and different molecular tracers exhibiting varying interaction strength has been examined in PNiPAAm hydrogels, under bad and good solvency conditions. In contrast to the non-interacting tracer Alexa 647, deviations from single Fickian diffusion have been observed for both the weakly (Alexa 488) and the strongly interacting (Rh6G) tracer. Like in the study related to PNiPAAm polymer solutions (3rd Chapter), the interacting tracer dynamics have been represented by a double Fickian diffusion fit. A pure crowding effect, free of interactions, was observed for both Alexa 647 and the fast diffusion process of the two interacting tracers, whereas the slow process for A488 and Rh6G was strongly biased by the tracer-polymer interactions. Unexpectedly, the weakly interacting tracer, in particular, exhibits pronounced sensitivity on the network topology at low PNiPAAm volume fractions (ϕ): its dynamics deviate from single diffusion only in presence of permanent crosslinks. Such trend, being interpreted as the interplay between Coulombic repulsions and short-range attractions, was not the case for the strongly attractive tracer, suggesting different nature of tracer-polymer interactions, as supported by monovalent salt perturbations. Notably, the A488 senses more sensitively the network topology, as for both A488 and Rh6G the slowdown of the slow diffusion becomes ϕ-independent above ϕ>0.1, while it continuously drops with ϕ for A488 in the PNiPAAm solutions. Moreover, IgG mobility and penetration in PNiPAAm grafted networks was found to sensitively depend on the crosslink density. The present FCS work outlines that although dynamics and swelling ratio are interdependent properties, the stimulus-dependent swelling ratio does not allow predicting the tracer dynamics.

4.1. Introduction

Tracer diffusion in crowded environments has attracted strong interest, because it is relevant for many macromolecular systems [50, 52, 59, 84, 85, 111, 114-130] and its understanding is pivotal for several applications[25, 26, 121]. Such tight conditions are frequently encountered in biology [131], ultrafiltration and soft matter [132], when examining for instance the diffusion of lipids [117] or proteins in cellular membranes or in the cytosol [118], while nanoparticle dynamics may also relate to viscoelastic properties in the polymer network [114, 126]. In recent years, significant interest has

arisen concerning tracer diffusion in soft matter and biological systems, using gels as the matrix. Polymer gels possess numerous advantages which justify their frequent use: biocompatibility [133, 134], inherent ability to swell by absorbing significant amounts of water and finally pronounced mechanical properties (tunable porosity and elasticity)[22, 135, 136]. A related scientifically active area in soft matter are the stimuli-responsive polymer materials [137], spanning from micelles and brushes to crosslinked grafted films[23]. Such materials exhibit specific response to external stimuli, such as temperature [77, 133, 138], pH [139], magnetic or electric fields and ionic strength alterations[140-142]. Thermoresponsive polymer networks [132] in particular, which exhibit an LCST close to human body temperature, have been frequently employed in biosensor platforms[26] and drug delivery applications [143]. Although mechanical properties of thermoresponsive networks have been systematically studied [141],[144, 145], the complexity of the network and the underlying tracer-network interactions render the exact elucidation of tracer dynamics rather non-trivial. The elucidation of effects on tracer mobility due to crowding as well as due to the strength and nature of interactions on the molecular diffusion in hydrogels is needed for both, fundamental and practical perspectives, as for example in biosensors[25]. To get the best benefit from the application of thermoresponsive polymers in biosensor-related applications [26] and in drug delivery, a stringent control of how different physicochemical parameters may be influencing complex solute dynamics in such thermoresponsive networks is required. Besides, experimental and theoretical studies investigating solute transport in real-time human body conditions, thus mimicking biosensor operating conditions, are highly desired.

The mobility of a tracer in dense macromolecular environments can be significantly influenced by some of the following parameters: the tracer size and shape [59, 111, 122, 128], matrix concentration [59, 111], matrix molecular weight [59, 120], presence of crosslinks [146-148], [123],[149], [53], pore-tracer size ratio [64], temperature [77], [150], solvency conditions [138], pH [139], [151], ionic strength[152, 153], as well as tracer-polymer interactions [152, 153],[77]. Crowded environments, due to both pronounced matrix concentration and to possible tracer-matrix interactions [84],[121] render a thorough investigation of tracer diffusivity not an easy task [52]. Under dense matrix conditions, tracer dynamics may deviate from single Fickian diffusive mode [60] [86],[50],[71],[82]. The number of theoretical works concerning tracer diffusion in hydrogels and dense polymeric networks in general, still remains rather limited [53],[154, 155]. In addition, most experimental works that deal with the mobility of molecular tracers [77, 156] or nanoparticles [123, 147, 157] in crosslinked matrices focus on non-interacting systems. The influence of interactions on tracer slowdown is significant for drug delivery [158] and biosensor-related [26] applications and an investigation of the influence of temperature and salt on the tracer diffusion in thermoresponsive

grafted polyelectrolyte layers has been missing so far. Concerning tracer mobility in grafted systems, it is fundamentally necessary to scrutinize the response of tracer dynamics in the bulk of the grafted network (micron-sized thicknesses), before studying effects in the proximity of the substrate[159].

FCS (2nd Chapter) has been employed to probe mobility of different tracers with varying attractive strength in aqueous PNiPAAm networks – homopolymer solutions (3rd Chapter) of various concentrations and grafted crosslinked hydrogels. To address the issue of attractive strength, three different molecular tracers - a strongly (Rhodamine 6G), a weakly (Alexa 488) and a non-interacting (Alexa 647) tracer – have been employed and their diffusion has been compared. Tracer diffusion has been examined in good solvency at various volume fractions of homopolymers and chemically crosslinked networks, respectively. Tracer diffusion has been also investigated under good and poor solvency conditions, using temperature or ionic strength as the external stimuli. In an attempt to mimic typical operating conditions of biosensor platforms, the diffusion of a fluorescent antibody (goat-anti mouse immunoglobulin, IgG) was also investigated in acetate buffered (pH=4) PNiPAAm solutions at $25^{\circ}C$ and in grafted PNiPAAm hydrogels swollen in acetate buffer (pH=4), at three different crosslink densities and different temperatures. The biosensor-inspired motivation is driven from the need to enrich current information available for thermoresponsive crosslinked networks [25, 26, 64, 77, 160] and has been threefold: (i) To interpret the nature of tracer-polymer interactions, assessed by the perturbation of different stimuli dynamics and network swelling ratio; (ii) to illustrate the effects of the network collapse and/or crosslink density on tracer mobility in hydrogels, for both molecular tracers and the antibody and (iii) to discuss about possible scaling relations by comparing the findings with analogous results reported in the literature.

4.2. Materials

The chemical structures of the PNiPAAm terpolymer unit and publicly available structures for the fluorescent tracers used in this Chapter, namely A488 and Rh6G, are shown in Fig.2.6 (2nd Chapter).The chemical structures of A647 (Alexa Fluor 647 cadaverine, disodium salt, A30679) and of the fluorescently labeled IgG (A-21235, Invitrogen) are not publicly available. As A647 lacked any attractive interactions with the examined PNiPAAm [77], it was simultaneously present in the studied polymer samples together with the other dyes, acting as a 'control' tracer. Regarding the tracer surface charges, Rh6G is a positively charged tracer [95], while zeta potential measurements in mili-Q water (Karmena Jaskiewicz, MPIP) revealed that A488 and PNiPAAm are strongly negatively charged and slightly negatively charged, respectively. Concerning the solvents used, the molecular tracers (sections I and II of this Chapter) were dissolved in mili-Q water (no buffer), while the antibody

experiments (section III) were accomplished in an already-prepared (Khulan Sergelen, AIT) 10mM acetate buffer (10mM sodium acetate trihydrate with acetic acid) at pH=4.The stock solution of IgG ($1\cdot10^{-4}$ L of $1.2\cdot10^{-6}$ M concentration) was allocated into 20 aliquots of $5\cdot10^{-6}$ L each. The aliquots were stored in the freezer for long time and were taken out to 4°C right before every measurement. The acetate buffer (ACT) was also stored in the fridge for long-time storage. The NiPAAm monomer concentrations (volume fractions $\phi(T)$ being inversely related to the swelling ratios $R_s(T)$, as: $\phi(T) = R_s^{-1}(T)$) for the different hydrogels (HG) studied in sections I and II (swollen in mili-Q water or in ACT), are shown in Table 4.1. In the same table, $\phi(T)$ for the HGs used in section III (swollen in ACT) as well, namely HG#2,HG#5 and HG#7 (their code names), are also depicted. The monomer volume fraction, $\phi(T = 25℃)$, exhibits an inverse proportionality to the UV irradiation time: The longer the UV irradiation, the more free radicals from benzophenone moieties would be created, leading to more covalent benzophenone bonds and thus, to higher crosslink densities.

Table 4.1. Corresponding $\phi(T))$ (±10%) values for the different PNIPAAm HGs examined (swollen in mili-Q water or ACT)

$\phi(T)$	$(T = 25°C)$	(T=29°C)	(T=32°C)	(T=35°C)	(T=37°C)
HG-1	0.013	0.013	0.013	-	0.013
HG-2	0.030	0.03	0.03	-	0.032
HG-3	0.084	0.084	0.087	0.12	-
HG-4	0.15	0.17	0.23	0.33	-
HG-5	0.18	-	-	-	-
HG-6	0.21	-	-	-	-
HG-7	0.26	0.26	0.28	-	-
HG#2	0.08	0.11	-	-	-
HG#5	0.1	0.17	-	-	-
HG#7	0.15	0.19	-	-	-

I. Tracer mobility in aqueous PNiPAAm grafted networks: effect of interactions and permanent crosslinks

4.3.1. Results

A recent work focused on the diffusion of A647 in grafted hydrogel layers of the same PNiPAAm terpolymer at different temperatures, up to the LCST of PNiPAAm [77]. In the current study, however, A647 has been employed as an internal standard in order to examine the mobility of two interacting tracers (A488, Rh6G) in PNiPAAm aqueous solutions (sol) and PNiPAAm grafted HG layers. The non-interacting A647 (Fig.S2, Appendix) has been utilized to prove whether concentration and interaction effects can be separately addressed, simply by examining the shape and the trend of the respective $G(t)$ in PNiPAAm solutions (sol) and grafted PNiPAAm hydrogels (HG) at the same monomer concentration. In either network type, the $G(t)$ curve for A647 conforms to a single Fickian diffusion that is slower relative to its free diffusion in pure water. Furthermore, the slowdown is slightly stronger in HG than in sol (polymer solution), at the same ϕ. Each examined tracer exhibits different strength of attraction with the particular PNiPAAm terpolymer, as can be seen by the normalized FCS intensity autocorrelation curves $G(t)$ and from the tracer density profiles (z-scans) shown in Fig. 3.1 (3rd Chapter).The two component Fickian model (eq.2.3.2, $n = 2$) has been successfully employed to describe the experimental $G'(t)$ for Rh6G everywhere (HG and solutions) in this Chapter. For A488, the two component Fickian model has been employed everywhere in HGs, but in semidilute solutions only at very high concentrations (Fig.3.6). The strongly interacting Rh6G deviates from single Fickian diffusion in both hydrogel and solutions (Fig.4.1.1a), even at relatively low ϕ (ϕ=0.08).

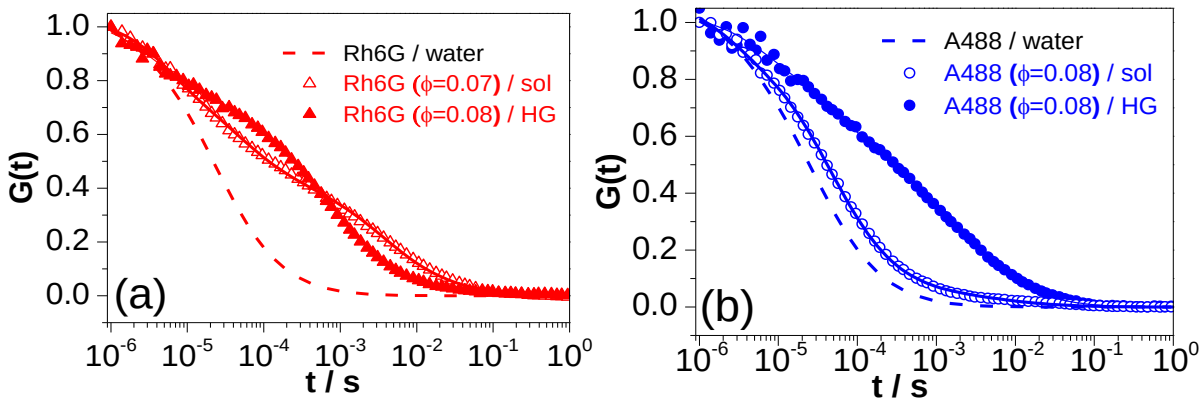

Fig.4.1.1. Influence of permanent crosslinking for (a) Rh6G and (b) A488. $G(t)$ for the two molecular tracers in PNiPAAm aqueous solutions and grafted PNiPAAm hydrogels at similar concentration, at $T = 25℃$. The fits to $G'(t)$ for each tracer were represented by eq. 2.3.2 from 2nd Chapter (solid lines) using either n=1 (A647-Fig.S2 Appendix; A488 in solution) or n=2 (Rh6G; A488 in HG). Dashed curves represent single component fits (n=1) to the experimentally measured $G'(t)$ (not shown) of the tracers in water.

On the other hand, at the same low ϕ(=0.08), $G(t)$ curves of A488 (Fig.4.1.1b) deviate from single Fickian diffusion in HG, but not in the homologous polymer solution. Therefore, it seems that the weakly repulsive A488 is a more sensitive probe of the polymer network topology (i.e. presence of crosslinking). Qualitative information about the strength of tracer-polymer interactions has been acquired from the corresponding tracer density profiles in the grafted PNIPAAm hydrogels (HG) at ambient conditions, shown in Fig.3.1 (3rd Chapter). Based on evidences from both Fig.3.1 (3rd Chapter) and Fig.4.1.1, Rh6G should not only exhibit stronger attractive strength than A488, but the relative strength of hydrophobic and electrostatic interactions for the two tracers should be different.

Effect of crosslinking density in permanent networks. Additional differences in the dynamics of the A488 and Rh6G have been revealed, as the crosslink density of the hydrogel increases. The autocorrelation function $G(t)$ of Rh6G is more strongly shifted to longer lag times than that of A488, at relatively low crosslink densities (ϕ=0.01-0.03), as seen in Fig.4.1.2a. However, at higher crosslink densities (Fig.4.1.2b; ϕ=0.26), $G(t)$ curves of A488 and Rh6G become comparable. Therefore, the evolution with crosslink density of the translational dynamics for the two molecular tracers having comparable size depends also on both the nature and the relative strength of hydrophobic and electrostatic interactions. The latter is an inevitable feature of weak polyelectrolytes (PNiPAAm terpolymer of this thesis).

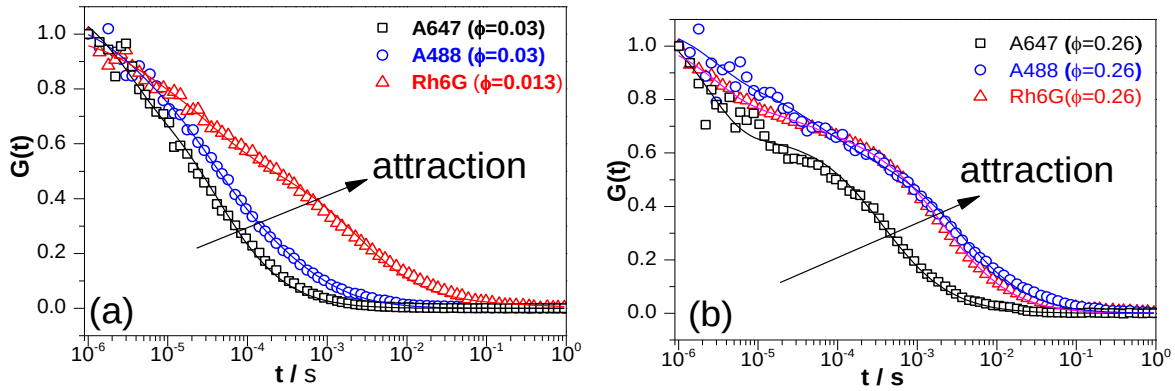

Fig.4.1.2. Crosslinking density effects: $G(t)$ for the molecular tracers of Fig.4.1.1, in PNiPAAm terpolymer hydrogels (HG) at $T = 25$ ℃ for extreme ϕ cases achieved through variation of the grafting densities: (a): ϕ=0.013 (HG-1) and ϕ=0.03 (HG-2); (b): ϕ=0.26 (HG-5).

The experimental $G(t)$ for A488 and Rh6G in all studied hydrogels were fitted using eq. 2.3.2, with n=2. From the extracted diffusion coefficients ($D(\phi)$), the diffusion slowdown values ($D(\phi)/D_0$) were then calculated (D_0 being the diffusion coefficient of the respective tracer in pure water). Fig.4.1.3 shows the diffusion slowdown for the fast (empty symbols) and the slow (solid symbols) processes, as well as the amplitude of the slow process ($F_{slow}(\phi)$) as a function of the monomer fraction, ϕ, in the four examined hydrogels, at 25℃. The slowdown of the fast diffusion process is

almost identical for both tracers in all studied hydrogels. On the other hand, there is a clear difference in the slow process slowdown between A488 and Rh6G at small ϕ (0.01- 0.03), where Rh6G diffuses about five times slower in the same matrix. However, this disparity progressively diminishes, with increasing ϕ. The observed differences in the slowdown between A488 and Rh6G may be attributed to differences in the underlying tracer-polymer interactions. Electrostatic interactions and presence of hydrophobic substructures in all molecular tracers need to be considered. The latter should exhibit attractive interactions with the polymer backbone of the polymer and particularly with the hydrophobic benzophenone groups.

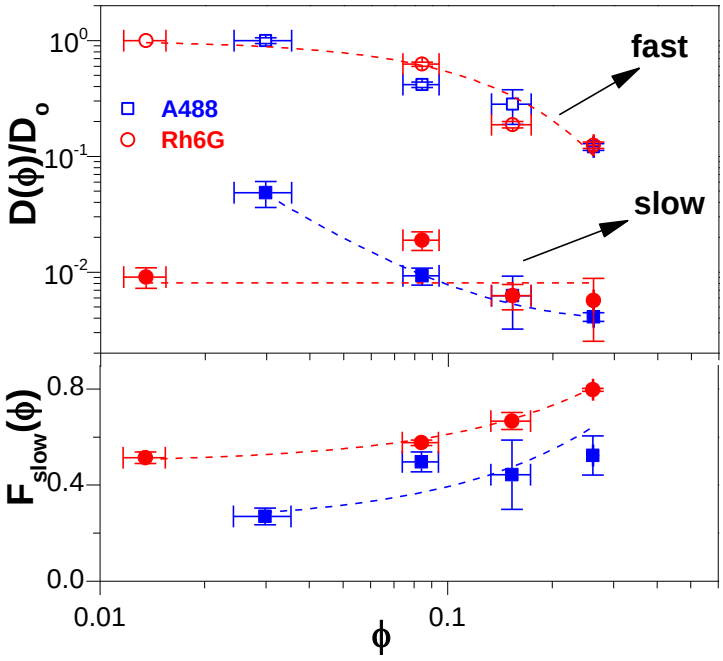

Fig.4.1.3. Diffusion slowdown $D(\phi)/D_0$ - upper panel - and amplitude of the slow process ($F_{slow}(\phi)$) – lower panel - as a function of concentration (ϕ) for A488 (squares) and Rh6G (circles) in hydrogels. Fast and slow processes are denoted by empty and solid symbols, respectively. The dashed lines are drawn to guide the eye. Black arrows denote the fast (empty symbols) and slow (solid symbols) processes, respectively.

Moreover, evidence for the different strength of tracer-polymer interactions is provided by the larger $F_{slow}(\phi)$ for the strongly interacting Rh6G compared to A488, at the same ϕ. One may recall that the crosslinking density in permanent PNiPAAm networks influences differently the tracer diffusion slowdown at low ϕ, based on the strength of the particular hydrophobic and electrostatic interactions: single Fickian for A647, deviations from single Fickian diffusion for the other tracers with stronger slowdown for Rh6G and intermediate slowdown for A488. To summarize the findings: (i) in PNiPAAm aqueous solutions, the tracer translational motion deviates from that of a single Fickian diffusion with increasing strength of tracer-polymer attractions, as judged by the tracer density profiles in grafted hydrogels (Fig.3.1a). (ii.a) PNiPAAm solutions vs. PNiPAAm hydrogels: The weakly

repulsive A488 is a more sensitive probe of the polymer network type –presence of crosslinks-than the more strongly attractive tracer Rh6G (Figs.4.1.1-4.1.3); (ii.b) in PNiPAAm hydrogels: Crosslinking density exerts distinct tracer diffusion slowdown based on the examined tracer(Fig.4.1.3).

4.3.2. Discussion

Deviation from single Fickian diffusion. The two component Fickian model (eq. 2.3.2, $n = 2$) has been successful in describing the experimental $\mathrm{G(t)}$ for either A488 or Rh6G, in PNiPAAm hydrogels. Some alternative models developed for FCS autocorrelation curves that measured diffusion in presence of interactions, such as the diffusion and rare strong adsorption [82] or a diffusion and reaction model [84] failed to describe satisfactorily the experimental data. As such, the two-component diffusion model (eq. 2.3.2,$n = 2$) has been chosen on account of both its good representation of the experimental $\mathrm{G(t)}$ in both PNiPAAm hydrogels and solutions and on the conformity of its adjustable parameters to a physically meaningful tracer mobility scenario. The two-component Fickian model can be rationalized by a dynamic equilibrium between states associated with different lifetimes, as discussed for the case of interacting molecular tracer mobility in PNiPAAm solutions (3rd Chapter) [112]. The quantitative differences between A488 and Rh6G in the ϕ-dependence of their $\mathrm{D_{slow}}(\phi)/\mathrm{D_0}$ and $\mathrm{F_{slow}}(\phi)$, in the two type of networks, are discussed next.

Slow tracer mobility in hydrogels and polymer solutions. The typical mesh size, ξ, of the swollen PNiPAAm gels in the present thesis are similar to the ones in the corresponding PNiPAAm semidilute solutions i.e. in the range 3-20 nm [77], being almost one order of magnitude larger than the diameter of the molecular tracers employed. Thus, anomalous diffusion related to viscoelasticity [130] or obstructed diffusion play no important role in the presented slowdown of the interacting molecular tracers. The latter is primarily controlled by crowding effects [111],[77] and/or by interactions. Figure 4.1.4 shows the slowdown $\mathrm{D_i}(\phi)/\mathrm{D_0}$ (i=fast, slow) for both the fast and the slow process for A488 and Rh6G along with the amplitude of the slow process ($\mathrm{F_{slow}}(\phi)$) as a function of ϕ, in PNiPAAm aqueous solutions and hydrogels at T=25°C. In the case of PNiPAAm solutions (3rd Chapter), the diffusion slowdown for the fast process conforms to a chain length independent 'master' curve observed for non-interacting tracers in polymer solutions (dashed curve) [111]. For the same process in hydrogels, the slowdown falls on a similar master curve (solid curve in Fig. 4.1.4) representing the single diffusion of the non-interacting A647 in the same hydrogels. This slowdown is attributed solely to crowding effect expressed by the concentration,ϕ [77]. For the slow process, however, the diffusion slowdown of Rh6G and A488 in PNiPAAm solutions and hydrogels clearly deviates from a superposition to a single curve. The value of $\mathrm{D_{slow}}(\phi)/\mathrm{D_0}$, in PNiPAAm aqueous

solutions, decreases monotonically with ϕ and becomes similar for both dyes, while its concentration dependence resembles that of the polymer self-diffusion slopes [9] (Fig.4.1.4).

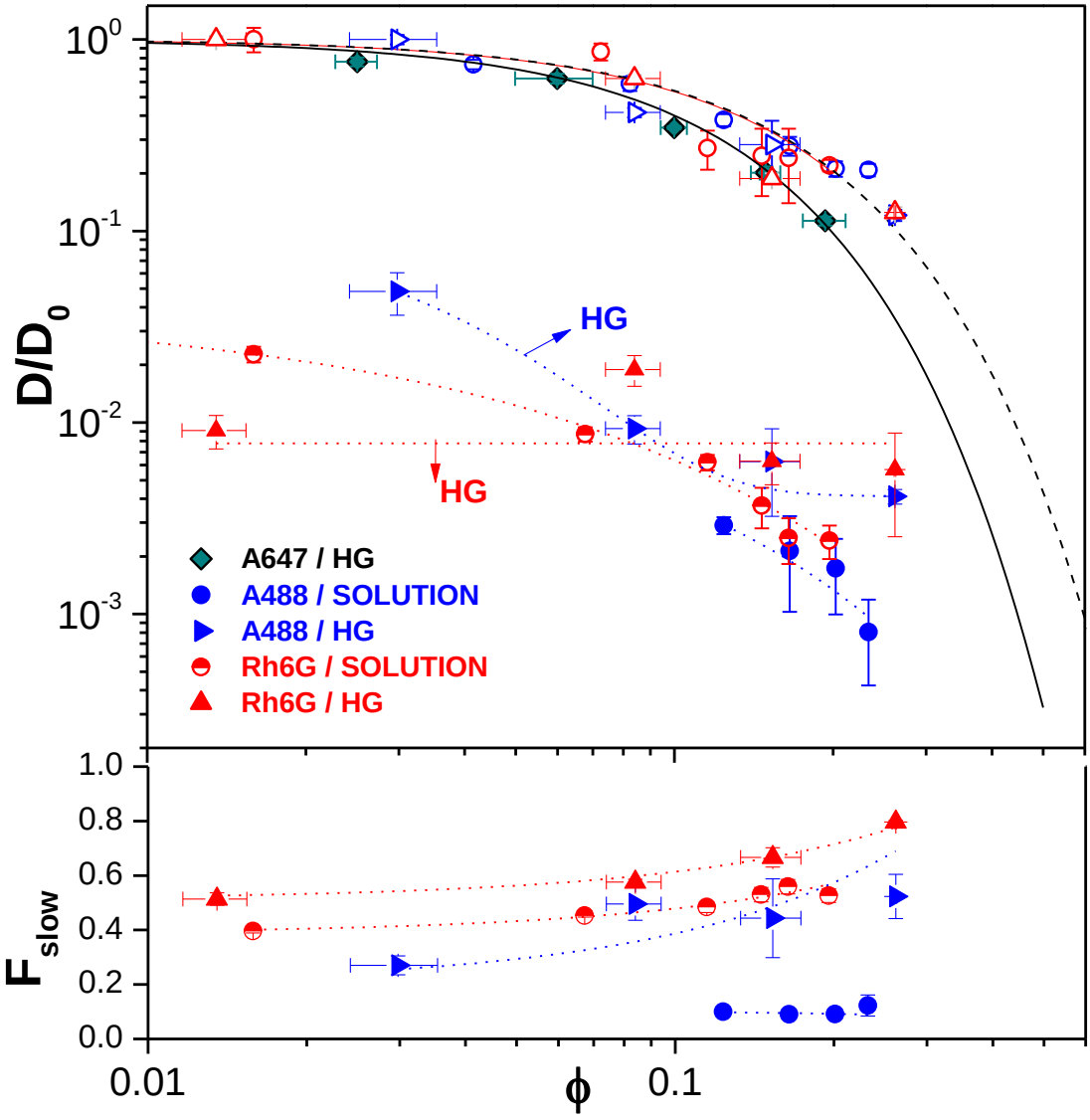

Fig.4.1.4. Mobility slowdown, $D(\phi)/D_0$, for the diffusive processes in the case of weak and strong attractions exemplified by A488 and Rh6G (fast: open symbols; slow: solid symbols) in solutions (circles) and in hydrogels (triangles). Arrows point to the datasets in hydrogels. The dashed and solid black curves denote stretched exponential concentration dependences recently reported for non-interacting molecular tracer diffusion slowdown, $D(\phi)/D_0$, in solutions [111] and hydrogels [77], respectively. Mobility slowdown data of non-attractive tracer (A647) in PNiPAAm hydrogels from an earlier study [77] are also shown (green rhombi). Lower panel: Amplitude of the slow process, $F_{slow}(\phi)$, in $G(t)$ of A488 and Rh6G in PNiPAAm solutions (circles) and hydrogels (triangles). The dotted lines are drawn to guide the eye.

In hydrogels, the slow process is distinctly different both in diffusion slowdown and in amplitude, $F_{slow}(\phi)$. It is worth noting that $F_{slow}(\phi)$ for A488 is measurable only above $\phi \sim 0.1$ in solutions, in contrast to the hydrogels with discernible slow process already above $\phi \sim 0.03$. Since the physical and chemical networks consist of the same polymer, the tracer-PNiPAAm interactions should be similar. The differences in diffusion in the two networks might reflect different durations of binding times (τ_{bound}) (3rd Chapter) for the interacting tracers in each network type. Such observation may

stem from differences in the inherent polymer chain dynamics in the two types of networks. The arrest of tracer's slow diffusion $D_{slow}(\phi)/D_0(\sim 0.01)$ in hydrogels appears to be tracer dependent as it occurs at $\phi \geq 0.1$ for A488, while it is present for Rh6G over all examined crosslinking densities. The tracer specificity of this effect excludes 'frozen-in' hydrogel dynamics as the lone reason, as indicated by the single diffusion of the non-interacting A647. The slowdown disparity between the two tracers at low ϕ is attributed to the different sign of Coulombic interactions (being attractive for Rh6G and repulsive for A488) as well as to coexisting short range hydrophobic interactions between each tracer and the negatively charged PNiPAAm. With increasing crosslinking density and hence ϕ, the number of chargeable acrylic groups increases proportionally with the total monomer concentration. However, as the total monomer concentration approaches the dissociation constant of the methacrylic acid ($10^{-4.2}$ M) [161], the degree of charging decreases. Beyond this concentration, the number of charged groups increases much slower than the increase in the total monomer concentration. In contrast, the total number of monomers available for hydrophobic binding increases proportionally with polymer concentration without constraints that would be due to dissociation constants. Therefore, one expects that the short range attractive hydrophobic interactions may dominate over the electrostatic A488-PNiPAAm repulsions at high ϕ, rationalizing the observed behavior in Figs.4.1.4. The anticipated increase of the slowdown in hydrogels with ϕ may be probably compensated by the concurrent increase of the PNiPAAm hydrogel's $D_{coop}(\phi)$ as ϕ increases [63]. Hence, the interplay among electrostatics, short-range attractions and the hydrogel cooperative diffusion might all control the complex slow tracer diffusivity.

II. Temperature and ionic strength effects on molecular mobility in responsive grafted PNiPAAm terpolymer hydrogels.

The description of the hydrogel swelling ratios and the D values of the different molecular tracers, at various hydrogel crosslink densities, are presented as follows: (i) Temperature and crosslink density effects are simultaneously investigated; (ii) the effect of monovalent salt is addressed separately.

4.4.1. Results

Using the most strongly interacting tracer, Rh6G, the hydrogel fully swollen thicknesses can be obtained with higher resolution, up to roughly the LCST of PNiPAAm ($T \sim 32$ °C) as shown for HG-4 in the inset to Fig.4.2.1.

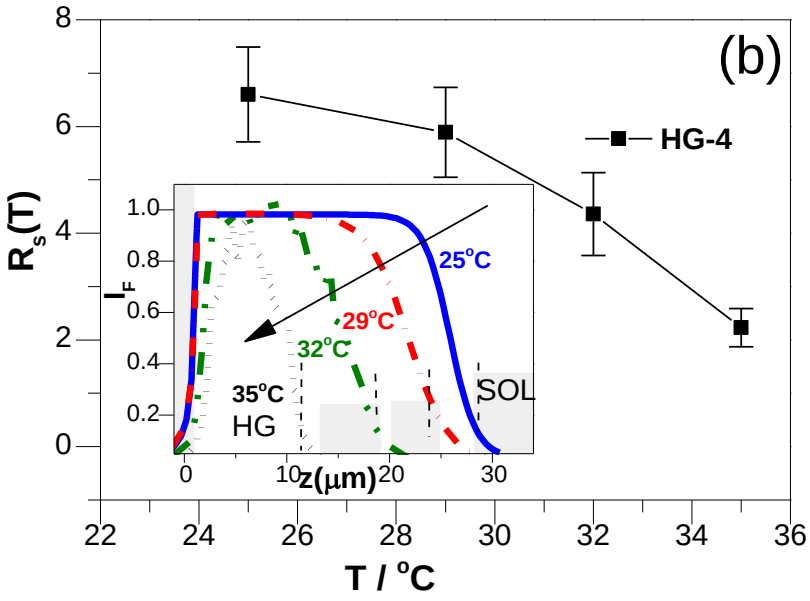

Fig.4.2.1. (Swelling ratios, $R_s(T)$, of HG-4 as a function of temperature, T. Inset: Rh6G tracer density profile in HG-4 represented by the normalized fluorescence Intensity (I_F) in HG-4 (white region) and supernatant solution (light grey) as a function of the distance, z, from the substrate. Arrow points to the direction of increasing T.

The corresponding swelling ratios, $R_s(T)$, are obtained by normalizing the fully swollen HG thicknesses by the dry gel's thickness. The swelling ratio, $R_s(T)$, decreased in HG-4 from about 7 (T= 25°C; good solvency) to about 2 (T= 35°C; collapse), in agreement with the T-dependent collapse of PNiPAAm [77]. The dynamics of both Rh6G and A488 exhibit deviation from a single Fickian diffusion as clearly demonstrated by the two decays of $G(t)$ in Fig.4.2.2. A rather T-independent fast diffusion time (vertical line at ~80 μs (A) and ~60 μs (B) in Fig.4.2.2) is related with a fast diffusion process, whereas the slow diffusion time, τ_{slow}, of Rh6G and A488 dyes increases with T (shown only for Rh6G, inset to Fig. 4.2.2a).

This increase in the slowdown of dynamics with increasing T apparently relates with the collapse of HG-4(Fig.4.2.1b). In addition, the permeation ($P'(T)$) of A488, estimated as the ratio of fluorescence intensity in the gel compared to the intensity in the supernatant solution (normalized A488 fluorescence Intensity, I_F), was also found to increase with T (inset of Fig.4.2.2b). This indicates increasing T-dependent affinity between A488 and PNiPAAm segments, when the hydrophobicity of the latter progressively increases towards LCST. Since electrostatic interactions are insensitive to T-variations, $P'(T)$ most likely reflects predominant changes in the A488-PNiPAAm hydrophobic interactions.

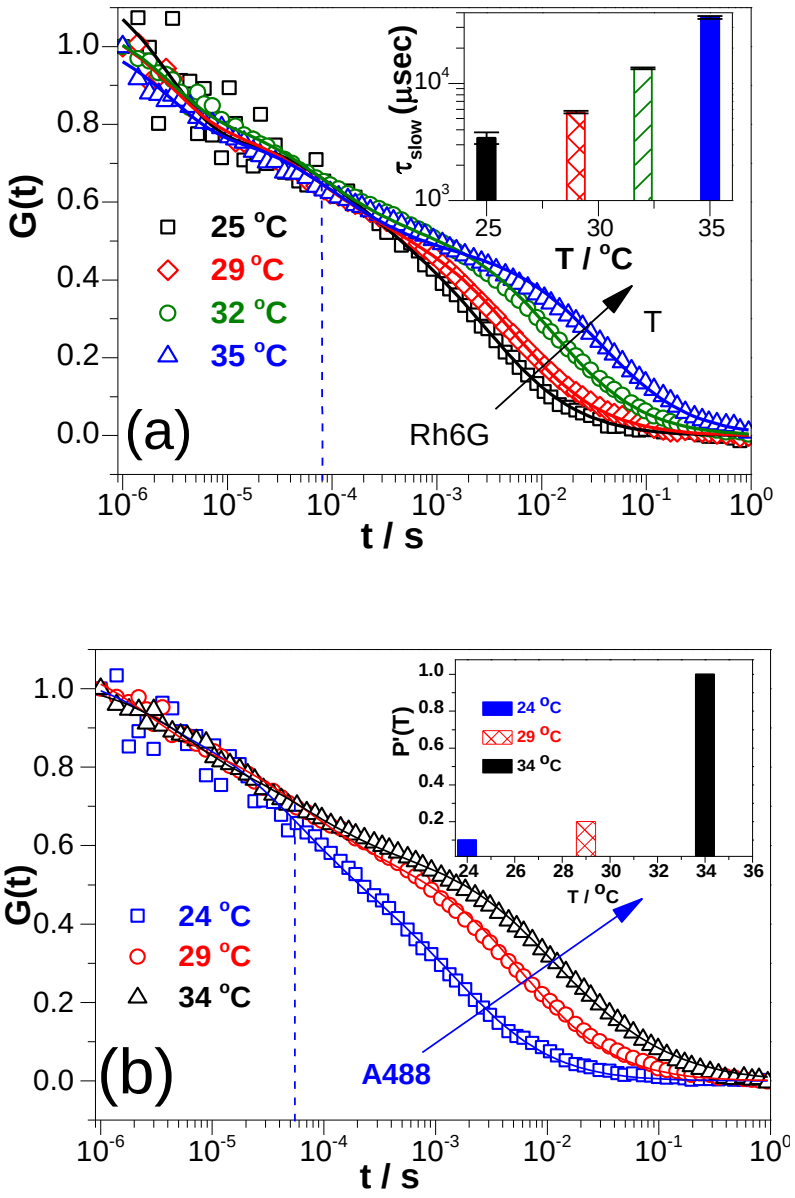

Fig.4.2.2. Normalized fluorescence intensity autocorrelation curves, $G(t)$, for (a) the strongly (Rh6G) and (b) weakly (A488) interacting dyes in HG-4 at different temperatures (T).The dashed vertical line indicates the fast T-independent diffusion time. Inset: (a) the diffusion time, $\tau_{slow}(T)$, of the slow process for Rh6G in HG-4 and (b) normalized partition coefficient, $P'(T)$, for A488 in HG-4.

As discussed in part I, the selection of certain crosslink density can control each examined tracer's diffusivity (Fig.4.1.4), since the interactions are differently weighed. At low ϕ (low crosslink densities), i.e. in HG-1 and HG-2-upper panels of Fig. 4.2.3a and b, respectively, a T-independent swelling ratio ($R_s(T)$) was obtained. At such ϕ values, the fast diffusion slowdown ($D_{fast}(T)/D_0(T)$) and the fraction of non-interacting species ($F_{fast}(T)$) are both T-independent for either tracer. This fraction is higher for A488 ($F_{fast}(T) \sim 0.75$) than for Rh6G ($F_{fast}(T)$) ~0.45), suggesting different interaction strength. On the other hand, a counterintuitive T-dependent trend

was observed for $D_{slow}(T)/D_0(T)$, where Rh6G (HG-1) exhibits both different trend and stronger slowdown than A488 (HG-2).

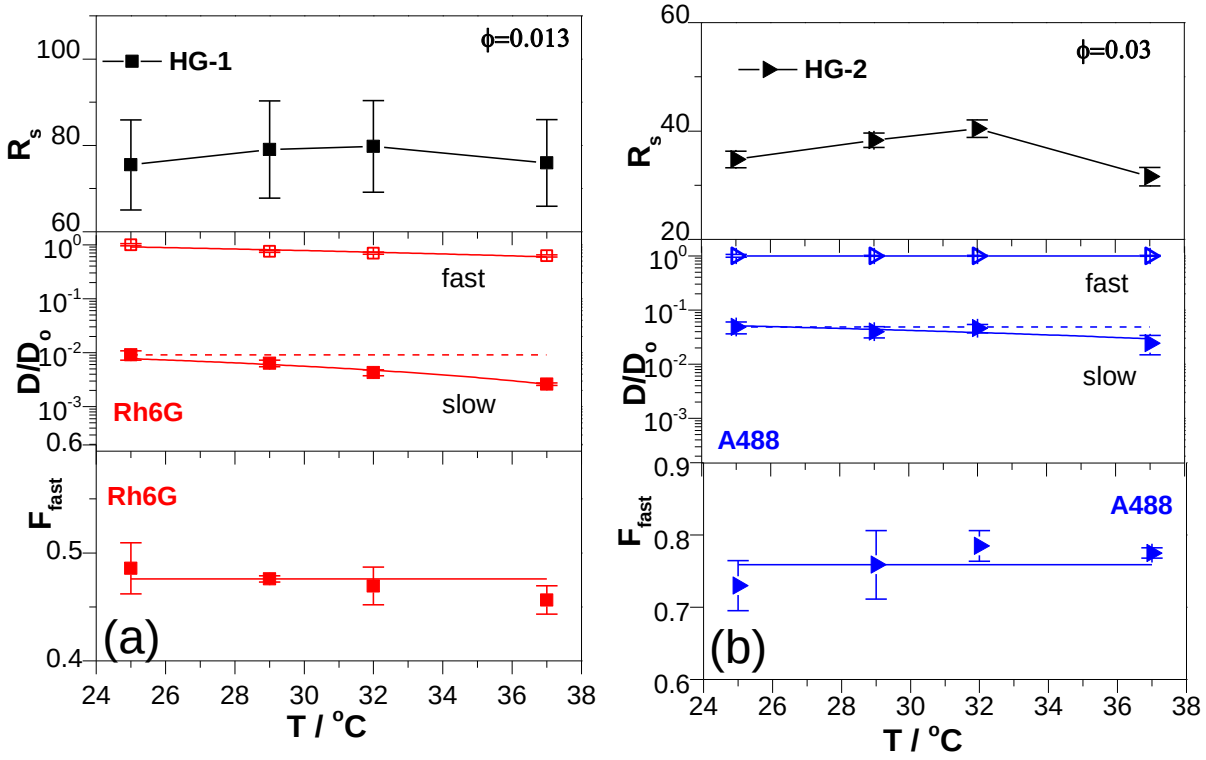

Fig.4.2.3. Swelling ratios $R_s(T)$ and tracer mobility (a) in HG-1 (for Rh6G, red squares) and (b) in HG-2 (for A488, blue triangles) along with the diffusion slowdown, $D(T)/D_0(T)$, for the fast and the slow process (empty and solid symbols in the middle panel, respectively) and the amplitude for the fast process, $F_{fast}(T)$, for A488 and Rh6G (lower panel). Dashed lines in the middle panel indicate the value of $D(T)/D_0(T)$ for the slow process of the color-matching tracer at 25°C, as reference lines. Solid lines in (a) and (b) are drawn to guide the eye.

The horizontal dashed lines in the middle panels of Fig.4.2.3 correspond to the $D_{slow}(T)/D_0(T)$ value in good solvency conditions ($T = 25°C$) for each tracer. The diffusion slowdown for Rh6G ($D_{slow}(T)/D_0(T) \sim 5 \cdot 10^{-3} - 10^{-2}$) is 5 to 10 times stronger than the corresponding value of A488 ($D_{slow}(T)/D_0(T) \sim 5 \cdot 10^{-2}$) at the same T, even though A488 was examined in a hydrogel with a slightly larger ϕ value (~0.03 vs. 0.013 for Rh6G). In both HG-1 and HG-2, the T-dependent tracer slowdown *does not* include any crowding effects (no collapse).This trend is not surprising, when considering the ϕ - dependent LCST of PNiPAAm, shown in a respective T vs. ϕ phase diagram of the thermoresponsive polymer [162, 163], qualitatively sketched in Fig. 4.2.4.

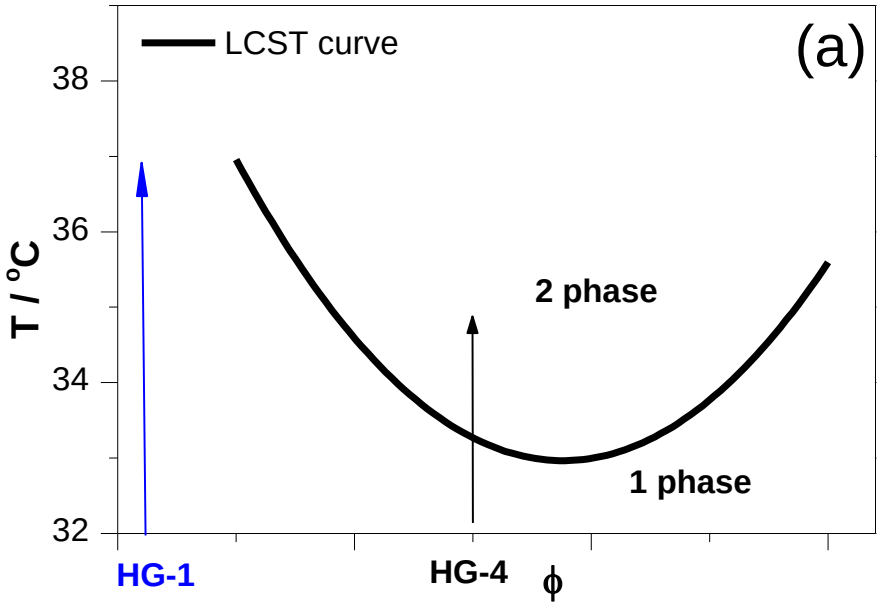

Fig.4.2.4. Schematic phase diagram – T vs. ϕ – of PNiPAAm hydrogels exhibiting a lower critical solution temperature in water [162].

At such low ϕ values in the as-prepared state (T=25 °C), HG-1 (Table 4.1) indeed exhibits a broader single phase regime (higher LCST), while lower LCST is expected at higher ϕ values, e.g., for HG-4.

Concurrent increase of temperature and concentration. In order to address possible influence of structural changes (crowding and thermal collapse) on the interacting tracer dynamics and on the associated interaction potential, the tracer dynamics were also monitored at higher crosslink densities and hence higher ϕ values. The elucidation of interacting tracer dynamics became more complex when they were probed in hydrogels of higher crosslink densities (HG-4, Fig.4.2.5). Fig.4.2.5 shows the swelling ratio, $R_s(T)$, the diffusion slowdown $D(T)/D_0(T)$ and the amplitude of the fast process, $F_{fast}(T)$, for Rh6G (squares) and A488 (triangles). Apart from the contribution of T - dependent interactions in the slowdown, as was the case in Fig.4.2.3, an additional significant effect due to crowding (decrease of $R_s(T)$) with increasing T appears.

The polymer solvency (Flory-Huggins interaction parameter, $\chi(T)$) [7] becomes T-dependent at such crosslink densities (HG-4), where ϕ spanned from 0.15 (good solvency) to 0.33 (collapse).The fast diffusion slowdown ($D_{fast}(T)/D_o(T)$) and the fraction of this process, ($F_{fast}(T)$), are again both insensitive to T variations, for either A488 or Rh6G. Next, the larger $F_{fast}(T = 25\ °C)$ resolved for A488 (~0.5) than for Rh6G (~0.3) again suggests that A488-PNiPAAm interactions are weaker compared to the corresponding Rh6G-PNiPAAm interactions.

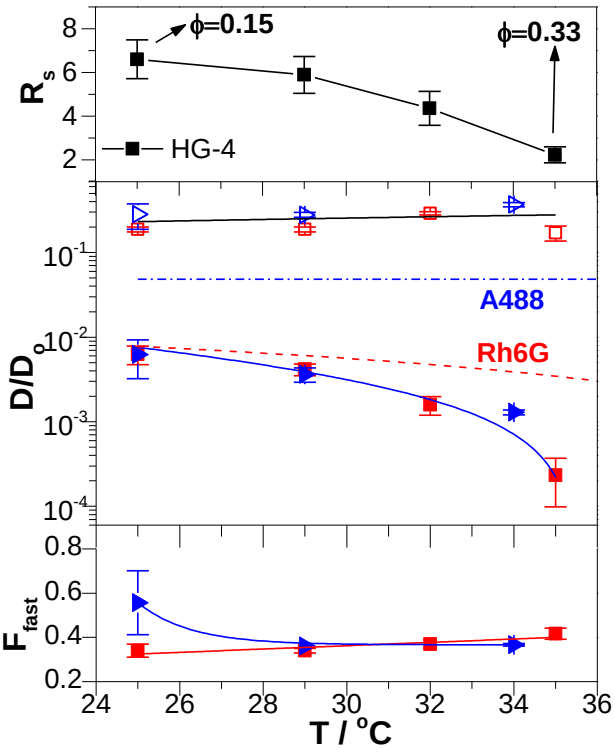

Fig.4.2.5. Variation of the swelling ratio, $R_s(T)$, of the diffusion slowdown $D(T)/D_0(T)$ and amplitude of the fast diffusion $F_{fast}(T)$ for Rh6G (red squares) and A488 (blue triangles) in HG-4. Dashed lines in the middle panel indicate the T-dependent slowdown for the slow process, at low φ's (Fig.4.2.3).

Other significant differences that were observed in $(D_{slow}(T)/D_0(T))$ compared to the cases of lower crosslink densities (HG-1, HG-2), are discussed below:

(i) Both Rh6G and A488 exhibit the same slowdown $(D_{slow}(T)/D_0(T))$ in HG-4 (Fig.4.2.5), over the examined T- range

(ii) Each tracer expresses different trend in its diffusion slowdown with varying crosslink densities, at the same T and at good solvency conditions: dashed lines in Fig.4.2.5 represent the color-matching $D_{slow}(T)/D_0(T)$ in HG-1 and HG-2. In the case of Rh6G, changes in ϕ do not influence the dynamics at good solvency, namely: $D_{slow}(T = 25\,°C)$. Additional slow diffusion slowdown for Rh6G beyond the corresponding slowdown at $T = 25°C$ in HG-1 (red dashed line in Fig.4.2.5) occurs only at T close to the collapse transition. Structural effects due to collapse may thus also affect the Rh6G slowdown. On the other hand, A488 (Fig.4.2.5) exhibits a strong uptake in its slowdown, even at good solvency conditions $(D_{slow}(T = 25°C))$ – exhibiting a significant deviation from the dashed blue line- from HG-2 to HG-4.

(iii) The slowdown $(D_{slow}(T)/D_0(T))$ for both tracers exhibits strong T-dependence close to the collapse –high ϕ values- (i.e. for Rh6G: $D_{slow}(35°C)/D_0(35°C) \sim 2\cdot 10^{-4}$), implying that

apart from changes exclusively related with T -dependent interactions, as is the case of HG-1 and HG-2, collapsing mechanisms affect tracer dynamics. On account of the T-dependent results, it appears that the different tracers manifest differently their dynamics in the same HG environment.

Monovalent salt (KNO_3) effects. Biosensor platforms [26] typically operate at physiological conditions (presence of salt). Since a central motivating argument for this thesis has been to investigate mobility under conditions that would mimic typical biosensor operating conditions, the examination of the influence of salt in the corresponding tracer mobilities and network's response is fundamentally necessary. Besides, the addition of salt can elucidate possible electrostatic nature of the tracer-PNiPAAm interactions. Hence, the dynamics of each interacting molecular tracer (A488, Rh6G) were investigated in the grafted hydrogels at good solvency conditions ($T = 25°C$), using a monovalent salt (KNO_3) as the external stimulus.

Significant insight for the nature of the tracer-PNiPAAm interactions was deduced from both tracer permeation profiles (z-scans) and the quantitative interpretation of tracer dynamics. In brief, the tracer mobility was distinctly differentiated as a response to the hydrogel's structural alterations, induced by salt addition. The permeation of Rh6G (Fig.4.2.6a, inset) is rather insensitive to ionic strength alterations, as compared to A488 (Fig.4.2.7a, inset) or to A647 (Fig. S5, Appendix). Fig.4.2.6.a shows $G(t)$ curves for Rh6G in HG-5 at different ionic strength (I) values, while the density profile for Rh6G in the same HG is shown in the inset, at the I values of the color-matching $G(t)$ in the main plot. On the other hand, the Rh6G diffusion slowdown, $D(I)/D_0(I)$, is plotted vs. I in Fig.4.2.6b, together with the corresponding $\phi = \phi(I)$ values.

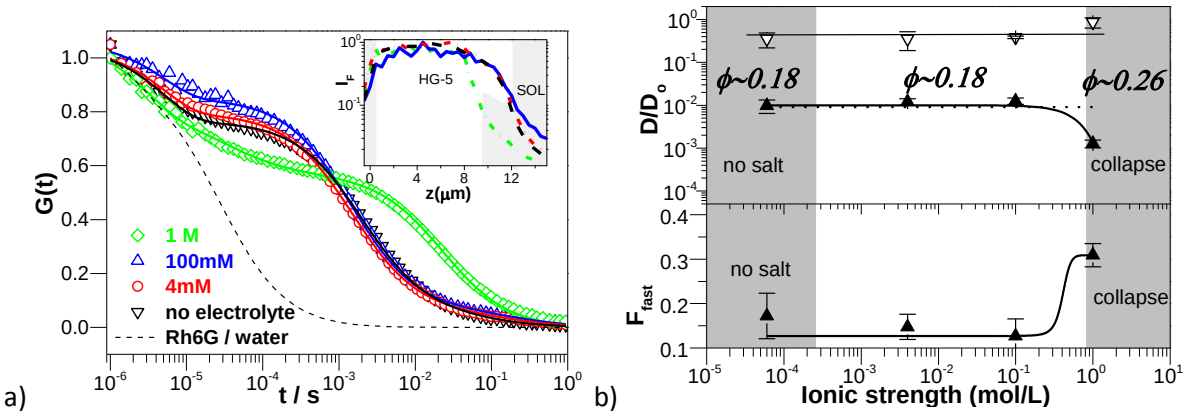

Fig.4.2.6. (a) Experimental $G(t)$ for Rh6G in water (dashed curve) and in HG-5 along with Rh6G density profile (inset: normalized Rh6G fluorescence Intensity, $I_F(z)$, in HG-5 (white) and in the supernatant solution (grey) vs. distance, z, normal to the substrate (grey), for different ionic strength (I) values, at 25°C. (b) Diffusion slowdown, $D(I)/D_0(I)$, for the fast (white triangles) and slow components (black triangles) and amplitude, $F_{fast}(I)$, for the system in (a). The values of the listed composition, ϕ, correspond to the swollen and collapsed (at I=1M salt) HG-5, at 25°C.

Even though Rh6G is a charged molecule, it was recently shown that the underlying hydrophobicity has a predominant influence on Rh6G-PNiPAAm interactions[112]. Beyond certain value of the ionic strength (I = 1M), the grafted hydrogel network collapses, as manifested by Rh6G in HG-6 (also by A488 in Fig.4.2.7). Such salt-dependent trend is consistent with recent reports concerning monovalent salt effects in the swelling properties of identical grafted PNiPAAm layers using surface plasmon resonance techniques [141] or atomic force microscopy (AFM) [164]. Rh6G exhibits a sharp change in its slow process ($D_{slow}(I)$) only in the collapsed state (I=1M). The fast component in Rh6G slowdown is rather salt-independent ($D_{fast}(I)/D_o(I)$~0.5), while the slow diffusion ($D_{slow}(I)/D_o(I)$) changes from 10^{-2} to 10^{-3}, only at the collapsed state. Counter-intuitively, it was found that the amplitude of the fast process ($F_{fast}(I)$) for Rh6G increases only at the collapse (0.1 to 0.3), in contrast to the qualitative trend using T as the external stimulus in HG-4 (Fig.4.2.5). This peculiar salt-dependent trend of $F_{fast}(I)$ can be associated with collapse-related effects. It might imply that the pore size decreases and either less Rh6G can penetrate the HG or the length scale requirements (3rd Chapter, Fig.3.8) for the resolution of the two processes by FCS have been changed. In the collapsed state, the slowdown upon addition of salt ($D_{slow}(I)/D_o(I)$~10^{-3} at ϕ=0.26, in HG-5) is weaker than the temperature-induced slowdown ($D_{slow}(I)/D_o(I)$~$3\cdot10^{-4}$ at ϕ=0.33, in HG-4). Therefore, the selection of stimulus affects significantly the resulting Rh6G slowdown at the corresponding collapse. It is therefore conceivable that the HG assumes different structure in the collapsed state, by temperature vs. salt as stimulus. On the contrary, electrostatic interactions seem to be much more significant for A488. By slight alterations (I=4mM) of the ionic strength, one may observe: (i) the higher sensitivity of A488 dynamics (Fig.4.2.7a and 4.2.7b), compared to Rh6G (Fig.4.2.6a and 4.2.6b) and (ii) alterations in A488 permeation through the HG (Fig.4.2.7a, inset).

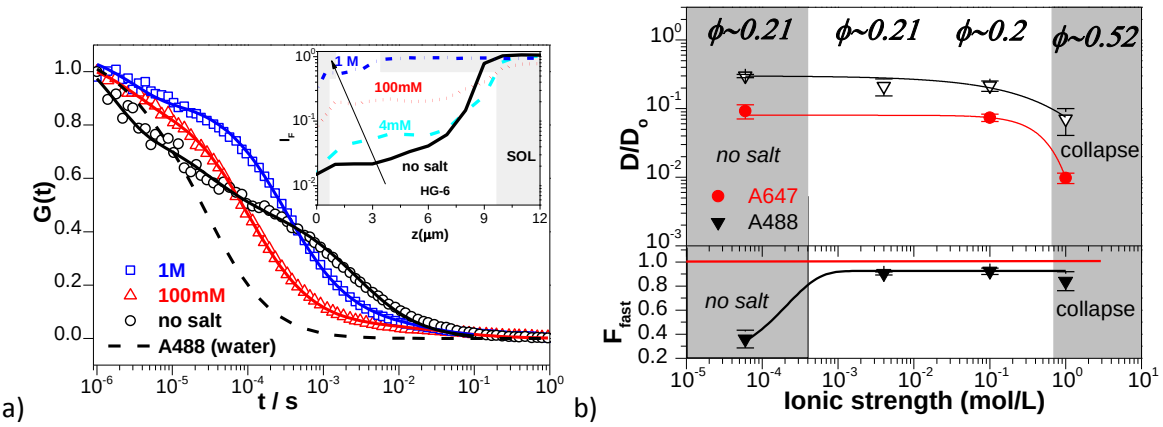

Fig.4.2.7. (a) Experimental $G(t)$ for A488 in water (dashed curve) and in HG-6 along with A488 density profile, I_F (inset: normalized A488 fluorescence Intensity, $I_F(z)$, in HG-6 (white) and in the supernatant solution (grey) vs. distance, z, normal to the substrate (grey), for different I values, at 25°C. (b) Upper panel: Diffusion slowdown, $D(I)/D_0(I)$, for the fast (white triangles) A488 component and for A647 (red triangles); lower panel: $F_{fast}(I)$ for the system in (a). The values of the listed composition, ϕ, correspond to the swollen and collapsed (at I=1M salt) HG-6, at 25°C.

Apart from opposite trends in permeation, A488 and Rh6G exhibited opposite trends also in their dynamics. As for A488, its $G(t)$ exhibited a crossover from double Fickian to a single Fickian with an increasing trend of $F_{fast}(I)$ (Fig.4.2.7). In contrast to Rh6G, already at low ionic strength (I =4mM KNO_3 – sufficient to screen Coulombic interactions and also well before collapse occurring at I=1M KNO_3), $F_{fast}(I)$ of A488 increases from 0.3 to 0.9. Hence, the slow A488 process cannot be resolved for I >4mM KNO_3. In the absence of salt, the slow component slowdown is approximately $D_{slow}(I)/D_o(I) \sim 6 \cdot 10^{-3}$, at ϕ =0.22 (HG-5), with $F_{fast}(I) \sim 0.3$.

4.4.2. Discussion

At low HG crosslink densities ($\phi < 0.1$), tracer-PNiPAAm specific slowdown exists, where Rh6G exhibits stronger attractions than A488. The observation that at low crosslink densities (HG-2) $D_{slow}(T)$ of A488 exhibits qualitative differences compared to that of Rh6G, reinforces the initial speculation based on their different charges that the two interacting tracers exhibit different form of interactions and also that a tracer-specific slowdown exists. Such speculation had been also proposed for A488 in PNiPAAm hydrogels at good solvency conditions (section I of this Chapter). Surprisingly, a crossover from single Fickian diffusion in polymer solutions- to double diffusion –in the crosslinked hydrogels- was observed for the weakly repulsive A488 only at $c \gg c^*$, being not the case for the strongly interacting Rh6G, where deviation from single Fickian diffusion was observed for Rh6G in both solutions and crosslinked PNiPAAm hydrogels. The observed differences in tracer dynamics and permeations using salt as stimulus and not temperature reinforce the evidence towards different nature of tracer-PNiPAAm interactions. The screening of electrostatic repulsions enhances the permeation of the hydrogel to A488 (Fig.4.2.7a), but it appears at odds with the simultaneous increase in $F_{fast}(I)$ with increasing ionic strength (I). The latter observation may relate either with size exclusion changes from the screened polyelectrolyte network or with biased resolution of FCS. Moreover, the diffusion slowdown trend is distinct for the two tracers, where increased slowdown was recorded for Rh6G only at the collapse (Fig.4.2.6b). Noteworthy, A647, acting as the internal standard (A647) concurrently present in the same sample with A488, exhibited single Fickian diffusion in the hydrogels, irrespective of the salt content, even at the collapsed state (I= 1 M KNO_3). At the collapsed state, the slowdown of Alexa647 ($\sim 10^{-2}$) was an order of magnitude stronger than that of A488($\sim 10^{-1}$), suggesting that A647 may be considered as a more sensitive tracer of the collapsed microstructure than A488. Even though electrostatic repulsions were found to be rather significant for A488, yet electrostatics –in general-seem to have a rather minimal influence on the Rh6G-PNiPAAm system. The observations from the network's swelling response and from the Rh6G dynamics support the assertion that Rh6G-PNiPAAm interactions are not that substantially affected by electrostatics, while hydrophobic interactions are significantly present. With regard to a possible

'structure-interaction' relationship, a conjecture from the aforementioned findings is that a T-dependent tracer-polymer interaction potential, $\varepsilon(T)$, maybe the underlying cause for the observed tracer diffusion slowdown, $D_{slow}(T)/D_o(T)$), at such low crosslink densities (HG-1, HG-2), where possibly $\varepsilon_{A488}(T) < \varepsilon_{Rh6G}(T)$.The ϕ-dependent A488 slowdown using T as the external stimulus (Fig.4.2.3 to 4.2.5) might suggest an additional ϕ-dependence in the A488-PNiPAAm interaction potential, $\varepsilon_{A488}(T,\phi)$. This assumption is corroborated by the change in $F_{fast}(T = 25°C)$ from HG-2 (ϕ=0.03) to HG-4 (ϕ=0.15) and the F_{fast} change between T=25 °C and T=29 °C in HG-4 (Fig.4.2.5). Finally, an attempt for superposition on a single curve vs. ϕ for the $D_{slow}(\phi)/D_o$ data for each tracer (Rh6G and/or A488) does not work (Fig. 4.2.8 for Rh6G), also witnessed under good solvency conditions (Fig.4.1.4).

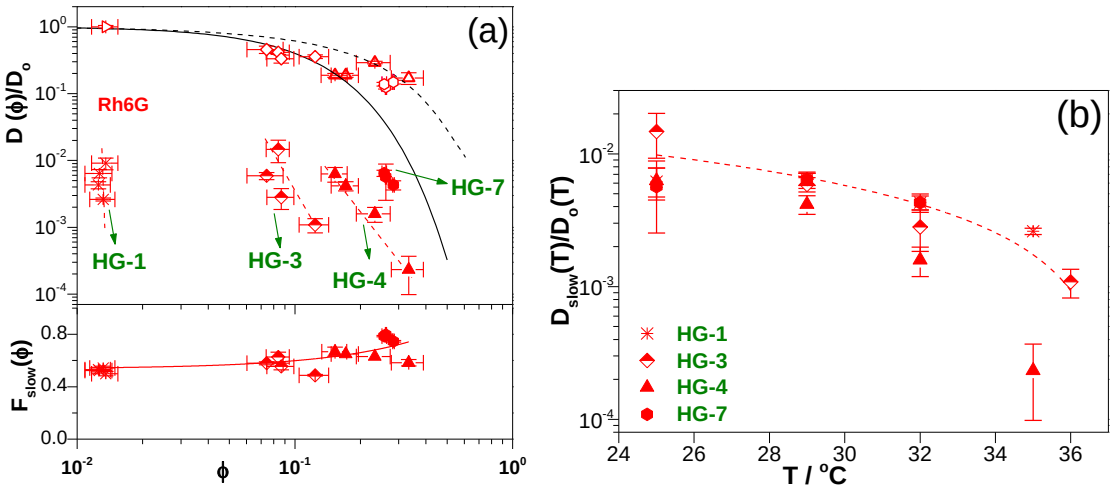

Fig.4.2.8. (a) Mobility slowdown presented as $D(\phi)/D_o$ together with $F_{slow}(\phi)$ vs. ϕ, in the case strong attractions exemplified by Rh6G in HGs. Green arrows denote the $D_{slow}(\phi)/D_o$ datasets from the same HG (same symbol type) shown in Table 4.1. Fast and slow processes are denoted by empty and solid symbols, respectively. Dashed and solid curves denote stretched exponential dependences vs. ϕ for recently reported for non-interacting molecular tracer diffusion slowdown, $D(\phi)/D_o$, in solutions [111] and in HGs [77], respectively; (b) Mobility slowdown, $D_{slow}(T)/D_o(T)$, vs. T for Rh6G using the same symbol for the different HGs examined. The dotted red lines in (a) and (b) are drawn to guide the eye.

Although a similar superposition vs. ϕ was found to hold for the $D_{fast}(\phi)/D_o$, a ϕ-dependent trend for the $D_{slow}(\phi)/D_o$ of the interacting tracer was revealed, depending on the ϕ at the 'as-prepared' state.

III. Towards biosensor optimization: temperature and crosslink effects on antibody mobility in responsive grafted PNiPAAm hydrogels.

In the present section, results from the influence of temperature (T) and gel's crosslink density on the mobility of an antibody (A647-labeled IgG) thermoresponsive PNiPAAm hydrogel layers at different crosslink densities are presented and discussed. A thorough understanding of transport features of antibodies through such networks, as a network's response of external stimuli, is fundamentally important for optimization of hydrogel-based affinity binding matrices [25, 26],[165].The single molecule sensitivity of FCS renders it an optimal method to resolve such dynamics. As mentioned in the Materials section of this Chapter, all measurements of IgG mobility in this section were performed in buffer conditions (acetate buffer, pH=4). The mobility of IgG was first measured in absence of polymers, at T=25 °C. As shown in Fig.4.3.1, $G(t)$ of the labeled IgG in buffer (no polymer) was represented by a double Fickian diffusion, where the fast process corresponds to the free molecular tracer (A647), simultaneously coexisting with A647-labeled IgG in the solution. This shows that although IgG is relatively well labeled, there is also a small amount of free, non-attached dye (A647) that also enters the gels in this study. While the influence of this molecular dye on the FCS autocorrelation function $G(t)$ can be relatively easily decoupled due to its much smaller size, it will still be desirable to make control experiments with the molecular dye (A647) only. The hydrodynamic radius of the antibody is $R_{h,np} = 7.2 \pm 0.5$ nm, as obtained from its diffusion coefficient D_o= (3.4±0.2)·10^{-11} in $m^2 \cdot s^{-1}$ measured in the buffer solution, in absence of any polymer, at T=25°C. The ϕ values of the HG, the diffusion coefficients D_{slow} of the IgG and D_{fast} for the free dye are all listed in Table 4.2.

Table 4.2. Physical quantities of the examined PNiPAAm gels and diffusion times of labeled IgG (in acetate buffer)

PNIPAAm HG(code)	**#2**	**#5**	**#7**
HG crosslinking time	5 min	10min	15 min
HG volume fraction,ϕ:			
ϕ(25℃)	0.08±0.01	0.098±0.02	0.15±0.02
(ϕ(29℃))	(0.11±0.02)	(0.17±0.04)	(0.19±0.03)
D_{fast}, (x$10^{-10}$$m^2s^{-1}$), D_{slow} (x$10^{-10}$$m^2s^{-1}$) – F_{slow} (T=25℃)	1.8±0.09, (0.11±0.01)-0.88	1.08±0.05, (0.018±0.005)-0.65±0.12	1.01±0.05, (0.015±0.004)-0.27
D_{fast}, (x$10^{-10}$$m^2s^{-1}$), D_{slow} (x$10^{-10}$$m^2s^{-1}$) – F_{slow} (T=29℃)	1.8±0.09, (0.10±0.01)-0.86	1.1±0.05, (0.018±0.003)-0.85	N/A

Experimental G(t) for IgG are shown in Fig.4.3.1 at various HG crosslink densities. The arrow points towards increasing T, while vertical dashed and solid lines denote the corresponding diffusion times from double Fickian diffusion fit, for the IgG in absence and in presence of PNiPAAm, respectively.

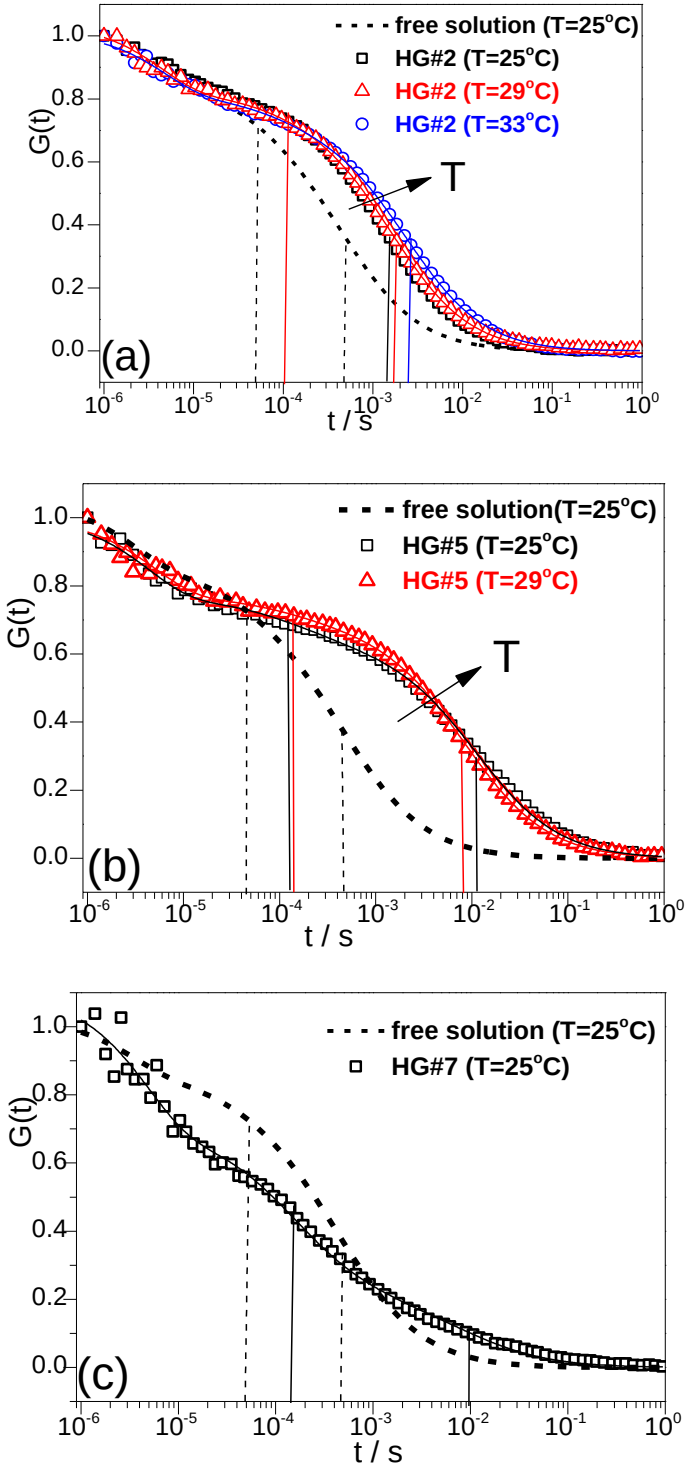

Fig.4.3.1. G(t) of IgG as a function of T in (a) HG#2 and in (b) HG#5, while only at T=25℃ in (c) HG#7. Dashed black G(t) curve corresponds to free IgG diffusion (fast process corresponds to A647). Vertical lines denote fast and slow diffusion times from double Fickian diffusion fits, corresponding to free dye and IgG, respectively. Dashed vertical lines denote the diffusion times by the fits for the tracers in absence of HG. The arrow points to the direction of increasing T.

The IgG mobility in dilute (c=1.3·10^{-3} g·ml^{-1}~0.5c*) PNiPAAm buffer solution also at T=25°C reveals practically no slowdown D= (3.2 ± 0.3)·10^{-11} m^2s^{-1} ~ D_o), implying absence of significant IgG-PNiPAAm interactions. Based on these results, IgG can easily enter the hydrogels of relatively low crosslink density, HG#2 and HG#5, when they are fully swollen at 25°C. Moreover, IgG enters also in HG#7 at 25°C, but its fraction of the double Fickian fit, F_{slow} (Table 4.2), is lower than in the other two HG's.

4.5.1. Results

The fast time (diffusion of A647) has been fixed to the value predicted by a master curve (solid black curve in Fig.4.3.2) for non-interacting molecular tracers in HGs[77]. The fit is unique for the slow time (IgG), regardless of fixing the fast time, or not. At T=25°C, the smooth trend between G(t) of IgG in buffer solution, HG#2 and HG#5, is interrupted in HG#7. The diffusion slowdown values in the HGs, ($D_{slow}(\phi)/D_0$), for IgG (solid symbols) and for the coexisting free dye A647 (empty symbols), at T=25°C (black) and T=29°C (red), are plotted vs. ϕ in Fig.4.3.2.The diffusion slowdown of IgG (solid symbols; red and black) was found not to superimpose on the master curve [77] for non-interacting molecular tracers.

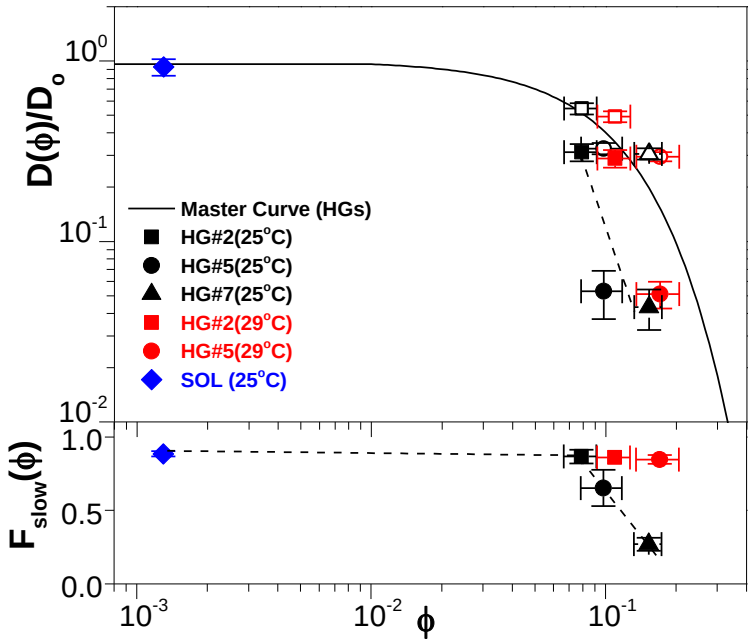

Fig.4.3.2. Diffusion slowdown per tracer,($D_{slow}(\phi)/D_0$), and amplitude of the slow process (IgG), $F_{slow}(\phi)$, vs. ϕ at T=25 °C (black symbols) and at T=29 °C (red symbols) in HG#2 (squares), HG#5 (circles) and HG#7 (triangles). Open and solid symbols denote the slowdown for the fast process (A647, coexisting free dye) and for the slow process (IgG), respectively, expressed for each symbol as the ratio of diffusivities of a given tracer in HG, D(ϕ(T)), divided to its diffusion coefficient in the supernatant solution, D_0(T). Diffusion slowdown and $F_{slow}(\phi)$, of IgG in dilute (ϕ=0.5ϕ*) PNiPAAm solution (blue rhombi) at T=25 °C is also shown. The amplitude $F_{slow}(\phi)$ corresponds to IgG fraction in the corresponding ϕ(T) value of a given HG or in the single measurement in the dilute PNiPAAm solution. Solid black curve denotes the diffusion slowdown for non-interacting molecular tracers[77].Dashed lines are drawn to guide the eye.

The $D_{slow}(\phi)/D_0$ for IgG was found to quite sensitively depend on the crosslink density at T=25°C, with a characteristic 10-fold increase in the slowdown going from HG#2 (ϕ=0.08) to HG#5 (ϕ=0.15). The fraction of IgG, $F_{slow}(\phi)$, strongly decreases from 0.8 (HG#2) to 0.3 (HG#7) at T=25°C, which means the HG acts as a filter for IgG, when the mesh size decreases. Moreover, $D_{slow}(\phi)/D_0$ for IgG was found to exhibit practically no T-dependence between 25°C and 29°C in HG#2 and HG#5. In addition, aggregation of IgG was recorded at 29°C only in the supernatant solution of HG#5 *and not* in the HG. On account of the decrease in fluorescent intensity at T=33°C, either due to IgG immobilization and subsequent photobleaching, and/or due to size exclusion, dynamics for IgG have not be recorded at T close to the LCST (T=33°C).

4.6. Conclusions/Outlook

By means of FCS, the effects of crosslink density, monomer volume fraction, interactions and the influence of external stimuli on the mobility of molecular tracers and of fluorescently labeled antibodies in temporary (3rd Chapter) and permanent PNiPAAm aqueous networks have been assessed. Even though interactions and crosslink density effects may be separately addressed using a non-interacting tracer A647, a sensitive interplay between crosslinking density with strength and nature of the tracer-polymer interactions is what dictates the emerging tracer mobility. The results of this Chapter have shown that interactions are significant, even for the simplest case of molecular tracers.

The experimental results on tracer diffusion in crosslinked hydrogels have provided a new viewpoint, concerning a variety of resolvable tracer diffusive dynamics and the influence on the tracer mobility from the synergistic effect of crosslink densities, tracer types and strength-nature of interactions. The unexpectedly resolved stronger molecular tracer diffusion slowdown in entangled temporary networks (solutions) compared to permanent networks (gels), for the same tracer, remains not fully understood, but it may relate with differences in inherent chain dynamics of the polymer network and with cooperative network dynamics. Moreover, the arrest in diffusion slowdown observed in permanent networks for Rh6G at good solvency, implies the simultaneous action of different competing mechanisms, among which osmotic, electrostatic and possibly short-range forces.

Due to repulsive Coulombic interactions with PNiPAAm, the weakly attractive A488 was found to be a more sensitive probe of the network type and of the network crowding conditions (volume fraction ϕ). A488 and Rh6G exhibit both different nature and strength of interactions with PNIPAAm, as deduced by the–to certain extent- opposing differences in permeation and dynamics, using salt or

temperature as external stimulus. At low concentrations in the 'as-prepared' state, e.g. low $\phi(25\,^{\circ}C)$, T-dependent FCS in HGs revealed that both A488 and Rh6G seem to be related with a T-dependent interaction potential, whereas the potential additionally involves crowding –apart from interaction- effects at larger $\phi(25\,^{\circ}C)$. The mobility at the collapsed state may depend on the stimuli it was induced by.

The transport features of antibodies, e.g. the diffusion of IgG in grafted PNiPAAm hydrogel layers, depend on the crosslink density in the fully swollen state (T =25°C). The IgG permeation is strongly reduced for ϕ>0.1, whereas the corresponding IgG mobility is much less sensitive. This trend does not change with increasing temperature in the range 25°C < T <33°C in spite of the increase of ϕ >0.1. Similar to the T-effects for the molecular tracers, this might suggest influence of hydrophobicity in tracer-PNiPAAm interactions.

Overall, the complex mobility in such hydrogels is tracer-specific and the obtainable information depends on at least some of the following factors: monomer concentration, crosslink density, external stimulus and tracer type. A future suggestion directly stemming from this study would involve a combination of experiments using smaller illumination spots (STED-FCS with higher axial resolution) with simulations that could not only provide further information about associated thermodynamic parameters and binding constants, but also verify the appropriateness of the employed two-component Fickian model, when deviations from single Fickian diffusion may be recorded.

Chapter 5: Tracer diffusion in ideal aqueous polymer networks

Abstract

The mobility of different tracers has been examined in ideal polymer networks (Tetra-PEG hydrogels) at ambient conditions, in good solvency. The ideality of the network stems from narrow polydispersity of the precursor four-arm Tetra-PEG polymers and the efficiency of the click reaction used to bound them in an extended polymer network with very uniform mesh size distribution. Diffusion of various tracers has been examined in these gels, with variability in sizes (molecular tracers vs. nanoparticles) and structure (biopolymers vs. nanoparticles). The diffusion slowdown has been found to vary, on account of the employed tracer. With decreasing mesh size of the gel, the molecular tracer A647 and the solid nanoparticles exhibit increasing single Fickian diffusion slowdown, while flexible polymers, such as PEO and single stranded DNA, exhibit weaker slowdown. Moroever, the polymeric tracer dextran experiences an even weaker dependence on the gel's mesh size of its diffusion. In order to examine whether this diffusive behavior relates with the particular network structure or not, diffusion in the homologous monodisperse PEO homopolymer aqueous networks has also been considered. Single Fickian diffusion slowdown has been unexpectedly revealed for nanoparticles (QD and PS nanoparticles (PS-NP)) in such polymer solutions, even at concentrations well below the PEO chain overlap concentration. In view of similar trend of QD in PNiPAAm aqueous solutions (3rd Chapter), this slowdown at ultralow concentrations is attributed to weak tracer-polymer interactions.

5.1. Introduction

Solute diffusion through porous materials has been frequently encountered in soft matter and nanotechnology, with substantial implementations in biosensors and separation membranes [134]. The need to develop membranes with stringent 'solute size cut-off' requirements is very strong [156, 166], as such networks could optimize various separation processes, such as: water desalination, ultrafiltration, biosensor applications. From a fundamental point of view, the elucidation of such complex diffusion phenomena would be seemingly more straightforward after an examination of diffusion in a rather more simplified and 'ideal' system has preceded [156]. The 'ideality' stands for as narrow distribution of the pore (mesh) size of the polymer networks as possible. Such an ideal network could give the opportunity to easily control solute permeation and diffusion, as well as selectively examine the effect of tracer size, shape and interactions, quite systematically. Both

fundamental (i.e. polymer physics-oriented)[167] and applied [134] [168, 169] problems would be benefited by an examination of diffusion through such ideal networks.

A complete and systematic investigation of tracer mobility through an ideal network would presuppose a similar study in aqueous homopolymer solutions of the same chemical structure. For polymer solutions, Rubinstein et al. [7] have provided scaling arguments concerning the diffusion slowdown of non-interacting nanoparticles (Chapter 1), by addressing the influence of tracer-polymer size ratio, polymer M_w and polymer concentration on diffusion slowdown. Tracer mobility studies quite frequently aim to verify the validity of generalized Stokes-Einstein equation, a property depending on the interplay between tracer and polymer size [170]. Even though a comparison of experimental results concerning nanoparticle diffusion in polymer solutions with such theoretical works seems appealing, a direct comparison and consolidation of the validity of such models has been still lacking. In addition, an examination of mobility in dilute polymer solutions provides the additional advantage that diffusion is examined on a rather simplified polymer system where underlying physics may be more easily understood. Such study in an ideal polymer network would also be a necessary prerequisite towards a clearer understanding and proper design of biosensor applications.

In this chapter, FCS has been employed to investigate diffusivities of different types of tracers (Alexa647, Quantum Dots, fluorescently labeled polystyrene nanoparticles (PS-NP), labeled Dextran molecules, Alexa488 labeled -single stranded DNA, labeled PEO), in various mesh sizes of an ideal crosslinked polymeric network, known as Tetra-PEG hydrogel[96], in its fully swollen state. The tracer types differentiate not only on their size (molecular tracers vs. nanoparticles), but also on their structure (core-shell nanoparticles vs. soft macromolecules). In contrast to the more polydisperse and charged PNiPAAm hydrogels in the 4th chapter, the Tetra-PEG network represents an ideal network, in terms of: absence of charge, very narrow mesh size distribution and extremely strong mechanical properties[16].

To solidify the findings on tracer diffusion in Tetra-PEG hydrogels, a systematic approach should also cater for the investigation of the influence exerted by the permanent crosslinks for a homopolymer of the same chemical structure, in the same solvent. Therefore, FCS experiments for selective tracers have been also performed in aqueous solutions of monodisperse PEO, with different M_w. Both PEO and Tetra-PEG networks lack thermoresponsivity, thus ruling out the additional complexity of temperature effects of the polymer matrix exerted on tracer mobility. Corresponding features of the fully swollen Tetra-PEG hydrogels and of the PEO polymers are reported in Table 5.1 of this chapter, while diffusion coefficients for the various tracers in water, in absence of additional polymer, are reported in Table 5.2.

5.2. Materials

Tetra-PEG hydrogels: The "ideal" structure of the Tetra-PEG (T-PEG) hydrogels originates from the way they have been prepared [96]. Briefly, four arm tetra-PEG polymers with well-defined and monodisperse arm length were first synthesized. Their chemical structure is shown in Fig.2.9. The arms ends are pairwise functionalized with groups capable of click-reaction with each other. Thus upon in-situ mixing of those macromers, click reactions between neighboring Tetra-PEG polymers in solution lead to a polymer network with very well defined distance between "crosslinks" (Fig.5.A). The concentration of the T-PEG gels in the as-prepared state has been 0.1 g·ml^{-1}. Three different gels, Tetra-PEG 10k, 20k and 40k, with arm M_w of 2.5k, 5k and 10k, respectively, have been studied. The corresponding mesh sizes for the fully swollen Tetra-PEG hydrogels are reported in Table 5.1. Assuming a segment length for PEG monomer, b=0.3 nm [171] and considering the monomer $M_w = 44$ g·mol^{-1} and the $M_{w,c}$ between neighboring crosslinks to be $M_{w,c} = 5000$ g·mol^{-1}, a mesh size (ξ^*) for a Flory chain in Tetra-PEG 10k is expected to be: $\xi^* = 0.3 \cdot (5000/44)^{0.59} \approx$ 5.1 nm (mesh size in the as-prepared state).When this gel is fully swollen at equilibrium (swelling rate ≈ 1.92), the mesh size, ξ, becomes: $5.1 \cdot (1.92)^{\frac{1}{3}} \approx$ 6.3 nm (according to affine deformation for rubbers, due to favorable swelling in water), as shown in Fig.5.A. The mesh size obtained by SANS (namely, $\xi^{\#}$) [16] has been much smaller than the end-to-end distance, R_e, of polymer chain fractions between nearest neighboring crosslinks[16]. As such, an assumption has been that the employed mesh sizes ξ in the T-PEG gels of thesis could obstruct the diffusion of nanoparticles only when $\xi \leq R_{H,np}$.

Likewise, $\xi = 7.8 \cdot (2.87)^{\frac{1}{3}} \approx$ 11.1 nm and $\xi = 11.8 \cdot (5.25)^{\frac{1}{3}} \approx$ 20.5 nm for T-PEG 20k and 40k, respectively. To that direction, Fig.5.A qualitatively illustrates the mesh size in the fully swollen state, ξ, as the center-to-center distance between two opposing T-PEG star macromers of the same end groups, having quadrupole functionality (one macromer can covalently bind to maximally four nearest neighbors). Specific features of the T-PEG gels and all materials employed in this chapter, being necessary to follow the discussion in this chapter, are also summarized in Table 5.1.

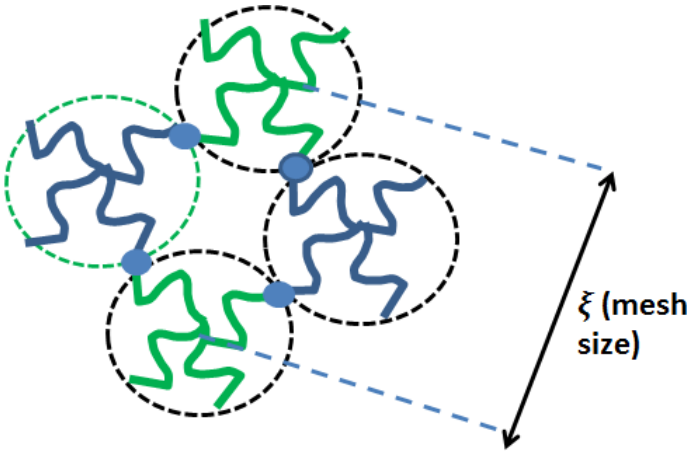

Fig.5.A. Schematic of the fully swollen T-PEG crosslinked network between T-PEG macromers with amine (green) and *N*-hydroxysuccinimidyl ester (blue) end groups with a corresponding mesh size in the fully swollen state (ξ), being the center-to-center distance between two opposing macromers bearing the same end groups. Different colors have been used to denote the different end groups. Blue dots connecting macromers of different color denote crosslinks. Redrawn based on [135].

PEO polymers. The repeat unit for the PEO employed in the experiments (sections II and III), the type of polymerization reaction and the associated PI values have been reported in the 2nd Chapter.

Fluorescein-Isothiocyanate (FITC) labeled Dextran. The repeat unit of FITC-dextran has been shown in Fig.2.8 (2nd Chapter). FITC-labelled dextran of 3 different sizes (M_w: 4k, 20k, 70k) have been used. The notation 'Dex-x' has been used everywhere in this chapter, where 'x' corresponds to the M_w of dextran. Additionally, A488 labelled single stranded DNA (PAGE purified) was employed in these experiments (Fig.2.7, 2nd Chapter). All fluorescent tracers in this Chapter were purchased from Sigma Aldrich.

Table 5.1. Physical quantities of the examined Tetra-PEG gels and of the PEO polymers

Tetra-PEG-x (2x: M_w of Tetra-PEG arm)	T-PEG-10k	T-PEG-20k	T-PEG-40k
[1] Mesh size (ξ)	6.3	11	21
[2]PEO M_w (g·mol^{-1})	20.4k	102k	481k
[3]PEO c* (g·ml^{-1})	0.014	$4.6 \cdot 10^{-3}$	$1.1 \cdot 10^{-3}$
[4]$D_{O,PEO}$x10^{11}(m^2·s^{-1})	4.0 [172],[173]	1.8 [172], [173]	0.76 [172], [173]

[1] Correlation lengths (mesh sizes), ξ, for the following M_w of Tetra-PEG samples: 10k, 20k, 40k
[2] Manufacturer values
[3] The c* (4th line) has been estimated from the experimental data of this thesis (Fig.S6, black squares with scaling law: $M_w^{-0.9}$).
[4] Self-diffusion coefficient D_p data for PEO (5th line) interpolated/extrapolated from reported literature values.

The value of c^*(Table 5.1) for the PEO homopolymer networks (section II) has been estimated from the nanoparticle diffusion data presented in the same section. In the associated scaling relation:

$c^* \sim M_w^{\varpi}$, the corresponding scaling exponent ($\varpi \sim -0.9$) (black squares, Fig.S6) from measured nanoparticle diffusion data is more realistic than literature-related ($\varpi \sim -0.6$) values [172, 173]. Hence, the estimated c^* values for the examined PEO (Table 5.1) from the former option only have been followed everywhere in this chapter. Table 5.2. summarizes the diffusion coefficients, D_0, for the different tracers used in each M_w of fully swollen Tetra-PEG and in aqueous PEO solutions. Especially in the case of dextran, a polymer M_w dependent expression for the diffusion coefficient has been retrieved. The diffusion of the labeled dextran in water was obtained from a fit (eq. 2.3.2, 2nd Chapter) to the corresponding representation of $G(t)$, using single (n =1) diffusion fit. The size dependence of the Dex-x diffusion coefficient, $D_0(N)$, has been fitted by the following equation[1]: $D_0 \sim 1.5 \cdot 10^{-8} \cdot N^{-0.5}$ $m^2 \cdot s^{-1}$ (Table 5.2), where N stands for the degree of polymerization and 'x' corresponds to the dextran M_w.

Table 5.2. Diffusion coefficients in water, D_0, for the various tracers examined in T-PEG gels and in PEO polymer solutions

Fluorescent tracers	A647	Dextran	QD	PS-NP	ssDNA 88bp	Labeled PEO 35k
$^6D_0$,x10^{11}(m^2/s)	33	$D_0 \sim 1.5 \cdot 10^{-8} \cdot N^{-0.5}$	3.9 (QD525) 2.6 (QD545) 2.7 (QD585)	1.6	6.0	5.6

[1] In fact, the scaling relation has been calculated by regression between the diffusion times for the different dextran M_w and the corresponding M_w (not N).

5.3. Diffusion in Tetra-PEG hydrogels

Results and Discussion

Different tracers (A647, QD, dextrans, ss DNA, labeled PEO) have been examined in three M_w of T-PEG gels. Selected $G(t)$ are shown in Fig.5.1.1 (A647 and QD) and 5.1.2 (Dextrans and ssDNA). The hyperbolic fitting function (eq.2.3.2, 2nd Chapter) has been used in all three different M_w of Tetra-PEG expressed as (i) single Fickian fit for A647 and Dex4k and as (ii) double Fickian fit for: Dex20k, Dex70k, labeled PEO 35k and ssDNA. On the other hand, a single Fickian diffusion using the blinking fitting model (n =1, eq.2.3.3, 2nd Chapter) has been employed for the different QDs in T-PEG 40k.

Both QD and A647 (Fig.5.1.1) experience retardation on their translational diffusion in the T-PEG gel, denoted by the time lag of the corresponding single Fickian $G(t)$. In particular, QD525 experiences a 5-fold retardation on its dynamics in T-PEG 40k than in water, while for A647 a two-fold slowdown in T-PEG 10k has been revealed (inset to Fig.5.1.1). Concerning the polymeric tracers (Dex, ssDNA and PEO), the major complication in the double Fickian fits has been that they are not unique. To address

this issue, the hypotheses have been that (i) the fast process is attributed to the free dye and (ii) the free dye is not interacting with the T-PEG.

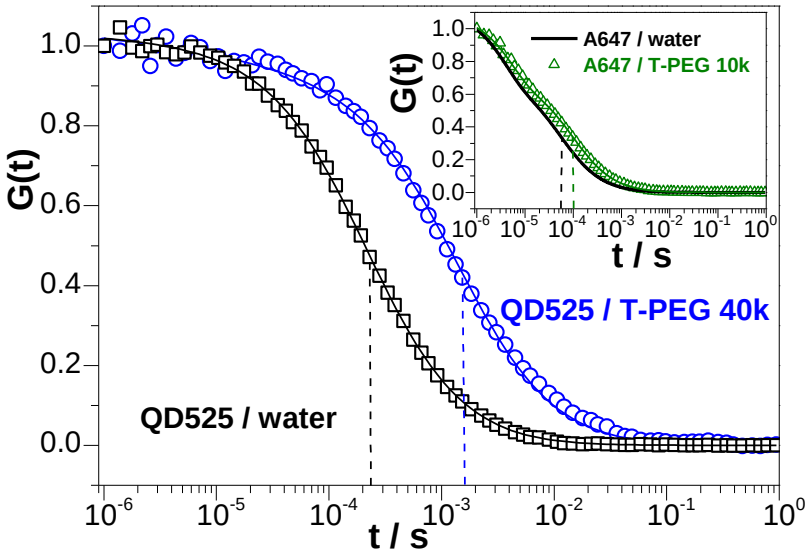

Fig.5.1.1. Normalized $G(t)$, represented by a single Fickian diffusion. Main plot: QD525 in water (black squares) and in T-PEG 40k (blue circles); inset: Alexa647 in water (black line) and in T-PEG 10k (green triangles). Dashed vertical lines denote the single Fickian diffusion times for the indicated systems.

The diffusion time of fast process for all these molecules has been fixed to the following value: the diffusion time of the non-interacting molecular tracer (A647), rescaled by the ratio of corresponding radii (FITC/A647, for dextran; A488/A647 for ssDNA or labeled PEO). In most cases, there has been agreement on the fitting deliverables by either approach (floating times or fast time been fixed). The dashed vertical lines in Fig.5.1.1 denote the extracted diffusion times using single Fickian fits for QD (eq.2.3.3) and A647 (eq.2.3.2), accordingly. In analogous manner, the solid and dashed vertical lines in Fig. 5.1.2 denote diffusion times using double and single Fickian diffusion model (eq.2.3.2). In the case of the denoted macromolecules, the double Fickian diffusion fit corresponds to free (unbound) molecular tracer and labeled macromolecule, respectively. In the case of Dex4k, a single Fickian diffusion has been found adequate for the representation of the experimental $G(t)$ due to the proximity of the diffusion times for the two components (free dye and dextran).

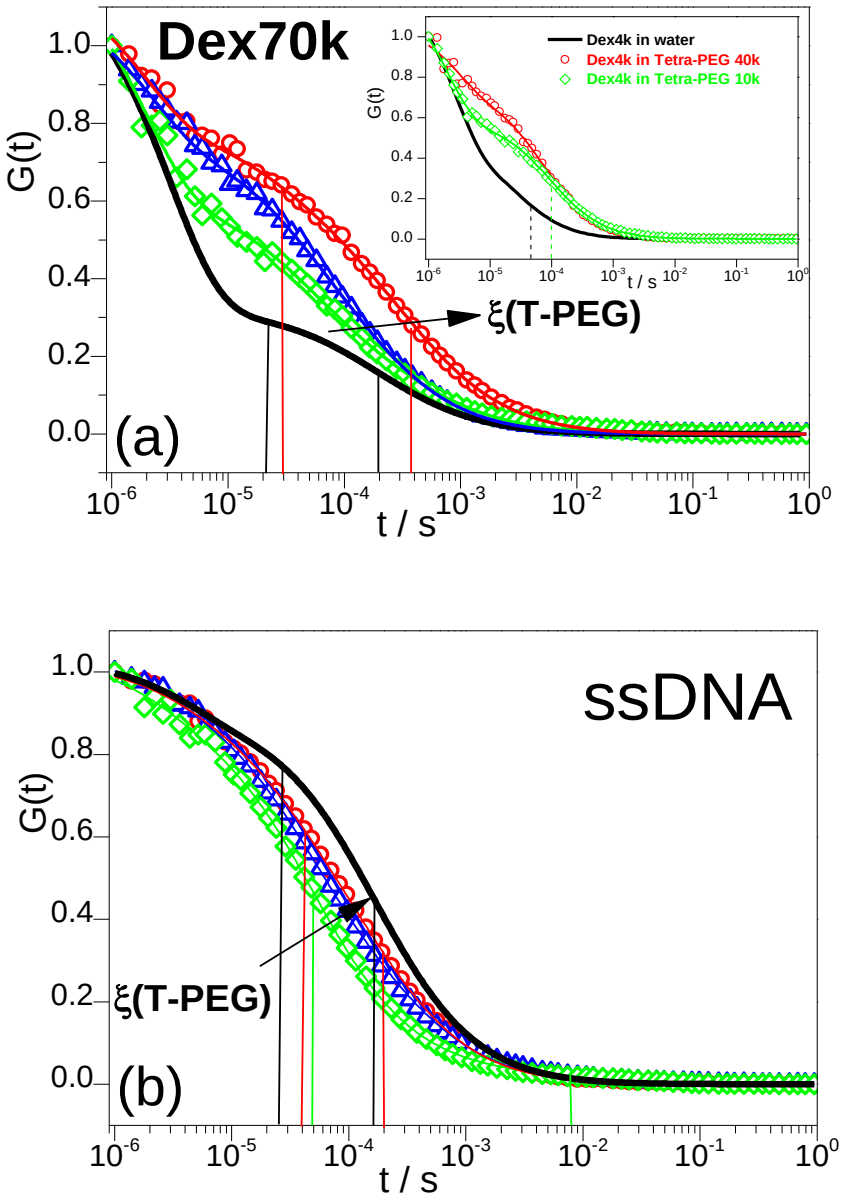

Fig.5.1.2.Normalized $G(t)$ curves for (a) Dex70k and Dex4k and (b) for ssDNA: in water (solid black curve), in T-PEG 10k (green rhombi), in T-PEG 20k (blue triangles) and in T-PEG 40k (red circles). The solid black $G(t)$ corresponds to tracer's free diffusion in water (Dex70k in (a); ss DNA in (b)). The arrow points to the direction of increasing mesh size, ξ, of T-PEG. Solid lines in the main plots and dashed lines in the inset of (a) denote the calculated diffusion times from double and single Fickian diffusion time in water (black) for the color-matching $G(t)$ of a given tracerin the corresponding HGs, respectively.

To illustrate the distinct mobility of tracers with different size in varying T-PEG mesh size, ξ, , the reduced diffusion $D_0/D(\xi)$, has been plotted vs. the frustration ratio, defined as $2R_{h,np}/\xi$ in Fig.5.1.3. The latter parameter represents the confinement parameter. An analogous representation vs. ϕ has been avoided, as it would not consider the influence of tracer size. As demonstrated in Fig.5.1.3, lines are drawn to guide the eye for the following cases: (i) a ξ-independent dashed-dotted (black) line is drawn to denote the tracer's diffusion in water ($D_0/D(\xi) = 1$); (i) one solid (black) line

through the diffusion trend by A647, Dex4k and QD; (iii) a dashed line through Dex20k (purple); (iv) a dashed line though Dex70k (blue) and (v) a dashed curve through labeled PEO tracers (green). Grey hashed region denotes the confinement region where penetration should not be expected for a solid nanoparticle. The lower panel of Fig.5.1.3 depicts the amplitude of the slow process, $F_{slow}(\xi)$, using the double Fickian fitting model, for the 'size and color'-matching data points of the upper panel.

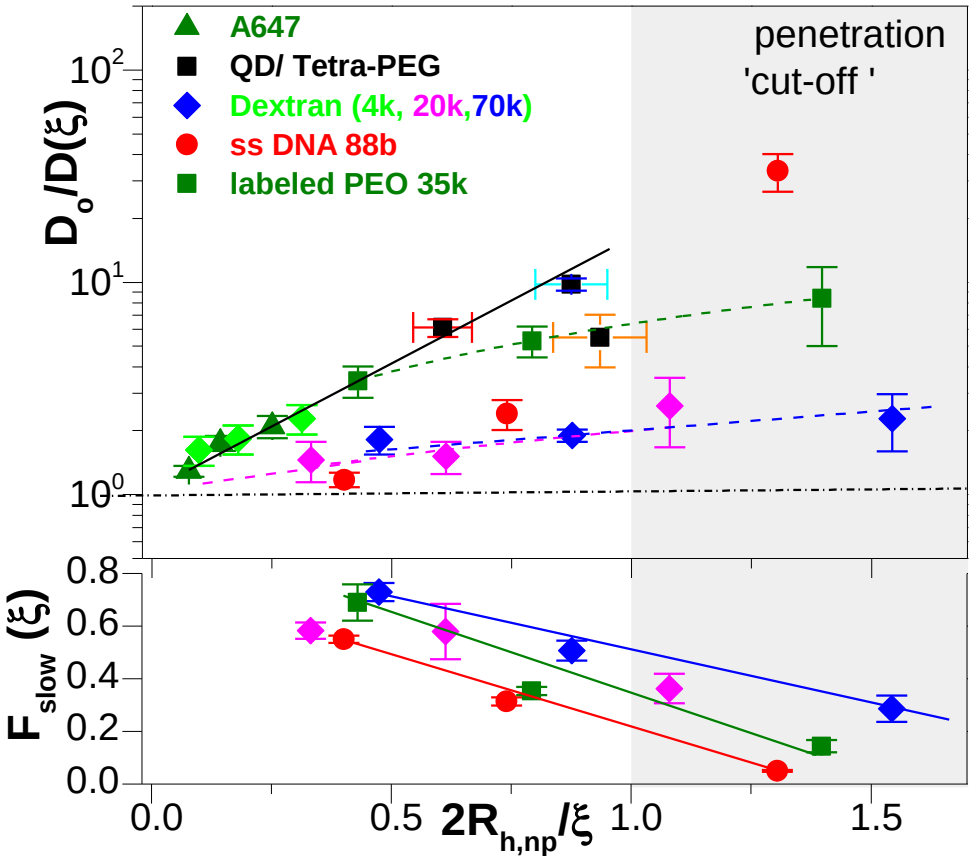

Fig.5.1.3. Diffusional retardation $D_0/D(\xi)$ and amplitude of the slow diffusion process $F_{slow}(\xi)$ vs. frustration ratio ($2R_{h,np}/\xi$): A647 (dark green triangles), ss DNA 88b (red circles), Dex4k (light green rhombi), Dex20k (pink rhombi), Dex70k (blue rhombi) and labeled PEO 35k (green triangles) in three M_w of T-PEG; $D_0/D(\xi)$ for three different QDs (QD525, QD545, QD585) (black squares) in T-PEG 40k is also shown. Grey-shaded zone denotes region of -presumably - no penetration of hard sphere. Dashed and horizontal lines are drawn to guide the eye.

Distinct diffusion retardation trends have been revealed for different tracers. The molecular tracer (A647) experiences an increase in its diffusional retardation ($D_0/D(\xi) \sim 1.5-2$) with decreasing ξ. Consistent with the intuition that increasing the confinement will induce stronger slowdown, the QD nanoparticles exhibit roughly five times stronger slowdown than A647, when compared at the same ξ. Hence, size indeed affects single Fickian tracer slowdown in T-PEG. A slight non-monotonicity in the slowdown trend of the QDs examined in Tetra-PEG 40k (at $2R_{h,np}/\xi \sim 0.8$ in Fig.5.1.3) may relate with sub-micrometric nano-inhomogeneities with the particular T-PEG 40k hydrogel (Fig.5.1.3). It is noted that permeation and mobility experiments were investigated in all three T-PEG mesh sizes for

QDs. In addition, blinking (periodic ON/OFF in the fluorescent emission) of QDs (Fig.2.4a) has been recorded on rare locations in the T-PEG 40k and even more frequently in T-PEG 20k and T-PEG 10k. The observations suggest: (i) Presence of structural defects, as one would assume that the QD would not have been able to penetrate the T-PEG 20k and T-PEG 10k gels, since $\xi < 2R_{h,np}$; Table 5.1); (ii) The QD diffusion time in gel has become comparable to the OFF state of the emitter. Due to blinking events, mobility data of QD from T-PEG 20k (and/or 10k) have not been included in the diffusion analysis of this thesis. Finally, positions in the T-PEG 40k gel where blinking of QD has been recorded have not been included in the diffusion analysis as well (Fig.5.1.3).

Concerning the other examined macromolecules, the larger dextrans examined seem to strongly contrast the afore-mentioned mobility trend: an almost negligible slowdown with decreasing ξ from 1.5 at $2R_{h,np}/\xi$~0.34 to 2.5 ($2R_{h,np}/\xi$~1.1) has been recorded for Dex20k (pink rhombi) and for the larger Dex70k (blue rhombi), in contrast to the stronger slowdown resolved for Dex4k (green rhombi). The qualitative trend of this counterintuitive retardation for those dextrans has been presented earlier by the corresponding $G(t)$ (Dex70k, Fig.5.1.2). So, even though the retardation for the smallest dextran examined (Dex4k, light green rhombi, Fig.5.1.3), having comparable size with A647, increases with $2R_{h,np}/\xi$, a counterintuitive diffusive trend has been observed for the next largest sizes of dextrans. The unexpected diffusion trend for dextrans with increasing dextran M_w in the Tetra-PEG gels may be attributed to the increased flexibility/compressibility of the corresponding biomacromolecules (more flexible than the relatively more compact QD). As has been recently shown by translocation studies in porous biomaterials, proteins may indeed get squeezed by increased cellular confinement or by means of increased crowding and/or by denaturing agents[174], while biopolymers (DNA) may be squeezed through nanopores [175-177], also assisted by electric fields. To aid the observations concerning dextran mobility in T-PEG, additional experiments have been performed in aqueous PEO homopolymer networks (Section II), with the intention that further information about the origin of this peculiar speed-up may be obtained.

Concerning the other macromolecules, the retardation for ssDNA (red circles) is about one third the retardation expected from the corresponding trend by the similarly sized QDs (black squares), at the same frustration ratio. The retardation of ssDNA increases from about 2.5 at $2R_{h,np}/\xi$~0.74 to 33 at $2R_{h,np}/\xi$~1.3 (T-PEG 10k), yet the population of ssDNA ($F_{slow}(\xi)$) has almost extinguished in the corresponding T-PEG 10k. Concerning the PEO (green squares), they exhibit an intermediate trend between the Dex20k (or Dex70k) and the QDs, with a minute increase in the corresponding diffusional retardation with increasing ξ. Alike the trend reported for ssDNA, the $F_{slow}(\xi)$ monotonically decreases and almost vanishes in T-PEG 10k for the following macromolecules as well: labeled PEO, Dex20k and Dex70k. In view of Fig.5.1.3, the conclusion from this section is two-fold:

first, $F_{slow}(\xi)$ decreases with increasing frustration ratio ($2R_{h,np}/\xi$) which is an evidence that T-PEG gels indeed act as efficient polymeric molecular sieves with cut-off size comparable to these macromolecules; second, solid particles exhibit different diffusion trend than flexible coils in T-PEG gels, when compared at the same value of $2R_{h,np}/\xi$.

5.4. Diffusion in homopolymer networks (PEO solutions)

Results and Discussion

The FCS experiments in T-PEG hydrogels have been reinforced by experiments of the same tracers in aqueous PEO homopolymer networks. The motivation for this section has been twofold: (a) to inspect whether the peculiar trend for Dex20k and De70k diffusion is an inherent feature of the T-PEG network structure and (b) to verify commensurability for the diffusion slowdown of QD in PEO homopolymer networks. Selected $G(t)$ for the different macromolecular tracers are presented in Figs. 5.1.4 and 5.1.5: for QD and PS-NP (Fig.5.1.4a,b), and for Dex70k (Fig.5.1.5). $G(t)$ of the tracers in water are denoted by the dashed black curve, while dashed and solid perpendicular lines denote the diffusion times from the fits, using single (n =1) and double (n =2) Fickian models, respectively. The single Fickian diffusion fit using blinking (eq.2.3.3) has been used for QD, while the hyperbolic fitting function (eq.2.3.2) has been used for PS-NP and Dex70k. The arrow in Fig.5.1.4a and 5.1.4b indicates the direction of increasing PEO concentration. A single Fickian diffusion representation of the $G(t)$ curves has been employed for QD at all PEO concentrations in this Chapter. On the other hand, for both Dex70k and for PS-NP, a double Fickian diffusion model was used at c>c*, where the fast process was attributed to the presence of unbound molecular tracer, coexisting with the macromolecule. The $G(t)$ curves for both PS-NP (Fig.5.1.4a) and QD525 nanoparticles (Fig.5.1.4b) in PEO 481k reveal an unexpected mobility slowdown in the dilute regime ($c < c^*$), where a c-independent free diffusion would have been normally anticipated for a non-interacting nanoparticle in dilute polymer solutions [59].

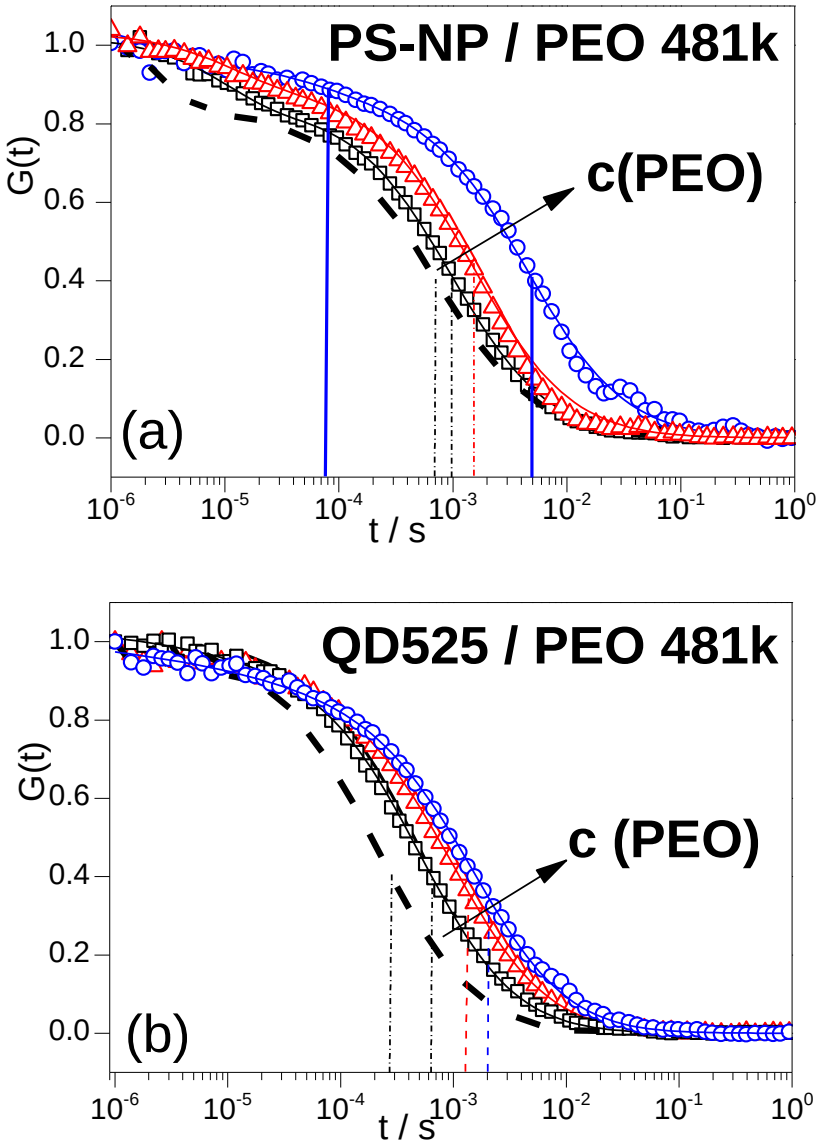

Fig.5.1.4.Normalized $G(t)$ for PS-NP (a) and QD525 (b) at three different monomer concentrations, c, in dilute aqueous solutions of PEO 481k (c^*=$1.1 \cdot 10^{-3}$ g·ml^{-1}); dashed black $G(t)$ corresponds to free diffusion in water. For PS-NP, single Fickian fits (n =1, eq.2.3.2) have been used for all displayed concentrations (c= $4.6 \cdot 10^{-5}$ g·ml^{-1}-black squares; c=$4.6 \cdot 10^{-4}$ g·ml^{-1}-red triangles) except the highest one (c = $4.6 \cdot 10^{-3}$ g·ml^{-1} -blue circles) which falls in the semidilute regime (4.6c^*). Single Fickian diffusion fits (n =1, eq.2.3.3) have been also used for QD525 at all three PEO concentrations ($4.6 \cdot 10^{-6}$ g·ml^{-1}-black squares; $4.6 \cdot 10^{-4}$ g·ml^{-1}-red triangles; $1.2 \cdot 10^{-3}$ g·ml^{-1}-blue circles). Dashed black G(t) in (a) and (b) corresponds to free diffusion in water and the arrow denotes direction of increasing PEO concentration. Vertical lines denote the extracted diffusion time from the fits at each corresponding concentration: single Fickian and double Fickian diffusion times (for PS-NP at c = $4.6 \cdot 10^{-3}$ g·ml^{-1} -blue circles) are indicated with dashed and solid vertical lines, respectively.

As the main scope of this chapter is the comparison of tracer mobilities with T-PEG, the findings in the semidilute PEO solution are first discussed in Section 5.II.1 and a rationalization of the unexpected diffusion slowdown in the dilute regime proceeds in 5.II.2. Concerning Dex70k, translational mobility was examined in dilute ($c < c^*$) and semidilute ($c > c^*$) aqueous PEO 100k solutions. The $G(t)$ curves and associated fits for selected c values, are plotted in Fig.5.1.5. The

corresponding $G(t)$ curves of Dex70k in aqueous PEO 100k solutions (Fig.5.1.5) were fitted by a single Fickian diffusion at $c < c^*$, yet crossing over to double diffusion at $c > c^*$. The increase in the system's viscosity above c^* enables diffraction-limited FCS to discriminate FITC unbound dye (fast process) coexisting with FITC-labelled Dex70k, due to the much stronger mismatch in the emerging diffusion times of the polymeric tracer compared to the free dye.

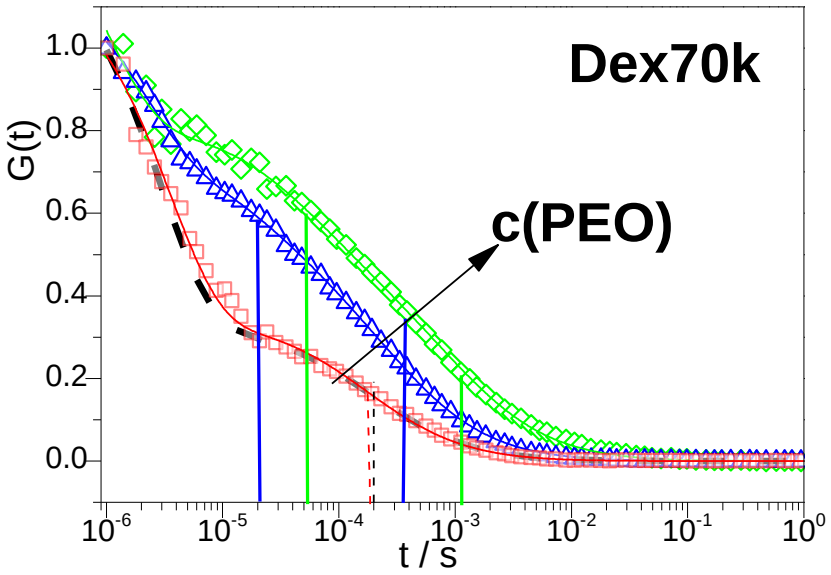

Fig.5.1.5.Normalized $G(t)$ for Dex70k in PEO 100k aqueous solutions. Single (n =1, eq.2.3.2, 2nd Chapter) Fickian diffusion time has been employed in dilute (c=7· 10^{-4} g·ml^{-1}-red squares) PEO solutions and double (n =2, eq.2.3.2) Fickian for semidilute (c>c^*; c=0.014 g·ml^{-1}-blue triangles; c=0.2 g·ml^{-1}-green rhombi) PEO solutions. Single and double Fickian diffusion times are indicated with dashed and solid vertical lines, respectively. Arrow indicates the direction of increasing PEO concentration.

The $D(c)$ values for the examined nanoparticles in aqueous (a) PEO 481k and (b) PEO 100k are first depicted in a $D(c)$ vs. c plot (Fig.5.1.6), over the examined c range below and above c^* (c^*denoted by the grey shaded region). The solid horizontal lines in (a) denote the D_0 values ($D_{0,PEO} < D_{0,PS-NP} < D_{0,QD}$) for PEO self-diffusion (black), QD (blue), PS-NP (cyan). Similarly in (b), the horizontal lines ($D_{0,PEO} < D_{0,QD} < D_{0,Dex\,70k}$) denote the D_0 values for PEO self-diffusion (black), QD (red) and Dex70k (blue). Dashed curves through the nanoparticle data in (a) and (b) are drawn to guide the eye.

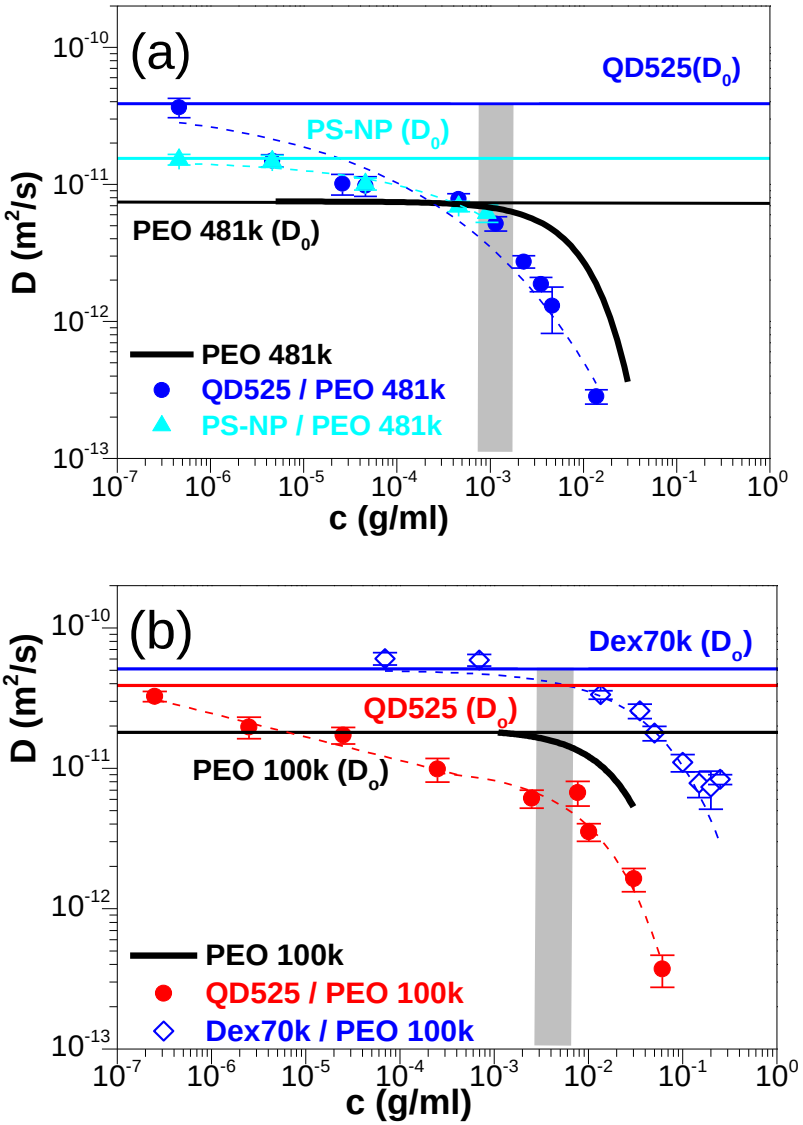

Fig.5.1.6. Tracer diffusion, $D(c)$, for (a) PS-NP (cyan triangles) and QD (blue circles) in aqueous PEO 481k solutions and for (b) QD (red circles) and Dex70k (blue rhombi) in aqueous PEO 100k solutions is shown as a function of PEO concentration, c, along with the reported self-diffusion of PEO 481k in (a) and 100k in (b) (solid black curves) [172], [173]. Solid horizontal lines denote the reported D_0 for (a) PEO 481k (black) and (b) PEO 100k (black) and the experimentally measured D_0 data for (a) QD525 (light blue) and PS-NP (dark blue) as well as for (b) QD525 (red) and Dex70k (dark blue). Shaded grey region denotes the estimated range of c^* (Table 5.1). Dashed curves through the diffusion data are curves to guide the eye.

Section 5.II.1 begins with the discussion of the mobility findings in the semidilute regime, in view of the $D(c)$ vs. c plot (Fig.5.1.6). Later on, different scaling options for the diffusion are presented, expressed either vs. c/c^* (Fig.5.1.7) or vs. ξ (Fig.5.1.8), where ξ is the correlation length of the semidilute polymer solution. The aim is to assess the validity of these approaches with respect to the scaling of nanoparticle mobility data in polymer solutions.

1. Semidilute regime

Even though $D_{0,PEO} < D_{0,PS-NP} < D_{0,QD}$, the diffusion coefficient, $D(c)$, of both PS-NP (Fig.5.1.6a) and QD(Fig.5.1.6b) at the same $c > c^*$ is smaller compared to the corresponding $D_{PEO}(c)$ [172, 173].

Moreover, $D(c)$ values of both PS-NP and QD, although originating from different D_0, seem to merge with increasing c. Likewise: $D_{0,PEO} < D_{0,QD} < D_{0,Dex\,70k}$, in Fig.5.1.6b. In consistency with its slowdown trend in PEO 481k, the mobility of QD is slower compared to the corresponding polymer (PEO 100k) at the same c, for almost all c examined. Based on Fig.5.1.6, the single Fickian diffusion for both QD and PS-NP tracers becomes slower compared to the polymer self-diffusion (at the same $c > c^*$).

From scaling theory of polymers [9], it is known that c^* (eq. 1.2.8)-and hence c/c^*, exhibits polymer M_w dependence. To examine such a scaling for the observed nanoparticle slowdown, Fig.5.1.7 displays D/D_0 vs c/c^* for the two nanoparticles and Dex70k using the associated c^* values listed in Table 5.1. Superposition of nanoparticle diffusion data on a single (same) curve would hold, when the slowdown is polymer M_w dependent, captured by the scaling of c^*. Moreover, such superposition of polymer self-diffusion vs. c/c^* would suggest that the slowdown scales with the solution viscosity, η. Data from recent works are also plotted in Fig.5.1.7 for comparison. This includes (Fig.5.1.7a) diffusion data for Au-NP spheres with 5nm (triangles) and 10nm size (crosses) in semidilute aqueous PEO 5k (orange) and 35k (black) solutions [178], as well as (in Fig.5.1.7b) data for PS-NP (20nm size) in both PEO 100k (red polygons) and PEO 300k (blue polygons) solutions [68]. The dashed black curve in Fig.5.1.7a represents a "master curve", onto which the diffusion slowdown values $D(c/c^*)/D_0$ of different non-interacting PS chains in polymer solutions at good solvency superimpose when plotted vs. c/c^*[111].The corresponding fit has the following stretched exponential form (eq.1.5.15):

$$D(c/c^*)/D_0 = e^{-\boldsymbol{\gamma}^* \cdot (c/c^*)^{\boldsymbol{u}}} \qquad (5.2)$$

The dashed black curve shown in Fig.5.1.7, is the one recently reported elsewhere [111], with parameter values: $\boldsymbol{\gamma}^*$=0.84 and $\boldsymbol{u}$=0.74. Likewise, eq.5.2. was used to fit Dex70k data (dashed blue curve) with the following parameter values: $\boldsymbol{\gamma}^*$=0.20 and $\boldsymbol{u}$=0.69. The values of $\boldsymbol{\gamma}^*$ are unsimilar between the two systems, in contrast to the similar values in $\boldsymbol{u}$. There is no consensus regarding the physical meaning of this useful parametrization. According to Phillies [179], the parameters $\boldsymbol{\gamma}^*$ and u are related with polymer M_w and polymer solvency, respectively. On the other hand, in scaling relations from de Gennes [9], $\boldsymbol{\gamma}^*$ and $\boldsymbol{u}$ are interpreted as topology (ξ-related) and scaling parameters, accordingly.

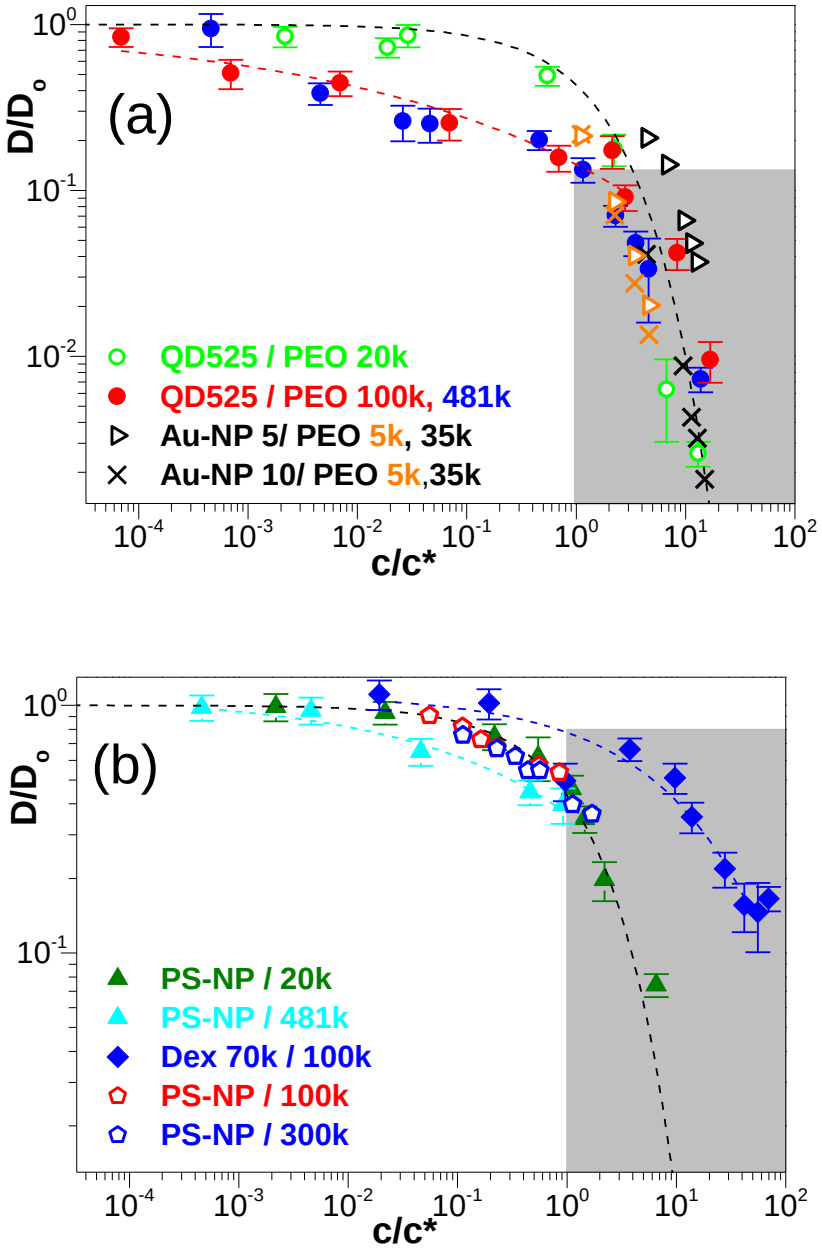

Fig.5.1.7. (a): Tracer diffusion slowdown ($D(c/c^*)/D_0$) for (a) QD525 (circles) and (b) Dex70k (blue rhombi) and PS-NP (green and cyan triangles) in aqueous solutions of PEO with different PEO M_w (present work). Tracer diffusion data from literature includes in (a): Au-NP (5 nm) in 5k (orange triangles) and in 35k PEO (black triangles), Au-NP (10nm) in 5k (orange crosses) and 35k (black crosses) PEO semidilute aqueous [178]; and in (b): PS-NP in 100k (red polygons) and in 300k (blue polygons) PEO aqueous solutions [68]. Dashed curves through the data are stretched exponential curves. Grey-highlighted region denotes the onset of semidilute solution.

Concerning the superposition on a $D(c/c^*)/D_0$ plot, the dependence over c/c^* in the semidilute regime ($c > c^*$) in Fig.5.1.7 and the comparison with Fig.5.1.6 reveals two main trends for the QD, PS-NP and the dextran: (i) the QD slowdown superimposes for the two PEO M_w (100k, 481k) while the reported data for Au-NP are relatively scattered in spite of a coarse superposition between the Au-NP data and the locus of the QD slowdown; (ii) the dextran in PEO M_w 100k scales with c/c^* but

with less severe diffusion slowdown as compared to the PS-NP data and the slowdown of PS chains in PS homopolymer solutions (dashed black curve).

On trend (i), diffusion slowdown data for PS-NP with 20nm size has already been reported from Phillies et al. [68] in both PEO 300k (blue polygons) and PEO 100k (red polygons) aqueous solutions. The afore-mentioned dataset, as well as the slowdown trend for PS-NP in PEO 20k (green triangles) superimpose on a representation vs. c/c^*(Fig.5.1.7b), suggesting dependency over η (solution's viscosity). Its dependency can be captured by the N dependency of c^* (eq.1.2.8), while the particle size-dependence is encountered by the D/D_0 normalization. Nevertheless, the particular offset in PS-NP diffusion slowdown at the same c/c^* between PEO 481k (cyan triangles) solutions and the locus of reported PS-NP data in Fig.5.1.7b might be due to the different type of PS-NP examined in each case, leading to different strength of tracer-polymer interactions. In addition, the scaling relations from theory [59] suggest no slowdown for non-interacting nanoparticles at $c < c^*$. Additional contributions in this mismatch of slowdown may be due to different sensitivities in the methods employed (FCS vs. light scattering [68]) and/or to the fact that some inaccuracy may exist concerning the estimated D_0 values in the reported PS-NP data. The explicit D_0 values have not been available from the authors [68].

On trend (ii), Dex70k exhibits practically no slowdown at $c < c^*$ (Fig.5.1.7b) in aqueous PEO 100k solutions, while in the semidilute regime it slows down, yet on a much weaker fashion compared to both QD (Fig.5.1.7a) and PS-NP slowdown (Fig.5.1.7b) at the same c/c^*. In a related FRAP paper[180], a comparison between the Dex70k and PS-NP diffusion led to the assertion that the lower fractal dimension of the former tracer could allow for larger compressibility and less constrained mobility through semidilute solutions, compared to the relatively more compact PS-NP. This conjecture, however, does account for the deviation of the Dex70k diffusion from the tracer diffusion of PS chains (dashed black line in Fig.5.1.7).This positive offset for Dex70k slowdown in aqueous PEO solutions compared to the master curve for non-interacting macromolecular excludes the presence of Dex70k-PEO attractive interactions. Additionally, this diffusion slowdown trend of Dex70k in semidilute PEO solutions does not contradict the analogous mobility resolved for Dex70k diffusion in T-PEG gels (Section I).It might relate in a still unclear mechanism on the impact of confinement in dextran mobility.

In view of possible superposition approaches of the tracer diffusion in crowded systems and in the absence of interactions, Fig.5.1.7 indicates that the attempt for a single master curve vs. c/c^* is partially successful and seems to be tracer-dependent. The simple alternative depiction of $D(c)/D_0$ vs. c applies for the diffusion slowdown for non-interacting *molecular* tracers ($R_{h,np}$~1nm) in polymer solutions at good solvency, using either organic [111] or aqueous solvents [112],[181],

where a superimposition on a single stretched exponential slowdown curve is achieved. There is consensus about this simple crowding effect for molecular tracers [111] which has been verified by the slowdown of non-interacting A647 (not shown), present as internal standard together with either QD or PS-NP. As already mentioned (Section 5.II.1), different scaling attempts have been examined for the nanoparticle diffusion slowdown. The reason for that has been to investigate possible dependence on the degree of polymerization (N), or on topological features with a mesh size, ξ. In a different scaling attempt vs. ξ, supported by several groups[9],[182], superposition of the diffusion slowdown, $D(c)/D_0$, on the same curve will imply N–independent slowdown, since ξ (eq.1.2.9,) depends only on concentration.

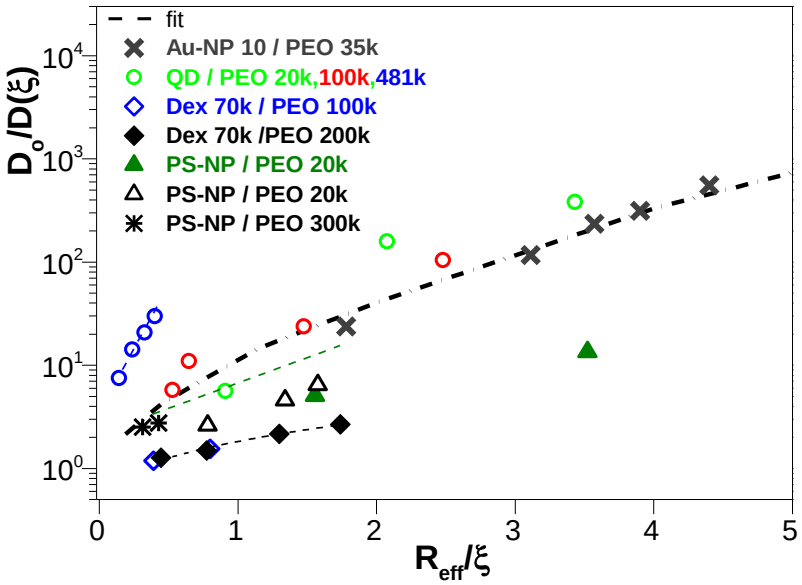

Fig.5.1.8. Retardation of nanoparticle diffusion, $D_0/D(\xi)$, plotted as a function of frustration ratio, R_{eff}/ξ, in semidilute polymer solutions, for: (a) QD525 in PEO 20k (green circles), PEO 100k (red circles) and PEO 481k (blue circles); (b) Dex70k (blue rhombi) in aqueous PEO 100k; (c) Dex70k (black rhombi) in aqueous PEO 200k [180]; (d) PS-NP in PEO 20k aqueous solutions (green triangles); (e) PS-NP in aqueous PEO 20k and 300k (black triangles and stars)[68] and (f) Au-NP of 10 nm size (grey crosses) in aqueous PEO 35k [178]. Dashed curves through the data are drawn to guide the eye. The dash-dotted black curve denotes the semiempirical scaling curve [125].

The retardation of diffusion, D_0/D, for the examined nanoparticles is compared in Fig.5.1.8 with reported data for various tracers, all in aqueous PEO solutions, expressed vs. R_{eff}/ξ [68, 125, 178, 180]. In the latter case: $R_{eff}^{-2} = R_{h,np}^{-2} + R_H^{-2}$, where $R_{h,np}$ is the nanoparticle's radius and R_H is the hydrodynamic radius of the polymer. It has been reported in some recent experimental works that superposition on a single curve (dashed-dotted black curve, Fig.5.1.8) vs. R_{eff}/ξ [125, 178] holds, concerning the diffusion retardation of molecular tracers and PS-NP in semidilute aqueous PEO solutions, in the M_w range from 0.4k to 8000k, irrespective of PEO M_w. This curve is described by the following semiempirical relation (Fig.5.1.8, dashed black curve) in aqueous PEO solutions [125]:

$$\eta/\eta_s = D_0/D(c) = (R_{eff}/\xi)^{0.62} \quad (5.3)$$

Eq. 5.3. describes that a diffusing particle, can either experience the nanoviscosity ($R_{h,np} < R_H$) or the solution's macroviscosity ($R_{h,np} > R_H$), depending on the tracer-polymer size ratio [125]. According to the authors[125], superposition is expected to hold for any type of particle in aqueous PEO solutions, having generalized their conclusions by successful superposition of the following tracers, differing in types and sizes: molecular fluorescent tracers (1nm size), lysozyme (4nm size) and PS latex (PS-NP) nanoparticles (25nm size). Even though this semiempirical diffusive trend (eq. 5.3) may additionally fit to certain extent the reported mobility data for Au-NP (grey crosses) in aqueous PEO 35 k solutions [178] and seemingly well the QD diffusion in aqueous PEO 100k solutions (red circles), significant deviations from the semi-empirical diffusive trend (dash-dotted black curve) have been recorded : (i) QD in PEO 481k (blue circles)-strong positive deviations from the trend; (ii) Weak negative deviations for PS-NP in PEO 20k (green triangles) and for reported data [68] for PS-NP in PEO 20k (black triangles) aqueous solutions, when $R_{eff}/\xi \geq 0.5$; (iii) Strong negative deviations for Dex70k in PEO 100k (blue rhombi) and Dex70k in PEO 200k (black rhombi) [180] in aqueous PEO solutions. As a concluding remark, a shortcoming of this approach is the involvement of the polymer size (R_g or R_H) i.e. suggesting a matrix molecular weight dependence in semidilute solutions, while a physical network (semidilute solution) is formed with the only relevant length being ξ. Involvement of R_g is self-inconsistent with the proposed eq. 5.3, which correctly predicts only c-dependence in addition to the explicit tracer size (R_{eff}) dependence. This is probably one of the reasons of polymer specificity in Fig.5.1.8. On the contrary, the presentation of Fig.5.1.7 implies N-dependence (via c^*) but assumes a tracer–size independence. Based on the present state-of-the-art, tracer diffusion in complex crowded media is still not understood.

2. Dilute regime

This section addresses the unexpected single Fickian slowdown in the dilute PEO regime ($c \ll c^*$) observed for both PS-NP and QD in PEO 481k ($G(t)$ in Fig.5.1.4). The chain connectivity effect can be qualitatively visualized in Fig. 5.1.9, where $G(t)$ curves for QD and PS-NP are presented at the same c ($< c^*$), yet at different M_w of PEO.

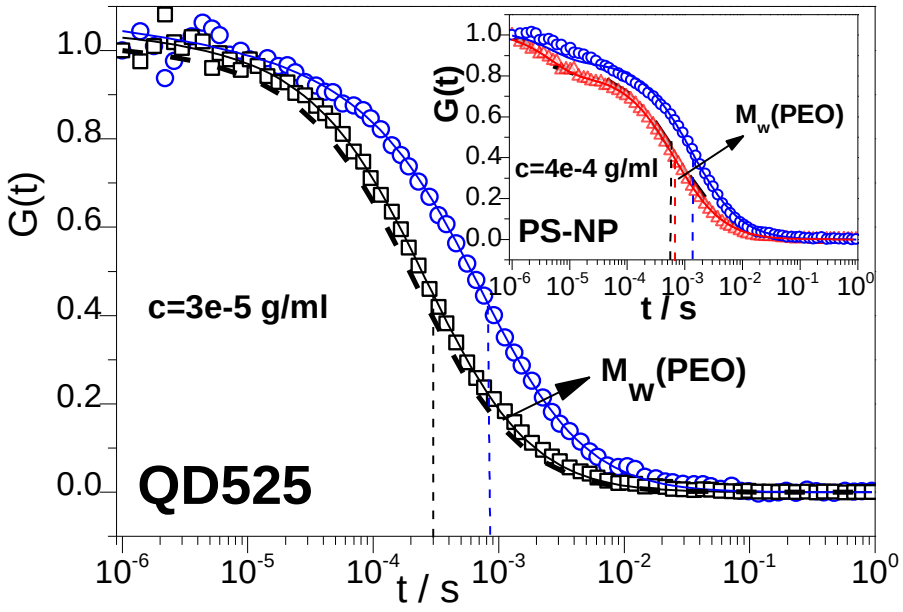

Fig.5.1.9. Normalized $G(t)$, for QD (PEO 20k-black squares; PEO 481k-blue circles) and PS-NP (PEO 20k-red triangles; PEO 481k-blue circles) in dilute aqueous PEO solutions well below c* (at c =3·10^{-5} g·ml^{-1} for QD; at c =4·10^{-4} g·ml^{-1} for PS-NP). The thick black-dashed $G(t)$ corresponds to QD525 diffusion in water (main plot), while the dashed black $G(t)$ corresponds to PS diffusion in water (inset). Vertical dashed lines denote the single Fickian diffusion time extracted from the fit at the corresponding $G(t)$ denoted by the same color. Arrows denote direction of increasing PEO M_w.

A clear polymer M_w effect (Fig.5.1.9) can be observed in the corresponding $G(t)$ of QD (main plot; c=3·10^{-5} g·ml^{-1}) and PS-NP (inset; c=4·10^{-4} g·ml^{-1}), although a recent theory for nonsticky nanoparticles in polymer solutions [59] predicts no slowdown at $c < c^*$. In the dilute regime ($c < c^*$), the polymer self-diffusion is c-independent as exemplified by Dex70K diffusion in Fig.5.1.6b. On account of the following observations from Fig. 5.1.7: (i) QD superposition vs. c/c^* for PEO 100k and 481k, yet not for PEO 20k (at $c < c^*$); (ii) lack of superposition for PS slowdown in PEO 20k and 481k;(iii) stronger offset in slowdown for QD between PEO 20k and 481k compared to PS-NP between PEO 20k and 481k, the conclusion is drawn that a polymer M_w effect is present on the corresponding slowdown for both QD525 (strongly) and PS-NP (less strongly) diffusion in ultradilute PEO solutions. Based on these observations, the conclusion is that chain connectivity matters for both QD and PS-NP diffusion in ultradilute aqueous PEO solutions, implying a dynamic association of a single particle per polymer coil. To support this conjecture, the ratio of particles per individual chains in dilute PEO solutions has been estimated. Using an approximate value for the FCS detection volume (V_{FCS} ≈2.8·10^{-16}L), the number of fluorescent tracers present in V_{FCS} can be resolved. The number of chains can be calculated by the ratio of chains present in V_{FCS}, over the total chain number in the given PEO concentrations of the prepared solution. Hence, the following fluorescent tracer/polymer chain ratios are displayed: about 3/1000 at c=4·10^{-7}g ml^{-1}(=4·10^{-4} c*) and 1/10^6 at c=1.1·10^{-3}g ml^{-1}(= c*).

To unravel further conclusions, it is stressed that similar to the ultradilute single Fickian slowdown of QD and PS-NP in aqueous PEO solutions, single Fickian slowdown has also been resolved for QD diffusion in ultradilute PNiPAAm aqueous solutions (3rd Chapter), where simulations have revealed an effective single Fickian diffusion, $\mathrm{D_{eff}(c)}$ [112] with a QD-PNiPAAm attractive strength of $2\,\mathrm{k_B}\cdot\mathrm{T}$ [112]. MD simulations have revealed that the bound and free diffusion states for the diffusing QD get averaged out before the tracer leaves the FCS illumination spot (Fig.3.8), thus yielding the experimentally resolved single diffusion coefficient, $\mathrm{D_{eff}(c)}$.In the same study was additionally shown that a slight increase in attractive strength ($2.5\,\mathrm{k_B}\cdot\mathrm{T}$), regardless of tracer size, would enable the experimental resolution of double Fickian diffusion (case of Rh6G in dilute PNiPAAm solutions) by FCS [112]. The conveyed message on account of the similarity between the single Fickian QD slowdown in dilute PNiPAAm solution and the resolved single Fickian diffusion in dilute aqueous PEO solutions for both QD and PS-NP (present chapter), implies that the intrinsic length scales of bound and free diffusion in this Chapter are also smaller than the dimensions of the diffraction limited FCS illumination spot [107, 112]. As such, the bound and free diffusion states for the diffusing nanoparticle most likely get averaged out before the tracer leaves the FCS illumination spot. Therefore, the only preliminary hypothesis would be that the strength of tracer-PEO attractive interactions are system-specific, being different for QD than for PS-NP at the same concentration. Moreover, such ultradilute QD-PEO and PS-NP with PEO interactions seem to wear off with the onset of semidilute solutions, as the slowdown (vs. $\mathrm{c/c^*}$) coarsely agrees with DLS findings for the mobility of non-interacting Au-NP [178] in semidilute PEO 5k and 35k aqueous solutions. It is noted that the authors of the last work claim agreement with a seminal theoretical work for mobility of nonsticky nanoparticles, at $\mathrm{c} > \mathrm{c^*}$[59].

To investigate possible influence of electrostatics in the QD diffusion ultradilute slowdown, monovalent salt (I=5mM KNO_3) was added in dilute aqueous solutions of both PEO 100k and PEO 481k. The diffusion slowdown for the QD nanoparticles was practically unaltered before and after addition of monovalent salt (I=5mM KNO_3, with screened Debye length: $\mathrm{K^{-1}} \cong 4\,\mathrm{nm}$). In fact, this is not unexpected, since PEO is a rather uncharged polymer. Phillies et al. [68] have also reported a like ultradilute slowdown for PS-NP of 20nm size, in aqueous solutions of different PEO $\mathrm{M_w}$ (20k, 100k, 300k), without accompanying their ultradilute slowdown observations with an explicit physical model. Yet, the authors have provided arguments [68] that such slowdown can wear off and eventually extinguish by slight addition of a nonionic surfactant (Triton-X) or a chaotropic salt ($MgSO_4$). Both suggestions from Phillies et al. have been employed in the present thesis, to investigate whether the slowdown for the QD in ultradilute PEO 481k solutions would disappear or not. Nevertheless, the ultradilute slowdown was still present.

In contrast to the substantial diffusion slowdown for QD particles in ultradilute PEO solutions, relatively weaker slowdown has been recorded for the (relatively larger) PS-NP in aqueous solutions of PEO 20k and PEO 481k (Fig.5.1.7b) at the same c/c^*. The reported mismatch in strength of such tracer-polymer interactions (stronger for QD) may relate with the different surface functionalization, thus regulating the particular nanoparticle affinities to the PEO: QD have carboxylic acid surface modification, whereas PS particles have sulfate groups. A hypothesis maybe that possible mismatch in acidic strength (different dissociation constants, pK_a), may lead to differences in induced dipole interactions between PEO and each type of the examined nanoparticles, thus possibly rationalizing the observed differences in slowdown (i.e. in PEO 481k).Even though the exact underlying mechanism behind the diffusion slowdown of QD or PS-NP particles has not been revealed, the findings in this section have been a rich platform to stimulate fruitful discussions with theoreticians, concerning the validity of the afore-mentioned slowdown scenarios and the underlying nature of tracer-PEO interactions. In any case, the control of tracer mobility in dilute polymer solutions is extremely important for both polymer physical and bio-related aspects.

5.5. Effect of permanent crosslinks in ideal aqueous polymer networks

Combining diffusion slowdown from T-PEG hydrogels and aqueous PEO solutions on a single plot, assists to clearly visualize the effect of permanent crosslink on QDs and Dex70k mobility. Frustration ratios,$2R_{h,np}/\xi$**,** for homopolymer networks have been obtained from the mesh size in semidilute unentangled polymer solutions under good solvency conditions, using well-known scaling relations [9]. The permanent crosslink effect on the diffusional retardation (Fig.5.1.10) is expressed differently on account of the given tracer type. Lines have been drawn through the data to guide the eye, namely for (i) QD in T-PEG (solid black line); (ii) QD in semidilute PEO solutions (dashed black and red line); (iii) for Dex70k (solid blue rhombi) in T-PEG (dash-dotted blue line); (iv) Dex 70k (empty blue rhombi) in semidilute PEO solutions (dashed blue line). An additional dash-dotted black line has been drawn at ($D_0/D(\xi)\sim1$), as a reference for the eyes.

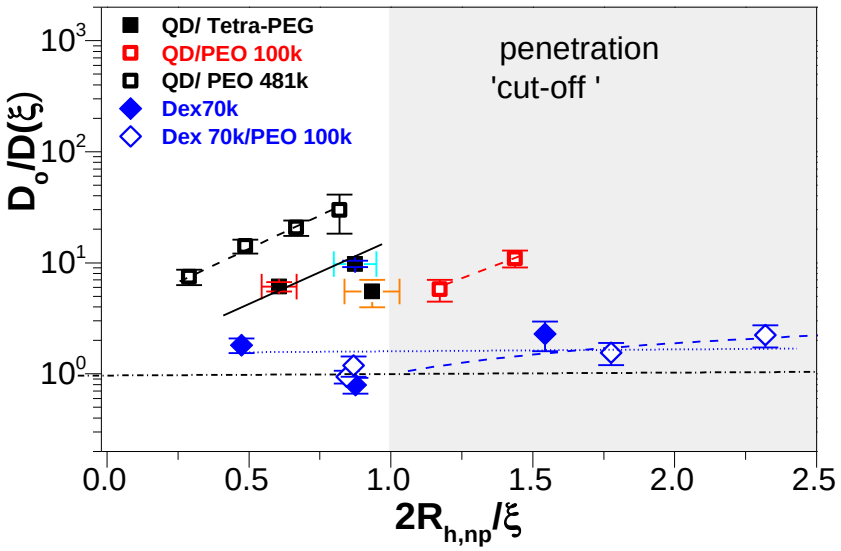

Fig.5.1.10. Effect of permanent crosslink: Diffusional retardation $D_0/D(\xi)$ vs. frustration ratio ($2R_{h,np}/\xi$) for: Dex70k (blue rhombi) in all three M_w of T-PEG; QDs in T-PEG 40k (black squares); Dex70k in semidilute aqueous PEO 100k solutions (open blue rhombi); QD525 in semidilute aqueous solutions of PEO 100k (red empty squares) and PEO 481k (black empty squares). Grey-shaded zone denotes region of -presumably - no penetration of hard sphere (assumption).

The QDs in PEO 481k and PEO 100k experience the same qualitative scaling trend (slope) with the different QDs examined in T-PEG 40k. Astonishingly, however, the QD diffusion retardation (at the same $2R_{h,np}/\xi$) in PEO 481k semidilute solutions is about two times stronger than in T-PEG gels (Fig.5.1.10). However, this comparison of diffusional retardation appears PEO M_w-dependent, as the QD retardation in PEO 100k (red squares) is weaker, compared to the analogous trend resolved in T-PEG hydrogel. The QD525 retardation in T-PEG 40k compared to the QD retardation in PEO 100k homopolymer is approximately the same ($D_0/D(\xi) \approx 6$), although resolved at twice as much frustration ratios in the latter case ($2R_{h,np}/\xi \approx 1.2$). Apart from further evidence on QD-PEO interactions discussed in Section 5.II, the observed differences may originate from topological differences in the two types of networks. Nevertheless, to unravel such structural differences, the frustration ratio alone is not a necessary condition as can be seen by the failure of a superposition in the mobility data of the examined tracers in the plot of Fig. 5.1.10. Further rationalization for the comparison of QD mobility comparison (in T-PEG vs. PEO), in particular, may be further supported by simulations or further sub-diffraction FCS experiments [102]. Finally, mobility of QD in T-PEG networks has been limited to frustration ratios ($2R_{h,np}/\xi \leq 1$, to avoid artifacts from blinking and trapping events. It should be also stressed that the QDs experience weaker retardation compared with the macromolecular tracer diffusion in other gels reported from different groups (BSA diffusion in either PVA hydrogels [183] or in PEG gels [124]) at the same $2R_{h,np}/\xi$, suggesting that interactions probably present in those works are stronger than that between QDs and Tetra-PEG in the present thesis.

Finally, a link may exist between the weaker slowdown for Dex70k in semidilute PEO solutions vs. the analogous slowdown for non-interacting polymer chains in polymer solutions (Fig.5.1.7) and the peculiar retardation of Dex20k and Dex70k in T-PEG. It might thus be useful to review recent works reporting on induced protein compressibility with increasing crowding conditions in cells that may provide further support [174]. It is possible that at least one of the following mechanisms underlies Dex70k mobility: hydrodynamics and/or cooperative dynamics of the semidilute homopolymer network [63-65]. Concerning size-fractionation (filtration) of an initially polydisperse dextran in T-PEG as another reason for the relatively weak retardation of dextrans, the polydispersity values reported from the manufacturer concerning the examined dextrans are not that broad to suggest fractionation as a probable scenario[184], yet it is a non-negligible possibility. If fractionation is proven as the reason for such counterintuitive mobility trend, then this would imply that diffraction-limited FCS cannot deconvolve the different coexisting dextran sizes for a given 'nominal' M_w of commercially available dextran. A physical description by a model and/or simulations would be of precious help.

5.6. Chapter's conclusions / Outlook

The controllable tuning of penetrant's mobility in polymer networks is highly important for a large number of bio-inspired applications. FCS has been applied to study the diffusion of tracers varying in size, type and emission features in an ideal crosslinked polymer hydrogel of pronounced mesh size homogeneity. By selecting these particular diffusants, the purpose of this experiment has been to constitute a model study, according to which future studies of tracer diffusion in gels may be compared with. The diffusion studies in Tetra-PEG gels have shown that non-interacting molecular tracers and quantum dots do indeed exhibit slowdown with increasing confinement. On the contrary, the softer dextran, having comparable size to the quantum dots, has shown weaker slowdown with increasing frustration. In addition, the dextran slowdown does not differentiate between T-PEG hydrogels and PEO solutions. This represents a major highlight of the T-PEG experiment. It seems that the mobility of solid nanoparticles can scale with frustration ratio; this was not the case for flexible coils (dextrans), where commensurate conformation fluctuations with T-PEG strand dynamics might also be important.

Concerning the diffusion in the absence of permanent crosslinks, exemplified by PEO homopolymer physical networks, three different scaling attempts have been employed to represent the diffusion slowdown of all examined nanoparticles (Dex70k, QD, PS-NP). They involve scaling: (i) with concentration (c); $D(c)$ applies for the diffusion slowdown for non-interacting molecular tracers

($R_{h,np}$~1nm). (ii) with c/c^*~$N^{3\nu-1}$; This superposition on a single master curve, which would suggest dependence on polymer M_w, seems to be system dependent and (iii) with the network topology (ξ~N^0), depending on the tracer size, $R_{H,np}$. The last superposition attempt for diffusion does not work, evidenced by the system specificity of the different $D_0/D(\xi)$ vs. R_{eff}/ξ curves in Fig.5.1.8. As such, a more reliable information about nanoparticle slowdown may be safely extracted from the scaling vs. c/c^*).

The additional highlight of this chapter has been the effective single Fickian nanoparticle slowdown revealed in ultradilute PEO solutions, by both QDs and PS particles, suggesting presence of tracer-PEO attractions. Theory for the mobility of non-interacting nanoparticles in polymer solutions, however, suggests absence of slowdown in the dilute regime ($D(c)=D_0$).The clear association the tracer slowdown with the individual PEO coils below c* can imply wrapping of a single polymer chain around a single sticky nanoparticle and not sticking of multiple PEO chains on the nanoparticle, on account of the superposition vs. c/c^* of the slowdown for the examined nanoparticles. Currently, efforts are undertaken to support the above findings with analytical theory (3rd Chapter).

Chapter 6: Concluding remarks

The findings from the thesis suggest that *tracer-polymer interactions* may exist even for molecular tracer diffusants, in the simplified case of dilute polymer solutions at good solvency. Under such conditions, combination of molecular dynamics simulations with Fluorescence Correlation Spectroscopy (FCS) experiments has shown that deviations from single Fickian diffusion in molecular tracer dynamics due to specific interactions can only be resolved by FCS, when the intrinsic length scales are larger than the resolution length scale. Due to the dynamic binding of Rh6G tracer to a polymer coil, it was found that chain connectivity matters, even though the Rh6G-PNiPAAm hydrophobic interactions have predominantly short-range nature.

With increased network complexity in thermoresponsive PNiPAAm hydrogels, tracer mobility becomes interdependent upon several mutually coupled parameters: tracer-polymer interaction strength, presence of permanent crosslinks, solvency and influence from external stimuli, such as salt and temperature. A proper strategy of decoupling the influence on tracer mobility from those parameters would enable to elucidate the nature of host-guest interactions, as well as the relation between network's swelling features and tracer mobilities.

In good solvency conditions, the onset of permanent crosslinks was found to exert distinct tracer diffusion slowdown on account of the different molecular tracer-PNiPAAm interactions. The employed Fickian diffusion fit of the labeled antibody IgG in crosslinked PNiPAAm grafted hydrogel layers depends critically on the employed crosslink density, at good solvency conditions. The nature of different molecular tracer-PNiPAAm interactions has been revealed: Rh6G-PNiPAAm interactions are predominantly hydrophobic, while for A488 electrostatic repulsions are significant. Remarkably, the more weakly interacting A488 was found to be a more sensitive probe of the network topology than the strongly interacting Rh6G. Using double Fickian diffusion fits for either A488 or Rh6G mobilities in hydrogels, the diffusion slowdown of the fast component was found to agree with earlier predictions from a master curve for non-interacting molecular tracers in hydrogels, while the slow component becomes ϕ-independent at $\phi > 0.1$. Moreover, the arrest in diffusion slowdown observed in permanent networks for Rh6G at good solvency, implies the simultaneous action of different competing mechanisms, among which osmotic, electrostatic and possibly short-range forces.

By perturbing the network with external stimuli, it was shown that the dynamics in the collapsed state depend on the external stimulus used; although interdependent properties, one may not predict tracer dynamics solely from the response of the network's swelling ratio, and vice versa. The coupling of friction, interactions and structural changes render a superposition of tracer mobilities

and predictability of mobilities on either ϕ or T a formidable task. At the thermally collapsed state (33°C), it was concluded that IgG could not penetrate the hydrogel.

In contrast to the PNiPAAm hydrogels with broad mesh size distribution, the uniformity of their mesh size in T-PEG networks renders the latter an ideal hydrogel platform to study diffusion slowdown and compare to other diffusion studies in hydrogels. Using FCS, flexible macromolecules were found to exhibit weaker diffusion slowdown as compared to solid spherical nanoparticles, at the same frustration ratio, in the ideal T-PEG hydrogels. This is commensurable with the distinct diffusion slowdown trend of these tracers in the homologous PEO homopolymer networks, suggesting that fluctuations of T-PEG network strands might be significant. The importance of FCS in studying mobility in polymer networks has been demonstrated by the novel information and insights into scalability of the nanoparticle diffusion slowdown in terms of reduced physical parameters, as follows:

(i) By providing strong evidence for the presence of tracer-polymer interactions in dilute polymer solutions, yet by an effective single Fickian diffusion. This chain length dependent slowdown is in contrast to the anticipated –from scaling theory- concentration independent mobility for non-interacting nanoparticles.

(ii) By examining tracer mobility in aqueous PEO solutions, it is suggested that no universal scaling relation exists, concerning the nanoparticle diffusion slowdown.

(iii) The slowdown for molecular tracers scales different (vs. c) than for nanoparticles and also the nanoparticle diffusion slowdown is system-specific; a recently reported scaling attempt vs. ξ does not universally hold.

Complex tracer dynamics in polymer networks may be distinctly expressed by FCS, depending on the specific synergy among differences in -at least some of the following: nature of interactions, external stimuli employed, tracer size and type, crosslink density and swelling ratio (mesh size).

Open questions/Outlook

Certain open questions have been born from the results discussed in this thesis and are presented below:

(i) The presence of stronger diffusion slowdown for the slow component for interacting molecular tracers in aqueous PNiPAAm solutions, compared to crosslinked hydrogels, at the same monomer concentration, in good solvency conditions. To seek an answer, further support from both sub-diffraction limited FCS (STED-FCS) experiments and simulations is needed. By seeking support to that direction, one would be able to also shine light in the answer to the question of ‘what is the physical significance of the 2nd, slow process in grafted PNiPAAm hydrogels, for A488 and Rh6G, when

employing a double Fickian diffusion model?' One should first bypass the present experimental limitation concerning the resolution along the axial direction for such sub-diffraction correlation spectroscopy.

(ii) To illustrate the physical mechanisms that take place during network's collapse and the decrease of the interacting fraction of A488, when electrostatic repulsions are screened, while no crowding/collapsing effects have come into play. The seemingly helpful direction would be again to seek support from simulation and/or super-resolution spectroscopic techniques. A successful answer would allow scrutinizing parameters controlling analyte immobilization in stimulus-responsive biosensor platforms.

So far, suggestions for the following experiments as an outlook have been proposed, in three directions:

(i) First, the idea was born to combine FCS with electron paramagnetic resonance (EPR) spectroscopy using the very same molecular tracer. The goal has been to unravel simultaneous influence of rotational dynamics apart from the translational dynamics, on the corresponding tracer's mobility, in thermoresponsive matrices (either PNiPAAm crosslinked hydrogels, or aqueous solutions of pluronic surfactants). In fact, efforts have been carried out to control the synthesis of a hybridized tracer, namely A488 coupled with a standard radical used in EPR experiments, 4-amino-TEMPO.

(ii) Second, based on the preliminary findings concerning IgG mobility in grafted PNiPAAm hydrogel layers (section III, 4th Chapter), to extend the investigation of antibody mobility in protein-functionalized hydrogel layers.

(iii) Concerning the T-PEG study, new sets of FCS experiments have been designed, regarding PEO self-diffusion in PEO homopolymer solutions, as well as diffusion of free dye (i.e. fluorescein isothiocyanate) in T-PEG networks. The former study would most probably verify commensurability of the existing findings for dextran in T-PEG and labeled PEO, while the latter would exclude any possibility that such trend comes from an interacting free dye (instead of the dextran itself).

My sincere hope is that the present findings may be a slight perturbation (!) towards enhancing our current knowledge in the vast field of what controls tracer diffusion in responsive polymer networks in general, benefitting both fundamental research as well as hopefully aiding analyte sensing applications.

Acknowledgments

At first, I need to express my deep and thankful appreciation and respect to my advisors. In particular, I would like to deeply thank first Prof. XXXX as my employer, for giving me the opportunity to work in his group for 3 years. It has been a memorable period in one of the best groups one could ever be, full of stimulating discussions. I am also sincerely grateful to my project leader Dr. XXXX, by whom I learnt a lot concerning theory and applications of the FCS technique. His support has been reflected in many ways to me and has been really helpful, being both a supervisor and a friend for me (XXXX, many thanx!). Last but not least, my deep cordial wishes are reserved for Professor XXXX. Anything I might say is scarce, to express my deep appreciation to and respect for him. He has been a Mentor, coach and friend (in various aspects) during this 3 year period. His rich experience, systematic academic approach, lust for research and appreciation of both 'machine' and 'human' aspect of his coworkers has been reflected in the series of successful graduates by him, hopefully me belonging to that 'family tree', as well (ευχαριστώ θερμά για όλα, Δάσκαλε!!). I have also had the honor to collaborate with some-of the very best- theory groups, concerning simulational support in various projects. Specifically, deep thankful wishes for Prof. Dr. XXXX (ICP Stuttgart) and Dr. XXXX (ICP Stuttgart & Uni Prague, Czech Republic) for their friendship and a successful trilogy (or more) of beautiful hydrogel stories, as well as support and friendship/djakuje! To my belief, there is no better theory group concerning FCS and polyelectrolytes and I enjoy a lot discussing with Prof. Holm and Peter. I am indebted to Mr. XXXX (Vielen Dank, Herr XXXX, daß Sie immer so hilfsbereit sind!) for the diligent training, the frequent troubleshooting and the SOS discussions related with FCS. We are all lucky to have been trained by you and the FCS subgroup owes a lot to you! I am grateful to Prof. Dr. XXXX (Uni Siegen/FORTH-Heraklion, Crete) for chemistry-related discussions, rapid provision of chemicals whenever needed and many valuable discussions. Same is true for Dr. XXXX (FORTH, Heraklion, Crete). I would like to acknowledge appreciation to the Deutsche Forschungs-gemeinschaft for financial support in the framework of SPP1259 "Intelligente Hydrogele", for the course of my PhD thesis. I have had remarkable moments both during the course of my PhD in Mainz, as well as during the participation in several SPP-related workshops in Germany. Next, I would like to convey my special acknowledgements to Prof. Dr. XXXX (Tokyo, Japan) and Dr. XXXX for collaboration and their support with Tetra-PEG samples for the diffusion studies of the 5th Chapter. I also thank XXXX (PNiPAAm synthesis), XXXX (FORTH/Heraklion) for SLS and DLS measurements and XXXX for technical support and discussions, by whom I inherited the baptism of hydrogel preparation scientific support (physics-related)-XXXX, tante grazie! Same holds for Ms. XXXX for technical support in spin coating, as well as. I would like to acknowledge my appreciation to Prof. XXXX (Mainz & Ioannina), Dr. XXXX, Dr. XXXX, Dr. XXXX and Dr. XXXX for helpful discussions, during my PhD. Moreover, I thank Dr. XXXX, XXXX, Herr XXXX (AK Spiess), Dr. XXXX (AK Müllen) for discussions concerning NMR data, XXXX (ela!), Dr. XXXX and Dr. XXXX for collaboration on projects and helpful discussions in many aspects and the whole FCS-subgroup, XXXX (synthesis of specialty chemicals-Danke, XXXX!), XXXX (for Rheology and for funny moments!), Polymer Analytics (MPI), XXXX (SEM), XXXX (ITC), the whole AK Butt and Kaffee Ecke (and many more who may not be listed above.. Last, I dedicate this thesis to my family, for the vast sacrifices they have undergone to secure for me a pleasant and enjoyable life, full of academic-scientific, mental, material and rich ethical resources; needless to say, I feel deeply obliged to them. Τέλος, ευχαριστώ τον Τριαδικό Θεό, για το Φως και την αγκαλιά Του σε ελάχιστες δύσκολες -και απλόχερη γενναιοδωρία Του σε πολλαπλάσιες ευχάριστες στιγμές -της ζωής μας!

List of symbols, abbreviations and units

Latin symbols

A: Helmholtz free Energy of a polymer chain, per chain

A_{conf}: total energy per chain for the confined section of chain (1st Chapter)

A_{int}: Term related with excluded volume interactions in free energy per polymer chain

A_{ent}:Entropic contribution in free energy per polymer chain

$A_{elastic}$: elastic contribution in free energy of swelling for a polyelectrolyte network

A_{ion}: ionic contribution (from counterions) in free energy of swelling for a polyelectrolyte network

A_2: second virial coefficient

Au-NP: Gold (Au) nanoparticles

b: segment length

B: blinking-related parameter (blinking fitting function)

c: polymer's (or polyelectrolyte's) concentration

c^*: overlap concentration of polymer chains (onset of semidilute solutions)

c_s: salt concentration

c_s^+, c_s^-: concentration of positive and negative salt ions in a solution

d_{pore}:pore's size (de Gennes' polymer translocation model)

d: actual particle's diameter

DLS: Dynamic Light Scattering

$\mathbf{D}_{blob}$: characteristic diameter of an electrostatic blob in poor solvency conditions

$\mathbf{D}_e$: characteristic diameter of an electrostatic blob (in absence of salt)

$\mathbf{D}_e^o$: characteristic diameter of an electrostatic blob (in presence of salt)

$\mathbf{D}_T$: thermal blob size in poor solvency conditions

$D(\phi)$): tracer's (or polymer's) diffusion coefficient at volume fraction ϕ

D_{bound}: tracer's diffusion coefficient bound to the polymer

$D_{coop}(c)$: cooperative diffusion coefficient in semidilute polymer solution

D_{eff}: effective tracer's diffusion coefficient (for quantum dots, QD, 3rd Chapter)

D_0: tracer's diffusion coefficient in absence of any polymer (in solvent only)

D_0: tracer's diffusion coefficient calculated from simulations (3rd Chapter)

$D_{pol}(c)$: concentration dependent polymer self-diffusion

$D_{slow}(c)$: slow component's diffusion coefficient using double Fickian fit (chapters 2,3,4,5)

D_s: diffusion coefficient based on solvent's viscosity (in SE relation)

D_t: diffusion coefficient based on an effective viscosity (Rubinstein's theory, 1st Chapter)

D_{Rouse}: polymer chain's diffusion coefficient (Rouse model)

D_{zimm}: polymer chain's diffusion coefficient (Zimm model)

$\frac{dn'}{dc}$:refractive index increment (light scattering)

DLVO: Derjaguin-Landau-Verweey-Overbeek Theory

DH:Debye-Hückel approximation

e: elementary unit charge

$F_B[n(r)]$: Functional of the free energy for a charged system with respect to function $n(r)$

$\boldsymbol{F}$: Force (any force described in the thesis)

f: fraction of bound tracers (calculated from simulations)

$\mathbf{f}'$: charged fraction along a polyelectrolyte chain (in absence of salt)

$\mathbf{f}^*$: charged fraction along a polyelectrolyte chain (in presence of salt)

F_{slow}: amplitude (fraction) of the slow process from a double Fickian fit to a tracer

F_i: amplitude of the ith process from a double Fickian diffusion fit to a tracer (fast,slow)

$g_1(\tau), g_2(\tau)$: Scattered Intensity autocorrelation functions in Dynamic Light Scattering

$\boldsymbol{G}'(\mathbf{p})$: shear storage modulus for extend of branching reaction, $\mathbf{p}$

$\boldsymbol{G}'_{\mathbf{affine}}$**:** shear modulus of a rubbery network described by the affine model

$\boldsymbol{G}'_{\mathbf{phantom}}$**:** shear storage modulus of a rubbery network described by the phantom model

$\boldsymbol{G}'_{\mathbf{ent,charged}}$**:** entanglement shear modulus in a polyelectrolyte network

$G(t)$: normalized fluorescence correlation spectroscopy autocorrelation function

$G'(t)$: non-normalized fluorescence correlation spectroscopy autocorrelation function (measured)

$G'_{dif}(t)$: diffusion-related term in the overall $G'(t)$, not including contributions from photophysical relaxations

g_e: number of monomers per electrostatic blob

$I_{exc}(\boldsymbol{r})$: spatial distribution of the excitation intensity (2nd Chapter)

$I_{exc,0}$: maximum value in the spatial distribution of the excitation intensity (2nd Chapter)

I_F: normalized tracer's fluorescence Intensity in the hydrogels compared to the supernatant solution

I: ionic strength

$I_{sc,A}$: residual scattering intensity of the analyte (relative difference in scattering intensity between solution and pure solvent) in Light Scattering

I_T: Incident intensity, respectively (Light Scattering)

IgG: goat-anti mouse immunoglobulin

$J_{AB}(t_0)$: momentum transferred from particle A to particle B at time t_0

$J_{suction}$: net hydrodynamic suction flow driving a polymer through a pore (translocation)

J_c: critical suction flow for translocation of a polymer through a pore to occur

k_B: Boltzmann's constant

K^{-1}: Debye length

$\overrightarrow{k_i}$: incident wavevector

$\overrightarrow{k_f}$: scattered wavevector (arriving at the photomultiplier)

K_{eq}: equilibrium binding constant (tracer-polymer)

K_{FENE}:stiffness constant of the simulated polymer

$K^{\#}$: optical constant in static light scattering

K°: scaling parameter in Mark-Houwink relation

L: length denoting parameter (i.e. polyelectrolyte rod's length)

L_{bound}:length over which tracer spends bound to the polymer

LCST: Lower critical solution temperature

l_B: Bjerrum length for a polyelectrolyte

$l_{p,tot}$: total persistence length for a polyelectrolyte chain

l_{scr}: electrostatic screening length

l_{string}: length of monomers connecting blobs in polyelectrolyte chains (poor solvency conditions)

L_{pore}: total pore's length (translocation model)

m: blinking-related parameter (blinking fitting function)

m: parameter for polyelectrolytes scaling relating properties in presence or absence of salt

$\mathbf{m}'$: mass of a Brownian tracer

$\mathrm{M_n}$: number average molecular weight of the polymer

$\mathrm{M_w}$:weight average molecular weight of the polymer

$\mathrm{M_{w,c}}$:polymer molecular weight between crosslinks

MSD:mean square displacement

$n^{\#}$: number of strands between crosslinks

$\mathrm{n_{c,1}}$: number of counterions distributed in the interior of a polyelectrolyte cylinder (region A)

$\mathrm{n_{c,2}}$: number of counterions distributed in the exterior of a polyelectrolyte cylinder (region B)

n: number of diffusing species in the fitting function for an FCS autocorrelation curve

n: number of charged species (1st Chapter)

$\boldsymbol{n}'$: refractive index

$\mathrm{n_i}, \mathrm{n_f}$: incident and scattered polarization

$\boldsymbol{n}_{\mathrm{T}}$: toluene's scattering intensity

$\mathrm{n(r)}$:charge density as a function of distance, r, from a charged surface

$\mathrm{n_i^{\infty}}$: charge density in the bulk solution (far from the charged surface) for the ith charged species

$\mathrm{N_A}$: Avogadro's constant

N: chain's degree of polymerization

N': average number of species in the observation volume

NA: numerical aperture of objective

$\mathrm{N_2}$: nitrogen

$\mathbf{p}$:extend of branching reaction for a growing polymer

$\mathbf{p}^*$:gelation point for a growing branched polymer

$\mathrm{P}'(\mathrm{T})$: partition coefficient of a tracer in the hydrogel

PEO: linear polyethylene oxide

PI: polydispersity index of a polymer

[P]: concentrations of polymer (equilibrium binding constant)

$P(\theta)$:scattering form factor

PAGE: gel electrophoresis

P: number of monomers translocated through a pore, from a chain with totally N monomers

$\mathrm{p}(\mathrm{R},\mathrm{t})$: probability distribution for particle's jumps of distance R at time t

P':partition coefficient for a given tracer in the hydrogel (4th Chapter)

$\mathrm{p}\#$:Rouse or Zimm mode (for chain section having N/ $\mathrm{p}\#$ monomer units)

P: confined monomers (out of totally N), in a translocated polymer chain

PNiPAAm: poly-(n-isopropylacrylamide)

PS-NP: polystyrene latex nanoparticles

$\boldsymbol{q_1}$: elementary unit charge of particle (or point-like particle) 1

q:scattering wavevector

$\mathrm{Q}(\mathrm{t})$: photophysical relaxation in FCS autocorrelation curve

Q': quantum yield for the fluorescent emitter

QD: quantum dots

r: size of fixed confinement domains (Chapter 3)

r: distance (Chapter 2)

$\mathrm{r}_{\mathrm{cut}}$: Critical distance beyond which Lennard Jones potential decays to zero

r_{o}: lateral dimension of the Gaussian confocal observation volume

r_0': tracer's initial, unperturbed position

r_f': tracer's final position

R:tracer's jump length in a diffusive process

R_{e}: end-to-end distance of a polymer chain at equilibrium

$\mathrm{R}_{\mathrm{e,el}}$: end-to-end distance of a polyelectrolyte chain at equilibrium

$\mathrm{R}_{\mathrm{eff}}$: effective particle's radius (Chapter 5)

R_{F}: equilibrium size of the fully swollen chain

$\mathrm{R}_{\mathrm{FENE}}$: cut-off radius in the simulated chain

R_{θ}:optical constant in light scattering (Rayleigh's ratio)

R_{g}: radius of gyration for a polymer chain

R_H: polymer's hydrodynamic radius

$R_{h,np}$: nanoparticle's hydrodynamic radius

$R_{non-solvent}$: characteristic chain size in non-solvent conditions

R_0: equilibrium size of the unperturbed chain

$R_s(T)$: swelling ratio of the hydrogel at a given temperature, T

$\boldsymbol{R}_T$:optical constant (scattering)

RW: random walk conformation for an ideal chain (no excluded volume interactions)

SAW: self-avoiding walk conformation for a real chain (presence of excluded volume interactions)

S:entropy

S:structural parameter of diffraction-limited FCS spot

$S_c(\boldsymbol{r})$: spatial collection efficiency distribution function

SLS: Static Light Scattering

STED-FCS: Stimulated emission depletion Fluorescence Correlation Spectroscopy

S_0, S_1, S_2: different energy levels in the Jablonski energy diagram

[T]: concentrations of free tracer (equilibrium binding constant)

T:temperature

T_1: triplet state (in Jablonski energy diagram)

T': fraction of the triplet state

t:time (in general)

t_{fast}, t_{slow}: fast and slow tracer's diffusion times provided by a double Fickian fit

t_{bound}: time the tracer spends bound to the polymer

t_{free}: time the tracer spends unbound (freely diffusing)

$t_{0:}$zero time

t_T: relaxation time from the triplet state to the ground state

τ_i:translational diffusion time for the ith process

$\boldsymbol{\tau_D}$: translational diffusion time for a tracer through the FCS observation volume (definition)

[TP]: concentration of tracer-polymer complex (equilibrium binding constant)

TIR-FCS: total internal reflection fluorescence correlation spectroscopy

u: interaction parameter for polyelectrolyte chains

$\boldsymbol{u}$: scaling parameter for nanoparticle diffusion slowdown (5th Chapter)

U: internal energy

$\mathbf{v}, \mathbf{v}(\mathbf{T})$: excluded volume interaction parameter

$V_A(t_0)$: velocity of particle A at time t_0

$V(0)$:particle's velocity at time t=0

$V'_{sr}(r)$:Short-range (Lennard-Jones type) interaction potential

$V'_{coulombic}(r)$:Coulombic potential

$V'_{Yukawa}(r)$:Yukawa form of the Coulombic potential

$V(r)$: long-range interaction potential

$V_{polymer}, V_{solvent}, V_{mixture}$: molar volumes of polymer, solvent and polymer-solvent mixture

V_{FCS}: FCS detection volume

x': functionality of a macromolecule

$\ddot{x}$: 2nd derivative of particle's position

$\dot{x}$: particle's velocity

y: a parameter related with the polymer molecular weight (Phillies' model)

y^*: critical sucked length of the macromolecule through a pore

z': monomer's coordination number in Flory-Huggins theory

$\mathbf{z}$: valency of the ions in a solution

z: perpendicular distance from the microscope objective

z_o: axial dimension of the Gaussian confocal observation volume

w: FCS illumination spot diameter

Hellenic characters

$\alpha'(c)$: Diameter of a virtual tube in an entangled semidilute polymer solution

$\alpha(c)$:concentration dependent subdiffusive exponential term

β: parameter related with the size of the diffusant (Phillies' model)

β:inverse thermal energy

γ: particle's friction coefficient

γ_b:friction coefficient per monomer bead

γ_{R}:Total friction coefficient according to the Rouse model

γ_0: Oosawa-Manning (counterion condensation) parameter

$\boldsymbol{\gamma}$:deformation applied to a polyelectrolyte network by the solvent

$\boldsymbol{\gamma}^*$:scaling parameter for nanoparticle diffusion slowdown (Chapter 5)

Γ:tracer's fractional mobility

ΔA_{mix}: Free energy of polymer-solvent mixing

$\Delta\mu_{\mathrm{gel}}$: chemical potential difference in a gel between elasticity and mixing

δ: hydrodynamic screening length

$\boldsymbol{\delta}(\mathrm{t})$:delta function

$\delta I_{\mathrm{F}}(\mathrm{t})$: fluorescence intensity fluctuations

$\delta c(\boldsymbol{r}, \mathrm{t})$: concentration fluctuations

$\delta\varepsilon_{\mathrm{r}}$: fluctuations in the dielectric constant of the medium

$\Delta r(\mathrm{t})$:particle's displacement

$\langle \Delta r^2(\mathrm{t}) \rangle$:particle's mean square displacement

$\Delta\mu_{\mathrm{gel}}$: chemical potential difference between mixing and elasticity for the fully swollen network

$\boldsymbol{\Delta t}$: measurement time

ε_0: dielectric permittivity of vacuum

ε: attractive well depth of the Lennard-Jones potential

$\varepsilon_{\mathrm{AA}}$: monomer-monomer attraction (Flory-Huggins theory)

ε_{r}: solvent's dielectric constant

ϵ': molecular brightness for the fluorescent emitter

η_{s}: solvent' s viscosity

η: viscosity of the polymer solution

$[\eta]$:Intrinsic viscosity

$\eta_{eff}(\tau_d)$: effective solution's viscosity due to a chain section with relaxation time τ_d

$n_f(r)$: charge density only from free ions in the solution

$\boldsymbol{\theta}$: theta temperature for a polymer chain

θ:scattering angle

λ_T:de Broglie's thermal wavelength

λ:wavelength of light

MΩ·cm: resistivity unit of mili-Q water

ν: solvent quality parameter for a polymer

ν_e: number of strands between entanglements

$[\eta]$:intrinsic viscosity

ξ_T: thermal blob size for an uncharged polymer chain

ξ: correlation blob size for an uncharged polymer chain (or, mesh size for a fully swollen gel)

$\xi_{suction}(y)$: correlation blob for a translocated chain, depending on the translocation length, y

ξ^*:mesh size for a hydrogel, in the as-prepared state (according to affine deformation model)

$\xi^{\#}$: mesh size for a gel by small-angle neutron scattering measurements

$\boldsymbol{\xi}(t)$:thermal noise in Langevin's equation of motion

Π_{osm}: osmotic pressure for a semidilute polymer solution or a gel

$\Pi_{osm,e}$: osmotic pressure in salt-free polyelectrolyte solutions

$\Pi_{osm,mac}$: Contributions to the osmotic pressure from the polyelectrolyte macromolecule (salt-free)

$\Pi_{osm,cn}$: Contributions to the osmotic pressure from the counterions (salt-free)

$\Pi_{osm,salt}$: total osmotic pressure of a semidilute polyelectrolyte solution in presence of salt

$\Pi_{pol,salt}$: polymeric contribution to the osmotic pressure for a semidilute polymer solution or a gel

$\Pi_{ion,salt}$: ionic contribution to osmotic pressure of a semidilute polyelectrolyte solution (in presence of salt)

ρ:total charge density in Poisson-Boltzmann expression

σ: hard sphere diameter (for Lennard-Jones interaction potential)

τ:time (in general, i.e. 2nd Chapter)

τ':time (in general, i.e. 2nd Chapter)

τ_{free}:time the tracer spends diffusing freely (unbound)

τ_{bound}: time the tracer spends bound to the polymer

τ_0:relaxation time of a monomer segment

τ_d: relaxation time of a chain section with size equal to the tracer's size, d

τ_ξ: relaxation time of a correlation blob, ξ

τ_{slow}: tracer's slow diffusion time (2nd process from a double Fickian model)

τ_T: relaxation time from the triplet state to the ground state

τ_ξ:relaxation time for a chain section with size equal to a correlation blob, ξ

τ_d: relaxation time for a chain section with size equal to $d(>\xi)$

τ_{zimm}:chain's relaxation time, according to the Zimm model

τ_p: relaxation time of a chain section containing $\frac{N}{p^{\#}}$ monomers

τ_{Rouse}: chain's relaxation time, according to the Rouse model

ϕ: monomer volume fraction

$\Phi^{\#}$: scaling parameter in Mark-Houwink relation

$\chi = \chi(T)$: Flory-Huggins interaction parameter (temperature-dependent)

$\psi(r)$:total surface electrostatic potential as a function of distance, r, from the surface

ψ_0:electrostatic potential at the charged surface (potential at th inner Hemholtz plane)

ψ_ζ:electrostatic potential at the outer Helmholtz plane (zeta potential)

$\psi_{free}(r)$: electrostatic potential due to free counterions

$\psi_f(r)$: electrostatic potential due to fixed ions on a surface

$\Psi(r'_f, r'_0; t)$: Conditional probability that a diffusant will diffuse at time t from r'_0 to r'_f

Ω: number of configurations for chain strands

ω:frequency of oscillations (rheology)

ϖ:scaling variant in polymer molecular weight dependence

Unit parameters

g ml^{-1}:concentration unit

$\frac{J}{cm^2}$: energy dose unit for UV irradiation (crosslinking of PNiPAAm gels)

$kg \cdot mol^{-1}$: unit of polymer molecular weight

$m^2 \cdot s^{-1}$: units of tracer's diffusion coefficient (SI)

Appendix

In Fig. S1, $G(t)$ for all three examined molecular tracers in aqueous solutions of the PNiPAAm terpolymer at the same c (c=0.13 g ml^{-1}), at $=25$℃, are shown together with the fits (color-matching solid curves), along with the fits to the $G(t)$ for each tracer in pure water (dashed curves).

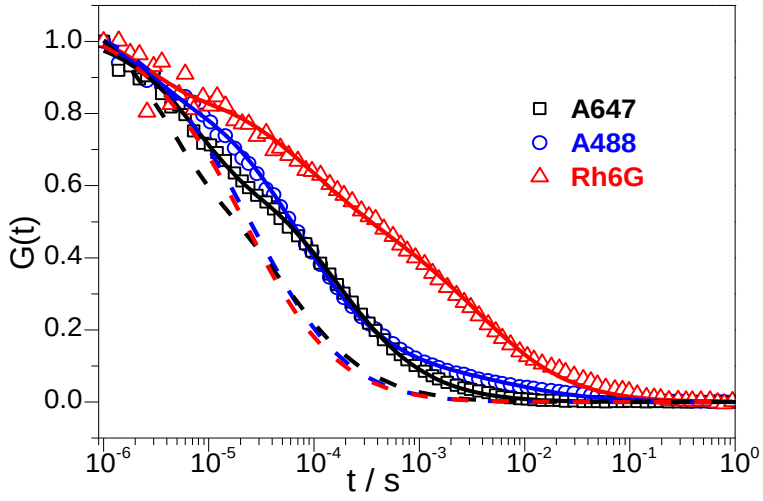

Fig.S1.Presence of interactions in PNiPAAm aqueous solutions: Normalized fluorescence intensity autocorrelation functions $G(t)$ for the three molecular tracers in non-dilute aqueous solutions of PNiPAAm (280k) at c=0.13 g·ml^{-1} and 25°C: A647 (squares), A488 (circles) and Rh6G (triangles). Solid lines denote the representation by eq. 2.3.4 (2nd Chapter) using either n=1 (for A647) or n=2. Dashed lines represent single Fickian diffusion fits (n=1) to the experimentally measured $G(t)$ (not shown) of the A647 (black), A488 (blue) and Rh6G (red) in water.

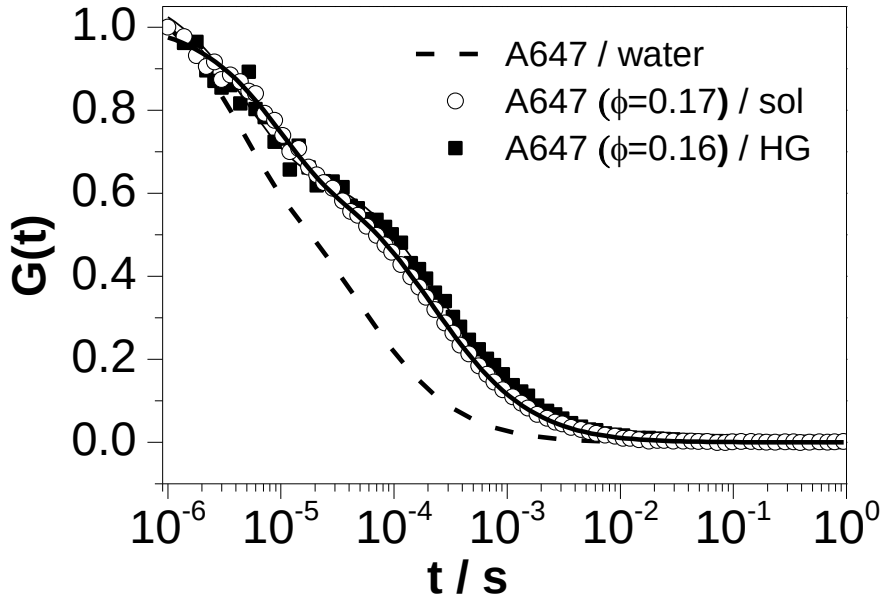

Fig.S2. Influence of permanent crosslinking for A647. $G(t)$ for A647 in PNiPAAm aqueous solutions and grafted PNiPAAm hydrogels with very similar monomer concentration at $T = 25$ ℃. The $G'(t)$ for each tracer was fitted by eq. 2.3.2 from 2nd Chapter (solid lines) using n=1. Dashed $G(t)$ curve represents the single component fits (n=1) to the experimentally measured $G'(t)$ (not shown) of A647 in water.

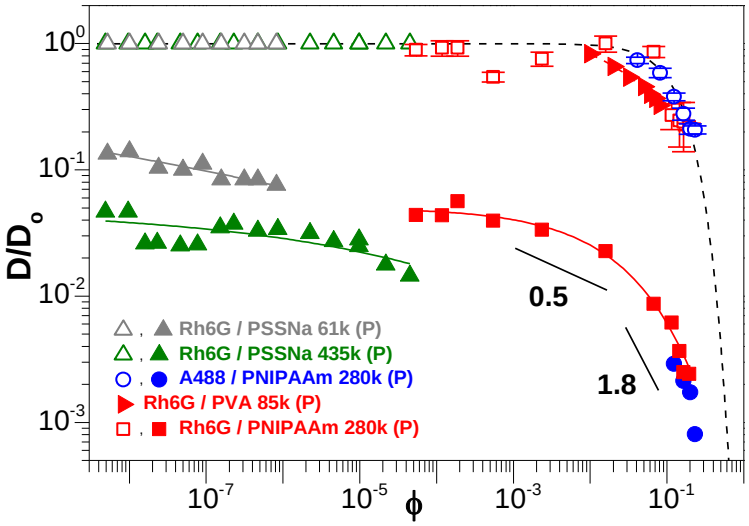

Fig.S3.Diffusion slowdown, $D(\phi)/D_0$, for the interacting tracers A488 and Rh6G in PNiPAAm aqueous solutions at 25 °C. Comparison with reported values for non-interacting [185] (red triangles) and interacting tracers (green and grey triangles) [186] in aqueous polymer solutions. Open and solid symbols denote fast and slow process, accordingly, whereas the dashed (black) curve denotes the concentration dependence of the single diffusion of non-interacting molecular tracer slowdown in polymer solutions [111]. The solid curves through the data are drawn to guide the eye and the slopes 0.5 and 1.8 are scaling predictions of polymer self-diffusion [9].

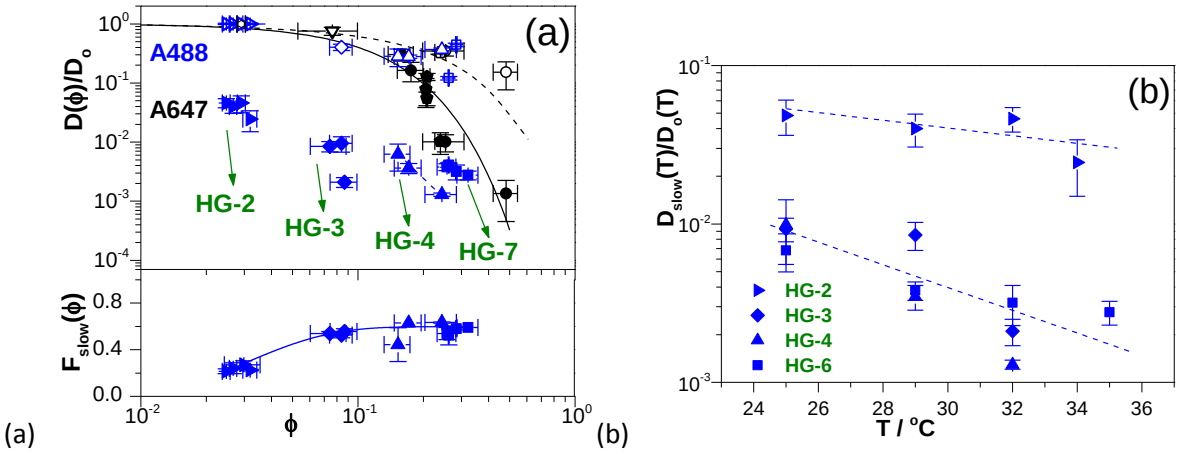

Fig.S4. (a) Mobility slowdown in the case of weak and strong attractions exemplified by A488 in HGs presented as $D(\phi)/D_o$, together with $F_{slow}(\phi)$. Green arrows denote the $D_{slow}(\phi)/D_o$ datasets from the same HG (same symbol type). Fast and slow processes are denoted by empty and solid symbols, respectively. Dashed and solid curves denote stretched exponential concentration dependences vs. ϕ for recently reported for non-interacting molecular tracer diffusion slowdown, $D(\phi)/D_o$, in solutions [111] and in HGs [77], respectively. (b) Mobility slowdown vs. T, $D_{slow}(T)/D_o(T)$, for A488 using the same symbol for the different HGs examined. The dotted lines are drawn to guide the eye.

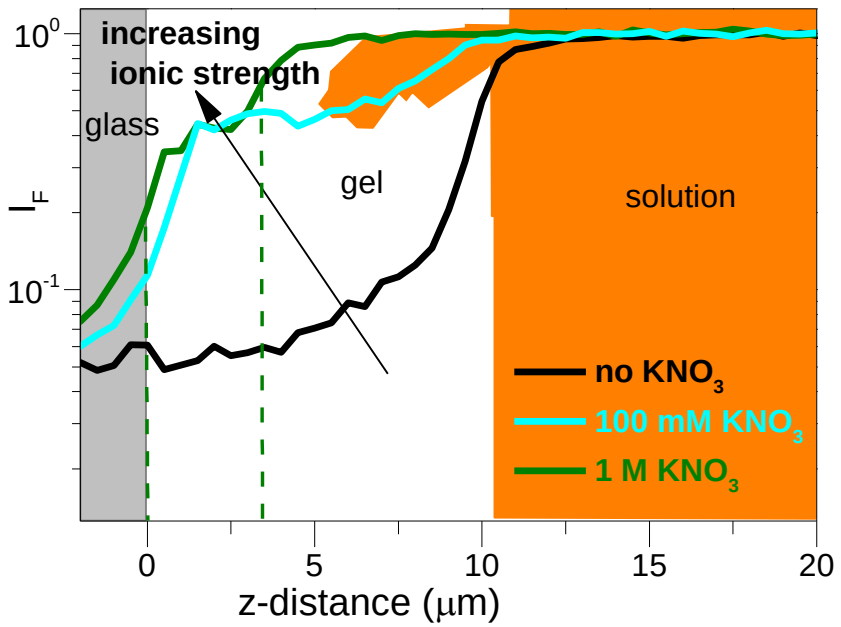

Fig.S5. A647 density profile, I_F (inset: normalized A647 fluorescence Intensity, $I_F(z)$, in HG-6 (white) and in the supernatant solution (grey) vs. distance z normal to the substrate (grey)), at different ionic strength (I) values, at 25°C.Grey, white and orange-shaded regions denote the glass substrate, the HG and the supernatant solution, respectively. Dashed perpendicular lines denote the fully swollen HG thickness at the collapsed state ($I = 1$ M KNO_3).

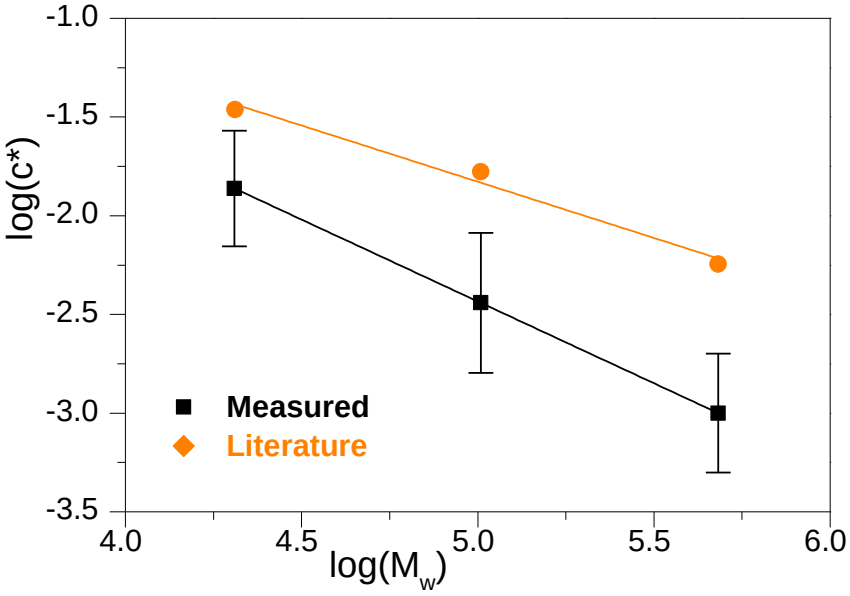

Fig.S6. Scaling relations of the form: $c^* \sim (M_w)^{\varpi}$ and comparison between estimations of c* by the measured c-dependent nanoparticle diffusion slowdown (black squares, ϖ=-0.9) shown in Fig.5.1.6 and Table 5.1, as well as estimations of c* using literature values [172, 173] of $D_{O,PEO}$ (m^2/s)(orange circles, ϖ=-0.6).The $D_{O,PEO}$ (m^2/s) are also listed in Table 5.1.

Firefox | 16) Mail :: ... | percolation ... | ChNE 575: S... | Redirect No... | No Job Na... | Flory- Reh

https://s100.copyright.com/AppDispatchServlet

Most Visited | Getting Started | Latest Headlines

Copyright Clearance Center RightsLink®

Home | Account Info | Help

Title: Theory of polyelectrolytes in solutions and at surfaces
Author: Andrey V. Dobrynin,Michael Rubinstein
Publication: Progress in Polymer Science
Publisher: Elsevier
Date: November 2005
Copyright © 2005, Elsevier

Logged in as:
Apostolos Vagias
Account #:
3000644953
LOGOUT

Order Completed

Thank you very much for your order.

This is a License Agreement between Apostolos Vagias ("You") and Elsevier ("Elsevier"). The license consists of your order details, the terms and conditions provided by Elsevier, and the payment terms and conditions.

Get the printable license.

License Number	3140210842910
License date	May 01, 2013
Licensed content publisher	Elsevier
Licensed content publication	Progress in Polymer Science
Licensed content title	Theory of polyelectrolytes in solutions and at surfaces
Licensed content author	Andrey V. Dobrynin,Michael Rubinstein
Licensed content date	November 2005
Licensed content volume number	30
Licensed content issue number	11
Number of pages	70
Type of Use	reuse in a thesis/dissertation
Portion	figures/tables/illustrations
Number of figures/tables /illustrations	6
Format	electronic
Are you the author of this Elsevier article?	No
Will you be translating?	No
Order reference number	
Title of your thesis/dissertation	Engineering tracer mobility in hydrogels using Fluorescence Correlation Spectroscopy
Expected completion date	Sep 2013
Estimated size (number of pages)	160
Elsevier VAT number	GB 494 6272 12
Permissions price	0.00 USD
VAT/Local Sales Tax	0.00 USD
Total	0.00 USD

ORDER MORE... | CLOSE WINDOW

Fig.S7. License agreement from Elsevier Ltd. (provided by the Copyright Clearance Center), with license number 3140210842910.

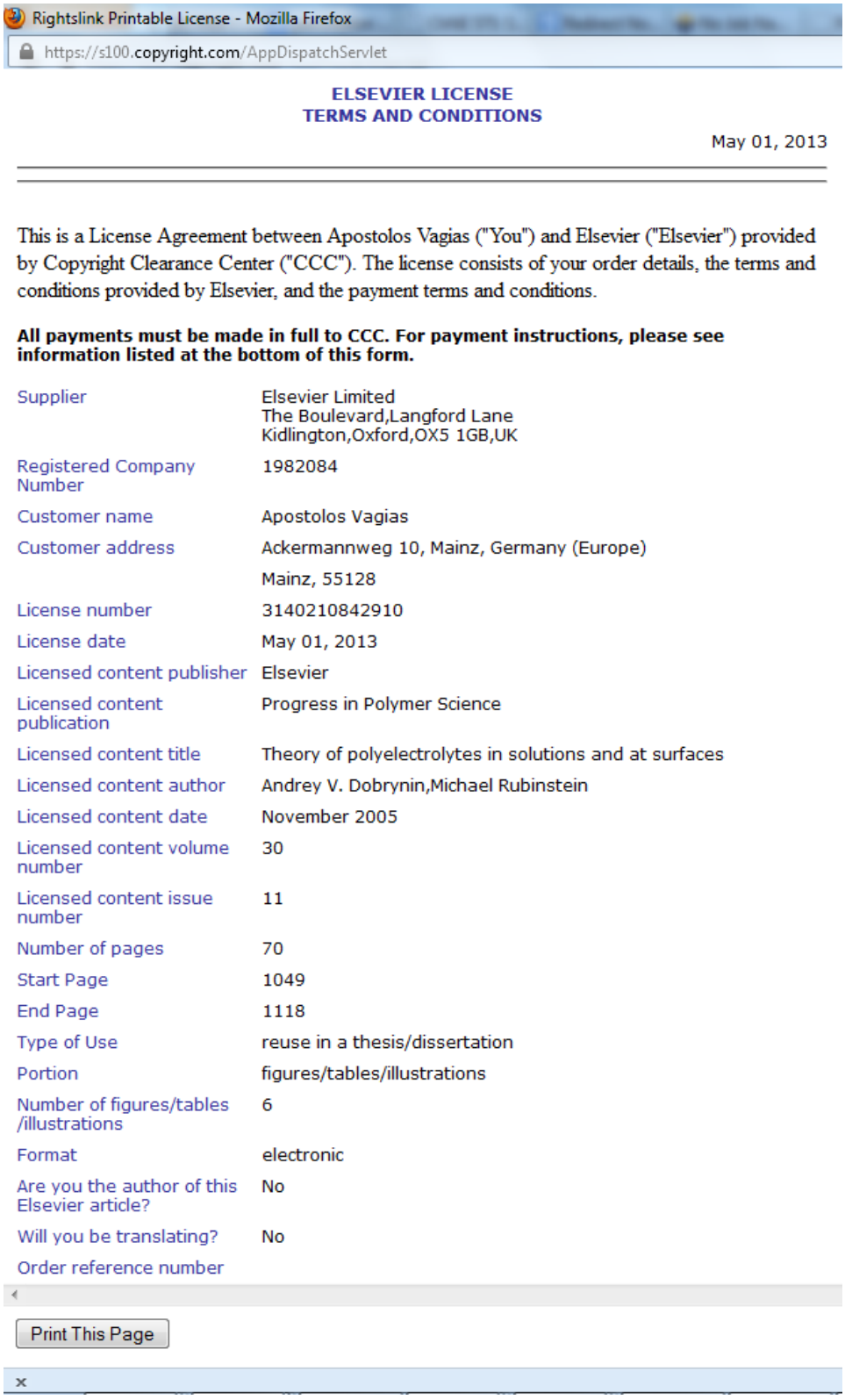

Rightslink Printable License - Mozilla Firefox

https://s100.copyright.com/AppDispatchServlet

ELSEVIER LICENSE
TERMS AND CONDITIONS

May 01, 2013

This is a License Agreement between Apostolos Vagias ("You") and Elsevier ("Elsevier") provided by Copyright Clearance Center ("CCC"). The license consists of your order details, the terms and conditions provided by Elsevier, and the payment terms and conditions.

All payments must be made in full to CCC. For payment instructions, please see information listed at the bottom of this form.

Supplier	Elsevier Limited The Boulevard,Langford Lane Kidlington,Oxford,OX5 1GB,UK
Registered Company Number	1982084
Customer name	Apostolos Vagias
Customer address	Ackermannweg 10, Mainz, Germany (Europe) Mainz, 55128
License number	3140210842910
License date	May 01, 2013
Licensed content publisher	Elsevier
Licensed content publication	Progress in Polymer Science
Licensed content title	Theory of polyelectrolytes in solutions and at surfaces
Licensed content author	Andrey V. Dobrynin,Michael Rubinstein
Licensed content date	November 2005
Licensed content volume number	30
Licensed content issue number	11
Number of pages	70
Start Page	1049
End Page	1118
Type of Use	reuse in a thesis/dissertation
Portion	figures/tables/illustrations
Number of figures/tables /illustrations	6
Format	electronic
Are you the author of this Elsevier article?	No
Will you be translating?	No
Order reference number	

Print This Page

Fig.S8. License agreement from Elsevier Ltd. (provided by the Copyright Clearance Center), with license number 3140210842910.

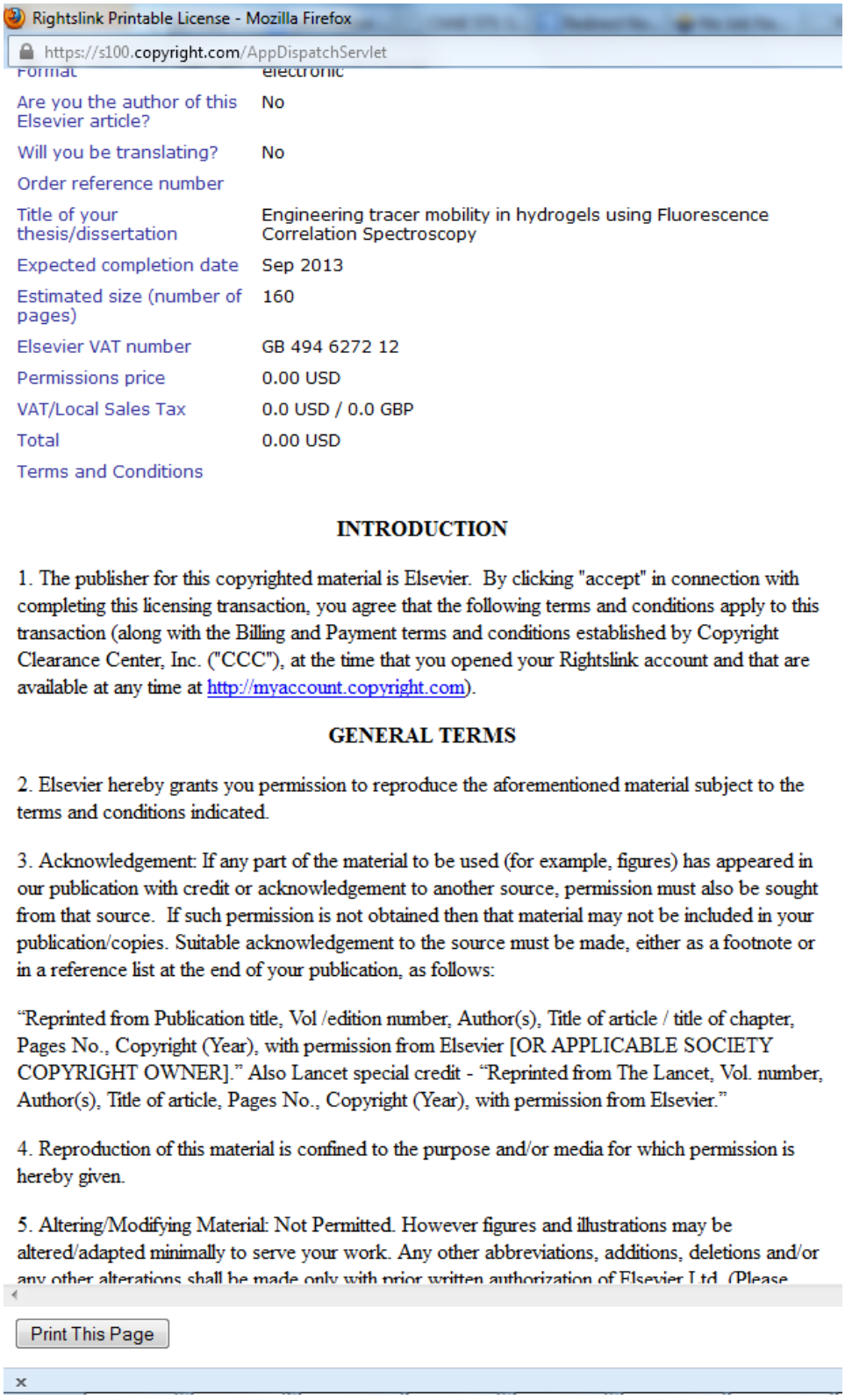

Fig.S9. License agreement from Elsevier Ltd. (provided by the Copyright Clearance Center), with license number 3140210842910.

Bibliography

1. Dhont, J.K.G., *An introduction to dynamics of colloids*, ed. R.M. D. Mobius1996: Elsevier Science B.V.
2. Franosch, T., et al., *Resonances arising from hydrodynamic memory in Brownian motion.* Nature, 2011. **478**(7367): p. 85-88.
3. Christian Holm, P.K., Rudolph Podgornick, *Electrostatic effects in soft matter and biophysics*. NATO Science Series2001: Kluwer Academic publishers.
4. Carrillo, J.M.Y. and A.V. Dobrynin, *Polyelectrolytes in salt solutions: Molecular dynamics simulations.* Macromolecules, 2011. **44**(14): p. 5798-5816.
5. Rowlinson, J.S., *The Yukawa potential.* Physica A: Statistical Mechanics and its Applications, 1989. **156**(1): p. 15-34.
6. Lennard-Jones, J.E., Proc.Roy.Soc., 1924. **106A**(463).
7. Rubinstein, M. and R. Colby, *Polymer Physics*2003, New York: Oxford University Press Inc.
8. M. Doi, S.F.E., *The theory of polymer dynamics*. International Series of monographs on physics1986: Oxford University Press.
9. Gennes, P.G.d., *Scaling concepts in polymer physics*1979, Ithaca,NY: Cornell University Press.
10. Flory, P., *Principles of Polymer Chemistry*1953: Cornell University Press.
11. Riehn, R., et al., *Nanochannels for Genomic DNA Analysis: The Long and the Short of It*, in *Integrated Biochips for DNA Analysis*, R. Liu and A. Lee, Editors. 2007, Springer New York. p. 151-186.
12. A.V. Dobrynin, M.R., *Theory of polyelectrolytes in solutions and at surfaces.* Progress in Polymer Science, 2005.
13. Scott, J.H.H.a.R.L., *The Solubility of Non-Electrolytes*. 3rd edn. ed1950, New York: Prentice-Hall.
14. Daoud, M., et al., *Solutions of Flexible Polymers. Neutron Experiments and Interpretation.* Macromolecules, 1975. **8**(6): p. 804-818.
15. Wong Po Foo, C.T.S., et al., *Two-component protein-engineered physical hydrogels for cell encapsulation.* Proceedings of the National Academy of Sciences, 2009. **106**(52): p. 22067-22072.
16. Matsunaga, T., et al., *SANS and SLS Studies on Tetra-Arm PEG Gels in As-Prepared and Swollen States.* Macromolecules, 2009. **42**(16): p. 6245-6252.
17. Celli, J.P., et al., *Rheology of Gastric Mucin Exhibits a pH-Dependent Sol–Gel Transition.* Biomacromolecules, 2007. **8**(5): p. 1580-1586.
18. Stockmayer, W.H., *Theory of Molecular Size Distribution and Gel Formation in Branched-Chain Polymers.* The Journal of Chemical Physics, 1943. **11**(2): p. 45-55.
19. Flory, P., *Molecular Size Distribution in Three Dimensional Polymers .I. Gelation.* Journal of the American Chemical Society, 1941. **63**: p. 3083-3090.
20. Stauffer, D., A. Coniglio, and M. Adam, *Gelation and critical phenomena*, in *Polymer Networks*, K. Dušek, Editor 1982, Springer Berlin Heidelberg. p. 103-158.
21. Stanley, H.E., *Introduction to Phase Transitions and Critical Phenomena*1971, Oxford: Clarendon Press
22. Sugimura, A., et al., *Mechanical properties of a polymer network of Tetra-PEG gel.* Polym J, 2012.
23. Stuart, M.A.C., et al., *Emerging applications of stimuli-responsive polymer materials.* Nat Mater, 2010. **9**(2): p. 101-113.
24. Kouwer, P.H.J., et al., *Responsive biomimetic networks from polyisocyanopeptide hydrogels.* Nature, 2013. **493**(7434): p. 651-655.
25. Chun Jen, H., J. Dostalek, and W. Knoll, *Long range surface plasmon and hydrogel optical waveguide field-enhanced fluorescence biosensor with 3D hydrogel binding matrix: On the role of diffusion mass transfer.* Biosensors & Bioelectronics, 2010. **26**(4): p. 1425-1431.

26. Mateescu, A., et al., *Thin Hydrogel Films for Optical Biosensor Applications.* Membranes, 2012. **2**(1): p. 40-6969.
27. Paul Hiemenz, T.L., *Polymer Chemistry*, New York: Marcel Dekker Inc.
28. Yin, D.-W.Y., Qiliang; de Pablo, Juan J., *Molecular dynamics simulation of discontinuous volume phase transitions in highly-charged crosslinked polyelectrolyte networks with explicit counterions in good solvent.* Journal of Chemical Physics, 2005. **123**(17): p. 9.
29. Joanny, J.L.B.a.J.F., *Advances in Chemical Physics*, ed. S.A.R. I. Prigogine. Vol. 94. 1996, New York.
30. Holm, C., *Polyelectrolytes-Theory and simulations*. Soft Matter Characterization, ed. R.B. Robert Pecora2008, New York: Springer Science and Business Media LLC.
31. Raphael, E. and J.F. Joanny, *Annealed and Quenched Polyelectrolytes.* EPL (Europhysics Letters), 1990. **13**(7): p. 623.
32. Shklovskii, B.I., *Wigner Crystal Model of Counterion Induced Bundle Formation of Rodlike Polyelectrolytes.* Physical Review Letters, 1999. **82**(16): p. 3268-3271.
33. Odijk, T., *Polyelectrolytes near the rod limit.* Journal of Polymer Science Part B-Polymer Physics, 1977. **15**(3): p. 477-483.
34. Skolnick, J. and M. Fixman, *Electrostatic Persistence Length of a Wormlike Polyelectrolyte.* Macromolecules, 1977. **10**(5): p. 944-948.
35. Gouy, C., J. Phys., 1910. **9**(4): p. 457.
36. Chapman, D.L., Phil. Mag., 1913. **25**(6): p. 475.
37. Hückel, P.D.a.E., Physik. Z., 1923. **24**: p. 185.
38. Hans Jürgen Butt, K.G., Michael Kappl, *Physics and Chemistry of Interfaces*. 2nd ed2006, Weinheim, Germany: Wiley-VCH Verlag GmbH & Co. KGaA.
39. De Gennes, P.G., et al., *Remarks on polyelectrolyte conformation.* J. Phys. France, 1976. **37**(12): p. 1461-1473.
40. Hooper, H.H., et al., *Monte Carlo simulations of hydrophobic polyelectrolytes. Evidence for a structural transition in response to increasing chain ionization.* The Journal of Chemical Physics, 1990. **93**(4): p. 2715-2723.
41. Higgs, P.G. and H. Orland, *Scaling behavior of polyelectrolytes and polyampholytes: Simulation by an ensemble growth method.* The Journal of Chemical Physics, 1991. **95**(6): p. 4506-4518.
42. Oosawa, F., *Polyelectrolytes*1971, New York: Marcel Dekker.
43. Manning, G.S., *Limiting Laws and Counterion Condensation in Polyelectrolyte Solutions. III. An Analysis Based on the Mayer Ionic Solution Theory.* The Journal of Chemical Physics, 1969. **51**(8): p. 3249-3252.
44. Dobrynin, A.V., *Theory and simulations of charged polymers: From solution properties to polymeric nanomaterials.* Current Opinion in Colloid and Interface Science, 2008. **13**(6): p. 376-388.
45. Fuoss, R.M., *Viscosity function for polyelectrolytes.* Journal of Polymer Science, 1948. **3**(4): p. 603-604.
46. Bruce J. Berne, R.P., *Dynamic light scattering: with applications to chemistry, biology, and physics*2000, New York: John Wiley & Sons.
47. Anac, I., et al., *Optical Characterization of Co-Nonsolvency Effects in Thin Responsive PNIPAAm-Based Gel Layers Exposed to Ethanol/Water Mixtures.* Macromolecular Chemistry and Physics, 2010. **211**(9): p. 1018-1025.
48. Huang, R., et al., *Direct observation of the full transition from ballistic to diffusive Brownian motion in a liquid.* Nat Phys, 2011. **7**(7): p. 576-580.
49. Banks, D.S. and C. Fradin, *Anomalous diffusion of proteins due to molecular crowding.* Biophysical Journal, 2005. **89**(5): p. 2960-2971.
50. Szymanski, J. and M. Weiss, *Elucidating the origin of anomalous diffusion in crowded fluids.* Physical Review Letters, 2009. **103**(3): p. 038102 (4 pp.).

51. Saxton, Michael J., *Wanted: A Positive Control for Anomalous Subdiffusion.* Biophysical Journal, 2012. **103**(12): p. 2411-2422.
52. Wang, B., et al., *Anomalous yet Brownian Diffusion.* Proceedings of the National Academy of Sciences of the United States of America, 2009. **106**(36): p. 15160-15164.
53. Tabatabaei, F., O. Lenz, and C. Holm, *Simulational study of anomalous tracer diffusion in hydrogels.* Colloid & Polymer Science, 2011. **289**(5-6): p. 523-534.
54. O. G. Berg, R.B.W., and P. H. von Hippel, *Diffusion-driven mechanisms of protein translocation on nucleic acids. 1. Models and theory.* Biochemistry, 1981. **20**(24): p. 6929-6948.
55. Saxton, M.J., *A Biological Interpretation of Transient Anomalous Subdiffusion. I. Qualitative Model.* Biophysical Journal, 2007. **92**(4): p. 1178-1191.
56. Sokolov, I.M. and J. Klafter, *From diffusion to anomalous diffusion: A century after Einstein's Brownian motion.* Chaos: An Interdisciplinary Journal of Nonlinear Science, 2005. **15**(2): p. 026103.
57. Caspi, A., R. Granek, and M. Elbaum, *Enhanced Diffusion in Active Intracellular Transport.* Physical Review Letters, 2000. **85**(26): p. 5655-5658.
58. Jain, A., B. Dünweg, and J.R. Prakash, *Dynamic Crossover Scaling in Polymer Solutions.* Physical Review Letters, 2012. **109**(8): p. 088302.
59. Cai, L.H., S. Panyukov, and M. Rubinstein, *Mobility of Nonsticky Nanoparticles in Polymer Liquids.* Macromolecules, 2011. **44**(19): p. 7853-7863.
60. Masaro, L. and X.X. Zhu, *Physical models of diffusion for polymer solutions, gels and solids.* Progress in Polymer Science, 1999. **24**(5): p. 731-775.
61. Sakaue, T., et al., *Flow injection of branched polymers inside nanopores.* Europhys. Lett., 2005. **72**(1): p. 83-88.
62. Prince E. Rouse, J., *A Theory of the Linear Viscoelastic Properties of Dilute Solutions of Coiling Polymers.* The Journal of Chemical Physics, 1953. **21**(7): p. 1272-1280.
63. Gianneli, M., et al., *Dynamics of swollen gel layers anchored to solid surfaces.* Soft Matter, 2008. **4**(7): p. 1443-1447.
64. Gianneli, M., et al., *Local and Global Dynamics of Transient Polymer Networks and Swollen Gels Anchored on Solid Surfaces.* The Journal of Physical Chemistry C, 2007. **111**(35): p. 13205-13211.
65. Zettl, U., et al., *Self-Diffusion and Cooperative Diffusion in Semidilute Polymer Solutions As Measured by Fluorescence Correlation Spectroscopy.* Macromolecules, 2009. **42**(24): p. 9537-9547.
66. Teraoka, I., *Polymer solutions-An introduction to physical properties*2002, New York: Wiley Interscience.
67. Brochard Wyart, F. and P.G. de Gennes, *Viscosity at small scales in polymer melts.* The European Physical Journal E, 2000. **1**(1): p. 93-97.
68. Ullmann, G.S., et al., *Probe diffusion of polystyrene latex spheres in polyethylene oxide-water.* The Journal of Physical Chemistry, 1985. **89**(4): p. 692-700.
69. Magde, D., E. Elson, and W.W. Webb, *Thermodynamic fluctuations in a reacting system: measurement by fluorescence correlation spectroscopy.* Physical Review Letters, 1972. **29**(11): p. 705-708708.
70. Rudolf Rigler, T.B., Michel Orrit, *Single Molecule Spectroscopy- Nobel Conference Lectures*. Springer Series in Chemical Physics, ed. T.B. Rudolf Rigler, Michel Orrit. Vol. 67. 2001, Germany.
71. R.Rigler and E.S. Elson, *Fluorescence Correlation Spectroscopy: Theory and Applications*, ed. S.S.i.C. Physics2000: Springer.
72. Elson, Elliot L., *Fluorescence Correlation Spectroscopy: Past, Present, Future.* Biophysical Journal, 2011. **101**(12): p. 2855-2870.
73. Koynov, K. and H.-J. Butt, *Fluorescence correlation spectroscopy in colloid and interface science.* Current Opinion in Colloid & Interface Science, 2012. **17**(6): p. 377-387.

74. Schwille Petra, H.E., *Fluorescence Correlation Spectroscopy: An Introduction to its Concepts and Applications.* 2005.
75. Wong, D. 2010; Available from: http://chemwiki.ucdavis.edu/Physical_Chemistry/Spectroscopy/Electronic_Spectroscopy/Electronic_Spectroscopy%3A_Theory.
76. Douglas A .Skoog, F.J.H., Stanley R. Crouch, *Principles of Instrumental Analysis*. 6th ed2006.
77. Raccis, R., et al., *Probing mobility and structural inhomogeneities in grafted hydrogel films by fluorescence correlation spectroscopy.* Soft Matter, 2011. **7**(15): p. 7042-7053.
78. Kapusta, P., *Technical Report*, 2010, PicoQuant GmbH.
79. Orrit, M. and T. Basché, *Steady Light from Quantum Dots, at Last. But How?* Chemphyschem, 2009. **10**(14): p. 2383-2385.
80. Galland, C., et al., *Two types of luminescence blinking revealed by spectroelectrochemistry of single quantum dots.* Nature, 2011. **479**(7372): p. 203-207.
81. Verberk, R., A.M. van Oijen, and M. Orrit, *Simple model for the power-law blinking of single semiconductor nanocrystals.* Physical Review B, 2002. **66**(23): p. 233202.
82. Wirth, M.J., M.D. Ludes, and D.J. Swinton, *Analytic Solution to the Autocorrelation Function for Lateral Diffusion and Rare Strong Adsorption.* Appl. Spectrosc., 2001. **55**(6): p. 663-669.
83. Michelman-Ribeiro, A., et al., *Direct Measurement of Association and Dissociation Rates of DNA Binding in Live Cells by Fluorescence Correlation Spectroscopy.* Biophysical Journal, 2009. **97**(1): p. 337-346.
84. Pramanik, A., *Ligand-receptor interactions in live cells by fluorescence correlation spectroscopy.* Current Pharmaceutical Biotechnology, 2004. **5**(2): p. 205-212.
85. Wachsmuth, M., W. Waldeck, and J. Langowski, *Anomalous diffusion of fluorescent probes inside living cell nuclei investigated by spatially-resolved fluorescence correlation spectroscopy.* Journal of Molecular Biology, 2000. **298**(4): p. 677-689.
86. Guigas, G. and M. Weiss, *Sampling the cell with anomalous diffusion-the discovery of slowness.* Biophysical Journal, 2008. **94**(1): p. 90-9494.
87. Fritsch, C.C. and J. Langowski, *Anomalous diffusion in the interphase cell nucleus: The effect of spatial correlations of chromatin.* Journal of Chemical Physics, 2010. **133**(2): p. 025101 (11 pp.).
88. Destainville, N., A. Saulière, and L. Salomé, *Comment to the Article by Michael J. Saxton: A Biological Interpretation of Transient Anomalous Subdiffusion. I. Qualitative Model.* Biophysical Journal, 2008. **95**(7): p. 3117-3119.
89. Sokolov, I.M., *Models of anomalous diffusion in crowded environments.* Soft Matter, 2012. **8**(35): p. 9043-9052.
90. Kremer, G.S.G.a.K., Phys. Rev. A, 1986. **33**: p. 3628.
91. J. D. Weeks, D.C., and H. C. Andersen, *Role of repulsive forces in forming the equilibrium structure of simple liquids.* J. Chem. Phys., 1971. **54**: p. 5237.
92. A. Arnold, O.L., S. Kesselheim, R. Weeber, and D.R. F. Fahrenberger, P. Kosovan, C. Holm, *Meshfree Methods for Partial Differential Equations VI*, in *Lecture Notes in Computational Science and Engineering*, M.A.S. M. Griebel, Editor 2013, Springer. p. 1-23.
93. Beines, P.W., et al., *Responsive Thin Hydrogel Layers from Photo-Cross-Linkable Poly(N-isopropylacrylamide) Terpolymers†.* Langmuir, 2007. **23**(4): p. 2231-2238.
94. Jaskiewicz, K.I., *Transport of nanoparticles into polymersomes: a minimal model system of particles passage through biological membranes*, in *Chemistry* 2012, Mainz: Mainz, Germany.
95. Gear, A.R.L., *Rhodamine 6G.A potential inhibitor of mitochondrial oxidative phosphorylation.* Journal of Biological Chemistry, 1974. **249**(11): p. 3628-3637.
96. Sakai, T., et al., *Design and Fabrication of a High-Strength Hydrogel with Ideally Homogeneous Network Structure from Tetrahedron-like Macromonomers.* Macromolecules, 2008. **41**(14): p. 5379-5384.
97. Hunt, G.J., *Size Exclusion Chromatography*1979, New York.

98. Yau, W.W.K., J.J. ; Bly, D.D. , *Modern Size-Exclusion Chromatography*1979, New York: J. Wiley & Sons.
99. Dublin, P.L., *Aqueous Size-Exclusion Chromatography.* Journal of Chromatography, 1988. **Lib. 40**.
100. Al-Soufi, W., et al., *Fluorescence Correlation Spectroscopy, a Tool to Investigate Supramolecular Dynamics:Inclusion Complexes of Pyronines with Cyclodextrin.* Journal of the American Chemical Society, 2005. **127**(24): p. 8775-8784.
101. Kim, S.A., K.G. Heinze, and P. Schwille, *Fluorescence correlation spectroscopy in living cells.* Nat Meth, 2007. **4**(11): p. 963-973.
102. Kastrup, L., et al., *Fluorescence Fluctuation Spectroscopy in Subdiffraction Focal Volumes.* Physical Review Letters, 2005. **94**(17): p. 178104.
103. Ruprecht, V., et al., *Spot Variation Fluorescence Correlation Spectroscopy Allows for Superresolution Chronoscopy of Confinement Times in Membranes.* Biophysical Journal, 2011. **100**(11): p. 2839-2845.
104. Kim, J., J. Yoon, and R.C. Hayward, *Dynamic display of biomolecular patterns through an elastic creasing instability of stimuli-responsive hydrogels.* Nat Mater, 2010. **9**(2): p. 159-164.
105. Lumma, D., et al., *Dynamics of Large Semiflexible Chains Probed by Fluorescence Correlation Spectroscopy.* Physical Review Letters, 2003. **90**(21): p. 218301.
106. Zustiak, S.P., R. Nossal, and D.L. Sackett, *Hindered Diffusion in Polymeric Solutions Studied by Fluorescence Correlation Spectroscopy.* Biophysical Journal, 2011. **101**(1): p. 255-264.
107. Enderlein, J., *Polymer Dynamics, Fluorescence Correlation Spectroscopy, and the Limits of Optical Resolution.* Physical Review Letters, 2012. **108**(10): p. 108101.
108. Kremer, K. and G.S. Grest, *Dynamics of entangled linear polymer melts: A molecular-dynamics simulation.* The Journal of Chemical Physics, 1990. **92**(8): p. 5057-5086.
109. Hoefling, F., K.-U. Bamberg, and T. Franosch, *Anomalous transport resolved in space and time by fluorescence correlation spectroscopy.* Soft Matter, 2011. **7**(4): p. 1358-1363.
110. Weiss, M., et al., *Anomalous Subdiffusion Is a Measure for Cytoplasmic Crowding in Living Cells.* Biophysical Journal, 2004. **87**(5): p. 3518-3524.
111. Cherdhirankorn, T., et al., *Diffusion in Polymer Solutions Studied by Fluorescence Correlation Spectroscopy.* Journal of Physical Chemistry B, 2009. **113**(11): p. 3355-3359.
112. Vagias Apostolos, R.R., Koynov Kaloian, Jonas Ulrich, Butt Hans-Jürgen, Fytas George, Kosovan Peter, Lenz Olaf, Holm Christian, *Complex Tracer Diffusion Dynamics in Polymer Solutions.* Physical Review Letters, 111, 088301, 2013.
113. Wawrezinieck, L., et al., *Fluorescence Correlation Spectroscopy Diffusion Laws to Probe the Submicron Cell Membrane Organization.* Biophysical Journal, 2005. **89**(6): p. 4029-4042.
114. Mason, T.G. and D.A. Weitz, *Optical Measurements of Frequency-Dependent Linear Viscoelastic Moduli of Complex Fluids.* Physical Review Letters, 1995. **74**(7): p. 1250-1253.
115. Schwille, P., J. Korlach, and W.W. Webb, *Fluorescence correlation spectroscopy with single-molecule sensitivity on cell and model membranes.* Cytometry, 1999. **36**(3): p. 176-182.
116. Grunwald, D., et al., *Diffusion and binding properties investigated by Fluorescence Correlation Spectroscopy (FCS).* Current Pharmaceutical Biotechnology, 2005. **6**(5): p. 381-386.
117. Zhang, L. and S. Granick, *Slaved diffusion in phospholipid bilayers.* Proceedings of the National Academy of Sciences of the United States of America, 2005. **102**(26): p. 9118-9121.
118. Bacia, K., S.A. Kim, and P. Schwille, *Fluorescence cross-correlation spectroscopy in living cells.* Nat Meth, 2006. **3**(2): p. 83-89.
119. Cherdhirankorn, T., et al., *Effects of Chain Topology on the Tracer Diffusion in Star Polyisoprenes.* Macromolecules, 2009. **42**(22): p. 9183-9189.
120. Cherdhirankorn, T., et al., *Fluorescence Correlation Spectroscopy Study of Molecular Probe Diffusion in Polymer Melts.* Macromolecules, 2009. **42**(13): p. 4858-4866.
121. Mathias, E., et al., *Properties of small molecular drug loading and diffusion in a fluorinated PEG hydrogel studied by 1H molecular diffusion NMR and 19F spin diffusion NMR.* Colloid and Polymer Science, 2010. **288**(18): p. 1655-1663.

122. Rusu, L., D. Lumma, and J.O. Rädler, *Charge and Size Dependence of Liposome Diffusion in Semidilute Biopolymer Solutions.* Macromolecular Bioscience, 2010. **10**(12): p. 1465-1472.
123. Susoff, M. and W. Oppermann, *Influence of Cross-Linking on Probe Dynamics in Semidilute Polystyrene Systems.* Macromolecules, 2010. **43**(21): p. 9100-9107.
124. Zustiak, S.P., H. Boukari, and J.B. Leach, *Solute diffusion and interactions in cross-linked poly(ethylene glycol) hydrogels studied by Fluorescence Correlation Spectroscopy.* Soft Matter, 2010. **6**(15): p. 3609-3618.
125. Kalwarczyk, T., et al., *Comparative Analysis of Viscosity of Complex Liquids and Cytoplasm of Mammalian Cells at the Nanoscale.* Nano Letters, 2011. **11**(5): p. 2157-2163.
126. Felderhof, B.U., *Estimating the viscoelastic moduli of complex fluids from observation of Brownian motion of a particle confined to a harmonic trap.* Journal of Chemical Physics, 2011. **134**(204910).
127. Hellmann, M., et al., *Challenges in determining anomalous diffusion in crowded fluids.* Journal of Physics-Condensed Matter, 2011. **23**(23): p. 234113.
128. Ochab-Marcinek, A. and R. Holyst, *Scale-dependent diffusion of spheres in solutions of flexible and rigid polymers: mean square displacement and autocorrelation function for FCS and DLS measurements.* Soft Matter, 2011. **7**(16): p. 7366-7374.
129. Eliazar, I. and J. Klafter, *On the generation of anomalous and ultraslow diffusion.* Journal of Physics A: Mathematical and Theoretical, 2011. **44**(40): p. 405006.
130. Ernst, D., et al., *Fractional Brownian motion in crowded fluids.* Soft Matter, 2012. **8**(18): p. 4886-4889.
131. Dethoff, E.A., et al., *Functional complexity and regulation through RNA dynamics.* Nature, 2012. **482**(7385): p. 322-330.
132. Roy, D., W.L.A. Brooks, and B.S. Sumerlin, *New directions in thermoresponsive polymers.* Chemical Society Reviews, 2013.
133. Kuckling, D., M.E. Harmon, and C.W. Frank, *Photo-Cross-Linkable PNIPAAm Copolymers. 1. Synthesis and Characterization of Constrained Temperature-Responsive Hydrogel Layers.* Macromolecules, 2002. **35**(16): p. 6377-6383.
134. Peppas, N.A., et al., *Hydrogels in Biology and Medicine: From Molecular Principles to Bionanotechnology.* Advanced Materials, 2006. **18**(11): p. 1345-1360.
135. Matsunaga, T., et al., *Structure Characterization of Tetra-PEG Gel by Small-Angle Neutron Scattering.* Macromolecules, 2009. **42**(4): p. 1344-1351.
136. Hao, J. and R.A. Weiss, *Viscoelastic and Mechanical Behavior of Hydrophobically Modified Hydrogels.* Macromolecules, 2011. **44**(23): p. 9390-9398.
137. White, E.M., et al., *Advances in smart materials: Stimuli-responsive hydrogel thin films.* Journal of Polymer Science Part B: Polymer Physics, 2013. **51**(14): p. 1084-1099.
138. Tanaka, F., et al., *Temperature- and Tension-Induced Coil−Globule Transition of Poly(N-isopropylacrylamide) Chains in Water and Mixed Solvent of Water/Methanol.* Macromolecules, 2009. **42**(4): p. 1321-1330.
139. Sato, K., et al., *PH- and sugar-sensitive layer-by-layer films and microcapsules for drug delivery.* Advanced Drug Delivery Reviews, 2011. **63**(9): p. 809-821.
140. Annaka, M., et al., *Salt-induced volume phase transition of poly(N-isopropylacrylamide) gel.* The Journal of Chemical Physics, 2000. **113**(14): p. 5980-5985.
141. Junk, M.J.N., et al., *Analysis of Optical Gradient Profiles during Temperature- and Salt-Dependent Swelling of Thin Responsive Hydrogel Films.* Langmuir, 2010. **26**(14): p. 12253-12259.
142. Longo, G.S., M.O. de la Cruz, and I. Szleifer, *Molecular theory of weak polyelectrolyte thin films.* Soft Matter, 2012. **8**(5): p. 1344-1354.
143. Li, P.H., et al., *Thermosensitive poly(N-isopropylacrylamide-co-glycidyl methacrylate) microgels for controlled drug release.* Colloids and Surfaces B-Biointerfaces, 2013. **101**: p. 251-255.

144. Melzak, K.A., et al., *Simultaneous Measurement of Mechanical and Surface Properties in Thermoresponsive, Anchored Hydrogel Films.* Langmuir, 2012. **28**(35): p. 12871-12878.
145. Bittrich, E., et al., *Temperature-Sensitive Swelling of Poly(N-isopropylacrylamide) Brushes with Low Molecular Weight and Grafting Density.* Langmuir, 2012. **28**(7): p. 3439-3448.
146. Reinhart, C.T. and N.A. Peppas, *Solute diffusion in swollen membranes. 2. Influence of crosslinking on diffusive properties.* Journal of Membrane Science, 1984. **18**(MAR): p. 227-239.
147. Seiffert, S. and W. Oppermann, *Diffusion of linear macromolecules and spherical particles in semidilute polymer solutions and polymer networks.* Polymer, 2008. **49**(19): p. 4115-4126.
148. Susoff, M. and W. Oppermann, *Dynamics of labeled linear polystyrenes in semi-dilute polystyrene matrices in the uncross-linked and cross-linked states.* Macromolecular Symposia, 2010. **291-292**(1): p. 212-220.
149. Yanbin, W., S. Joseph, and N.R. Aluru, *Effect of cross-linking on the diffusion of water, ions, and small molecules in hydrogels.* Journal of Physical Chemistry B, 2009. **113**(11): p. 3512-3520.
150. Kurzbach, D., et al., *How Structure-Related Collapse Mechanisms Determine Nanoscale Inhomogeneities in Thermoresponsive Polymers.* Macromolecules, 2012. **45**(18): p. 7535-7548.
151. Yang, Y.F., et al., *Reversible Changes in Solution pH Resulting from Changes in Thermoresponsive Polymer Solubility.* Journal of the American Chemical Society, 2012. **134**(17): p. 7378-7383.
152. Fang, F. and I. Szleifer, *Controlled release of proteins from polymer-modified surfaces.* Proceedings of the National Academy of Sciences, 2006. **103**(15): p. 5769-5774.
153. Carr, J.K., et al., *Heterogeneous Translational Dynamics of Rhodamine B in Polyelectrolyte Multilayer Thin Films Observed by Single Molecule Microscopy.* Langmuir, 2009. **25**(14): p. 8330-8339.
154. Goychuk, I., *Viscoelastic subdiffusion: Generalized Langevin equation approach*, in *Advances in Chemical Physics, Vol 150*, S.A. Rice and A.R. Dinner, Editors. 2012, Wiley-Blackwell: Malden. p. 187-253.
155. Jeon, J.H. and R. Metzler, *Inequivalence of time and ensemble averages in ergodic systems: Exponential versus power-law relaxation in confinement.* Physical Review E, 2012. **85**(2).
156. Modesti, G., et al., *Diffusion in Model Networks as Studied by NMR and Fluorescence Correlation Spectroscopy.* Macromolecules, 2009. **42**(13): p. 4681-4689.
157. Michelman-Ribeiro, A., et al., *Fluorescence Correlation Spectroscopy Study of Probe Diffusion in Poly(vinyl alcohol) Solutions and Gels.* Macromolecular Symposia, 2005. **227**(1): p. 221-230.
158. Ward, M.A. and T.K. Georgiou, *Thermoresponsive Polymers for Biomedical Applications.* Polymers, 2011. **3**(3): p. 1215-1242.
159. Yordanov, S., et al., *Note: An easy way to enable total internal reflection-fluorescence correlation spectroscopy (TIR-FCS) by combining commercial devices for FCS and TIR microscopy.* Review of Scientific Instruments, 2011. **82**(3).
160. Berger, J., et al., *Structure and interactions in covalently and ionically crosslinked chitosan hydrogels for biomedical applications.* European Journal of Pharmaceutics and Biopharmaceutics, 2004. **57**(1): p. 19-34.
161. Echeverria, C., N.A. Peppas, and C. Mijangos, *Novel strategy for the determination of UCST-like microgels network structure: effect on swelling behavior and rheology.* Soft Matter, 2012. **8**(2): p. 337-346.
162. Heskins, M. and J.E. Guillet, *Solution Properties of Poly(N-isopropylacrylamide).* Journal of Macromolecular Science: Part A - Chemistry, 1968. **2**(8): p. 1441-1455.
163. Zhou, X., et al., *Constructing the Phase Diagram of an Aqueous Solution of Poly(N-isopropyl acrylamide) by Controlled Microevaporation in a Nanoliter Microchamber.* Macromolecular Rapid Communications, 2008. **29**(16): p. 1363-1367.

164. Junk, M.J.N., R. Berger, and U. Jonas, *Atomic Force Spectroscopy of Thermoresponsive Photo-Cross-Linked Hydrogel Films.* Langmuir, 2010. **26**(10): p. 7262-7269.
165. Sinner, E.K., et al., *Molecularly controlled functional architectures.* Materials Today, 2010. **13**(4): p. 46-55.
166. Raccis, R., et al., *Confined Diffusion in Periodic Porous Nanostructures.* Acs Nano, 2011. **5**(6): p. 4607-4616.
167. Szymanski, J. and M. Weiss, *Elucidating the origin of anomalous diffusion in crowded fluids.* Physical Review Letters, 2009. **103**(3): p. 038102 (4 pp.)-038102 (4 pp.)038102 (4 pp.).
168. Forbes, D.C. and N.A. Peppas, *Oral delivery of small RNA and DNA.* Journal of Controlled Release, 2012. **162**(2): p. 438-445.
169. Lee, S.C., I.K. Kwon, and K. Park, *Hydrogels for delivery of bioactive agents: A historical perspective.* Advanced Drug Delivery Reviews, 2013. **65**(1): p. 17-20.
170. Kruger, M. and M. Rauscher, *Diffusion of a sphere in a dilute solution of polymer coils.* Journal of Chemical Physics, 2009. **131**(9): p. 094902 (8 pp.)-094902 (8 pp.).
171. Shvartzman-Cohen, R., et al., *Selective Dispersion of Single-Walled Carbon Nanotubes in the Presence of Polymers: the Role of Molecular and Colloidal Length Scales.* Journal of the American Chemical Society, 2004. **126**(45): p. 14850-14857.
172. Brown, W., *Diffusion of poly(ethylene oxide) in semidilute aqueous solution: Dynamic light scattering and gradient diffusion.* Polymer, 1985. **26**(11): p. 1647-1650.
173. Håkansson, B., M. Nydén, and O. Söderman, *The influence of polymer molecular-weight distributions on pulsed field gradient nuclear magnetic resonance self-diffusion experiments.* Colloid and Polymer Science, 2000. **278**(5): p. 399-405.
174. Homouz, D., et al., *Crowded, cell-like environment induces shape changes in aspherical protein.* Proceedings of the National Academy of Sciences of the United States of America, 2008. **105**(33): p. 11754-11759.
175. Schneider, G.F. and C. Dekker, *DNA sequencing with nanopores.* Nat Biotech, 2012. **30**(4): p. 326-328.
176. Manrao, E.A., et al., *Reading DNA at single-nucleotide resolution with a mutant MspA nanopore and phi29 DNA polymerase.* Nat Biotech, 2012. **30**(4): p. 349-353.
177. Mihovilovic, M., N. Hagerty, and D. Stein, *Statistics of DNA Capture by a Solid-State Nanopore.* Physical Review Letters, 2013. **110**(2): p. 028102.
178. Kohli, I. and A. Mukhopadhyay, *Diffusion of Nanoparticles in Semidilute Polymer Solutions: Effect of Different Length Scales.* Macromolecules, 2012. **45**(15): p. 6143-6149.
179. Phillies, G.D.J., *Quantitative prediction of .alpha. in the scaling law for self-diffusion.* Macromolecules, 1988. **21**(10): p. 3101-3106.
180. Cheng, Y., R.K. Prud'homme, and J.L. Thomas, *Diffusion of Mesoscopic Probes in Aqueous Polymer Solutions Measured by Fluorescence Recovery after Photobleaching.* Macromolecules, 2002. **35**(21): p. 8111-8121.
181. A.Vagias , P.K., C. Holm, H.-J.Butt, K.Koynov, G. Fytas, *Tracer mobility in aqueous poly (N-isopropyl-acrylamide) grafted networks.Effect of interactions and permanent crosslinks.* Special Issue in 'Progress in Colloid and Polymer Science', 2013.
182. Brochard, F. and P.G.d. Gennes, *Polymer-Polymer Interdiffusion.* EPL (Europhysics Letters), 1986. **1**(5): p. 221.
183. Burczak, K., E. Gamian, and A. Kochman, *Long-term in vivo performance and biocompatibility of poly(vinyl alcohol) hydrogel macrocapsules for hybrid-type artificial pancreas.* Biomaterials, 1996. **17**(24): p. 2351-2356.
184. Peng, P., et al., *Concurrent elution of calcium phosphate and macromolecules from alginate/chitosan hydrogel coatings.* Biointerphases, 2008. **3**(4): p. 105-116.
185. A. Michelman-Ribeiro, F.H., R. Nossal, and H. Boukari, *Probe diffusion in linear Poly(Vinyl) Alcohol polymer solutions by Fluorescence Correlation Spectroscopy.* BioMacromolecules, 2007. **8**(5): p. 1595-1600

186. Jia, P., et al., *Dynamic exchange of counterions of polystyrene sulfonate.* The Journal of Chemical Physics, 2012. **136**(8): p. 084904.